

© 2009 Brian Alan Tom

NUCLEAR SPIN DEPENDENCE IN REACTIONS OF  $\text{H}_3^+$  IN THE  
LABORATORY AND THE INTERSTELLAR MEDIUM

BY

BRIAN ALAN TOM

B.S., University of California at San Diego, 1991

M.A., The George Washington University, 1999

M.S., Air Force Institute of Technology, 2006

DISSERTATION

Submitted in partial fulfillment of the requirements  
for the degree of Doctor of Philosophy in Chemical Physics  
in the Graduate College of the  
University of Illinois at Urbana-Champaign, 2009

Urbana, Illinois

Doctoral Committee:

Assistant Professor Benjamin J. McCall, Chair

Professor James M. Lisy

Professor Martin H. Gruebele

Assistant Professor Benjamin L. Lev

# Abstract

Hydrogen is the most abundant element in the universe. For this reason, the chemistry of the interstellar medium is largely dominated by the interaction of hydrogenic neutrals and ions. The hydrogen molecule,  $\text{H}_2$ , and the simplest polyatomic ion,  $\text{H}_3^+$ , each exist in one of two forms identified as *ortho* or *para*, which are defined by their total nuclear spins. These spin modifications have different spectral signatures which can be observed both in the laboratory and the interstellar medium.  $\text{H}_2$  and  $\text{H}_3^+$  have been used to probe the conditions of interstellar clouds, but there are gaps in our understanding of the mechanisms by which the *para*- $\text{H}_3^+$  fraction is enriched in diffuse clouds and *para*- $\text{H}_2$  is enriched in dense molecular clouds.

Dissociative recombination is the primary destruction mechanism for  $\text{H}_3^+$  in diffuse clouds. The rate coefficient for this process has been measured for highly enriched *para*- $\text{H}_3^+$  and compared with the rate coefficients for less *para*-enriched plasmas. The results show that dissociative recombination for *para*- $\text{H}_3^+$  occurs at a faster rate than for *ortho*- $\text{H}_3^+$ , which validates recent theoretical predictions but does not explain the enrichment of *para*- $\text{H}_3^+$  in the diffuse interstellar medium.

The  $\text{H}_3^+ + \text{H}_2$  reaction, which is arguably the most common bimolecular reaction in the universe, is explored as the possible mechanism by which the enrichment of both species can occur. Two models that we developed from recent theoretical work are used to predict the behavior of the reaction under low temperature conditions. Laboratory measurements were taken over a range from 300 K down to 80 K, and demonstrate that the branching ratio of proton hop to hydrogen exchange is temperature dependent. This is the first study of this reaction at the cold astrophysical temperatures where it occurs most of the time.

A comparison of the experimental results with observational data provides strong evidence that this reaction is the driving mechanism for the steady state enrichment of *para*- $\text{H}_3^+$  in diffuse clouds, and predictions from the models imply that it is also responsible for the enrichment of *para*- $\text{H}_3^+$  and *para*- $\text{H}_2$  in dense clouds. The results of this work have implications for the use of the  $\text{H}_3^+$  spin modifications as astrophysical probes, for understanding the deuterium chemistry of the interstellar medium, and for the fundamental chemical physics of these very simple molecules.

*To Nicole, Lauren, and Emma, who once endured dad's childish delight in noisy flying machines, and who lately have endured his childhood dream of exploring the universe. But mostly to Julie without whose love, support, and infinite patience he would be forced to grow up.*



# Acknowledgments

This dissertation would certainly not have been possible without the guidance and support of Ben McCall. He was willing to take in this non-traditional student who wanted to learn how to become a scientist. He stepped back and gave me enough space to stumble when I absolutely needed to stumble, but stepped in to rescue me when I needed rescuing. For his patience I will always be thankful, and I have learned more from his example than he will ever know.

I'd like to express my sincere thanks to Professors Jim Lisy, Martin Gruebele, and Benjamin Lev for their time, thoughtful review, inputs, and guidance, as well as their flexibility in light of my unusual timeline. I'm also thankful to, and will miss my friends in the School of Chemical Sciences machine shop, as well as the women of the Inorganic, Materials, and Physical Chemistry administrative office for their tireless efforts and support. Finally, I'm thankful to Jim Wentz who spent untold hours instructing me while troubleshooting many of my broken electronic devices.

I will always be indebted to my labmates for their help and guidance. In particular I would like to thank Brian Brumfield for his example of careful, analytical thought (and humorous discussions), and Andrew Mills who was always willing to help and who re-arranged his schedule to build a difference frequency laser without which this research would not have been possible. Without Brian Siller's expertise and help with computers and software, some projects would have taken much longer than they did, so I thank him in addition to Carrie Kauffman for her work on the second difference frequency laser. Special thanks to Kyle Crabtree, to whom I always felt a kinship but whose intellect I will never match, for his work on the difference frequency lasers and for his help in countless other areas, as well as to Susanna Widicus Weaver whose calming scientific wisdom was priceless to me. Finally, I am indebted to 'Team Hydrogen;' Brett McGuire, Michael Wiczer, Lauren Moore, Siddartha Bhasker, Tom Wood, and Preston Buscay...dedicated undergrads who kept me on my toes and who built the instruments and collected the data described in the pages that follow.

I would especially like to thank my kids, Nicole (who drew some of the diagrams in this document), Lauren, and Emma for enduring my absence in so many ways over the last three years. Most importantly I am so very blessed by my wife Julie, who worked as hard as I did but as a single parent as I went through this process.

Finally, I am thankful to God, the Spirit, and my Lord Jesus. Together and as One They have given me the strength to persevere through this challenging program, and are the focus and guiding source of inspiration and purpose in my life.

# Table of Contents

<b>List of Tables</b> . . . . .	<b>vii</b>
<b>List of Figures</b> . . . . .	<b>ix</b>
<b>Chapter 1 Introduction</b> . . . . .	<b>1</b>
1.1 Molecular H <sub>2</sub> . . . . .	2
1.2 The simplest polyatomic ion, H <sub>3</sub> <sup>+</sup> . . . . .	4
1.3 Spin modifications and the interstellar medium . . . . .	8
<b>Chapter 2 <i>Para</i>-H<sub>2</sub> production and measurement</b> . . . . .	<b>10</b>
2.1 Theory . . . . .	10
2.2 The converter . . . . .	11
2.2.1 Generating <i>para</i> -H <sub>2</sub> . . . . .	14
2.2.2 Storage . . . . .	15
2.3 Quantifying the enrichment . . . . .	16
2.3.1 Thermal conductance . . . . .	16
2.3.2 Nuclear magnetic resonance . . . . .	18
<b>Chapter 3 Laser systems and spectroscopic methods</b> . . . . .	<b>21</b>
3.1 Difference frequency generation system I . . . . .	21
3.1.1 Titanium:sapphire pump laser . . . . .	21
3.1.2 Nd:YAG signal laser . . . . .	24
3.1.3 Additional DFG components . . . . .	25
3.1.4 The LiNbO <sub>3</sub> nonlinear crystal . . . . .	26
3.1.5 Mid-IR light path after the conversion . . . . .	28
3.2 Difference frequency generation system II . . . . .	28
3.2.1 Nd:YVO <sub>4</sub> pump laser . . . . .	28
3.2.2 Dye signal laser . . . . .	29
3.2.3 Additional DFG components . . . . .	29
3.2.4 The MgO-doped LiNbO <sub>3</sub> nonlinear crystal . . . . .	30
3.3 Spectroscopic methods . . . . .	30
3.3.1 Continuous wave cavity ringdown spectroscopy . . . . .	30
3.3.2 Multipass absorption spectroscopy . . . . .	32
<b>Chapter 4 Plasma sources</b> . . . . .	<b>34</b>
4.1 Pulsed solenoid . . . . .	34
4.1.1 Design . . . . .	35
4.1.2 Operation . . . . .	35
4.1.3 Plasma characteristics . . . . .	38
4.2 Hollow cathode cell . . . . .	41
4.2.1 Design . . . . .	41
4.2.2 Operation . . . . .	42

4.2.3	Plasma characteristics . . . . .	44
4.3	Future sources . . . . .	52
4.3.1	CW supersonic expansion source . . . . .	52
4.3.2	Pulsed piezo source . . . . .	52
<b>Chapter 5</b>	<b>Dissociative recombination . . . . .</b>	<b>55</b>
5.1	History and theory of $\text{H}_3^+$ dissociative recombination . . . . .	55
5.2	Experiments . . . . .	58
5.2.1	Spectroscopy . . . . .	58
5.2.2	Storage ring . . . . .	64
5.3	Results . . . . .	66
5.3.1	Astrophysical implications . . . . .	69
<b>Chapter 6</b>	<b><math>\text{H}_3^+ + \text{H}_2</math> reaction dynamics . . . . .</b>	<b>72</b>
6.1	Theory . . . . .	72
6.1.1	Statistical weights . . . . .	72
6.1.2	The high temperature model . . . . .	77
6.1.3	Low temperature model . . . . .	85
6.2	Experiments . . . . .	90
6.2.1	Hollow cathode cell experiments . . . . .	90
6.2.2	Expansion experiments . . . . .	100
6.2.3	Future work . . . . .	104
6.3	Analysis and astrophysical implications . . . . .	105
6.3.1	Comparison of experimental results and models . . . . .	106
6.3.2	Temperature . . . . .	107
6.3.3	Astrophysical implications for the $\text{H}_3^+$ <i>ortho/para</i> ratio . . . . .	110
6.3.4	Astrophysical implications for the $\text{H}_2$ <i>ortho/para</i> ratio . . . . .	112
<b>Chapter 7</b>	<b>References . . . . .</b>	<b>113</b>
<b>Appendix A</b>	<b>Spectroscopic data . . . . .</b>	<b>119</b>
<b>Appendix B</b>	<b>Boltzmann distributions . . . . .</b>	<b>131</b>
<b>Appendix C</b>	<b>Select derivations . . . . .</b>	<b>140</b>
C.1	Deriving the branching weights for the identity, hop and exchange reactions . . . . .	141
C.2	The detailed derivation of equation (6.20) from equation (6.18) . . . . .	142
<b>Appendix D</b>	<b>Schematics . . . . .</b>	<b>145</b>
<b>Appendix E</b>	<b>Solid hydrogen experiment . . . . .</b>	<b>149</b>
E.1	Experimental details . . . . .	150
E.1.1	Indium gaskets . . . . .	150
E.1.2	Temperature controller . . . . .	150
E.1.3	Making the crystal . . . . .	151
E.1.4	Taking index measurements . . . . .	152
E.2	Data analysis . . . . .	152
<b>Author's biography</b>	<b>. . . . .</b>	<b>159</b>

# List of Tables

1.1	$S_2^*$ character table that results from $E^* \otimes S_2$ . . . . .	3
1.2	Tallying the effects of nuclear spin permutations in $H_2$ . . . . .	3
1.3	$S_3^*$ character table. . . . .	5
1.4	$H_3^+$ selection rules. . . . .	6
1.5	$H_3^+$ states, and lines from $\nu_2 \leftarrow 0$ used in this work. . . . .	7
2.1	The back conversion of <i>para</i> - $H_2$ in various storage vessels as measured by thermal conductance and NMR. . . . .	15
4.1	Excitation and rotational temperatures measured using normal, <i>para</i> , and argon-diluted $H_2$ . The ‘a’ and ‘b’ designations identify temperatures measured in close succession. Points 5 were not used to determine the average $T_{rot}$ for the experiment, but are included to show that $T_{rot}$ can be accurately measured for a hydrogen sample diluted in argon. . . . .	39
4.2	Pulsed source number densities. All values were calculated except for the $H_3^+$ at 39 mm, which was measured spectroscopically. . . . .	41
4.3	Some of the data used to calculate the kinetic temperature of the water-cooled plasma in the hollow cathode cell. . . . .	45
4.4	Data used to calculate the kinetic temperature of the liquid $N_2$ -cooled plasma in the hollow cathode cell. . . . .	48
4.5	Hollow cathode number densities. The $H_2$ values are calculated, while the $H_3^+$ values were measured spectroscopically. . . . .	52
5.1	The <i>para</i> - $H_3^+$ enrichments used in the DR experiments. . . . .	61
5.2	Boltzmann distributions for <i>para</i> - $H_3^+$ ( $80 \pm 20$ K). . . . .	62
5.3	Boltzmann distributions for <i>ortho</i> - $H_3^+$ ( $80 \pm 20$ K). . . . .	63
5.4	Thermal rate coefficients for a range of $T_e$ . . . . .	70
6.1	The product spin weights for $H_2 + H_2^+ \rightarrow H_3^+ + H_2$ . . . . .	74
6.2	The product spin weights for $H_3^+ + H_2 \rightarrow H_2 + H_3^+$ . . . . .	75
6.3	The product spin weights for $H_3^+ + H_2 \rightarrow H_2 + H_3^+$ , broken down by reaction pathway. . . . .	76
6.4	A concise summary of product spin fractions for $H_3^+ + H_2 \rightarrow H_2 + H_3^+$ . . . . .	77
6.5	The <i>para</i> - $H_3^+$ enrichment and $\alpha$ calculated for different <i>para</i> - $H_2$ enrichments in the $310 \pm 20$ K hollow cathode discharge. The average $\alpha$ and the best fit $\alpha$ for the high temperature model are also presented. The uncertainties are $1 \sigma$ . . . . .	93
6.6	The <i>para</i> - $H_3^+$ enrichment and $\alpha$ calculated for different <i>para</i> - $H_2$ enrichments in the $180 \pm 10$ K hollow cathode discharge. Best fit $\alpha$ ’s for high and low temperature models are also presented. The uncertainties are $1 \sigma$ . . . . .	97
6.7	The <i>para</i> - $H_3^+$ enrichment and $\alpha$ calculated for different <i>para</i> - $H_2$ enrichments in the $130 \pm 10$ K hollow cathode discharge. Best fit $\alpha$ ’s for high and low temperature models are also presented. The uncertainties are $1 \sigma$ . . . . .	101

6.8	The $para\text{-H}_3^+$ enrichment and $\alpha$ calculated for different $para\text{-H}_2$ enrichments in the $80\pm 20$ K supersonic expansion. Best fit $\alpha$ 's for high and low temperature models are also presented. . . . .	102
6.9	The $para\text{-H}_3^+$ fraction over a range of $para\text{-H}_2$ enrichments and dilutions. . . . .	104
6.10	The excitation temperature ( $T_{ex}$ ) calculated for different $para\text{-H}_2$ enrichments at 310 K. . . . .	108
6.11	The excitation temperature ( $T_{ex}$ ) calculated for different $para\text{-H}_2$ enrichments at 180 K. . . . .	108
6.12	The excitation temperature ( $T_{ex}$ ) calculated for different $para\text{-H}_2$ enrichments at 130 K. . . . .	108
6.13	The excitation temperature ( $T_{ex}$ ) calculated for different $para\text{-H}_2$ enrichments at 80 K. . . . .	108
6.14	The temperature dependence of the ratio $g_{I(ortho)}Z_{para}/g_{I(para)}Z_{ortho}$ . . . . .	109
A.1	Expansion data for normal- $\text{H}_2$ ( $80\pm 20$ K). This is representative data, there were many more normal- $\text{H}_2$ measurements. . . . .	120
A.2	Expansion data for 99% enriched $para\text{-H}_2$ ( $80\pm 20$ K). Data for sample 3 could not be fit with a Gaussian curve. . . . .	121
A.3	Expansion data for 97% enriched $para\text{-H}_2$ ( $80\pm 20$ K). . . . .	122
A.4	Expansion data for a 1% dilution of 97% enriched $para\text{-H}_2$ in Ar ( $80\pm 20$ K). . . . .	123
A.5	Expansion data for a 90% enriched $para\text{-H}_2$ ( $80\pm 20$ K). . . . .	124
A.6	Expansion data for a 75% enriched $para\text{-H}_2$ ( $80\pm 20$ K). $R(1,0)$ data for points 1 and 3 could not be fit with a Gaussian curve. . . . .	125
A.7	Hollow cathode cell data for $p_2=.990\pm.005$ , $(1)/(0)=.018\pm.005$ , ( $310\pm 20$ K). . . . .	126
A.8	Hollow cathode cell data for $p_2=.989\pm.005$ , $(1)/(0)=.020\pm.005$ , ( $310\pm 20$ K). . . . .	126
A.9	Hollow cathode cell data for $p_2=.809\pm.007$ , $(1)/(0)=.411\pm.007$ , ( $310\pm 20$ K). . . . .	126
A.10	Hollow cathode cell data for $p_2=.757\pm.007$ , $(1)/(0)=.559\pm.007$ , ( $310\pm 20$ K). . . . .	127
A.11	Hollow cathode cell data for $p_2=.659\pm.025$ , $(1)/(0)=.898\pm.025$ , ( $310\pm 20$ K). . . . .	127
A.12	Hollow cathode cell data for $p_2=.441\pm.007$ , $(1)/(0)=2.205\pm.007$ , ( $310\pm 20$ K). . . . .	127
A.13	Hollow cathode cell data for $p_2=.251$ , $(1)/(0)=5.189$ ( $310\pm 20$ K). . . . .	128
A.14	Hollow cathode cell data for $p_2=.251$ , $(1)/(0)=5.189$ ( $310\pm 20$ K). . . . .	128
A.15	Hollow cathode cell data for $p_2=.990\pm.005$ , $(1)/(0)=.013\pm.005$ , ( $180\pm 10$ K). . . . .	129
A.16	Hollow cathode cell data for $p_2=.815\pm.007$ , $(1)/(0)=.289\pm.007$ , ( $180\pm 10$ K). . . . .	129
A.17	Hollow cathode cell data for $p_2=.251$ , $(1)/(0)=3.791$ , ( $180\pm 10$ K). . . . .	129
A.18	Hollow cathode cell data for $p_2=.989\pm.005$ , $(1)/(0)=.012\pm.005$ , ( $130\pm 10$ K). . . . .	130
A.19	Hollow cathode cell data for $p_2=.900\pm.025$ , $(1)/(0)=.122\pm.025$ , ( $130\pm 10$ K). . . . .	130
A.20	Hollow cathode cell data for $p_2=.637\pm.025$ , $(1)/(0)=.625\pm.025$ , ( $130\pm 10$ K). . . . .	130
B.1	Boltzmann distributions for $para\text{-H}_3^+$ ( $310\pm 20$ K). . . . .	132
B.2	Boltzmann distributions for $ortho\text{-H}_3^+$ ( $310\pm 20$ K). . . . .	133
B.3	Boltzmann distributions for $para\text{-H}_3^+$ ( $180\pm 10$ K). . . . .	134
B.4	Boltzmann distributions for $ortho\text{-H}_3^+$ ( $180\pm 10$ K). . . . .	135
B.5	Boltzmann distributions for $para\text{-H}_3^+$ ( $130\pm 10$ K). . . . .	136
B.6	Boltzmann distributions for $ortho\text{-H}_3^+$ ( $130\pm 10$ K). . . . .	137
B.7	Boltzmann distributions for $para\text{-H}_3^+$ ( $80\pm 20$ K). . . . .	138
B.8	Boltzmann distributions for $ortho\text{-H}_3^+$ ( $80\pm 20$ K). . . . .	139

# List of Figures

1.1	The astronomer's periodic table (reproduced from [6]). . . . .	1
1.2	The reaction network that begins with $\text{H}_3^+$ (reproduced from [6]). . . . .	2
1.3	Ground state energy levels of $\text{H}_3^+$ . . . . .	7
2.1	(a) Schematic of the <i>para</i> - $\text{H}_2$ converter with and without the vacuum shroud installed. (b) The approximate dimensions of the stainless tubing. . . . .	12
2.2	Coil section where the catalytic conversion from <i>ortho</i> - $\text{H}_2$ to <i>para</i> - $\text{H}_2$ takes place. . .	13
2.3	The thermal conductance cell. . . . .	17
2.4	A calibration curve for the thermal conductance cell. . . . .	18
2.5	Comparison of thermal conductance and NMR measurements made with TMS. Error bars for the thermal conductance measurements are displayed, and are $\pm 0.8\%$ . . . .	19
2.6	Difference between NMR measurements without TMS and the predicted values of <i>para</i> - $\text{H}_2$ enrichment. Error bars represent $1\sigma$ . . . . .	20
3.1	DFG System I (drawn by N. Tom). . . . .	22
3.2	The ring arrangement of the titanium sapphire laser (adapted from [77, pg. 33]). . .	24
3.3	Phase matching in a non-linear crystal (adapted from [81, Fig. 11]). . . . .	27
3.4	DFG system II (drawn by N. Tom). . . . .	29
3.5	An illustration of a typical buildup/ringdown profile. . . . .	31
3.6	White cell mirror configuration (M1,M2,M3) and their centers of curvature (open circles 1,2,3). . . . .	33
3.7	White cell mirrors (M1,M2,M3). . . . .	33
4.1	The pulsed solenoid source. The cutaway shows the interior spring, armature, and poppet. . . . .	34
4.2	The ringdown/pulsed source experimental setup. The source was mounted horizontally in the experiment, but is shown here in a vertical orientation through a cutaway for simplicity. . . . .	36
4.3	Gas pulses were synchronized with ringdown events, which occurred periodically with the dithering of one of the ringdown mirrors. . . . .	37
4.4	The predicted temperature, and collisions (per 0.1 mm step) in a hydrogen expansion, calculated using [99, pg. 18]. . . . .	39
4.5	The hollow cathode plasma cell. . . . .	42
4.6	The hollow cathode cell experimental setup. . . . .	43
4.7	The hollow cathode current pulse (a 100 $\mu\text{s}$ pulse is shown, but a 200 $\mu\text{s}$ pulsewidth was used in the experiment). . . . .	43
4.8	Spectra taken for the calculation of kinetic temperature in the hollow cathode cell plasma. (a) normal- $\text{H}_2$ , (b) 99.9% <i>para</i> - $\text{H}_2$ . . . . .	45
4.9	$\text{H}_3^+$ excitation temperature measured in a water-cooled, normal- $\text{H}_2$ plasma in the hollow cathode cell. . . . .	46
4.10	$\text{H}_3^+$ excitation temperature in a liquid $\text{N}_2$ -cooled, normal- $\text{H}_2$ plasma in the hollow cathode cell. . . . .	47

4.11	An example where $T_{ex}=135.8$ K, as measured by comparing the peak heights of scanned $R(1,0)$ and $R(1,1)^u$ absorption features. . . . .	48
4.12	$H_3^+$ rotational temperature in 99% enriched <i>para</i> - $H_2$ measured in the $130 \pm 10$ K liquid $N_2$ -cooled plasma. . . . .	49
4.13	$H_3^+$ rotational temperature in two water-cooled plasmas. The $T_{rot}$ is colder than expected. . . . .	50
4.14	The InSb voltage response to power changes at the $R(1,0)$ , $R(1,1)^u$ , and $R(2,2)^\ell$ wavelengths. . . . .	51
4.15	Continuous flow supersonic expansion ion source (courtesy of K. Crabtree). . . . .	53
4.16	New piezo pulsed source (drawings by P. Buscay). . . . .	54
5.1	Direct dissociative recombination; the arrow represents the capture of an electron (energy $E_{Direct}$ ) into an eigenstate of a dissociating potential. . . . .	57
5.2	Indirect dissociative recombination; the arrow represents an electron that has been captured into a Rydberg state which subsequently mixes with a dissociating state. . . . .	57
5.3	Tunneling dissociative recombination; the arrows represent electrons excited to states from which they tunnel to dissociating states. . . . .	58
5.4	Current-normalized spectrum (normal $H_2$ ). . . . .	59
5.5	Current-normalized spectrum (97% <i>para</i> - $H_2$ ). . . . .	60
5.6	Current-normalized spectrum (diluted 97% <i>para</i> - $H_2$ ). . . . .	60
5.7	The CRYRING ion storage ring. . . . .	64
5.8	The dissociative recombination rate coefficient for three different <i>para</i> - $H_3^+$ enrichments. . . . .	66
5.9	Extrapolated dissociative recombination rate coefficients for 100% <i>para</i> and 100% <i>ortho</i> - $H_3^+$ . . . . .	67
5.10	Comparison between previous $H_3^+$ DR experiments and the present results (normal- $H_2$ ). Error bars are removed for ease the comparison. . . . .	68
5.11	The thermal rate coefficient $\alpha(T_e)$ for 49.1% enriched <i>para</i> - $H_3^+$ (normal- $H_2$ ). . . . .	70
5.12	The extrapolated thermal rate coefficients $\alpha(T_e)$ for <i>ortho</i> - and <i>para</i> - $H_3^+$ . . . . .	71
6.1	The time dependence of <i>para</i> - $H_2$ ( $p_2$ ) and <i>para</i> - $H_3^+$ ( $p_3$ ) enrichments, as predicted by the high temperature model. . . . .	83
6.2	Relationship between $p_2$ and $p_3$ based on the high temperature model. . . . .	84
6.3	Relationship between $p_2$ and $p_3$ based on the low temperature model. . . . .	87
6.4	The time dependence of $p_2$ and $p_3$ at low temperature. . . . .	89
6.5	A typical discharge pulse; the nominal time from discharge turn-on to the measurement point is depicted. . . . .	92
6.6	$R(1,1)^u$ and $R(1,0)$ absorption data taken in the hollow cathode at $310 \pm 20$ K. The % labels indicate the <i>para</i> - $H_2$ enrichment of the feed gas. . . . .	94
6.7	Measured <i>para</i> - $H_3^+$ enrichments at $310 \pm 20$ K plotted along with a high temperature model for $\alpha=2.15$ . . . . .	95
6.8	$R(1,1)^u$ and $R(1,0)$ absorption data taken in the hollow cathode at $180 \pm 10$ K. The % labels indicate the <i>para</i> - $H_2$ enrichment of the feed gas. . . . .	96
6.9	Measured <i>para</i> - $H_3^+$ enrichments at $180 \pm 10$ K plotted along with high and low temperature model results. . . . .	98
6.10	$R(1,1)^u$ and $R(1,0)$ absorption data taken in the hollow cathode at $130 \pm 10$ K. The % labels indicate the <i>para</i> - $H_2$ enrichment of the feed gas. . . . .	99
6.11	$R(1,1)^u$ and $R(1,0)$ absorption scan data taken in the hollow cathode at $130 \pm 10$ K. The % indicate the <i>para</i> - $H_2$ enrichment of the feed gas. . . . .	100
6.12	Measured <i>para</i> - $H_3^+$ enrichments at $130 \pm 10$ K plotted along with high and low temperature model results. . . . .	101
6.13	A comparison of $R(1,0)$ and $R(1,1)^u$ absorption peaks for various <i>para</i> - $H_2$ enrichments. . . . .	102
6.14	Measured <i>para</i> - $H_3^+$ enrichments at $80 \pm 20$ K plotted along with high and low temperature models. . . . .	103
6.15	The fraction of <i>para</i> - $H_3^+$ ( $p_3$ ) as a function of dilution in argon. . . . .	105

6.16	Data from the hollow cathode and expansion experiments, fit with 3rd order polynomials. . . . .	106
6.17	$T_{ex}$ as a function of $T_{Rot}$ for different $para\text{-H}_3^+$ enrichments ( $p_3$ ) . . . . .	110
6.18	A comparison of laboratory and astronomically observed ratios of <i>ortho</i> and <i>para</i> ground states of $\text{H}_3^+$ and $\text{H}_2$ . . . . .	111
D.1	The ringdown comparator. This device takes the voltage input from a detector, and when the voltage exceeds a pre-set value (set by a potentiometer), it sends a negative voltage signal to an acousto-optic modulator (AOM) driver which causes the AOM to stop deflecting the beam into the ringdown cavity. Another potentiometer allows the operator to set the length of the output voltage signal, and an LED indicates when the device has been triggered. (Drawn by J. Wentz) . . . . .	146
D.2	The pulse driver used to activate the source valve in the pulsed experiments. This device was modeled after a driver designed and built at UC Berkeley. Upon receiving a TTL trigger pulse, the device sends a high voltage (HV) pulse for the length of the input TTL, up to 2.5 ms. Coaxial connections include the HV out and return, the TTL and HV inputs, and an output which allows the operator to monitor the current drawn across the HV terminals. The maximum input and output voltage is -1000 V. (Drawn by J. Wentz) . . . . .	147
D.3	The high voltage pulse driver that was used to modulate the discharge voltage for the pulsed experiments. This driver was designed and built at UC Berkeley. Upon receiving a TTL trigger pulse, the device sends an HV pulse for the length of the input TTL, up to 2.5 ms. Coaxial connections include the HV out and return, an input for a 5V power supply and the HV, the TTL input, and an output which allows the operator to monitor the current drawn across the HV terminals. The maximum input and output voltage is -1200 V. (Drawn by J. Wentz) . . . . .	148
E.1	The direction of travel for a beam propagating through the intentionally tilted window of the solid hydrogen cell. . . . .	152



# Chapter 1

## Introduction

Hydrogen is the most abundant element in the universe comprising more than 90% of elements by total number. If one were to re-design the periodic table of the elements based on cosmic abundances, it would appear as in Figure 1.1. Due to this abundance, chemical processes in the interstellar medium are largely governed by hydrogenic species [1, 2]. The  $\text{H}_2$  in these regions of space is ionized by cosmic rays, and the ensuing reaction between  $\text{H}_2$  and  $\text{H}_2^+$  forms  $\text{H}_3^+$ . The simplest of all polyatomic molecules,  $\text{H}_3^+$ , is one of the dominant ionic species in hydrogen plasmas in the laboratory [3], and in interstellar plasmas as well. In turn,  $\text{H}_3^+$  reacts to form many heavier polyatomics as depicted in Figure 1.2 [4, 5].

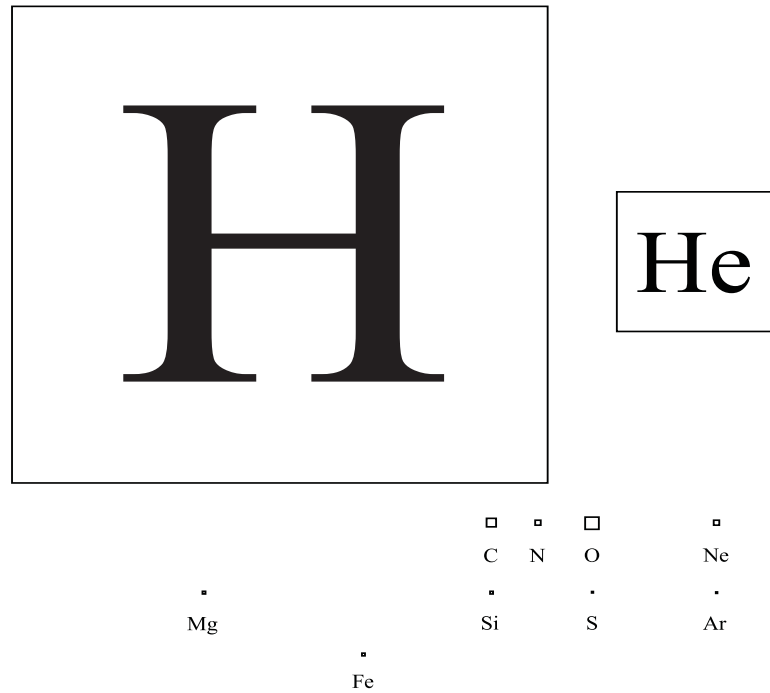


Figure 1.1: The astronomer's periodic table (reproduced from [6]).

Both the  $\text{H}_2$  molecule and the molecular ion  $\text{H}_3^+$  exist in one of two different nuclear spin modifications which can be treated as different chemical species. The symmetrically-aligned *ortho*- $\text{H}_2$  spin modification ( $I=1$ ) and the anti-aligned *para*- $\text{H}_2$  ( $I=0$ ) exist with a spin degeneracy ratio of 3:1. The two forms of  $\text{H}_3^+$  are *ortho* ( $I=3/2$ ) and *para* ( $I=1/2$ ). Interchange between the spin

modifications does not readily occur, except by chemical reaction [7, 8] or in the presence of strong inhomogeneous magnetic fields [9]. This property makes the hydrogenic spin modifications useful for studying the processes that occur in distant astrophysical environments, and to help us gain a deeper understanding of the most fundamental and widespread bimolecular reaction in the universe,  $\text{H}_3^+ + \text{H}_2 \rightarrow \text{H}_2 + \text{H}_3^+$ . This chapter will lay the theoretical foundation for this work in addition to explaining its relevance.

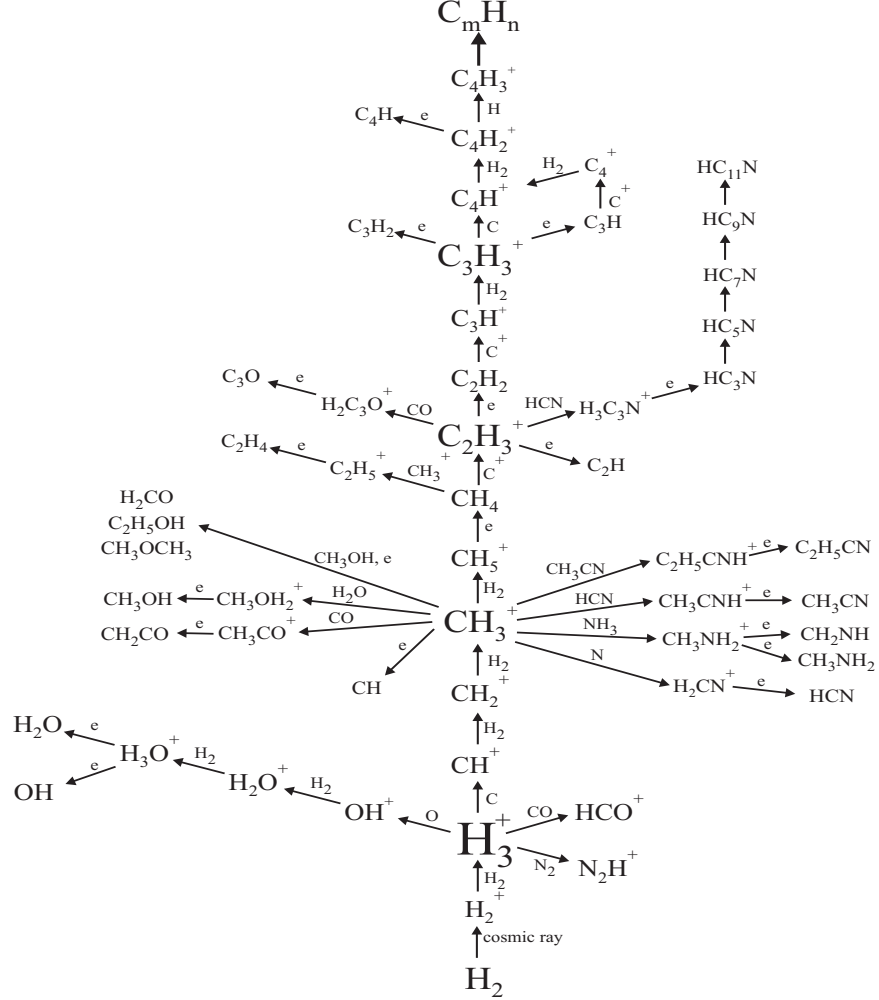


Figure 1.2: The reaction network that begins with  $\text{H}_3^+$  (reproduced from [6]).

## 1.1 Molecular $\text{H}_2$

Hydrogen has been instrumental in the development of quantum mechanics because its relative simplicity made it an ideal system with which to build and exercise new theories. The existence of the *ortho* and *para* forms of  $\text{H}_2$  was first predicted by Heisenberg and Hund in 1927 [10, 11], and experimentally observed shortly thereafter by Bonhoeffer [12, 13]. The weighting of the two spin modifications was calculated around the same time as the experimental verification. It is useful to

have a basic understanding of the origin of these weighting coefficients, and group theory can be used to provide this. This section assumes that the reader has a basic knowledge of group theory and symmetry. If not, good background texts include [14] and [15] for group theory and spectroscopy, and [16] for permutation and inversion.

The  $\text{H}_2$  molecule can be represented by the ground state electronic term symbol  $^1\Sigma_g^+$  and the permutation inversion group  $S_2^*$ . The permutation-inversion group is formed by multiplying the  $S_2$  permutation group by the group  $E^*$ , which comes from the inversion operation (Table 1.1).

$E^*$	$E$	$E^*$	$\otimes$	$S_2$	$E$	$(12)$	$=$	$S_2^*$	$E$	$(12)$	$E^*$	$(12)^*$
$A'$	1	1		$A$	1	1		$A'$	1	1	1	1
$A''$	1	-1		$B$	1	-1		$B'$	1	-1	1	-1
								$A''$	1	1	-1	-1
								$B''$	1	-1	-1	1

Table 1.1:  $S_2^*$  character table that results from  $E^* \otimes S_2$ .

The total representation for  $\text{H}_2$  can be written as the product of its representations

$$\Gamma_{total} = \Gamma_{electronic} \otimes \Gamma_{vibrational} \otimes \Gamma_{rotational} \otimes \Gamma_{nuclear\ spin}. \quad (1.1)$$

The electronic term symbol  $^1\Sigma_g^+$  shows that the representation for the electronic wavefunction must be symmetric with respect to reflection (+) and ‘gerade’ or ‘even’ with respect to inversion  $(12)^*$  through its center of symmetry. This corresponds to the character of the  $A'$  irreducible representation in  $S_2^*$ . Because this is a diatomic, its vibrational states will also be totally symmetric,  $A'$ . The rotational representation transforms as  $(12)|J\rangle = (-1)^J|J\rangle$  and  $E^*|J\rangle = (-1)^J|J\rangle$ . This corresponds to  $A'$  for even  $J$ , and  $B''$  for odd  $J$ .

The representation for nuclear spin, the parameter we are most interested in, can be found by first creating a list showing whether a class (or symmetry operation) can permute a particular nuclear spin modification into itself. The end product is a list of 1’s and 0’s, where a ‘1’ indicates that the class can permute the spin modification without having to change the spin of its constituents, and a ‘0’ means it cannot. The inversion operations do not affect the nuclear spin wavefunction, so the  $S_2$  character table can be used instead of  $S_2^*$  in order to simplify the calculation. The results are

Spin	$E$	$(12)$
$\uparrow\uparrow$	1	1
$\uparrow\downarrow$	1	0
$\downarrow\uparrow$	1	0
$\downarrow\downarrow$	1	1
$\Gamma_{nuclear\ spin}$	4	2

Table 1.2: Tallying the effects of nuclear spin permutations in  $\text{H}_2$ .

presented in Table 1.2, and can be decomposed using the usual methods into  $3A \oplus B$ , indicating that the ratio of *ortho:para*=3:1.

In order to determine which  $J$  states correspond with which *ortho* and *para* nuclear spin states,

it is necessary to first find the product of equation 1.1 for the two states

$$\begin{aligned}\Gamma_{total}(J_{even}) &= A' \otimes A' \otimes A' \otimes (3A' \oplus B') = 3A' \oplus B' \\ \Gamma_{total}(J_{odd}) &= A' \otimes A' \otimes B'' \otimes (3A' \oplus B') = 3B'' \oplus A''\end{aligned}$$

The Pauli principle states that the overall wavefunction must have antisymmetric character with respect to the exchange transformation (12), because the wavefunctions of fermions must be antisymmetric when transformed by (12). Of the representations for  $\Gamma_{total}$ , only  $B'$  and  $B''$  satisfy this requirement (see Table 1.1). Therefore, by following the multiplication in the equation above, one can see that the *ortho* spin modifications correspond to the odd  $J$  states (represented by  $3B''$ ), and the *para* spin modifications correspond to even  $J$  states (represented by  $B'$ ).

Because  $H_2$  lacks a dipole moment, there are no dipole-allowed pure rotational or vibrational transitions. Electronic transitions in the UV are frequently used in astronomical observations [17–19], as are observations of the weak quadrupole transitions in the mid-IR [20]. There were no direct laser spectroscopic measurements of *ortho* or *para*- $H_2$  performed in this work. Instead, the enrichment of *para*- $H_2$  was determined using various other methods (see Chapter 2).

## 1.2 The simplest polyatomic ion, $H_3^+$

$H_3^+$  was first observed in a laboratory plasma by J. J. Thomson in 1911 [21] by way of early mass-spectrometric measurements. Within 5 years, Dempster observed that  $H_3^+$  is the dominant ionic species in a hydrogenic plasma [3], and later, Hogness and Lunn determined that the reaction



is the mechanism by which it is formed [22]. Although these early experiments were performed at higher pressures than found in the interstellar medium, the timescales over which the processes occur in space are much greater and the end result is an abundance of  $H_3^+$  ions.

Despite the relatively rapid succession of these early discoveries with  $H_3^+$ , observation of its rovibrational spectrum did not occur for another 55 years. In 1980, Oka obtained the first spectrum of the infrared  $\nu_2$  band in a liquid nitrogen cooled plasma [23]. All of the laser spectroscopic experiments in the present work involve transitions that Oka observed in this first spectrum.

As with  $H_2$ , it is useful to have an understanding of the states of  $H_3^+$ , as well as the selection rules governing its transitions. A thorough derivation of the symmetries of  $H_3^+$  can be found in [6, pg. 5-27], but a brief summary is provided here for completeness.

The symmetry of  $H_3^+$  is described by the  $S_3^*$  permutation-inversion group. As mentioned earlier, the Pauli principle requires any valid representation to be antisymmetric with respect to the exchange of two protons. Additionally for  $H_3^+$ , this representation must also be symmetric with respect to the interchange of all three protons (which is equivalent to two successive exchange operations). The product of the representations must be

$$\Gamma_{electronic} \otimes \Gamma_{rovibration} \otimes \Gamma_{nuclear\ spin} \supset A'_2 \text{ or } A''_2 \quad (1.3)$$

where  $A_2'$  and  $A_2''$  are the irreducible representations of  $S_3^*$  in which an exchange operation (12) is antisymmetric and the (12)(23)=(123) is symmetric (see Table 1.3).

$S_3^*$	$E$	$3(12)$	$2(123)$	$E^*$	$3(12)^*$	$2(123)^*$
$A_1'$	1	1	1	1	1	1
$A_2'$	1	-1	1	1	-1	1
$E'$	2	0	-1	2	0	-1
$A_1''$	1	1	1	-1	-1	-1
$A_2''$	1	-1	1	-1	1	-1
$E''$	2	0	-1	-2	0	1

Table 1.3:  $S_3^*$  character table.

The lowest electronic energy state of the  $H_3^+$  ion has no nodes [6, pg. 7], meaning that the electronic wavefunction of  $H_3^+$  must be symmetric with respect to exchange. Consequently  $\Gamma_{electronic}$  must be totally symmetric, leaving

$$\Gamma_{rovibration} \otimes \Gamma_{nuclear\ spin} \supset A_2' \text{ or } A_2''. \quad (1.4)$$

In addition, the lowest lying excited electronic state is a barely bound triplet, with a small Franck-Condon overlap with the singlet ground state. Therefore, electronic spectroscopy is not a useful tool for the study of  $H_3^+$ .

The  $H_3^+$  symmetric stretch  $\nu_1$  is infrared inactive, whereas the  $\nu_2$  vibration is doubly degenerate, IR active, and possesses vibrational angular momentum of  $\pm\ell$ . This vibrational motion couples with rotational manifolds to produce a useful rovibrational spectrum for laboratory spectroscopy and astronomical observations ( $H_3^+$  does not possess a permanent dipole, and therefore does not have an allowed rotational spectrum). Defining the quantum number  $g = k - \ell$ , where  $k$  is the projection of the rotational quantum number  $J$  onto the molecular axis, an analysis of the rovibrational symmetries shows that

$$\Gamma_{rovibration} = A_1' \oplus A_2' \text{ or } A_1'' \oplus A_2'' \text{ for } g = 3n \quad (1.5)$$

and,

$$\Gamma_{rovibration} = E' \text{ or } E'' \text{ for } g = 3n \pm 1 \quad (1.6)$$

where  $n$  is an integer. In all cases, the  $'$  and  $''$  represent the parity of the representation. The  $\Gamma_{nuclear\ spin}$  can be decomposed to  $4A_1' \oplus 2E'$  using the a slightly more complicated version of the method described in §1.1. Hence, the  $A_1'$  are the *ortho* states, and  $E'$  are the *para*. Note that this gives a spin degeneracy ratio of *ortho:para* = 2:1. With the requirement that  $\Gamma_{total} \supset A_2' \text{ or } A_2''$ , this means

$$\begin{aligned} ortho &\leftrightarrow g = 3n \\ para &\leftrightarrow g = 3n \pm 1 \end{aligned}$$

because only the product of  $A_2'$  or  $A_2''$  with  $A_1'$ , and  $E'$  or  $E''$  with  $E'$  will produce  $A_2'$  or  $A_2''$  as required by Eq (1.4). At high temperatures where a significant number of excited states are

populated, these expressions for  $g$  dictate that there will be twice as many *para* states as there are *ortho*. This difference in available states effectively cancels with the nuclear spin degeneracy, meaning that a normal H<sub>2</sub> plasma will have  $ortho:para\text{-H}_3^+ = 1:1$ .

Selection Rule	Reason
$\Delta k = 2n \pm 1$	parity must change in a transition
$\Delta I = 0, \Delta g = 3n$	$(123)\langle J' k' \ell'   \mu   J k \ell \rangle \neq 0$
$\Delta J = 0, \pm 1$	triangle rule
$J = 0 \leftrightarrow J = 0$	triangle rule

Table 1.4: H<sub>3</sub><sup>+</sup> selection rules.

Selection rules for dipole-allowed transitions can be derived using the representation of the electric dipole  $\hat{\mu}$  which has the character of  $A_1''$ , and are summarized in Table 1.4. Due to the selection rules  $\Delta k = 2n \pm 1$  and  $\Delta g = \Delta(k - \ell) = 3n$  (where the  $n$  do not have to be the same integer), a change in angular momentum of  $\Delta \ell = \pm 1$  and  $\Delta k = \pm 1$  means that  $\Delta g$  must be 0. This is the only vibrational selection rule with which we are concerned because the spectroscopy in this work occurs exclusively in the fundamental band.

For excited vibrational levels of H<sub>3</sub><sup>+</sup> where  $\ell \geq 1$ , the increase in Coriolis coupling with the higher  $\ell$  mixes states to the degree that  $k$  is no longer a ‘good’ quantum number. As a result, the number  $g = (k - \ell)$  is used exclusively instead of  $k$ . The quantum number  $g$ , however, does not uniquely define specific states under certain conditions when  $\ell \geq 1$ . Whenever  $J - 1 \geq |g| \geq 1$ , there will be two sets of quantum numbers  $k$  and  $\ell$  that have the same  $g$  in the rovibrationally excited state. These states can be distinguished by identifying the upper or the lower state of a pair with the same  $J$  and  $G$ , where  $G = |g|$ . This brings us to the notation used in the remainder of the text to describe H<sub>3</sub><sup>+</sup> rovibrational transitions. Specifically,

$$R(J, G)^{u|\ell}$$

where  $R$  represents a transition in which  $\Delta J = +1$ ,  $J$  is the rotational quantum number,  $G = |g|$ , and the  $u|\ell$  represent the upper or lower excited state of the transition when a state is not uniquely defined by  $G$ . The transition from the use of  $g$  to  $G$  requires some explanation. If angular momentum is subject to time reversal, then the sign of the angular momentum changes. The magnitude of  $g$  will not change under time reversal because the signs of both angular momentum quantum numbers  $k$  and  $\ell$  will be reversed in the relation  $g = k - \ell$ . This, combined with the fact that energy is invariant to time reversal implies that  $g = (k - \ell) \rightarrow (-k - -\ell) = -(k - \ell) = -g$ , therefore  $G = |g|$  [6]. The quantum numbers  $(J, G)^{u|\ell}$  are used to describe a particular state of H<sub>3</sub><sup>+</sup>. This notation can be far more complex and descriptive than portrayed here depending on the types of transitions, and a more in-depth discussion can be found in [24].

To observe the *ortho* and *para* modifications of H<sub>3</sub><sup>+</sup>, the  $\nu_2 \leftarrow 0$  transitions from the ground rotational states of *ortho* (1, 0), and *para* (1, 1) were spectroscopically probed, along with a transition from the first rotationally excited state of *para*, (2, 2). The key parameters were taken from [24–26] and are listed in Table 1.5. The transitions are also depicted in Figure 1.3.

Ground state	Energy (cm <sup>-1</sup> )	Transition	Frequency (cm <sup>-1</sup> )	$\mu^2$ (D <sup>2</sup> )	Einstein A (s <sup>-1</sup> )
(1,1)	64.121	$R(1,1)^u$	2726.219	.0158	60.2
(1,0)	86.960	$R(1,0)$	2725.898	.0259	98.7
(2,2)	169.295	$R(2,2)^\ell$	2762.070	.0177	83.8

Table 1.5:  $\text{H}_3^+$  states, and lines from  $\nu_2 \leftarrow 0$  used in this work.

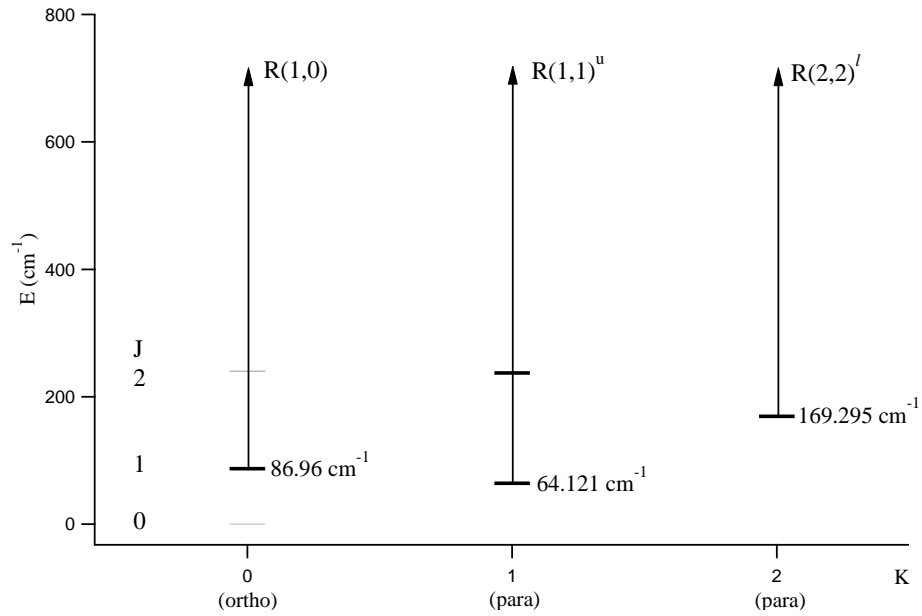


Figure 1.3: Ground state energy levels of  $\text{H}_3^+$ .

### 1.3 Spin modifications and the interstellar medium

In 1961, Martin, McDaniel, and Meeks first proposed that  $\text{H}_3^+$  could be found in interstellar space [27]. In 1996, when detection capabilities had sufficiently improved, Geballe and Oka found  $\text{H}_3^+$  in dense molecular clouds [28]. Shortly thereafter, in 1997, McCall, Geballe, Hinkle, and Oka observed  $\text{H}_3^+$  in diffuse clouds [29]. The abundance of  $\text{H}_2$  and a high cosmic ray ionization rate make  $\text{H}_3^+$  a major ionic constituent in the interstellar medium.

Observations of the column densities of hydrogenic species along various sightlines have been used as tools in determining cloud dimensions, cloud densities, and the aforementioned cosmic-ray ionization rate. Temperature has been inferred in diffuse interstellar clouds using both the ratio of *ortho*- to *para*- $\text{H}_2$ , and the ratio of *ortho*- to *para*- $\text{H}_3^+$  [28–34]. Surprisingly, the temperature inferred using the  $\text{H}_3^+$  spin modifications is 30–40 K lower than that measured with  $\text{H}_2$  or by other means. This indicates a gap in our understanding of how  $\text{H}_3^+$  is partitioned between the *ortho* and *para* spin modifications [35, 36], specifically, what mechanism is driving the steady state enrichment of *para*- $\text{H}_3^+$ .

The formation of  $\text{H}_3^+$  is well understood, even if the mechanisms that guide the steady state fractions of its spin modifications are not. Destruction of  $\text{H}_3^+$  occurs primarily by way of proton donation to CO in dense molecular clouds, and by dissociative recombination with electrons in diffuse clouds [37, pg. 209–220]. The former is due to the highly acidic character of  $\text{H}_3^+$  (the proton affinity of  $\text{H}_2$  is a mere 4.4 eV) and the abundance of CO in dense clouds as compared to diffuse clouds in which carbon is mostly found in the form of  $\text{C}^+$ . Dissociative recombination dominates in diffuse clouds because of the abundance of free electrons and a relatively high recombination rate coefficient. Both theory and experiment have indicated that the dissociative recombination rate of  $\text{H}_3^+$  should be different for the *ortho* and *para* spin modifications. Therefore, one of the main thrusts of this research is to measure a state-specific recombination rate for the two species, and determine whether this could be the mechanism that is driving the observed *para*- $\text{H}_3^+$  enrichment in the diffuse interstellar medium.

The *ortho:para* distribution of molecular hydrogen in dense clouds presents another interesting astrochemical problem. The *para*- $\text{H}_2$  fraction is enriched to a level consistent with thermalization at the temperatures of these clouds [18, 20, 38, 39], but the process by which this occurs has not been satisfactorily explained. The likely mechanisms for the partitioning of spin modifications observed in  $\text{H}_2$  are the chemical reactions between hydrogenic species. It has long been assumed that the reaction  $\text{H}_2 + \text{H}^+$  drives the  $\text{H}_2$  *ortho:para* ratio in shocked [40, pg. 123–130], photodissociative [41, pg. 143–149], and prestellar regions [42] of the interstellar medium. This assumption is probably correct for the diffuse interstellar medium where  $\text{H}^+$  number densities exceed those of  $\text{H}_3^+$  by 4 orders of magnitude [43]. In dense clouds, however, the abundance of  $\text{H}_3^+$  in comparison to  $\text{H}^+$ , and the higher rate constant for the reaction,



over that of  $\text{H}_2 + \text{H}^+$  [8], make  $\text{H}_3^+$  the more likely candidate. It is likely that this would also affect the  $\text{H}_3^+$  steady state *ortho:para* ratio, as alluded to in [30, 44]. Hence, the other major focus of this work is to explore the dynamics of reaction (1.7) at cold astrophysical temperatures, which will ultimately enhance our understanding of how the *ortho* and *para* spin modifications of both  $\text{H}_2$  and  $\text{H}_3^+$  reach steady state in the interstellar medium.



The importance of these *ortho:para* ratios goes beyond mere temperature and enrichment considerations. Recent studies have examined how the  $\text{H}_2$  *ortho:para* ratio affects the deuteration of  $\text{H}_3^+$ , which in turn serves as the pathway for introducing deuterium into many of the species found in the interstellar medium [42, 45]. The extent of  $\text{H}_3^+$  deuteration is strongly dependent on the fraction of *ortho*- $\text{H}_2$ . This is due to the higher energy of *ortho*- $\text{H}_2$  with respect to *para*, and the contribution this energy can make to the equilibrium condition of the reaction by which  $\text{H}_3^+$  is deuterated. The fact that reaction (1.7) is so widespread, coupled with its astrochemical implications and the wealth of physical insight we can gain from this simple system make it not only worthwhile, but essential to understand.

Both the dissociative recombination and reaction dynamics experiments form the heart of this work, and are dependent on using  $\text{H}_2$  gas of varying levels of *para*- $\text{H}_2$  enrichment. Because of this, we have developed methods for efficiently producing and testing highly enriched *para*- $\text{H}_2$ , which are discussed in Chapter 2. Details regarding the dissociative recombination and reaction dynamics experiments are presented in Chapters 3 through 6. The capability to produce highly enriched *para*- $\text{H}_2$  allowed us to perform an ancillary project of general spectroscopic interest in which we attempted to measure the index of refraction of solid hydrogen. This was done in the hopes of building a solid hydrogen Raman laser, and is discussed in Appendix E.

# Chapter 2

## *Para*-H<sub>2</sub> production and measurement

In a sample of room temperature H<sub>2</sub>, the *ortho* modification in which the proton spins are symmetrically combined ( $I = 1$ ) occurs with 74.93% abundance, while the remainder consists of the *para* modification in which the proton spins combine anti-symmetrically ( $I = 0$ ). In the absence of external magnetic fields, the interconversion between the two states is extremely slow and the spin modifications can be treated as separate species. This chapter will briefly present the theory of *ortho* to *para*-H<sub>2</sub> conversion, followed by a description of the *para*-H<sub>2</sub> converter that was designed and built for this project. Finally, the two methods that were used to measure the enrichment will be discussed.

### 2.1 Theory

In 1933, Wigner [9] suggested a mechanism for the conversion of *ortho*-H<sub>2</sub> to *para*-H<sub>2</sub>. In his theory, the magnetic dipoles of the *ortho*-H<sub>2</sub> spin modification interact with the magnetic fields produced by nearby *ortho*-H<sub>2</sub> molecules. The triplet *ortho* and singlet *para* spin states are able to mix in the presence of the magnetic gradients [46]. The transition rate between spin modifications is enhanced by the presence of inhomogeneous magnetic fields, as provided by a paramagnetic catalyst. Below  $\sim 77$  K, the mixing of the triplet and singlet states leads to a thermalized distribution where *para*-H<sub>2</sub> is the dominant species [47]. However, Wigner’s theory predicts conversion rates that are orders of magnitude less than those observed in experiment [48].

Minaev and Ågren proposed a ‘spin catalysis’ mechanism wherein paramagnetic-induced mixing between the nuclear and electronic wavefunctions increases contact between the *ortho* and *para*-H<sub>2</sub> spin modifications [49]. A separate theory by Milenko, Sibileva, and Strzhemechny incorporated temperature-dependent interaction distances to more accurately predict gas phase conversion rates [50]. Understanding the interconversion between *ortho*- and *para*-H<sub>2</sub> has been, and continues to be, an active area of research [51, 52]. Whatever the state of theoretical development, however, the experimentalist requires an effective method for producing highly enriched *para*-H<sub>2</sub>.

Scientific applications requiring precisely controlled samples of *para*-H<sub>2</sub> include nuclear magnetic resonance techniques that exploit the signal-enhancing *para*-H<sub>2</sub> effect [53], the production of solid hydrogen crystals for matrix isolation spectroscopy [54–57], and superfluidity studies [58]. In addition, dissociative recombination experiments with astrochemical implications [59–62], mass spectroscopic experiments to study deuterium fractionation in dense molecular clouds [45], and fundamental chemical physics studies involving the spin modifications of hydrogenic species [63, 64] receive continued attention.

The first device built to convert *ortho*-H<sub>2</sub> to *para*-H<sub>2</sub> used a tube filled with an activated charcoal catalyst [12]. The tube was immersed in a cryogen such as liquid nitrogen or liquid hydrogen (for higher *para* enrichments), and the backing pressure was set such that the H<sub>2</sub> was forced to flow through the catalyst. Variations on this method, such as a glass bulb containing a bed of paramagnetic catalyst, have also been successfully employed [65]. Both nickel silica gel (also known as ‘Apache’) and ferric oxide have been used as the paramagnetic catalyst, with the former exhibiting higher conversion efficiency [46].

There is a limit to the enrichment that can be achieved when using liquid nitrogen or hydrogen as the cryogen. A temperature of 77 K results in a 51% *para*-H<sub>2</sub> enrichment, and liquid hydrogen temperatures ( $\sim 20$  K) result in an enrichment of 99.8% [46]. With the goal of obtaining higher ( $\geq 99.99\%$ ) enrichments, others have used liquid helium as a cryogen in similar types of systems [64].

A more automated converter was developed by Tam and Fajardo [66] using a closed cycle <sup>4</sup>He cryostat. This system merged automated control over a range of temperatures with the high enrichment that comes from using liquid helium as a cryogen. It was optimized to deposit solid *para*-H<sub>2</sub> for matrix isolation spectroscopy at a rate of  $\sim 0.11$  standard liters per minute (SLM).

## 2.2 The converter

The *para*-H<sub>2</sub> converter designed and built for this work consists of a locally modified closed-cycle <sup>4</sup>He cryostat (Janis CCS-100/204 Optical 10K Refrigerator), and is conceptually similar to the design by Tam and Fajardo. The cold-head/piston section of the cryostat is mounted upright on a 0.37 m<sup>2</sup> (2 $\times$ 2 ft<sup>2</sup>) piece of 1.27 cm (1/2 inch) thick aluminum in order to provide stability, safe transport, and ease of access to interior components. Two small ports near the base of the cold head were covered by the manufacturer with square aluminum blanks (sealed by o-rings). These were removed and replaced with similar-sized pieces of aluminum into which 1.59 mm (1/16-inch) union bulkheads (Swagelok SS-100-61) were welded.

Both bulkheads are connected on the interior to 1.59 mm (1/16-inch) stainless steel tubing that traverses the length of the cryostat (see Figure 2.2). Two trombone-like bends in the tubing on both the ingoing and outgoing sides provide enough elasticity to allow easy movement of the coiled conversion section. A schematic can be found in Figure 2.2 with and without the vacuum shroud installed (2.2a). Part b of the figure shows the approximate dimensions of the 1.59 mm (1/16”) stainless steel tubing. Sections ① and ② are themselves curved (when viewed from above). ① has a radius of curvature of 1.91 cm (0.75”), and ② has a radius of 3.2 cm (1.26”).

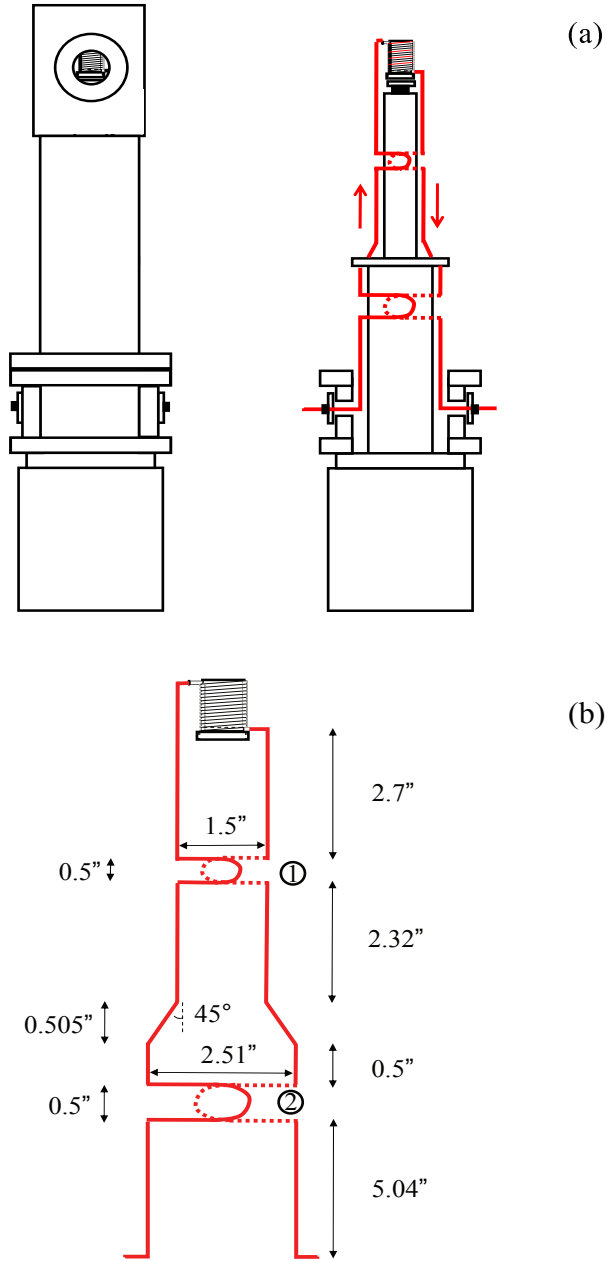


Figure 2.1: (a) Schematic of the  $para$ -H<sub>2</sub> converter with and without the vacuum shroud installed. (b) The approximate dimensions of the stainless tubing.

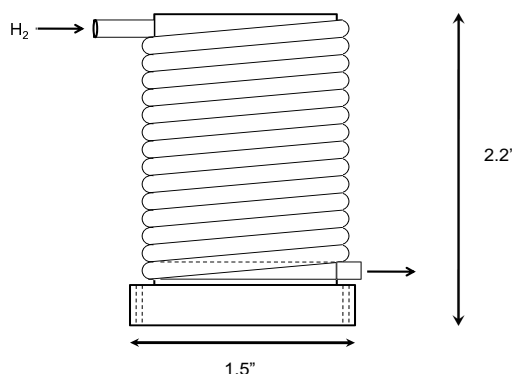


Figure 2.2: Coil section where the catalytic conversion from *ortho*-H<sub>2</sub> to *para*-H<sub>2</sub> takes place.

There is no contact between the stainless steel tubing and any surface of the cryostat, except at one point where the input tubing is thermally shorted to the first stage of the cold head to allow the inflowing hydrogen gas to begin cooling before it reaches the coil.

The coil itself is a solid piece of oxygen free high conductivity copper (OFHC) around which 3.18 mm (1/8 inch) copper tubing has been wound (Figure 2.2). The input to the coil reactor is at the top end of the device (see Figure 2.2). The copper tubing winds downwards around the OFHC, and passes through the center adjacent to the cold head before attaching to the outgoing 1.59 mm (1/16 inch) stainless steel tubing. The solid piece was machined with a single groove, one copper tubing outer diameter (OD) in width and one-half OD in depth, that winds continuously around the plug from top to bottom just above the base. This groove allows the copper tubing to be recessed into the OFHC. The coiled tubing, which makes approximately 14 loops around the OFHC core, provides approximately 1.3 m of path length. After the tubing was wound, it was permanently attached to the OFHC using soft solder.

The tubing was filled with 3.3 grams of a ferric (III) hydroxide (C-Chem Ionex-type O/P) catalyst. The catalyst was fed into the tubing with a glass eyedropper followed by slowly tapping and rotating the assembly in order to pack the entire length. A thin ramrod (paperclip) and blasts of gaseous N<sub>2</sub> were also used to aid in filling. The mass of the catalyst was closely tracked in order to determine if the tube was completely full, or if a blockage occurred that would prevent complete filling. The catalyst was held in the tubing by a small disc cut from porous 60-mesh stainless steel filter material (Small Parts, Inc. F060X-12-10 Type 304). After filling, another disc was positioned at the opposite end of the tube to prevent the catalyst from spilling out. The discs were set inside the tube then crimped into place.

The introduction of catalyst after soldering the tube/OFHC assembly together, as well as the crimping of the filter discs into the 3.18 mm (1/8 inch) copper tubing, was necessary in order to avoid exposing the catalyst to temperatures in excess of 200 °C. After packing the catalyst and installing the filter discs, the ends of the copper tubing were soldered to the aforementioned input and output 1.59 mm (1/16 inch) stainless steel tubing before installation in the cryostat.

Before its first use, the coil was wrapped with a resistive heating band and heated under vacuum to 105 °C for 48 hours (hot enough to activate the catalyst without destroying it). The activation was necessary to remove molecules such as water that had adsorbed to the catalyst surface when it was exposed to air. If not removed, these impurities would reduce the surface area available for hydrogen adsorption. This process could also be carried out under the constant flow of H<sub>2</sub> gas to increase efficiency. During heating, the coil section was pulled and suspended 2 cm away from the cold head of the cryostat using wires, and the two were further thermally isolated from one another using alumina felt. This was done to protect the cold head, which had a temperature damage threshold of  $\sim 50$  °C. It is important to note that the catalyst in the coil section should be kept under vacuum after this step.

After cooling, the coil section was attached to the cold head by capscrews, with a thin ‘wiping’ of vacuum grease (Apiezon N) between. The temperature of the cold head is monitored using a silicon diode sensor that is connected to a temperature controller (Lakeshore DRC-91C).

Stainless steel tubing with an outer diameter of 6.35 mm (1/4 inch) routes the gas into or around the cryostat. This tubing consists of type-300 austenitic (non-magnetic) steel. Stopcock valves (Swagelok SS-42GS4) are used to direct the flow of normal hydrogen upstream of the converter, and to direct the outflow of converted gas. A high purity stainless pressure regulator with a 7.9 bar (100 psig) gauge (Matheson Tri Gas 3433-NV-5, M63-2216) controls the backing pressure of hydrogen into the converter, and an identical pressure gauge is positioned downstream of the cryostat in order to monitor the pressure of converted *para*-H<sub>2</sub>.

### 2.2.1 Generating *para*-H<sub>2</sub>

To produce highly enriched *para*-H<sub>2</sub>, the temperature controller was set to 13.9 K, which corresponds thermodynamically to 99.996% *para*-H<sub>2</sub>. The cryostat typically took 1 hour to cool down to this temperature, followed by another hour to allow thermal equilibration across the entire coil. Another option, not employed in this converter, would be to attach temperature sensors at both ends of the coil section, allowing the operator to constantly monitor the temperature extremes of the coil. Once the cooling period was over, H<sub>2</sub> was slowly introduced into the converter using a backing pressure of  $\sim 330$  mbar. As the H<sub>2</sub> entered the coil it underwent a phase change to liquid. Until the entire coil was filled with liquid, a process taking up to 30 minutes, the downstream pressure would not increase above the vapor pressure of H<sub>2</sub> at low temperature ( $\sim 100$  mbar). H<sub>2</sub> was not allowed to flow into the storage tank during the phase change. Once the phase change was complete (indicated by pressure equilibration on both the upstream and downstream pressure gauges), gas was allowed to flow through the converter for a few minutes (approximately a standard liter in this case) to ensure the line had been purged of any gas that did not have sufficient time to completely equilibrate. This gas was then evacuated.

Once these preparatory steps were completed, the *para*-H<sub>2</sub> was produced by increasing the upstream pressure, while monitoring the voltage applied to the cryostat’s heater element. The pressure was increased incrementally so that the difference between upstream and downstream pressures was  $\sim 1$  bar. The difference between these pressures had to be increased for higher downstream pressures. For example, at 2.4 bar (20 psig) downstream, the pressure difference was set to greater than 2 bar to maintain a high flow rate. This value seemed to change from day to day. The heater element

Type	<i>para</i> -H <sub>2</sub> back conversion
Stainless Steel, Teflon-lined	1.7±0.4% per week
Aluminum, Unlined	1.9±0.7% per week
Glass NMR Tube (with TMS)	0.8±0.1% per hour
Glass NMR Tube (without TMS)	0.4±0.2% per hour

Table 2.1: The back conversion of *para*-H<sub>2</sub> in various storage vessels as measured by thermal conductance and NMR.

voltage was used to monitor the thermal load on the converter caused by the introduction of warm H<sub>2</sub> gas. If the voltage approached zero, then the H<sub>2</sub> flow rate was too high. It was essential to maintain a constant coil temperature during the conversion process because a  $\geq 0.2$  K temperature excursion could result in a 0.01% change in the *para*-H<sub>2</sub> enrichment.

The heater voltage and pressure also served to indicate a blockage due to frozen air, which could result from leaks upstream of the converter. If the upstream pressure was higher than the downstream (with no sign of change), and there was no change from the baseline voltage on the temperature controller, then a blockage had occurred and the entire system had to be warmed to between 95-100K in order to evacuate the offending materials (oxygen and nitrogen).

The converter was typically used to fill a teflon-lined storage vessel to  $\sim 7.6$  bar (95 psig). One could also provide a continuous gas feed to an experiment by using a unidirectional valve to prevent back-flow into the converter. A 99.99% pure *para*-H<sub>2</sub> sample was routinely produced at rates of up to 0.34 SLM for pressures below 1 bar, and at lower rates for higher downstream pressures. This was a threefold increase in production rate over other converters reported in the literature.

### 2.2.2 Storage

To minimize back conversion due to contact with paramagnetic materials, the prepared *para*-H<sub>2</sub> gas was stored in a 3.79 L (1 gallon), 124 bar (1800 psi), teflon-lined sample cylinder (Swagelok 304L-HDF4-1GALC-T). The ends of the cylinder were sealed with a brass valve and end cap (Swagelok B-14DKM4-S4-A and B-4-P). The rate of back conversion in the sample cylinder was 1.7% per week (see Table 2.1 for other back conversion rates), and was most likely due to small sections of exposed stainless steel threading near the brass fittings. The starting sample enrichment was 99.99% *para* for the first two entries in Table 2.1.

The conversion rate seemed to increase with the introduction of impurities into the storage vessel. As an added precaution, the entire system was evacuated by a turbomolecular pump (Pfeiffer TSH 071E) for 24-48 hours before a new sample of *para*-H<sub>2</sub> was produced. A high rate of back conversion was observed in the glass NMR tubes when tetramethylsilane (TMS) was used as an NMR reference standard. The paramagnetic O<sub>2</sub> molecule was the likely culprit. As described earlier, spin catalysis brought about by collisions with O<sub>2</sub> permit the mixing of H<sub>2</sub> triplet and singlet nuclear spin states [49]. The O<sub>2</sub> was probably introduced as the TMS was being prepared to flow into the NMR sample tubes. Two freeze-pump-thaw cycles were used for the preparation, however, there were probably small pockets of ambient laboratory air that remained in the solid TMS.

## 2.3 Quantifying the enrichment

There are many methods one can use to measure the enrichment of *para*-H<sub>2</sub>. Two in particular were used in this work: thermal conductance and nuclear magnetic resonance.

### 2.3.1 Thermal conductance

The thermal conductance method takes advantage of the different thermal conductivities of *ortho*- and *para*-H<sub>2</sub> at low temperatures. This stems from the different temperature dependencies of the rotational partition functions, which are in turn due to the fact that *para*-H<sub>2</sub> consists only of even rotational states and *ortho*-H<sub>2</sub> of odd rotational states. The difference in thermal conductivity of the two spin modifications is greatest at a temperature of  $\sim 175$  K, and consequently this method has the highest precision near this temperature.

A wire inside a liquid nitrogen-cooled cell is immersed in a sample of hydrogen gas and held close to 175 K by resistive heating. The resistance of the wire will change with temperature according to Eq. (2.1).

$$R = R_o(1 + \alpha\Delta T) \quad (2.1)$$

$R_o$  is the resistance of the filament at a known temperature (usually close to 300K),  $\alpha$  is its thermal resistance coefficient ( $4.9 \times 10^{-3} \text{ K}^{-1}$  for tungsten), and  $\Delta T$  is the temperature change [67, pg. 114]. The higher thermal conductivity of *para*-H<sub>2</sub> will result in a cooler wire, which in turn will have a lower resistance (and voltage) at a given current. This method is the easiest to use for quick measurements such as spot checks of the products from the converter, or to measure the enrichment of a sample prepared at some time in the past.

The design of glass thermal conductance measurement cells is thoroughly discussed by Farkas [68, pg. 20-28] and by Stewart [69]. Our cell is an improvement on their designs because of its construction from stainless steel flanges and nipples. This makes for easier access to the filament in case it needs replacing, and circumvents the need for glassware altogether (see Figure 2.3).

The top part of the cell (a) was a 3.81 cm (1.5 inch) long stainless conflat half-nipple with a 3.38 cm (1.33 inch) flange diameter (Kurt Lesker Inc. HN-0133). To this, a 3.38 cm (1.33 inch) flange (b) with two nickel feedthroughs (Kurt Lesker Inc. EFT0021032) was tightened with a seal provided by a copper gasket. Another 3.38 cm (1.33 inch) flange (c) was welded on the other end, again with two nickel feedthroughs. The two sets of feedthroughs were connected by insulated copper wires (d), and a 3.18 mm (1/8 inch) diameter stainless tube (e) was welded to a hole drilled mid-way up the side of the nipple in order to allow its interior to be evacuated.

A separate custom 20.32 cm (8 inch) long half-nipple (f) (Kurt Lesker Inc. HN-C111080) was modified by welding an end cap to the end without a flange, and attaching 3.18 mm (1/8 inch) tubing through which the cell could be evacuated, or the test-gas could be introduced (g). The two nickel feedthroughs protruded into the space provided by this nipple. A  $\sim 2.5$  cm strand of 12  $\mu\text{m}$  tungsten wire (h) was spot welded between these nickel feedthroughs. Part-way up the feeder tube (g) was a small welded cylinder (i). This cylinder could also be evacuated (e). In conjunction with the nipple described in the previous paragraph (a), the purpose of this cylinder was to act as a dewar to isolate the test gas from changing cryogen levels which could cause unwanted convection currents.

When making a measurement, the cell was immersed nearly to the top of the small cylinder (i)



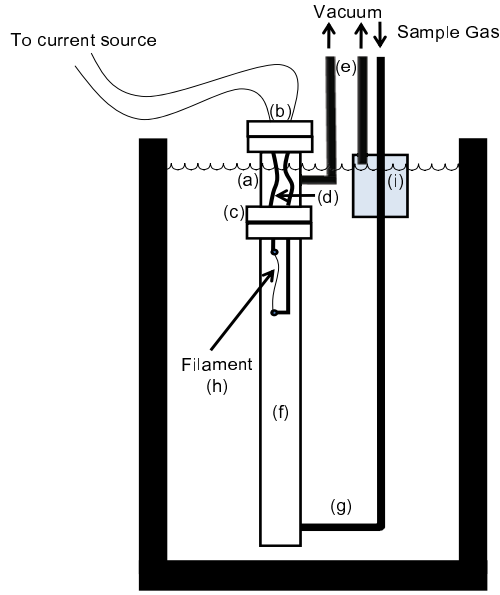


Figure 2.3: The thermal conductance cell.

in liquid nitrogen. A pressure of 50.05 mbar of hydrogen, measured by a capacitance pressure sensor (Keller America PAA-41X/81955.60/ 10mbar), was introduced via a bellows seal valve (Swagelok SS-4BRG). When the cell was filled to this pressure, a 105 mA current was applied using a current meter (Keithley 2420). This current will heat the tungsten filament to  $\sim 185$  K in a sample of normal  $H_2$  gas. The system was allowed to thermally stabilize for 5 minutes from the application of current, after which the voltage (or resistance) was read from the current meter. Although it was not difficult to consistently fill the cell to 50.05 mbar, the precision of the pressure measurement was important because an average pressure dependence of  $-0.78$  mV/mbar was observed. The error of the pressure sensor (0.1% typical) resulted in an error of 0.05 mV. It was also important that gas was present in the cell when current was applied in order to provide a means of heat dissipation, otherwise the wire would need to be replaced or re-calibrated (an experience which highlights the benefits of the flange/nipple design).

The thermal conductance cell was calibrated using gases of known *para*- $H_2$  enrichment. *Para*- $H_2$  was produced at different converter temperature settings, and it was assumed that the enrichment matched thermodynamic predictions. Figure 2.4 presents the typical results of a calibration. Duplicate measurements using samples of the same *para*- $H_2$  enrichment typically fell within  $\pm 0.5$  mV of each other. The calibration slope was  $0.75$  mV percent $^{-1}$  at low *para*- $H_2$  enrichment and  $0.65$  mV percent $^{-1}$  at high. This resulted in a precision of  $\pm 0.7\%$  and  $\pm 0.8\%$ , respectively. It should be noted that this level of precision was determined from measurements taken over a period of 6 months. Measurements taken within a short time of each other were usually within  $\pm 0.3\%$  for both the high and low enrichment regimes, which is comparable to the precision found by Assael and co-workers when using the transient hot wire method [70].

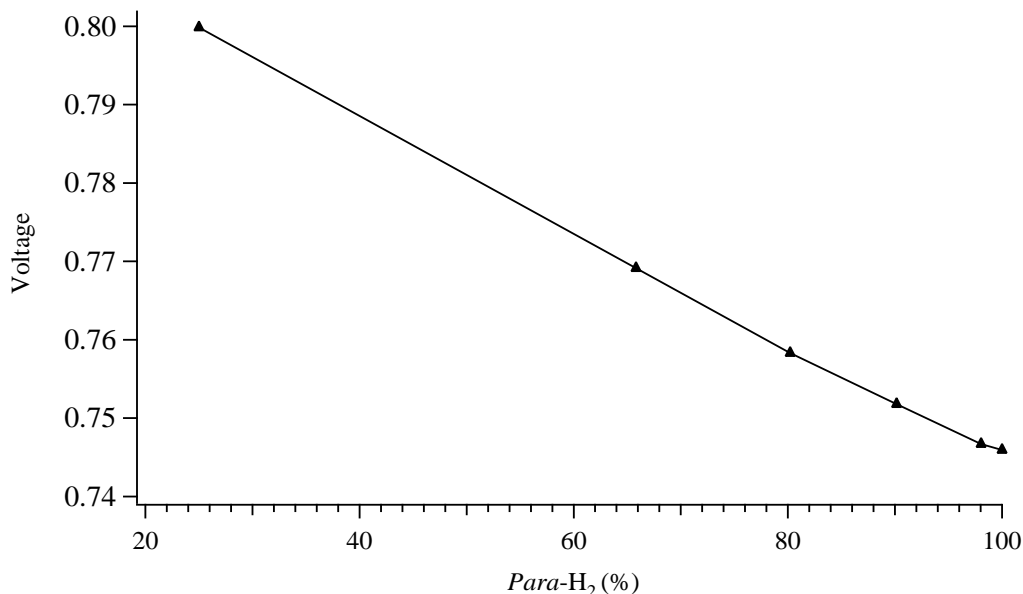


Figure 2.4: A calibration curve for the thermal conductance cell.

### 2.3.2 Nuclear magnetic resonance

Nuclear magnetic resonance is a method for measuring the enrichment of *para*-H<sub>2</sub> that is readily available to most laboratories given the ubiquity of NMR spectrometers. *Ortho*-H<sub>2</sub> possesses a net magnetic dipole that responds coherently in a strong magnetic field and when interacting with an electromagnetic pulse. This makes it possible to observe an *ortho*-H<sub>2</sub> free induction decay (FID) in NMR. The integrated area of the Fourier transformed FID is dependent on the number density in the sample [71]. In contrast, *para*-H<sub>2</sub> has no net magnetic moment and cannot be aligned in a strong magnetic field, and therefore produces no spectral signature (FID). Consequently, the *para*-H<sub>2</sub> enrichment can be calculated by comparing the integrated peak of an unknown sample with that of a known sample, such as normal-H<sub>2</sub> with *ortho:para* = 3:1.

Gas NMR tubes (Wilmad Lab Glass 528-PV-7) fitted with J. Young valves were used to take the measurements. It was important to ensure a good seal to these tubes when filling, otherwise the introduction of oxygen resulted in a higher back-conversion rate to *ortho*-H<sub>2</sub>. A tube with the unknown *para* enrichment was filled with 2.4-3.8 bar (20-40 psig) of the test gas, and another tube of normal H<sub>2</sub> (*ortho:para* = 3:1) was prepared at the same pressure. The use of normal H<sub>2</sub> makes it unnecessary to calibrate the spectrometer by means of an outside source, as was required for the thermal conductance cell. However, we did compare the NMR results with those of the thermal conductance cell, and temperature-based predictions, in order to determine the validity of this assumption.

In addition to the hydrogen, approximately ~500 mbar (7.5 psi) of spectroscopic-grade tetramethyl silane (TMS, Si(CH<sub>3</sub>)<sub>4</sub>) was introduced into the sample tubes to serve as a reference standard. The TMS was added at room temperature from a glass ampule. To minimize the ambient air introduced along with the TMS, two freeze-pump-thaw cycles were performed by immersing the ampule in a liquid nitrogen bath. At 500 mbar, there was a small amount of liquid TMS at the bottom

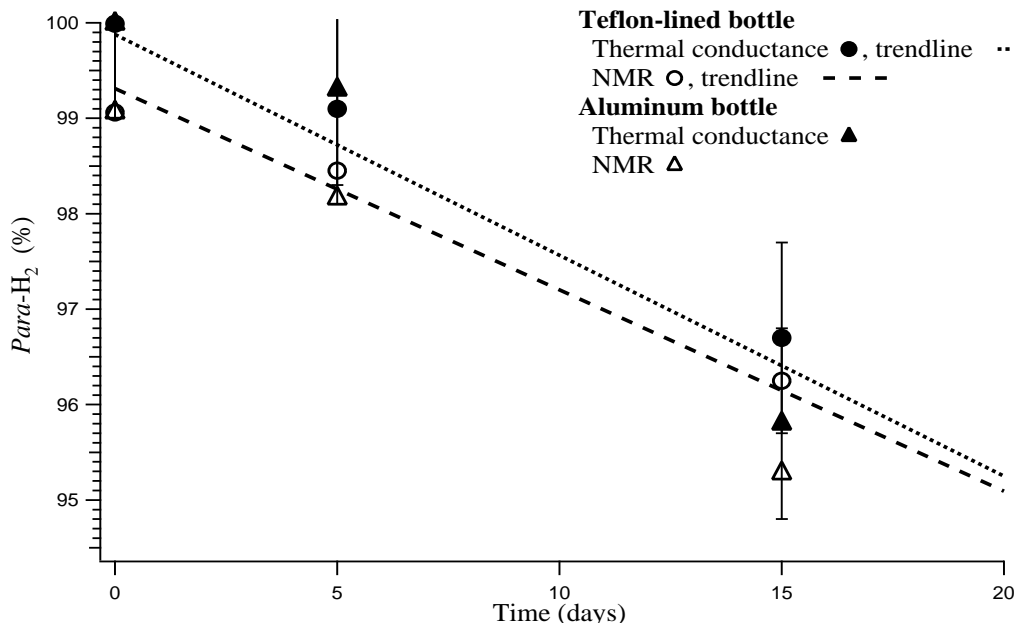


Figure 2.5: Comparison of thermal conductance and NMR measurements made with TMS. Error bars for the thermal conductance measurements are displayed, and are  $\pm 0.8\%$ .

of the NMR tube. It was assumed that this liquid would provide the same vapor pressure of TMS at a given temperature inside the NMR spectrometer, thereby providing a good reference between samples.

Measurements were taken as quickly as possible after the sample tubes were prepared (within 10 minutes) in a Varian Unity Inova 500 Narrow Bore NMR spectrometer. Minimizing the time between sample preparation and measurement was important because of the high rate of back conversion in the NMR tubes (see Table 2.1). The integrated peak areas were compared between the unknown and known samples to determine the amount of *ortho*-H<sub>2</sub> in the unknown. The TMS peaks were used to normalize the hydrogen peaks in case there were differences introduced by the sample tubes themselves, or by changing conditions in the spectrometer. Standardization using this TMS technique typically gave values within  $\pm 0.1\%$  of the unstandardized data. On only one occasion did the use of TMS provide a significant correction. Aside from its standardization role, TMS also provided a signal strong enough to shim the NMR spectrometer magnets.

As seen in Table 2.1, the rate of back conversion to *ortho*-H<sub>2</sub> was higher in sample tubes prepared with TMS than without. This was probably due to the limited effectiveness of the freeze-pump-thaw cycle in removing oxygen. A comparison of measurements taken with NMR (using TMS) and the thermal conductance cell is presented in Figure 2.5. The NMR-measured *para*-H<sub>2</sub> fractions were consistently lower than those measured by thermal conductance (again, it was assumed in the thermal conductance calibration that the converter produced *para*-H<sub>2</sub> at enrichments consistent with thermodynamic predictions). This was attributed to two factors; the aforementioned back conversion rate in TMS-infused sample tubes, and the distortion effects of the TMS resonance on the spectrum. In the latter case, the errors could arise from distortion in the nearby *ortho*-H<sub>2</sub> peak which was difficult to remove by phasing.

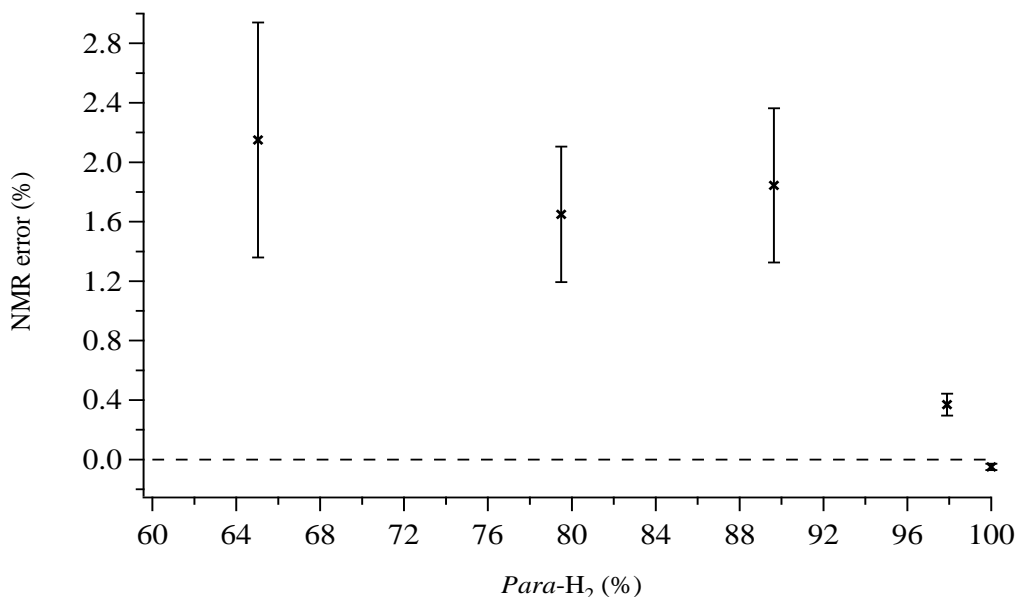


Figure 2.6: Difference between NMR measurements without TMS and the predicted values of *para*-H<sub>2</sub> enrichment. Error bars represent  $1\sigma$ .

These results were compared with NMR measurements taken without TMS, which are presented in Figure 2.6. In stark contrast, these measurements were consistently higher than the thermodynamically predicted *para*-H<sub>2</sub> enrichment, but by approximately the same amount ( $\sim 1\%$ ). At the highest enrichment, the measurement without TMS was lower than expected (99.95% versus 99.99%), but this could be explained by the  $0.4\%$  hour<sup>-1</sup> back conversion rate observed even in TMS-free sample tubes (Table 2.1). Both the accuracy and precision were lower at reduced *para*-H<sub>2</sub> enrichments ( $< 95\%$ ). This could be partially attributed to the fractional nature of the errors. In other words, a 10% error in the measurement of a small *ortho*-H<sub>2</sub> peak at 99.9% enrichment was not as significant as the effect of the same error in a 25% *para*-H<sub>2</sub> sample. The consistent sign of the offsets in both techniques indicated some sort of systematic error that is not well understood at present. It should be mentioned that there was also an error due to the limited precision of the pressure gauge used on the converter, which could only be read to  $\pm 35$  mbar ( $\pm 0.5$  psi). The resulting error was on the order of  $\pm 0.02\%$ , which was unlikely to be a factor even at high *para* enrichments.

Considering the steps necessary in carrying out the actual measurement, combined with the relative similarity in accuracy and precision, performing NMR measurements without TMS was the better option. Based on limited data, this method demonstrated a precision of  $\pm 0.1\%$  for  $> 95\%$  *para*-H<sub>2</sub>, and  $\pm 1.0\%$  below this enrichment. The accuracy was  $\sim 0.5\%$  for enrichments  $> 95\%$ , and  $\sim 2.5\%$  at lower enrichments.

Both the thermal conductance and NMR techniques are ideal for relatively simple and quick measurements of *para*-H<sub>2</sub> enrichment. The strength of the thermal conductance technique is in the ease of construction, however, it is only as accurate as the method used for calibration. The advantage of the NMR technique is its availability and the fact that no external calibration is needed.

# Chapter 3

## Laser systems and spectroscopic methods

Although the types of experiments performed in this work sometimes involved techniques other than laser spectroscopy, each experiment depended on the use of lasers in some fashion. The lasers that were used ranged from helium neon at one end of the complexity spectrum, to systems such as the two locally-built difference frequency lasers on the other. This chapter will focus on the two difference frequency lasers, and will describe the two spectroscopic techniques in which one of them was used; continuous wave cavity ringdown and multipass absorption spectroscopy.

### 3.1 Difference frequency generation system I

Difference frequency generation (DFG) is a process in which beams of light at different frequencies are combined in a material possessing nonlinear optical properties. As the name implies, the output frequency that results from the interaction between light and matter is at the difference between the two input frequencies. The two input beams and the output beam are referred to (respectively) as the ‘pump,’ ‘signal,’ and ‘idler,’ where  $\omega_{idler} < \omega_{signal} < \omega_{pump}$ . The first DFG system constructed in our laboratory, shown in Figure 3.1, consists of a tunable titanium sapphire (Ti:Sapph) ring laser and a single-frequency neodymium yttrium aluminum garnet (Nd:YAG) laser, the beams of which are combined in a periodically poled lithium niobate (PPLN) nonlinear crystal. This system was used for characterizing the ion source used in the dissociative recombination experiment as well as for the  $\text{H}_3^+ + \text{H}_2$  reaction dynamics experiments in the pulsed supersonic expansion and the hollow cathode cell. These components, along with essential sub-components, are discussed below.

#### 3.1.1 Titanium:sapphire pump laser

The Ti:Sapph laser, which serves as the pump laser for this DFG, actually consists of three lasers: a diode laser that is used to pump a neodymium vanadate laser, which in turn pumps the Ti:Sapph. The diode laser (Spectra Physics) uses semiconductor material that has spatially separated electron donor (n-type) and electron acceptor (p-type) regions. When negative and positive voltages are applied to the regions, respectively, electrons are driven (forward biased) into the junction between them. The recombination of electrons with acceptors is the equivalent of electron transitions from conduction to valence bands, and photons are released in the process. Continuously pumping current through this region provides population inversion, and the material is shaped in such a way as to form a cavity in which reflected photons can stimulate further emission. This diode laser is composed of gallium aluminum arsenide semiconductor material that emits at 809 nm [72, pg. 312-318].

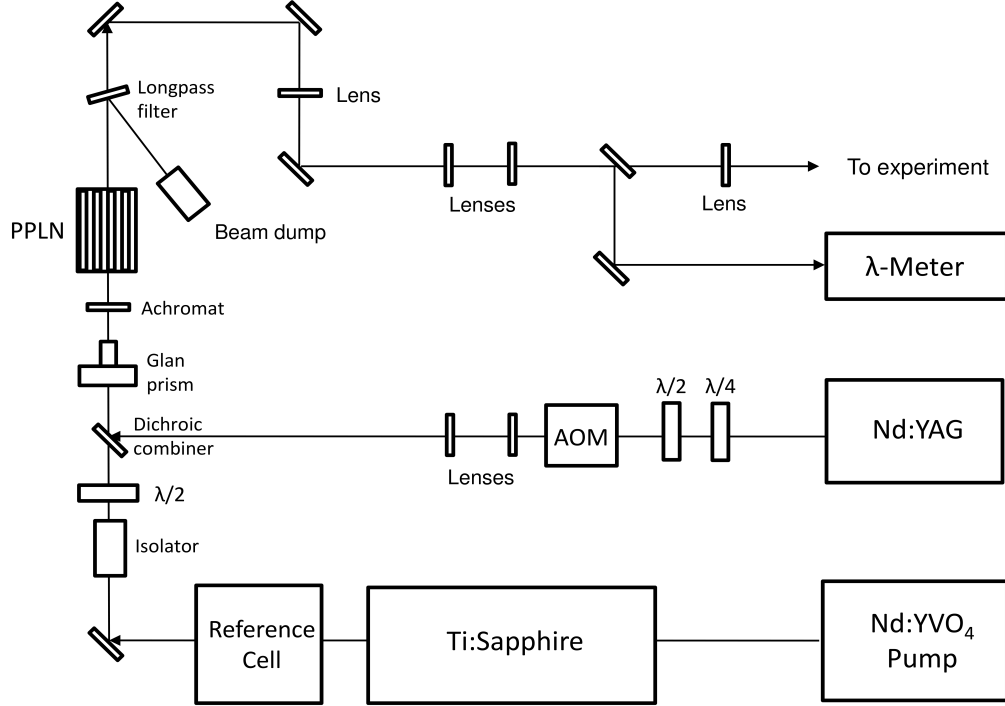


Figure 3.1: DFG System I (drawn by N. Tom).

The diode output is used to pump a Spectra Physics Millennia neodymium-doped yttrium orthovanadate solid state laser (Nd:YVO<sub>4</sub>, also referred to as ‘neodymium yttrium vanadate’). In the yttrium vanadate lasing medium, the Nd<sup>3+</sup> ions are pumped from their ground state to an excited band from which they quickly and nonradiatively relax to the <sup>4</sup>F<sub>3/2</sub> electronic state before fluorescing to the <sup>4</sup>I<sub>11/2</sub> state [73,74]. It is interesting to note that the benefits of Nd:YVO<sub>4</sub> as a lasing medium have been known since the 1960’s, however, the technology to grow optical-quality crystals and the need for single line pumping (provided by diode lasers) were not realized until years later. One of the benefits of using the vanadate oxide host is output lines that are not multi-peaked, a consequence of reduced Stark splitting in VO<sub>4</sub> as compared to the splitting found in yttrium-aluminum-garnet host crystals [75].

The resultant 1064 nm emission from the Nd:YVO<sub>4</sub> is frequency doubled by a second harmonic generating (SHG) crystal, the first of two nonlinear optic components in this difference frequency laser. The crystal is made of lithium triborate (LiB<sub>3</sub>O<sub>5</sub>), also abbreviated LBO. When considering the interaction between electromagnetic radiation and matter the parameter of interest is the intensity of the induced polarization in the matter, which is expressed by elements of the electric susceptibility tensor ( $\chi^{(2)}$ ). In addition to the electric susceptibility, the properties that govern the SHG power output include frequency, crystal length, beam area, and the phase mismatch condition ( $\Delta k$ ). The mismatch condition expresses how well the induced polarization and the electromagnetic waves can remain in-phase, with higher efficiency resulting when there is no mismatch,  $\Delta k = 0$ . In a

given system with a constant frequency, the SHG power ( $P_{2\omega}$ ) is proportional to the phase mismatch

$$\frac{P_{2\omega}}{P_{\omega}} \propto \frac{\sin \Delta k}{\Delta k}, \quad (3.1)$$

which is a sinc function that approaches 1 as  $\Delta k$  approaches 0. The mismatch condition has an index of refraction dependence  $\Delta k \propto n_1 - n_2$ , and can best be minimized with the use of birefringent materials. One can control the indices (to a small degree) by the choice of alignment angles in a material, and this is known as critical phase matching. It is also possible to tune the temperature of the birefringent crystal in order to precisely control the index matching, a process known as non-critical phase matching [72, pg. 582-596]. The LBO in this system employs the latter technique. It was sometimes necessary to manually re-optimize the temperature of the crystal, as indicated by fluctuating power from the Nd:YVO<sub>4</sub> laser.

The 532 nm output beam goes on to pump the Ti:Sapph laser (Sirah Matisse TS), a four-level solid state laser tunable over the range 700-990 nm. For titanium doped in sapphire, there is a coupling between the crystal field and electronic states of the ion that makes vibrational manifolds available. This coupling with phonon transitions provides a continuum of lasing wavelengths. The levels consist of two excited states,  $e_g$ , and three ground states,  $t_g$ . The symbols are derived from the Mulliken notation for irreducible representations, where the  $e$  representations imply a degeneracy of 2, the  $t$  representations imply a degeneracy of 3, and the ' $g$ ' represents 'gerade' or 'even,' referring to the character of the representation with respect to inversion through a molecule's center of symmetry (in this case Ti<sub>2</sub>O<sub>3</sub>). The upper levels are split by Jahn-Teller distortions that are caused by the crystal field, as are two of the lower states.

More specifically, the lasing medium consists of a sapphire host (Al<sub>2</sub>O<sub>3</sub>) which has been doped with Ti<sup>3+</sup> ions (0.1% Ti<sub>2</sub>O<sub>3</sub> by weight). The Ti<sup>3+</sup> ions possess a single valence electron ( $3d^1$ ) that is available for vibronic excitation into the band of vibrational levels which make up the higher of the two upper levels,  $e_g$  (this is another advantage of this four-level system; that it is widely 'pumpable'). The electron quickly and nonradiatively relaxes into the lower of the two upper levels, where the majority of the population resides due to the fluorescence lifetime of this level ( $\sim 3.2\mu\text{sec}$ ). Lasing occurs when these electrons relax to the higher of the ground states ( $t_g$ ), followed by a quick relaxation to the lower ground state, from which the cycle can begin anew [76].

Figure 3.2 is a diagram of the interior ring arrangement of the Ti:Sapph laser. The 532 nm pump beam enters from the right, and is aligned using the pump mirrors (PM 1 and PM 2) so that it passes centered through the two focusing/folding mirrors (FM 1 and FM 2) and the Ti:Sapph crystal. The fluorescence beam is then reflected off of M4 which is controlled by a slow piezo, through the thick etalon and TGG to the tweeter mirror M3, which is controlled by a fast piezo. The TGG isolator, so named because the beam passes through a window of terbium-gallium-garnet situated between two strong magnets, rotates the polarization of both counterpropagating beams. This works in concert with mirror M2 which also changes the polarization of the light because it is positioned slightly out of plane with the other mirrors. The out of plane mirror induces a polarization change that only 'corrects' the counterclockwise beam.

The birefringent filter (BiFi) serves to select a several hundred GHz-wide range over which lasing modes will occur in the cavity. It does so by adjusting three birefringent plates that are oriented in such a way as to increase reflective losses of s-polarized light in undesired wavelengths. A thin etalon

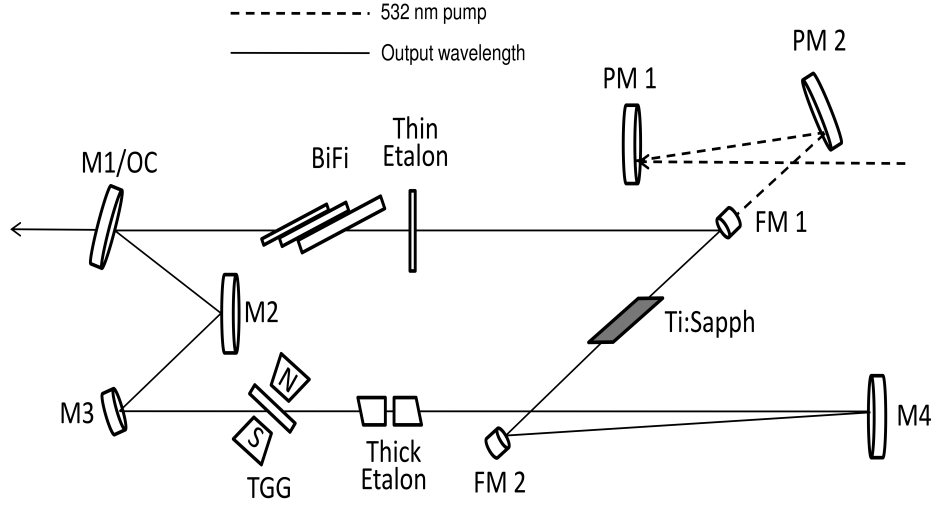


Figure 3.2: The ring arrangement of the titanium sapphire laser (adapted from [77, pg. 33]).

is used to further narrow the tuning of the laser. It has a free spectral range of  $\sim 250$  GHz, and is positioned by a piezo controller so that it suppresses all but a narrow range of frequencies in the laser cavity. The thin etalon has a relatively low finesse, which means that the range of frequencies that are allowed to pass are broader than if the finesse was high. A photo diode monitors the light being passed through the thin etalon, and a control loop generates an error signal to keep the intensity of this light constant with respect to the overall output intensity of the laser. A thick etalon with a free spectral range of 20 GHz is formed by two prisms that have an air gap between, the size of which is controlled by another piezoelectric actuator. The spacing between the prisms is controlled to select only one mode within the cavity [77, pg. 33-35]. Approximately 1-2 Watts pass through the output coupler (M1). An external reference cell incorporating a Fabry-Perot cavity is used to lock the laser to a specific frequency (within 1 MHz) by sending error signals to the laser cavity that control the fast and slow piezo-actuated mirrors, M3 and M4.

Three sets of interchangeable optics (MOS 1-3) make the laser tunable over 700-990 nm. The various actuators in the cavity are controlled by a Sirah-generated application called ‘Matisse Commander.’ This program allows the operator to tune the laser by selecting BiFi and thin etalon positions, as well as by tuning the thick etalon in selectable voltage increments ( $\sim 107$  GHz/volt).

### 3.1.2 Nd:YAG signal laser

The signal laser in this DFG is an Innolight Mephisto 1000NE Nd:YAG. The laser is diode-pumped, and the medium consists of a  $\text{Y}_3\text{Al}_5\text{O}_{12}$  crystal in which 1% of the  $\text{Y}^{3+}$  have been replaced with  $\text{Nd}^{3+}$  ions. The  $\text{Nd}^{3+}$  ions are excited to the pump band by 810 nm light from an internal diode laser. They subsequently de-excite to the  $^4\text{F}_{3/2}$  level. The 1064 nm fluorescence occurs in the transition  $^4\text{F}_{3/2} \rightarrow ^4\text{I}_{11/2}$ . Rapid nonradiative de-excitation occurs to the  $^4\text{I}_{9/2}$  ground state, making the Nd:YAG a four-level system like the Ti:Sapph and Nd:YVO<sub>4</sub> [72, pg. 48-52]. The laser can output up to 1 W with a 1 kHz linewidth (per 100 ms), however, the current was typically set to



$\sim 2.2$  A, which correlated with a  $\sim 600$  mW output.

### 3.1.3 Additional DFG components

Both the Ti:Sapph and Nd:YAG beam paths have additional components that isolate the lasers, focus, polarize, and combine the beams. After the Ti:Sapph reference cell, the beam passes through an isolator that contains a Faraday rotator and polarizers that effectively prevent the passage of a returning beam. This is done so that a reflected beam will not interfere in the Ti:Sapph ring laser cavity. Cavity ringdown setups involve very precise alignment of back reflections, and beams returning to and interfering with the laser source must be eliminated. After the isolator, the beam proceeds through a zero-order half-wave plate that is used to change the beam's polarization from horizontal to vertical. A typical half-wave plate works because the birefringent material in the plate is cut so that its optical axis (the 'fast' axis) is oriented parallel to the faces of the crystal, and the thickness of the plate is equal to  $n\lambda/2$ . In linearly polarized light where the electric and magnetic fields propagate with phase difference  $\Delta\phi = 0, 180^\circ$ , the half wave plate slows one of the propagating fields for a distance  $n\lambda/2$ , thereby shifting its phase by  $180^\circ$ . If the half-wave plate is oriented so that the fast axis is  $45^\circ$  to the polarization of the incident beam, the polarization of the outgoing beam will be orthogonal to that of the incident beam. A zero-order half-wave plate is constructed so that it will work over a range of wavelengths.

The Nd:YAG laser beam passes through quarter and half-wave plates before entering an acousto-optic modulator (AOM). The quarter-wave plate is constructed similarly to the half-wave plate, however the thickness is equivalent to a multiple of  $n\lambda/4$ . Instead of rotating the axis of polarization by retarding one of the electromagnetic components by  $\Delta\phi = 180^\circ$ , the quarter-wave plate will shift the relative phase difference by  $90^\circ$ , thereby changing elliptically polarized light (which the Nd:YAG is) to linearly polarized light. The half-wave plate is then used to rotate the polarization to the vertical.

The AOM (Brimrose TEM-85-2-1064), or a system of equivalent functionality, is an essential component of a laser system used for cavity ringdown. Its purpose is to deflect a beam from one direction of travel to another within tenths of a microsecond so that the light can be decoupled from the cavity to allow a ringdown event to take place. A driver box provides an 85 MHz signal to a transducer that drives sound waves in the AOM material. The sound waves cause variations in the index of refraction. Light impinging on these index fluctuations will be Brillouin scattered into one of many different beams, each Doppler shifted by the frequency of the sound wave in the material [78, pg. 6]. When a negative voltage TTL is sent to the driver box, the transducer stops vibrating for a length of time equal to the width of the TTL, the scattering ceases, and the entire beam returns to the undeflected, zeroth-order path. In this setup, when a ringdown is detected by a home built comparator box (circuit diagram, Figure D.1), the comparator sends a TTL pulse to the AOM driver which stops the Nd:YAG beam from going into the crystal, effectively extinguishing the mid-IR light.

The Ti:Sapph and Nd:YAG beams are made co-linear starting at a dichroic beam combiner that is highly reflective in the 1064 nm range, but transmits at shorter wavelengths. One flaw in our implementation of this was the fact that the substrate for the dichroic was not a highly polished optical material, nor was it antireflective coated for the shorter wavelengths. A future upgrade

would seek a custom optic that is both highly reflective at 1064 nm and more highly transmissive for shorter wavelengths.

After the dichroic, both beams pass through a Glan polarizing prism. The purpose of the Glan prism is to filter the polarized light such that almost all of the undesired polarization is removed. This optic consists of two prisms with a narrow gap of air in between. The input and output sides of the prisms are normal to the incident and exiting light. The plane of the prisms at the point they come together is at an angle that is optimized to internally reflect s-polarized light. The beam that enters the air gap between the prisms is almost exclusively polarized in one direction, which is vertical in this setup. The purpose of the second prism is to refract the beam back to a path that is parallel to its original path (before it was refracted by the angled surface of the first prism).

The final optic before the nonlinear crystal (discussed in §3.1.4) is a 20 cm achromatic doublet lens. The purpose of this lens is to focus the beams into the nonlinear crystal while minimizing chromatic aberration. Both beams are focused to a 140  $\mu\text{m}$  diameter waist with a Rayleigh range that is approximately 1/3 the length of the crystal. This is a rule of thumb that if followed will ensure that the beam does not become too large before exiting the crystal. Reducing the chromatic aberration ensures that the two beams of differing wavelength will focus in roughly the same location, a point just inside the leading edge of the crystal. This is accomplished by the dispersive properties of the doublet, which is made of two materials possessing dispersions that counterbalance one another.

### 3.1.4 The $\text{LiNbO}_3$ nonlinear crystal

Difference frequency generation combines two beams such that  $\omega_{\text{pump}} - \omega_{\text{signal}} = \omega_{\text{idler}}$ . In this system, the Ti:Sapph served as the pump laser and the Nd:YAG as the signal. As mentioned in §3.1.1, matching the phases is important for optimizing conversion efficiency in nonlinear processes. This is all the more challenging when  $\omega_{\text{pump}} \neq \omega_{\text{signal}}$ . The first DFG was built by Pine, who observed an output power of  $\sim 500$  nW [79]. This early system generated a modicum of power because of the destructive interference that can take place at the coherence length of the beams,  $l_{\text{coherence}} = \pi/\Delta k$  if  $\Delta k \neq 0$  [80] [81, pg. 97-140]. Recall that  $\Delta k$ , the phase mismatch, is a measure of the phase difference between the electromagnetic waves,  $\Delta k = k_{\text{pump}} - k_{\text{signal}} - k_{\text{idler}}$ . It can also be considered the degree to which momentum is not conserved in the mixing of the beams. The further the light propagates past the coherence length, the more of the difference generated light ( $\omega_{\text{idler}}$ ) is destroyed, as depicted in Figure 3.3. This cycle is repeated every even multiple of  $l_{\text{coherence}}$ , making it necessary in such systems to use nonlinear crystals that are an odd multiple of the coherence length.

This limitation can be overcome by using a periodically poled crystal. In such a crystal, the polarization axis of the nonlinear material is inverted after every coherence length. This has the effect of changing the sign of the nonlinear coefficient in the electric susceptibility tensor,  $\chi^{(2)}$ , which in turn will cause constructive interference as the light propagates through the crystal. This is referred to as quasi-phase matching. It is not nearly as efficient as a birefringent phase-matched system ( $\Delta k = 0$ ) such as in SHG, but a significant intensity of light at the difference frequency is generated nonetheless. These polarization directions are normal to the upper and lower surfaces of the crystal, and this necessitates the vertical polarization of the incoming light as is provided by the Glan laser prism. Others have used this technique to build systems similar [82], or almost identical to

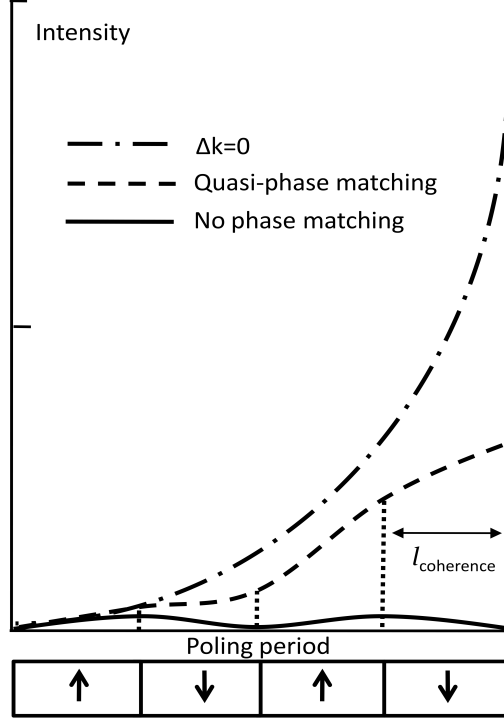


Figure 3.3: Phase matching in a non-linear crystal (adapted from [81, Fig. 11]).

this one [83,84]. In these and the current system, the periodically polled crystal was manufactured from lithium niobate ( $\text{LiNbO}_3$ ; Stratophase DFG2-40). The crystal has an antireflection coating covering 700-1064 nm wavelengths. The combination of pump and signal wavelengths, along with the poling periods of the nonlinear crystal, make this DFG capable of generating light from 2.8-4.8  $\mu\text{m}$ .

The equation that governs the power output of a DFG is [81, pg 118]

$$\text{Power} = \frac{2\omega_{idler}^2}{c^3\epsilon_o n_{pump} n_{signal} n_{idler}} \left( \frac{2d_{33}}{m\pi} \right)^2 L^2 P_{pump} P_{signal} \frac{1}{A} \quad (3.2)$$

where  $c$  is the speed of light,  $\epsilon_o$  is permittivity of free space,  $n$  are the indices of refraction,  $d_{33}$  is the effective nonlinear coefficient from the electric susceptibility tensor,  $m$  is the order of the quasi phase matching (the odd multiple of coherence lengths after which polarization is switched),  $L$  is the interaction length (the length of the crystal),  $P$  are the pump and signal powers, and  $A$  is the area of the overlapped beams. The crystal used in this work is 4 cm long, with 13 channels, each with a different poling period enabling wider tunability. Each channel has a  $0.5 \times 0.5$  mm cross section. Matching the pump and signal beam profiles is also important as can be seen by the term  $A$  in equation (3.2).

The poling period and indices of refraction are established in the design of a given crystal and by the material from which it is manufactured. However, they can be optimized by controlling the temperature of the crystal because both the index of refraction and the poling period have a

temperature dependence (in the latter, the crystal expands along the axis of beam propagation with higher temperature). This can be achieved by minimizing the equation

$$\Delta k = 2\pi \left( \frac{n_{pump}}{\lambda_{pump}} - \frac{n_{signal}}{\lambda_{signal}} - \frac{n_{idler}}{\lambda_{idler}} - \frac{1}{\Lambda} \right) \quad (3.3)$$

where the  $\lambda$  are the respective wavelengths and  $\Lambda$  is the poling period. Minimizing equation 3.3 is accomplished by solving the Sellmeier equations for a given system [85]. The crystal temperature is adjusted using an oven (Thorlabs OV40) and oven controller (Thorlabs TC200).

In each of the DFG lasers described in [82–84], output power was typically on the order of tens of  $\mu\text{W}$  when using pump and signal powers from hundreds of mW to 1-2 Watt. Our system achieved an idler output ranging from 450-700  $\mu\text{W}$  using  $P_{pump} = 1.6 \text{ W}$  and  $P_{signal} = 550 \text{ mW}$ . Using higher pump and signal power will result in higher idler power, however, with higher pump power there is a potential increase in the efficiency of optical parametric generation and optical parametric amplification effects [81, pg. 113]. Both can increase the idler linewidth, a problem which should be investigated before this DFG is used for even higher-resolution spectroscopy.

### 3.1.5 Mid-IR light path after the conversion

After the mid-IR is generated in the nonlinear crystal, a longpass filter deflects the high powered pump and signal beams into a beam dump. We attempted to use germanium and AR coated silicon windows, however, in both cases the heating of the windows increased their opacity to mid-IR light.

After the beam dump, four  $\text{CaF}_2$  lenses are positioned in order to focus the beam as required for the various spectroscopic methods that were employed. In addition, a  $\text{BaF}_2$  window or a  $\text{ZnSe}$  neutral density filter (attenuation = 0.15) were used (at different times) to deflect the beam into a Michelson interferometer (Bristol 621A) for precise wavelength measurement.

## 3.2 Difference frequency generation system II

The second DFG uses an  $\text{Nd:YVO}_4$  laser and a dye laser as its pump and signal, respectively. The wavelengths of these lasers are very different from those of DFG system I, as are the specifications of the nonlinear crystal. These differences are highlighted below. This DFG system was not used in any of the measurements described in this work, however, the DFG components (excluding the pump and signal lasers) were researched and acquired by the author, and so are discussed here. The general layout for the DFG system is found in Figure 3.4. This DFG was assembled by K. Crabtree and C. Kauffman, and at the time of writing has produced its first mid-IR light.

### 3.2.1 $\text{Nd:YVO}_4$ pump laser

The physics of the  $\text{Nd:YVO}_4$  laser (a Coherent Verdi V10) are as described in §3.1.1. It is pumped by a proprietary diode array, and is capable of 10 W total output power. A major difference between this DFG and system I is the fact that the  $\text{Nd:YVO}_4$  is used as both the pump for the DFG process, and as the pump for the dye laser. An 80/20 beamsplitter passes  $\sim 7 \text{ W}$  to pump the dye laser, and the remaining 2-3 W is routed through the AOM (Brimrose TEM-85-2-532) and focusing BK-7 lenses before combining with the dye laser beam.

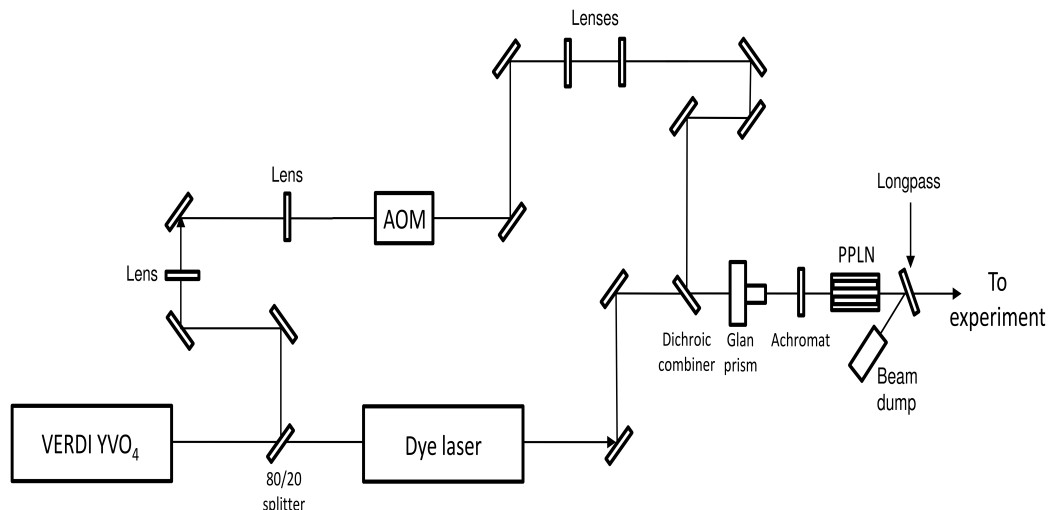


Figure 3.4: DFG system II (drawn by N. Tom).

### 3.2.2 Dye signal laser

The dye laser is a Coherent 899-29, which is tunable between 375-890 nm depending on the dye and the internal optics used. Dye lasers were the first truly tunable laser systems available. The governing phenomenon was discovered during experiments with irradiated organic and organometallic compounds in the mid-1960s [86, pg. 1-5]. In the lasing medium (currently rhodamine 640 perchlorate), a molecule is raised to an excited singlet state, from which it quickly relaxes to the lowest vibronic level of that singlet state. Light is emitted when the molecule de-excites from the lowest vibronic level of the singlet state down to an excited vibronic level of the ground state [86, pg. 34-35].

The dye in this system is circulated by a pump (Coherent Model 5920) which also cools the dye to  $\sim 4^\circ\text{C}$ . This pump forces the dye in a planar jet that is intersected by the 532 nm pump laser beam. The lasing cavity is established between 4 mirrors, one of which is an output coupler.

A birefringent filter narrows the bandwidth in the cavity to approximately 2 GHz, and a thin etalon and a thick etalon are included in an intracavity assembly to further reduce the bandwidth of the cavity to 10 MHz. An external reference cavity provides error signals to a tweeter that is driven by a fast piezo actuator, and a rotating Brewster plate that is also motor-driven to account for slower changes in the cavity. These active elements enable the laser to achieve a linewidth of  $\sim 500$  kHz. The laser can be scanned up to 30 GHz by rotating the Brewster plate, and by varying the tilt of the thin etalon and the width of the thick etalon [87, pg. 2.2-2.6].

### 3.2.3 Additional DFG components

The beams are made co-linear at a custom dichroic beam combiner that is highly reflective at 532 nm. Unlike in system I, the substrate for this dichroic is optical grade and its back side is antireflective coated for the dye laser wavelengths. After combining, the vertically polarized light is filtered by a Glan prism, and focused into the nonlinear crystal by an achromatic doublet. Both components have been antireflective coated for the wavelengths of the dye and pump lasers. A simplifying property

of this system is that the light from both the pump and signal lasers is vertically polarized, which eliminates the need for waveplates.

### 3.2.4 The MgO-doped LiNbO<sub>3</sub> nonlinear crystal

The processes that occur in the nonlinear crystal are similar to those described in §3.1.4 in most respects. Differences include the poling period and antireflective coatings which are optimized for 532 nm pump and 600-720 nm signal wavelengths, which will make the idler output tunable down to  $\sim 2.2 \mu\text{m}$ . The crystal is also 5 cm long, which results in higher output power as can be seen by inspection of equation (3.2). In addition, it was manufactured from MgO doped LiNbO<sub>3</sub>. Optical damage to these nonlinear crystals is not uncommon given the high beam power and small waist sizes, and many techniques have been suggested to prevent it [88]. In a doped crystal a small amount of Mg replaces Nd which has the effect of reducing certain characteristic electromagnetic absorptions of purely Nd-doped crystals. This increases the strength of the crystal lattice and in so doing increases its resistance to photorefractive damage [89].

## 3.3 Spectroscopic methods

Two methods were used to perform the laser-based spectroscopic measurements of this study: cavity ringdown and multipass direct absorption. The theory and implementation of each will be described here. In the case of ringdown, additional experimental details pertaining to the different plasma sources are provided in Chapter 4. Cavity ringdown was used to perform the spectroscopic measurements required for the dissociative recombination experiments as well as the  $\text{H}_2 + \text{H}_3^+$  reaction dynamics experiments (Chapters 5 and 6), and direct absorption was used solely for the reaction dynamics experiments.

### 3.3.1 Continuous wave cavity ringdown spectroscopy

Cavity ringdown spectroscopy (CRDS) is a highly sensitive method for observing trace constituents in the gas phase [90]. The ability to determine absorptive properties such as the cross section and the number density of a material is dependent on the precision with which one can measure changes in the intensity of light as it passes through a medium ( $I_t/I_o$ ). This is expressed by the familiar Beer's law,

$$I_t = I_o e^{-\sigma n L}, \quad (3.4)$$

in which  $I_t$  is the intensity of the transmitted light after passing through the medium,  $I_o$  is the intensity of the incident light,  $\sigma$  is the wavelength-dependent cross section,  $n$  is the number density of absorbers ( $\text{cm}^{-3}$ ), and  $L$  is the path length through the absorbing medium. The high sensitivity of CRDS is a direct result of the increased path length ( $L$ ) it affords, and the fact that the technique does not require the direct measurement of  $I_t/I_o$ . Each of these aspects is discussed below.

In an ideal system, light will only couple into a cavity if the space between its reflective surfaces is an integral multiple of the light's wavelength. Real systems, however, have a finite linewidth. The build up and subsequent loss due to light leakage through the reflective surfaces is depicted in Figure 3.5. If a cavity is constructed with highly reflective mirrors, then the ratio of the light that stays and

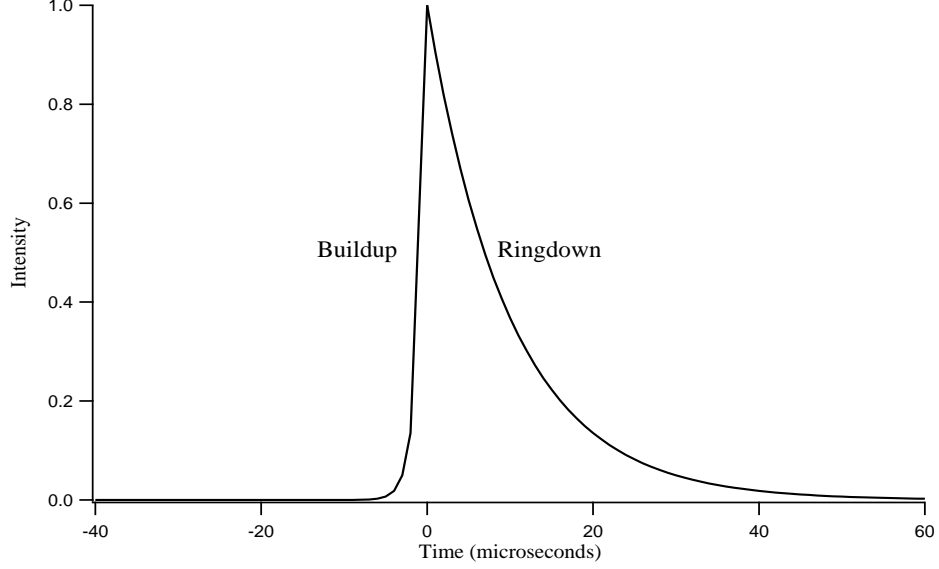


Figure 3.5: An illustration of a typical buildup/ringdown profile.

continues to reflect within the cavity to that which is lost (the quality factor ‘Q’) is high. The result of a high Q is a beam that makes many round trips within the cavity, meaning a long pathlength through the absorbing medium. Ideally, CRDS is performed in cavities of high Q constructed with highly reflective mirrors. The resulting path lengths are on the order of hundreds to thousands of meters. In this work, the mirrors possessed a 6 m radius of curvature and were 99.98% reflective at  $4\ \mu\text{m}$  (Los Gatos, 901-0008-4000). These mirrors actually served both to form the optical cavity, and to seal the vacuum chamber.

The time dependence of the intensity of light stored in a cavity is related to the reflectivity of the mirrors ( $R$ ) by,

$$I(t) = I(0)e^{-(1-R)\frac{tc}{L}}, \quad (3.5)$$

where  $I(t)$  is the intensity of stored light after time  $t$ ,  $I(0)$  is the intensity of light at  $t=0$ ,  $c$  is the speed of light, and  $L$  is the distance between the mirrors. The quantity  $tc/L$  represents the number of times the light has been reflected between the mirrors, and  $(1-R)$ , by Kirchhoff’s law, represents the light that is lost to transmission with each reflection. If an absorbing species is present in the cavity, then  $-\sigma nL\frac{tc}{L}$  is added to the argument of the exponent, representing the absorption loss per pass over  $tc/L$  passes,

$$I_t = I(0)e^{-\{(1-R)+\sigma nL\}\frac{tc}{L}}. \quad (3.6)$$

The time constant is defined as the time it takes for  $I(t)$  to equal  $1/e$  of  $I(0)$ . This happens when the argument of the exponent is equal to  $-1$ , which occurs when  $t$  is replaced by the time constant  $\tau$ , where,

$$\tau_{no\ sample} = \frac{L}{c(1-R)} \quad (3.7)$$

$$\tau_{with\ sample} = \frac{L}{c\{(1-R) + \sigma nL\}}. \quad (3.8)$$

These equations indicate that the addition of an absorptive species will reduce the time constant,  $\tau$ . By substituting the absorption coefficient  $\alpha = \sigma n$ , and algebraically solving equations (3.7) and (3.8) to eliminate  $R$ , the result is

$$\alpha = \frac{1}{c} \left( \frac{1}{\tau_{with\ sample}} - \frac{1}{\tau_{no\ sample}} \right) \quad (3.9)$$

So the absorption coefficient ( $\alpha$ ) of a species can be determined knowing only the time constants of ringdown when there is sample present and when there is no sample present [91]. Thus, the need to measure small changes in  $I_t/I_o$ , and any dependence on laser intensity, no longer exists.

The first implementations of CRDS used pulsed lasers. A drawback to this is the fact that the linewidth of a pulsed laser is inherently larger than that of a CW laser. In addition, the speed with which measurements can be taken is limited by how quickly the pulsed laser can regenerate for subsequent pulses. A continuous wave (CW) laser, as used in our experiment, eliminates these limitations [92]. In CW-CRDS, the cavity length is periodically changed so that it is brought in and out of resonance with the incident light. This is accomplished by using a piezo mount that dithers one of the cavity mirrors. In this work, the piezo (Piezomechanik HPSt 150/20-15/12 VS 35) was dithered by a driver that was coupled to an 8 Hz sawtooth waveform. The applied signal typically ranged between 30-60 V, and resulted in a change in cavity size that equated to approximately two free spectral ranges.

The ringdown time constants were measured using a 500 Hz to 1 MHz bandwidth AC indium antimonide (Infrared Associates InSb 1000) detector positioned downstream of the cavity, along with focusing optics to collect the light ‘leaking’ from the downstream mirror. An AC detector with a fast response time was necessary in order to properly sample the fast signal decay in the cavity. Data were processed by a locally created ringdown data acquisition program, discussed in [93], and the time constant was determined using an exponential curve fitting algorithm. Typically 40 ringdown measurements were taken per data point (at each frequency step as the laser was scanned).

### 3.3.2 Multipass absorption spectroscopy

Direct absorption spectroscopy was also used, specifically for the reaction dynamics experiments. Some of the dynamics experiments were originally designed to measure the time-dependent behavior of the hydrogen spin modifications. These measurements would be difficult using cavity ringdown, requiring a large number of ringdowns with sample in order to monitor even one of the spin modifications over a period of 200  $\mu$ s. In contrast, the time dependence of direct absorption signals is easily observed.

A multipass configuration produces a long pathlength through the absorbing medium which helps in the observation of low density samples, but of course to a lesser extent than in CRDS. In these experiments a White cell scheme was employed which provided  $\sim 16$  m of pathlength through the plasma. The probed plasma source was a hollow cathode, further details of which will be provided in Chapter 4.

White’s multipass configuration makes use of three mirrors. The first is positioned exactly one radius of curvature away from two others that are placed next to each other. The mirrors are oriented such that the center of curvature for the first mirror is positioned between the two mirrors



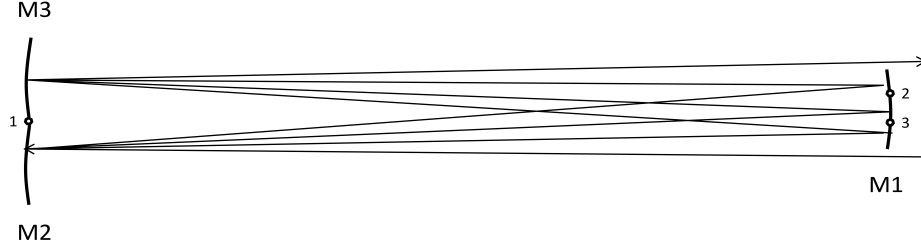


Figure 3.6: White cell mirror configuration (M1,M2,M3) and their centers of curvature (open circles 1,2,3).

on the opposite side, and the number of passes is set by positioning the centers of the other two mirrors onto the first mirror (see Figure 3.6). Adjusting the spots of the two close mirrors allows the operator to select the number of passes the light will make through the cell, in multiples of four. An advantage of placing the mirrors at exactly the center of curvature of one another is the beam is re-focused every time it traverses the cell. The only losses are due to scattering and absorption [94].

Two 1-in diameter gold mirrors were used in our experimental setup. One mirror was cut in half, providing two half-moon surfaces for one end of the cell. The remaining mirror was cut in a mushroom shape to make space for the incoming and outgoing beams to pass. These are depicted in Figure 3.7. Unlike the ringdown setup where the mirrors were structural members of the experimental chamber, these mirrors were positioned outside of the hollow cathode cell on kinetic mirror mounts.

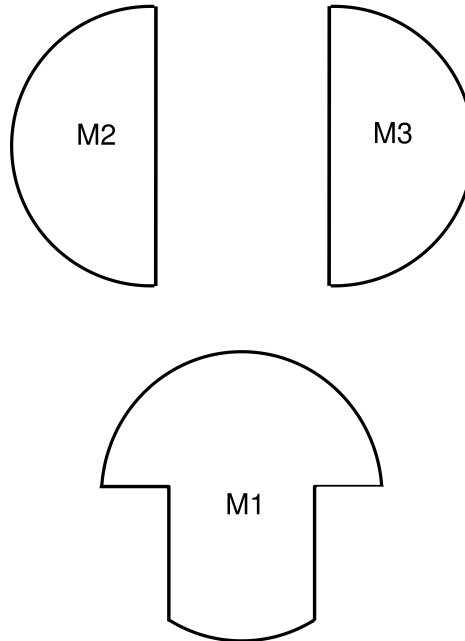


Figure 3.7: White cell mirrors (M1,M2,M3).

# Chapter 4

## Plasma sources

The experiments in this work were carried out under a diverse set of conditions. Sometimes this was motivated by the desired parameters of a particular experiment (e.g. temperature), and at others it was driven both by these parameters and limitations of the experimental apparatus, as was the case for dissociative recombination. This chapter provides a description of the two plasma sources that were used, as well as the conditions produced by each. Two additional sources that are currently under design will also be introduced.

### 4.1 Pulsed solenoid

The pulsed solenoid source was designed to produce ions for the CRYRING ion storage ring at the University of Stockholm, Sweden. It had been built for a previous experiment [95]. In addition to producing rotationally cold ions via a pinhole supersonic expansion, this source's low duty cycle was suitable for the pumping capacity of the storage ring's vacuum systems. The pulsed solenoid source was also used to explore the  $\text{H}_3^+ + \text{H}_2$  reaction.

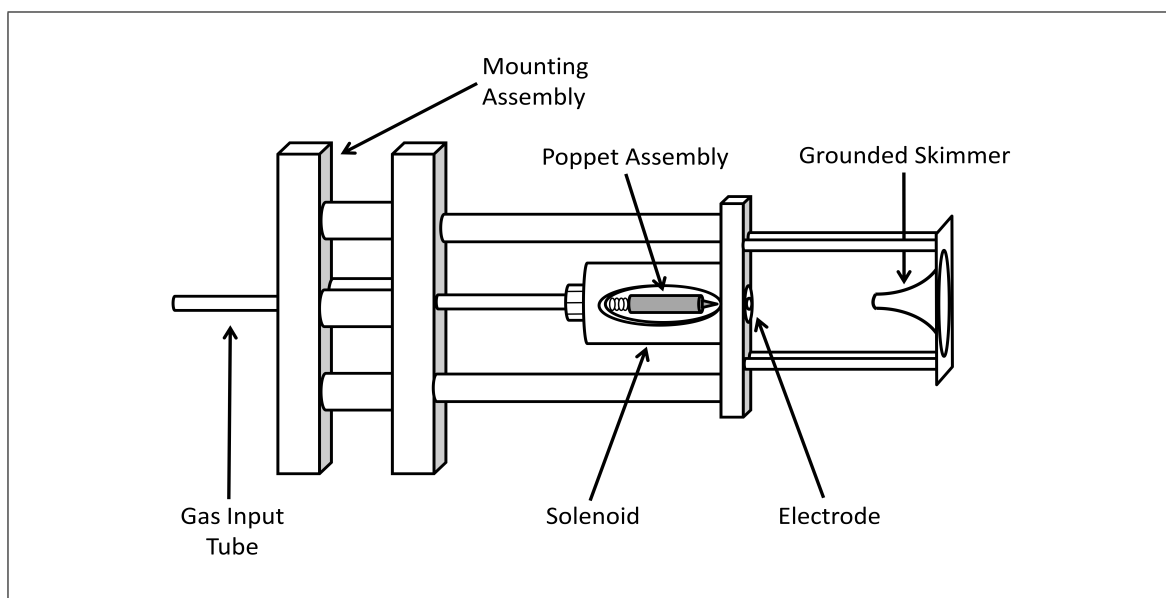


Figure 4.1: The pulsed solenoid source. The cutaway shows the interior spring, armature, and poppet.

### 4.1.1 Design

The source is a solenoid valve (Parker Hannafin General Series 9) with a  $500\text{ }\mu\text{m}$  diameter pinhole. The pinhole opening is located 1 mm upstream of a ring electrode. Approximately 4.2 cm downstream from the electrode is a grounded skimmer that serves to collimate the ion beam for injection into the ion storage ring. A spring-mounted iron armature, designed to hold a teflon poppet in place in the pinhole, moves to extract the poppet and form a gas pulse (see Figure 4.1).

The entire assembly was mounted to aluminum plates that could be slid over metal rods, making it possible to translate the source along the axis of the gas pulse. These rods were attached to a square plate at the back of the vacuum chamber which was sealed to the chamber by a large o-ring. Combined with a micrometer, this made it possible to translate the source vertically as well as horizontally. Moving the source in either direction allowed the spectroscopic sampling of different regions of the expansion in order to characterize the rotational temperature of the ions.

The source was electrically isolated from the rest of the chamber (many of the rods and the gas feed tube depicted in Figure 4.1 are made of non-conducting material). This made it possible to monitor the plasma current via a resistive circuit in an external discharge driver box.

### 4.1.2 Operation

The solenoid source was activated using a home-built driver box (circuit diagram, Figure D.2) coupled to an external power supply and pulse generator. The experimental setup is shown in Figure 4.2. The high voltage power supply provided -300 V of potential to six  $22\text{ }\mu\text{F}$  capacitors in the driver box. These capacitors would discharge their voltage to the solenoid upon receipt of a trigger pulse from a pulse generator (Quantum Composers 9518+).

The trigger pulse itself was  $100\text{ }\mu\text{s}$  in duration, but the source would typically produce a 0.75-1.0 ms gas pulse due to delays imparted by the mechanical movement of the poppet. The gas pulse was embedded in a 1 ms discharge pulse that was provided by a separate power supply and driver (circuit diagram, Figure D.3). The discharge pulse was between -450 and -800 V, and was applied to the electrode  $\sim 200\text{-}500\text{ }\mu\text{s}$  before the gas pulse. Previous experiments indicated that the temperature of the expansion was independent of the pulse duration, however, the possibility existed that embedding the gas pulse in the discharge pulse had a heating effect. This was not tested during the course of the experiment.

The rotational temperature had a strong dependence on the condition and seating of the poppet. As a result it was sometimes necessary to ‘tune’ the seating of the poppet in the pinhole by twisting the gas feed tube. This was possible because the tube was fed through an Ultra-Torr connection on the translatable aft section of the chamber, which could be loosened when adjustments were necessary.

The test gases were fed into the solenoid with a backing pressure of 2 bar. The chamber was evacuated to a pressure of approximately 15 mbar at the rate of  $3500\text{ L s}^{-1}$  by a 2-stage Roots blower that was backed by a rotary vane pump (Leybold).

The plasma was probed by the laser on the center axis of the expansion, approximately 3.9 cm downstream of the electrode. This position was immediately in front of the skimmer, and was selected with the assumption that the ions in this region were the ones that were going to be injected into the ion storage ring.

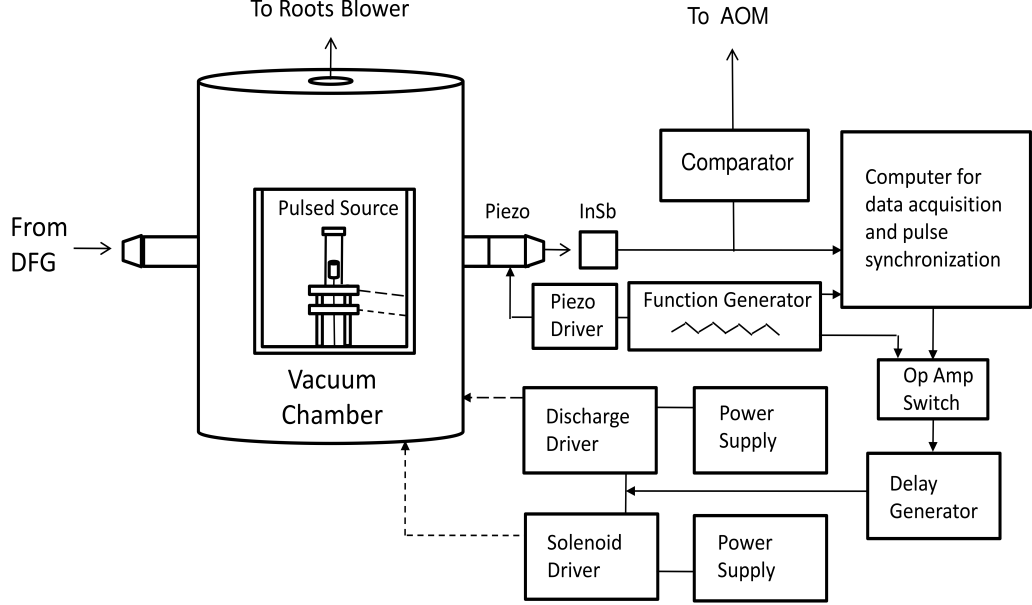


Figure 4.2: The ringdown/pulsed source experimental setup. The source was mounted horizontally in the experiment, but is shown here in a vertical orientation through a cutaway for simplicity.

### Integration of pulse timing with ringdown

The integration of continuous wave cavity ringdown with the pulsed source provided an interesting challenge. As described in §3.3.1, one of the cavity mirrors was dithered by a piezo actuator. This caused the cavity to periodically move in and out of resonance with the incident light. Spectroscopy would be relatively straightforward if the test gas were continuously present, but a pulsed source requires anticipation of the ringdown event as discussed in Birza *et al.* [96].

To account for this, a ringdown prediction code was integrated with the LabWindows data acquisition routine (developed by M. Zwier and discussed in [93]). The ringdown data and the piezo ramp voltage (a sawtooth function) were fed to the computer via a 14-bit digitizer (National Instruments 5122). The sawtooth function (depicted in Figure 4.3) was analyzed to determine peak and minimum voltage, as well as the frequency of the sweep. Up to two ringdown events were recorded per upsweep of the sawtooth along with the voltage at which the ringdowns occurred. After approximately 3 ms of exponential fitting of the ringdown decay and other calculations, another measurement was taken to determine the sign of the slope of the piezo sweep. This was done to ensure the measurements were only being taken on the upsweeps of the piezo ramp. If a ringdown event was detected at the same voltage on the next piezo upsweep, the ringdown was considered repeatable. The resulting trigger voltage was then offset to a lower voltage than measured. This ‘lead’ voltage was calculated from  $dV/dt$ , which was derived from the measured sawtooth frequency and a lead time which could be set by the operator in  $\mu\text{s}$ . The intent of the lead voltage was to account for valve actuation and ion time of flight so the heart of the discharge pulse would be in the laser beam path at the time of the ringdown ( $\sim 3.9$  cm downstream).

If a ringdown actually occurred when the source had been triggered, then the absorbance data from that ringdown event was recorded in an array of ‘sample’ events. The majority of ringdown

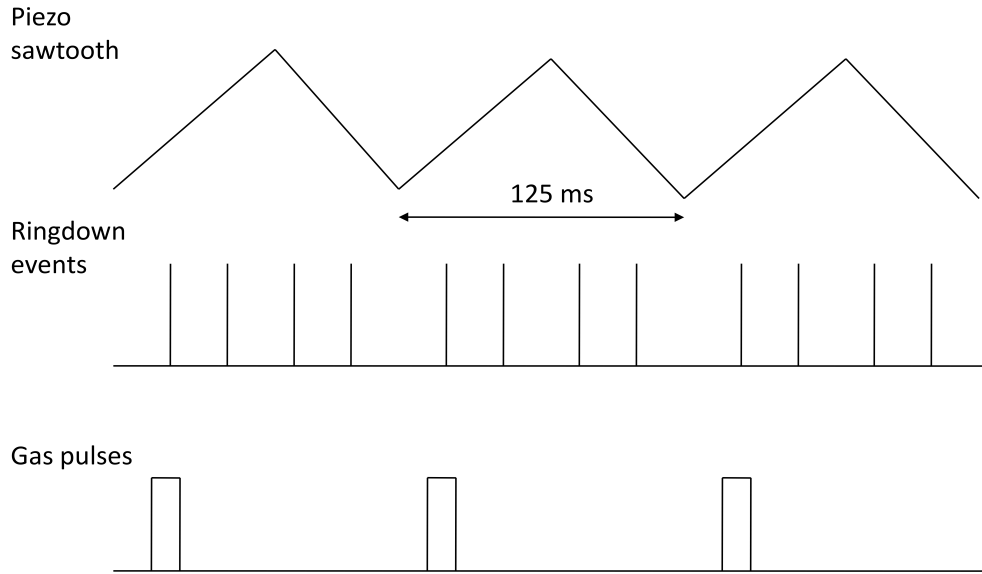


Figure 4.3: Gas pulses were synchronized with ringdown events, which occurred periodically with the dithering of one of the ringdown mirrors.

events, however, were deemed unrepeatable by the prediction code. The absorbances from these events were recorded in a ‘baseline’ array. The average of the baseline absorbance was subtracted from the average of the sample absorbance in order to calculate the final absorbance spectrum (see §3.3.1). In order to reduce the influence of time constants measured from ringdown events formed by higher order transverse modes, the ringdown code only stored points that were among the 50% closest to the mean. Additional logic was added to reject data if the predicted and actual ringdown events occurred outside of an operator-set time tolerance, and ringdowns that occurred too close to the peak of the piezo sweep were rejected in order to prevent accidental measurements on the down-sweep.

In order to initiate the solenoid and discharge pulses, a trigger circuit was designed to allow the ringdown prediction code to interface with the pulse generator. The prediction code sent an output voltage to a homebuilt op-amp switch. The voltage was held at a low value as long as there were no predicted ringdowns. The op amp switch was also fed with the same piezo sawtooth voltage as was sent to the prediction code. If a repeatable ringdown was detected, the output voltage was set to the calculated lead voltage and the op-amp would send a trigger pulse to the pulse generator as soon as it detected equivalence between the two voltages. An additional op-amp was included in the circuit as a Schmitt trigger in order to sharpen the output TTL signal that was sent to the digital delay generator. There were typically 40-50 ringdowns per second, 5 of which were ringdowns with sample present.

The DFG was scanned by tuning the Ti:Sapph laser. Voltage commands were sent from the ringdown code to the Ti:Sapph laser by way of virtual interface storage architecture (VISA). Forty ringdown samples were taken at each point, after which the ringdown code would step the laser by

$\sim 50$  MHz.

Although the code successfully predicted the ringdown events, the measurements varied in such a way as to lead to significant (factor of two to three) differences in the lineshape or the calculated peak height, even after averaging over forty samples. There were multiple causes of this variation, such as arcing and pulse timing jitter. Arcing arose from deposits on the electrode as well as inhomogeneity in the gas pulses. With regards to timing jitter, if the resonance was slightly earlier or later than predicted, the measurement would occur in different locations along the gas pulse. There were also long-term effects which may have been due to the flushing of impurities through the gas feed line. The short-term variations were mitigated by normalizing the data, which was accomplished using a boxcar integrator (Stanford Research SR250) to record an average discharge current during the measurements. The spectra were then divided by this current. In addition, each peak was fit with a Gaussian lineshape (Doppler broadening was the source of line broadening) and it was the peak height of this Gaussian that was measured and recorded. The effectiveness of these techniques was evident from the shrinking standard deviation that occurred with their application.

### 4.1.3 Plasma characteristics

Measurements with the solenoid pulsed source required knowledge of the rotational temperature as well as the  $\text{H}_2$  and  $\text{H}_3^+$  number densities of the plasma. Temperatures were monitored spectroscopically during the experiments, and the number densities were predicted or observed at different locations in the plasma.

#### Temperature

Expansions are ideal for rapid translational and rotational cooling of constituent molecules. The conversion of internal energy to translational energy in expansions has been well documented [97], with the mechanism being the collisional transfer of the internal energy to the bulk translation of the molecules. Vibrational modes are not as easily cooled because the energy spacing between vibrational levels is large, decreasing the probability of direct energy transfer to the translational states by inelastic collisions. The pressure conditions used with this source fell within the limits of a Campargue-type expansion [98], and the predicted behaviors for temperature and collisions are presented in Figure 4.4. It should be emphasized that these curves are rough estimates only, because they were calculated assuming a constant heat capacity ratio for the  $\text{H}_2$  gas ( $\gamma = C_p/C_v = 7/5$ ). This is imprecise because the heat capacity of  $\text{H}_2$  changes with temperature, and with the ratio of *ortho:para* (see §2.3.1) [99, pg.17]. In addition, the temperature prediction in Figure 4.4 does not account for the higher temperatures of a plasma.

The temperature of the expansion was measured using two different methods. First, the so-called excitation temperature of the ions was measured by comparing the populations of the ground states of *ortho*- and *para*- $\text{H}_3^+$ , as measured by observing the  $R(1,0)$  and  $R(1,1)^u$  transitions, respectively. This was accomplished using the following equation,

$$\frac{n_{(1,0)}}{n_{(1,1)}} = \frac{g_{(1,0)}}{g_{(1,1)}} e^{-\Delta E_{(1,0)-(1,1)}/k_B T_{ex}} \quad (4.1)$$

where the  $n$  terms represent number densities ( $\text{cm}^{-3}$ ),  $\Delta E_{(1,0)-(1,1)} = 22.84 \text{ cm}^{-1}$  [24], and  $g_{(1,0)}/g_{(1,1)}$

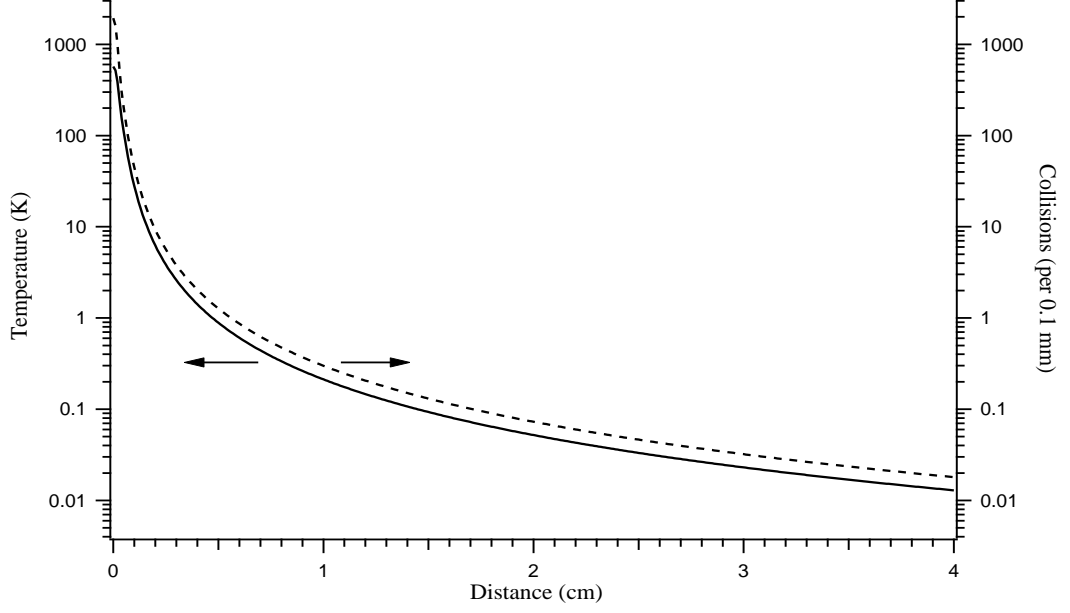


Figure 4.4: The predicted temperature, and collisions (per 0.1 mm step) in a hydrogen expansion, calculated using [99, pg. 18].

$=2$ , where  $g_i$  is the degeneracy of the state which includes  $I$  and  $J$ . Values that are proportional to the number density ( $n$ ) were calculated by dividing the measured intensities of the transitions by the transition dipoles ( $\mu^2$ ) listed in Table 1.5. As mentioned in the introduction, the practice of eliciting rotational and kinetic temperatures from the excitation temperature has been widely used, and a more detailed discussion on this topic can be found in Chapter 6. The results of the excitation temperature measurements using normal- $\text{H}_2$  are presented in Table 4.1.

	$\text{H}_2$	Absorbance ( $\times 10^{-6} \text{ cm}^{-1}$ )			$T_{ex}(\text{K})$	$T_{rot}(\text{K})$
		$R(1,1)^u$	$R(1,0)$	$R(2,2)^\ell$		
1	normal	0.35	0.84	-	97.7	-
2	para	0.41	-	0.07	-	60.5
3a	normal	1.32	2.83	-	77.0	-
3b	normal	1.32	-	0.43	-	79.2
4	normal	0.25	0.56	-	89.5	-
5a	normal	0.49	1.22	-	115.2	-
5b	diluted	0.09	-	0.04	-	115.8
6a	normal	0.98	2.1	-	76.3	-
6b	normal	0.98	-	0.28	-	74.6

Table 4.1: Excitation and rotational temperatures measured using normal, *para*, and argon-diluted  $\text{H}_2$ . The ‘a’ and ‘b’ designations identify temperatures measured in close succession. Points 5 were not used to determine the average  $T_{rot}$  for the experiment, but are included to show that  $T_{rot}$  can be accurately measured for a hydrogen sample diluted in argon.

Second, the rotational temperature was measured. This was accomplished by comparing transitions from the ground state ( $R(1,1)^u$ ) and from the first rotationally excited state ( $R(2,2)^\ell$ ) of

*para*-H<sub>3</sub><sup>+</sup> using the equation,

$$\frac{n_{(2,2)}}{n_{(1,1)}} = \frac{g_{(2,2)}}{g_{(1,1)}} e^{-\Delta E_{(2,2)-(1,1)}/k_B T_{rot}}, \quad (4.2)$$

where  $\Delta E_{(2,2)-(1,1)} = 105.17 \text{ cm}^{-1}$ . The results, also presented in Table 4.1, correlate well with the temperatures elicited from the *ortho* and *para* ground states, and together indicated an average temperature of  $80 \pm 20 \text{ K}$ .

For these measurements, the plasma was probed approximately 3.9 cm downstream of the pinhole. The results were different than the predicted temperature profile in Figure 4.4. This could partially be attributed to the fact that the curve in the figure does not account for the elevated temperature of a plasma. Nevertheless, this source was used in a previous experiment with H<sub>2</sub>, and the excitation temperatures measured at that time were between 30-50 K [95]. It is unclear why the expansion was hotter in this experiment, but the pulse sequencing could have played a role as discussed in §4.1.2.

### Number density

The number density of H<sub>2</sub> molecules at the pinhole was calculated using the ideal gas approximation with,

$$\frac{6.02 \times 10^{23} P}{RT} = [\text{H}_2], \quad (4.3)$$

with  $P = 2 \text{ atm}$ ,  $R = .08206 \text{ L atm mol}^{-1} \text{ K}^{-1}$ , and  $T = 300 \text{ K}$ . A model similar to the one used to calculate collisions for Figure 4.4 was used to extrapolate the number density for locations further downstream [99, pg. 18].

The number density of H<sub>3</sub><sup>+</sup> was assumed to be  $\sim 4$  to 6 orders of magnitude less plentiful than H<sub>2</sub> near the electrode based on [64], and was spectroscopically measured further downstream. This *in situ* measurement was accomplished using the equivalent width ( $W_\nu$ ) for both the  $R(1,0)$  and  $R(1,1)^u$  transitions. The equivalent width is the width of a rectangle with an area equal to that of the absorption peak, but whose height has been set equal to 1. It is a tool used to compare the relative strengths of absorption features. Equivalent width is calculated using the equation,

$$W_\nu = \int \frac{I_o - I_t}{I_o} d\nu, \quad (4.4)$$

which, if calculating numerically can be replaced with,

$$W_\nu = \sum \frac{I_o - I_t}{I_o} \Delta\nu, \quad (4.5)$$

in which  $\Delta\nu$  is equal to the width of the scan increments in frequency space. Starting with Beer's law,

$$\frac{I_t}{I_o} = e^{-\sigma N L}, \quad (4.6)$$

one can write,

$$W_\nu = \sum \left(1 - \frac{I_t}{I_o}\right) = \sum (1 - e^{-\sigma N L}) \Delta\nu. \quad (4.7)$$



The column density can be determined by inserting the equivalent width in the following equation.

$$N = \frac{3hc}{8\pi^3|\mu^2|} \frac{W_\nu}{\nu_{center}}, \quad (4.8)$$

where  $\nu_{center}$  is the center frequency, and the transition dipole moment  $\mu$  is in units of esu-cm (1 Debye<sup>2</sup> =  $1 \times 10^{-36}$  esu<sup>2</sup> cm<sup>2</sup>) Here, Planck's constant and the speed of light are in cgs units. Column density can then be converted to a number density if divided by the path length through the absorbing medium, in this case  $\sim 6.3$  cm. Finally, the excited (unobserved) rotational states were accounted for by applying a Boltzmann correction for 80 K. The concept of the Boltzmann correction will be thoroughly discussed in §5.2.1. In short, the correction term is the proportion of ions predicted to be in the ground state at a given temperature. Dividing the observed number density of the ground state by the Boltzmann correction accounts for ions in the rotationally excited states. The total  $\text{H}_3^+$  number density was found by summing the results of these calculations for both the *ortho* and *para*- $\text{H}_3^+$  ground states. This number density, as well as those for the neutral  $\text{H}_2$  are presented in Table 4.2.

	Distance from pinhole	
	1 mm	39 mm
$[\text{H}_2]$	$\sim 5 \times 10^{19} \text{ cm}^{-3}$	$\sim 8 \times 10^{14} \text{ cm}^{-3}$
$[\text{H}_3^+]$	$\sim 1 \times 10^{14} \text{ cm}^{-3}$	$\sim 2 \times 10^9 \text{ cm}^{-3}$

Table 4.2: Pulsed source number densities. All values were calculated except for the  $\text{H}_3^+$  at 39 mm, which was measured spectroscopically.

## 4.2 Hollow cathode cell

The hollow cathode cell constructed and used in this work was similar in many respects to other designs in the literature [100–102], but was primarily modeled after plans provided by T. Amano. In this design, various coolant fluids can be used to produce plasmas at different temperatures. The hollow cathode was used to investigate the  $\text{H}_3^+ + \text{H}_2$  reaction at temperatures that were cold, but warmer than could be produced by a supersonic expansion.

### 4.2.1 Design

The specifics regarding the design and dimensions of the hollow cathode can be found in the senior thesis by McGuire [103], however, an overview will be provided here for completeness. A thick-walled glass tube that is 1.6 m in length provides the outer vacuum sleeve for the cell. The tube is capped on the ends by 4.625-inch conflat flanges, custom machined to provide the capability to seal to the large glass tube using o-rings, as well as to smaller diameter glass tubes that protrude outward from the centers of the flanges. At one end, the conflat is fitted with feed-throughs that are used to connect the coolant tubes to the hollow cathode itself (Figure 4.5).

The small diameter glass tubes on both ends are also fitted with glass appendages, providing Ultra-Torr connection points for sample inflow, vacuum outflow, and pressure gauge attachment.

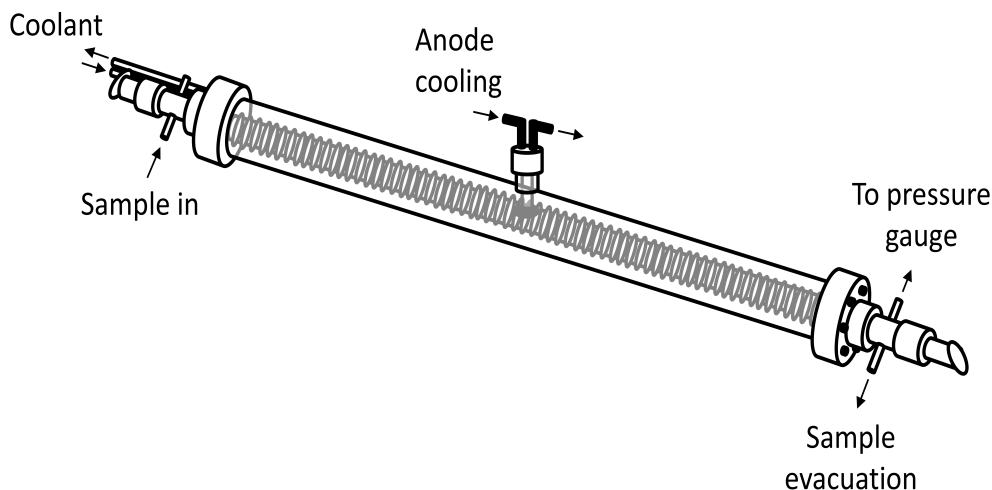


Figure 4.5: The hollow cathode plasma cell.

Both glass tubes are connected by Ultra-Torr to hollow stainless steel tubes (of 1/16 inch wall thickness). These tubes were cut at Brewster's angle ( $55.4^\circ$ ) at the outer ends, and  $\text{BaF}_2$  windows were epoxied to these ends to allow laser light to pass, while separating the laboratory atmosphere without from the test gases within.

The hollow cathode itself is a 1.4 m long, 3.8 cm diameter copper tube around which a smaller 1/4-inch diameter copper tube is wound and soldered. The smaller tubing is the conduit for the coolant, and is wound the entire length of the cathode. The cathode tube is held in place inside the large glass tube by teflon spacers.

There is a 2.54 cm hole located in the mid-point of the cathode, and the outer glass tube has a small glass appendage attached above this point. It is here that a water-cooled anode is inserted with a seal that is provided by o-rings. A small quartz connecting tube provides an isolated path from the anode to the interior of the cathode in order to prevent arcing. A vespel ring is used to attach the quartz tube to the anode, and to shield the parts of the anode that are not contained within the connecting tube.

### 4.2.2 Operation

The hollow cathode was operated by discharging the gas with a 1 kV pulse to the anode for 200  $\mu\text{s}$ . The pulse was initiated by a digital delay generator (Quantum Composers 9518+) which sent a TTL to a driver box (see Figure 4.6). The driver box was fed by an external power supply, and output a square pulse to the cell with a rise time of  $\sim 2.5 \mu\text{s}$  (see Figure 4.7). The test gas was continuously fed into the hollow cathode cell, and evacuated by a 8.33 L/s Welch mechanical pump. A constant  $\sim 1.85 \pm 0.1$  Torr pressure was maintained by adjusting an upstream regulator and needle valve. Because the experimental results required a precise knowledge of the *para*-enrichment of the  $\text{H}_2$  feed gas, it was necessary to provide sufficient time for the discharged gas to be replaced by a new sample before another discharge pulse was sent to the cell. At 1.85 Torr, the time to

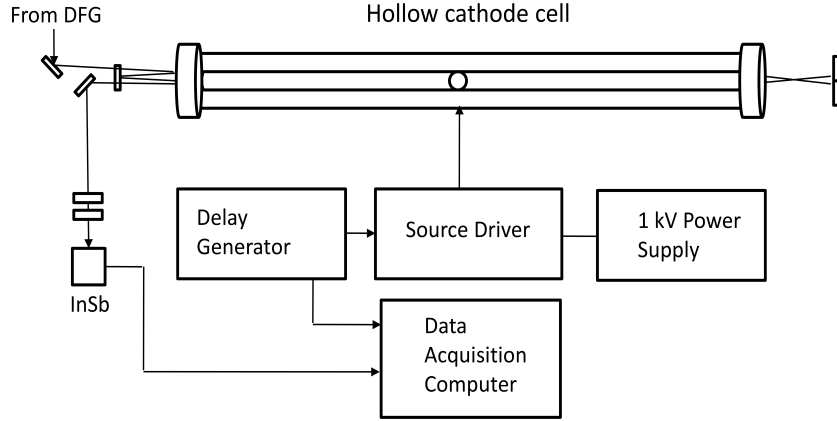


Figure 4.6: The hollow cathode cell experimental setup.

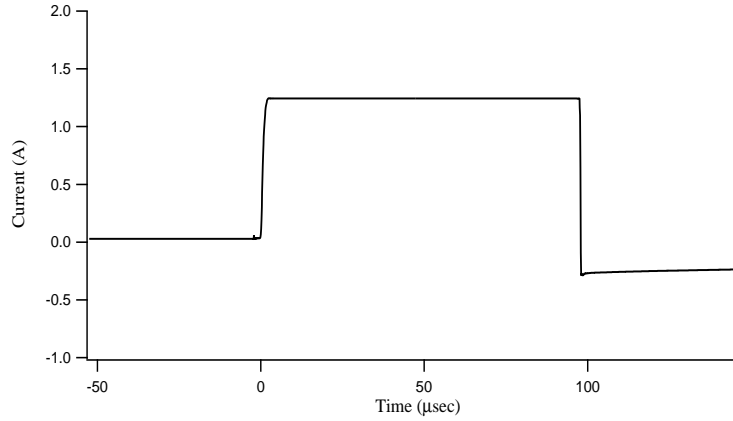


Figure 4.7: The hollow cathode current pulse (a 100  $\mu\text{s}$  pulse is shown, but a 200  $\mu\text{s}$  pulsewidth was used in the experiment).

completely evacuate the 8.5 L cell was 1.2-1.5 s, depending on whether the gas was at 100 or 300 K (the conductance is based on the temperature-dependent viscosity of the gas, see [103] for detailed calculations). Tests were performed with highly enriched *para*-H<sub>2</sub> sample gases to see if it was possible to observe changes in the H<sub>3</sub><sup>+</sup> absorption features when the discharged gas had not been completely replaced. The *para*-H<sub>3</sub><sup>+</sup>  $R(1,1)^u$  absorption intensity is expected to be especially sensitive to changes in the *para*-H<sub>2</sub> enrichment. The pulse frequency was slowly increased from .2 Hz to 2 Hz while observing the  $R(1,1)^u$  transition, however, no change was observed in the peak intensity. This was most likely an indicator that the *para* enrichment of the H<sub>2</sub> gas was not significantly changed during the course of the 200  $\mu\text{s}$  pulse. As an added precaution during the experiments, a 5 second period was used to ensure complete gas replacement.

Cooling was provided by flowing either water or liquid nitrogen through the copper tubing wound around the hollow cathode. The water was flowed directly from the closed laboratory cooling loop, which was held at 290 K. The liquid nitrogen flowed directly from a 160 L dewar that provided approximately 100 psi of backing pressure. For liquid nitrogen-cooled experiments, measurements

were begun when the outgoing line had a significant frost buildup, an indication that liquid was flowing along the entire length of the cathode. The cell could only be used for approximately 2 hours at liquid N<sub>2</sub> temperatures because the teflon and viton o-ring seals would start to fail, as indicated by the quenching of the absorption feature of the ions and by a steady rise in cell pressure. If a leak occurred, it was necessary to warm the cell to room temperature before continued use. Alternative o-ring materials such as silicone should be investigated before further use of the hollow cathode at liquid N<sub>2</sub> temperatures.

### 4.2.3 Plasma characteristics

As with the pulsed source, it was important to understand the temperature and number density characteristics of the hollow cathode plasma.

#### Temperatures

The plasma temperature was characterized in two ways: by measuring the excitation temperature and the kinetic temperature. Measurements were made for both the water and the liquid N<sub>2</sub>-cooled discharges. The excitation temperature data was analyzed in the fashion described in §4.1.3, using the  $R(1,0)$  and  $R(1,1)^u$  transitions of H<sub>3</sub><sup>+</sup>. Rotational temperature was measured by comparing  $R(1,1)^u$  and  $R(2,2)^\ell$ , however, the results were in many cases un-physical. Consequently, the rotational temperatures were considered suspect and were not used to assign temperature in the hollow cathode plasma. The problems with the rotational temperature measurements will be discussed towards the end of this section.

The kinetic temperatures that were measured from the Doppler broadening of the lines were more repeatable than the excitation temperature measurements. To measure the line broadening, the laser was scanned across the transition frequency at a rate of  $\sim 6$  MHz s<sup>-1</sup>, and the data acquisition software took measurements at regular intervals so that an absorption peak could be reconstructed in the IGOR data analysis application. This method required the operator to synchronize the start times for the laser scanning and the digital delay generator that sent the trigger pulses to the discharge driver. The operator was also required to record the start and end frequencies for the scan, as well as the starting and ending voltages on the laser. These were input parameters that the IGOR procedure would use to convert the width of the absorption peak from a laser voltage to an meaningful width in frequency space.

The IGOR procedure then fit the absorption peak with a Gaussian function from which the width of the feature was extracted. The procedure returned a value equivalent to  $w$  in the following equation for a normal distribution,

$$f(x) = ae^{-\left(\frac{x-x_0}{w}\right)^2} = ae^{-\frac{(x-x_0)^2}{2\sigma^2}}, \quad (4.9)$$

from which the standard deviation for the Gaussian fit was obtained using,

$$\sigma = \frac{w}{\sqrt{2}}. \quad (4.10)$$

The kinetic temperature was then calculated using the following relation,

$$T_{kin} = \frac{mc^2}{k_B} \left( \frac{\sigma}{\nu_{center}} \right)^2, \quad (4.11)$$

where  $m$  is the mass of an  $\text{H}_3^+$  ion. Figure 4.8 presents a sampling of data taken using the scanning method for kinetic temperature measurement. The data were taken when the hollow cathode cell was being cooled with water. Table 4.3 presents a sample of the measured laser voltages, frequencies and

Laser voltage		Freq. ( $\text{cm}^{-1}$ )		Width ( $\text{cm}^{-1}$ )	$\sigma$	Temp. (K)
Start	End	Start	End			
.22258	.19564	2725.85	2725.94	.01197	.00847	312.9
.04530	.02377	2726.18	2726.26	.01192	.00843	310.0
.26861	.24169	2725.85	2725.94	.01179	.00833	303.4

Table 4.3: Some of the data used to calculate the kinetic temperature of the water-cooled plasma in the hollow cathode cell.

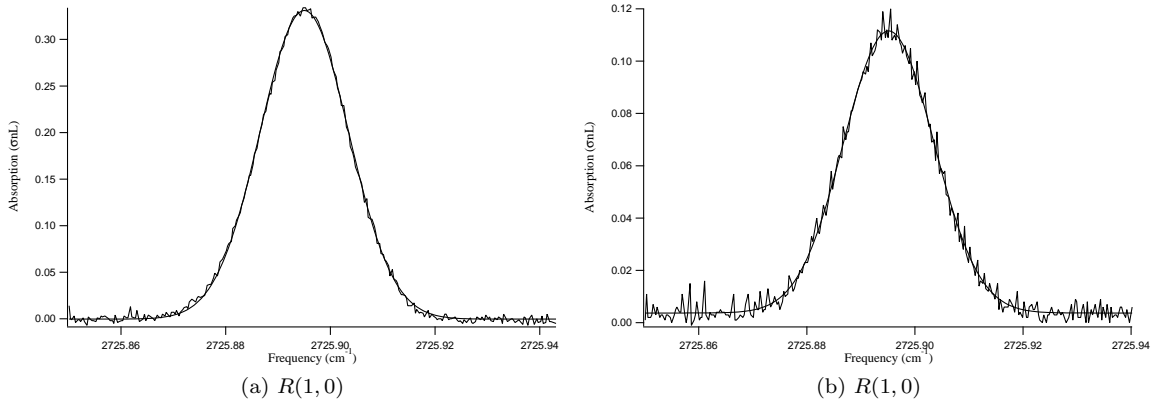


Figure 4.8: Spectra taken for the calculation of kinetic temperature in the hollow cathode cell plasma. (a) normal- $\text{H}_2$ , (b) 99.9% *para*- $\text{H}_2$ .

results for the water-cooled kinetic temperature measurements. The average temperature calculated from 10 such measurements was  $308 \pm 10$  K.

Some of the measurements for excitation temperature (using normal- $\text{H}_2$ ) are presented in Figure 4.9. There were a few instances when the calculated excitation temperature was significantly hotter than the nominal value of 300 K ( $\sim 400$  K), however, these measurements were limited in number, and were not included in the average value of temperature for the water-cooled plasma. These high temperature excursions could be explained by the nature of the excitation temperature calculation. Recall that the expression for excitation temperature involves an exponential function, and small errors in the absorption measurement will translate to large errors in temperature.

The upper panel of Figure 4.9 shows a constant temperature condition, and the lower panel shows a plasma in which the temperature was increasing. Both static and changing conditions like these were observed at times throughout the measurements. It is important to note that it was the

temperature at the beginning of the pulse that was used to characterize the temperature for both water and liquid N<sub>2</sub>-cooled experiments. This was because the pertinent data were taken at the beginning of the pulse. A more detailed explanation will be provided in Chapter 6, but in short, the enrichment of the *para*-H<sub>2</sub> feed gas was better known at the beginning of the pulses, enabling a more accurate interpretation of the results. Combining the kinetic temperature from the Doppler-broadened absorption lines and the excitation temperature data, the average temperature in the water-cooled hollow cathode plasma was  $310 \pm 20$  K.

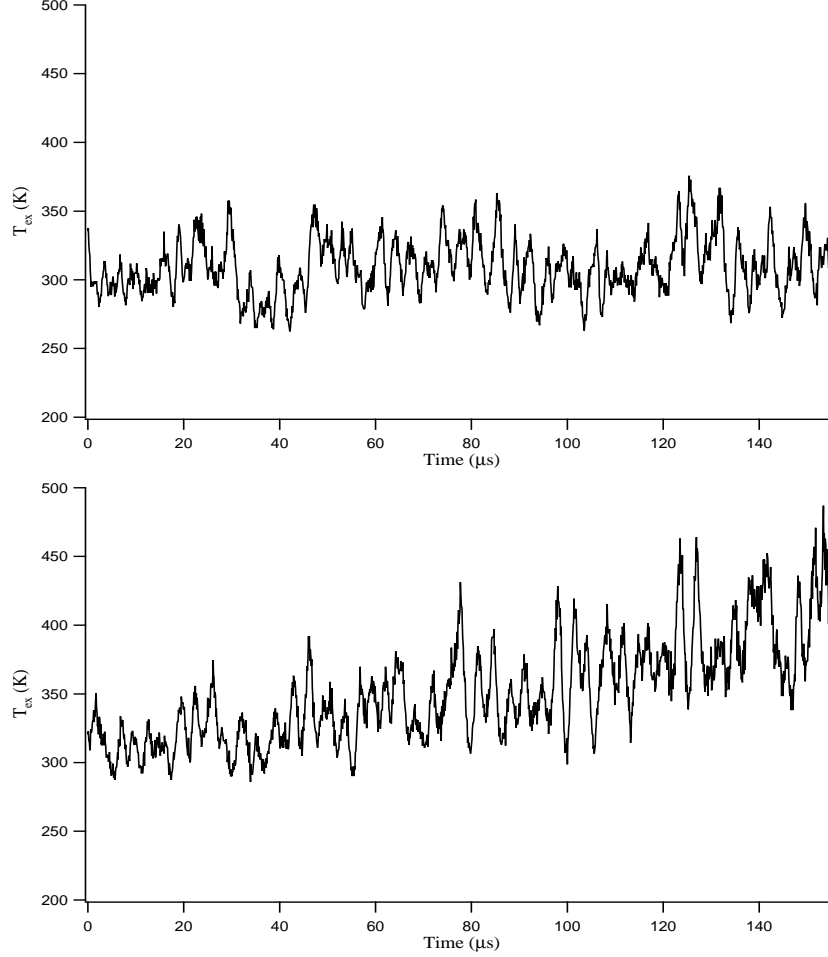


Figure 4.9: H<sub>3</sub><sup>+</sup> excitation temperature measured in a water-cooled, normal-H<sub>2</sub> plasma in the hollow cathode cell.

Post-experiment data analysis indicated that the liquid N<sub>2</sub>-cooled plasmas were grouped in two separate temperature regimes. These two regimes were likely the result of different cryogen flow rates due to different backing pressures in the liquid N<sub>2</sub> dewar. For the warmer of the two plasmas, only excitation temperature measurements were obtained because these warmer conditions were grouped early on in the cryogenically cooled experiments, and the scanning method for measuring temperature from Doppler-broadened lines had not yet been developed. Typical results for this temperature range, observed in normal-H<sub>2</sub> plasmas, are plotted in Figure 4.10. In this figure, the lower panel shows a larger, more abrupt change in temperature than observed in the lower panel of

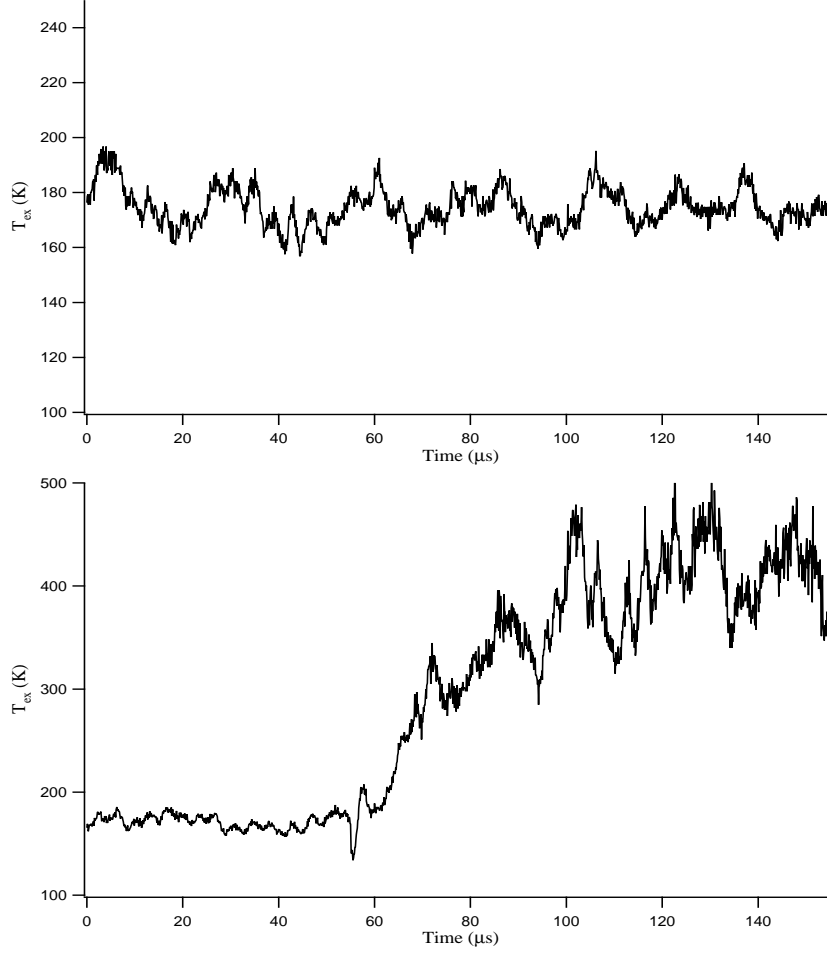


Figure 4.10:  $\text{H}_3^+$  excitation temperature in a liquid  $\text{N}_2$ -cooled, normal- $\text{H}_2$  plasma in the hollow cathode cell.

in Figure 4.9. Although rare, this type of temperature change was most likely due to the onset of an arcing condition, and demonstrates how drastically the plasma temperature could be affected. Overall, the data indicated that the temperature range for this set of liquid  $\text{N}_2$ -cooled experiments was  $180 \pm 10$  K.

The second temperature condition measured with liquid  $\text{N}_2$  was confirmed by both kinetic and excitation temperature measurements. The kinetic temperatures were obtained by observing the transitions in both normal- and highly enriched *para*- $\text{H}_2$  plasmas. Some of the data are presented in Table 4.4. Excitation temperature was also measured, but this time by comparing the peak heights of the  $R(1,0)$  and  $R(1,1)^u$  scans. A typical result is presented in Figure 4.11, and the excitation temperature calculated from these data is 135.8 K. Combining measurements of 16 kinetic temperatures and  $\sim 4$  excitation temperatures under these conditions gave an average temperature of  $130 \pm 10$  K. With two separate temperature regimes for the liquid  $\text{N}_2$ -cooled plasmas, it was important to be sure the data were being analyzed in the appropriate temperature range. Occasional temperature checks that had been performed during data collection, along with careful assignment of the data sets based on the sequence of experiments, provided the necessary information for this.

Voltage		Freq. (cm <sup>-1</sup> )		Width (cm <sup>-1</sup> )	$\sigma$	Temp. (K)
Start	End	Start	End			
.27129	.25031	2725.850	2725.917	.00743	.00526	120.6
.18873	.16779	2726.180	2726.259	.00780	.00552	132.8
.24006	.21911	2762.020	2762.090	.00776	.00549	128.0

Table 4.4: Data used to calculate the kinetic temperature of the liquid N<sub>2</sub>-cooled plasma in the hollow cathode cell.

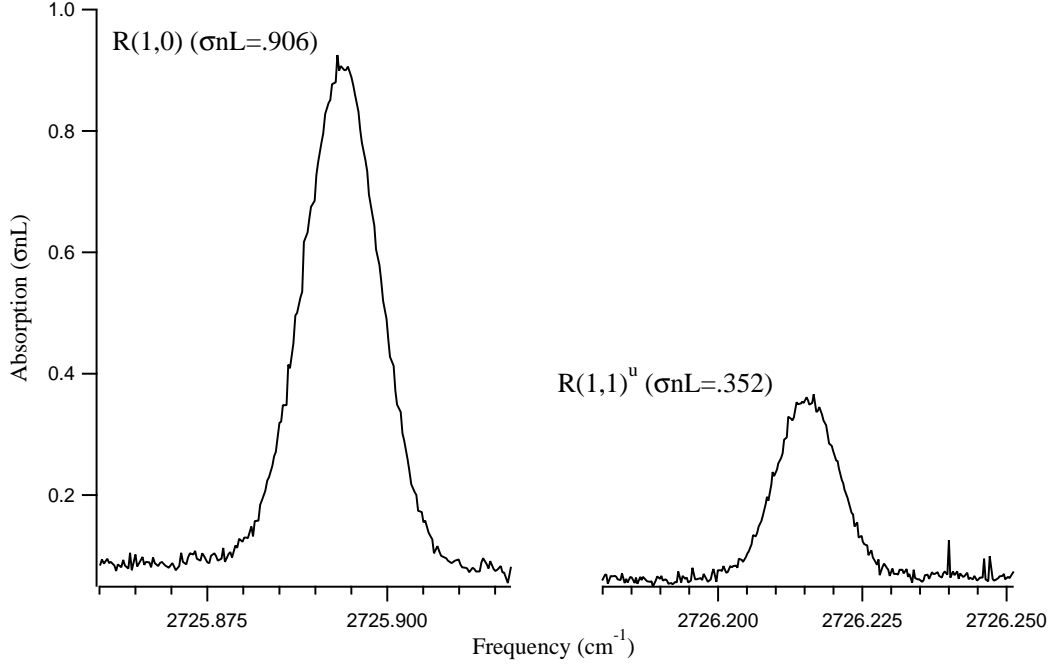


Figure 4.11: An example where  $T_{ex}=135.8$  K, as measured by comparing the peak heights of scanned  $R(1,0)$  and  $R(1,1)^u$  absorption features.

### Rotational temperature in the hollow cathode cell

Even though the data were not used, the rotational temperature of the plasma was measured along with the excitation and kinetic temperatures during the experiments, and for different *para*-H<sub>2</sub> enrichments. In many of the rotational temperature measurements, the results showed a temperature that was close to that measured by the other means (see Figure 4.12). In contrast, many of the  $T_{rot}$  measurements indicated colder than expected temperatures. Figure 4.13 shows the rotational temperatures measured from an enriched and a normal-H<sub>2</sub> water-cooled plasma. Both are indicators of anomalous behavior, because the temperature of the plasma could not have been colder than the temperature of the cooling water ( $\sim 290$  K) especially considering that energy was being pumped into the system in order to form the plasma. Similar behavior was observed by comparing the scanned  $R(1,1)^u$  and  $R(2,2)^\ell$  absorption peaks in the 130 K plasma, where the rotational temperature was calculated to be  $\sim 90$  K. There are two possible explanations for this behavior. Either the rotational temperature was not thermal, or there was a problem with the measurement itself.



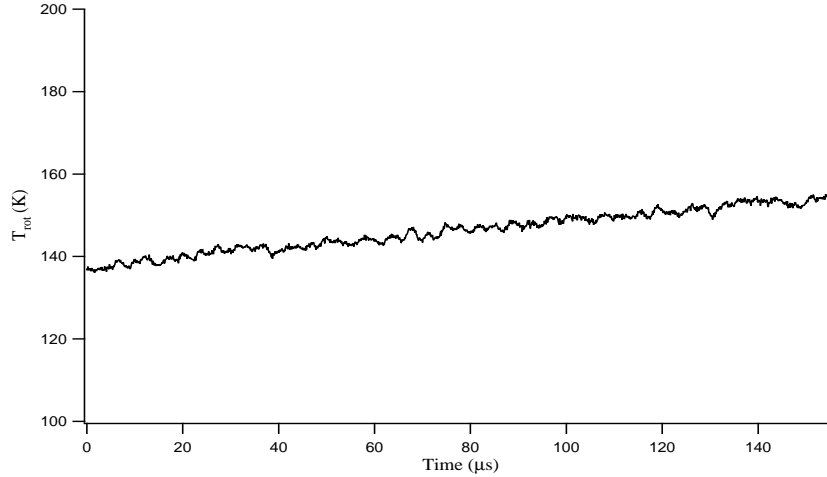


Figure 4.12:  $\text{H}_3^+$  rotational temperature in 99% enriched *para*- $\text{H}_2$  measured in the  $130 \pm 10$  K liquid  $\text{N}_2$ -cooled plasma.

Nonthermal rotational behavior of  $\text{H}_2$  has been observed in supersonic expansions [104,105] and after the passage of shocks in *para*- $\text{H}_2$  gases [106]. Specifically, the more highly excited rotational states of  $\text{H}_2$  do not quickly relax to thermal distributions. Although the measurements in this work involved the  $T_{rot}$  of  $\text{H}_3^+$ , these ions are most likely to relax via collisions with neutral  $\text{H}_2$ , and it is reasonable to expect that some of the character of the  $\text{H}_2$  rotational distribution would be transferred to the  $\text{H}_3^+$  ions during such collisions. This argument is strengthened by the fact that many of these reactions involve the  $\text{H}_2$  nuclei being incorporated into new  $\text{H}_3^+$  and vice versa (see Chapter 6).

An alternative explanation was that there was an error in the measurement of rotational temperature. To ensure that the InSb detector used in this experiment had a linear response to mid-IR intensity changes, the detector was calibrated over a wide range of DFG power settings at each of the wavelengths for  $R(1,0)$ ,  $R(1,1)^u$ , and  $R(2,2)^\ell$ . The data are shown in Figure 4.14. The detector response was fairly linear at each wavelength, however, the voltage range over which this linearity exists became more limited as the frequency of the incident light increased. In addition, the scatter of the data was higher at the  $R(2,2)^\ell$  frequency than at the others. Care was taken to reject data that did not fall within the linear detector response, but given the scatter and limited range of the linear response for  $R(2,2)^\ell$ , it is possible that the rotational temperatures that were measured using this transition had a higher probability of error. Amano, whose cathode design was most similar to ours, performed experiments measuring rotational temperature of  $\text{H}_3^+$  with different cooling fluids [107]. Although the temperatures he measured were surprisingly close to the temperature of the coolant, he never observed a condition in which the rotational temperature was significantly colder than expected, as observed in this work. Further investigation of this phenomenon in this experimental setup is warranted.

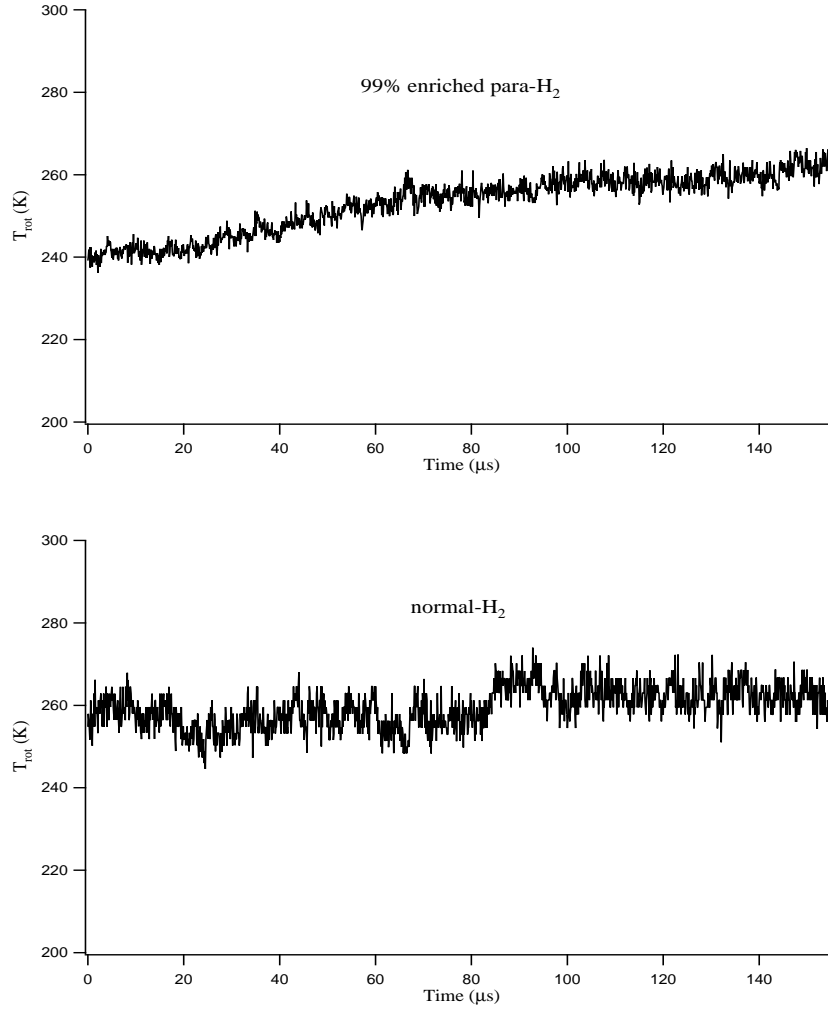


Figure 4.13:  $\text{H}_3^+$  rotational temperature in two water-cooled plasmas. The  $T_{rot}$  is colder than expected.

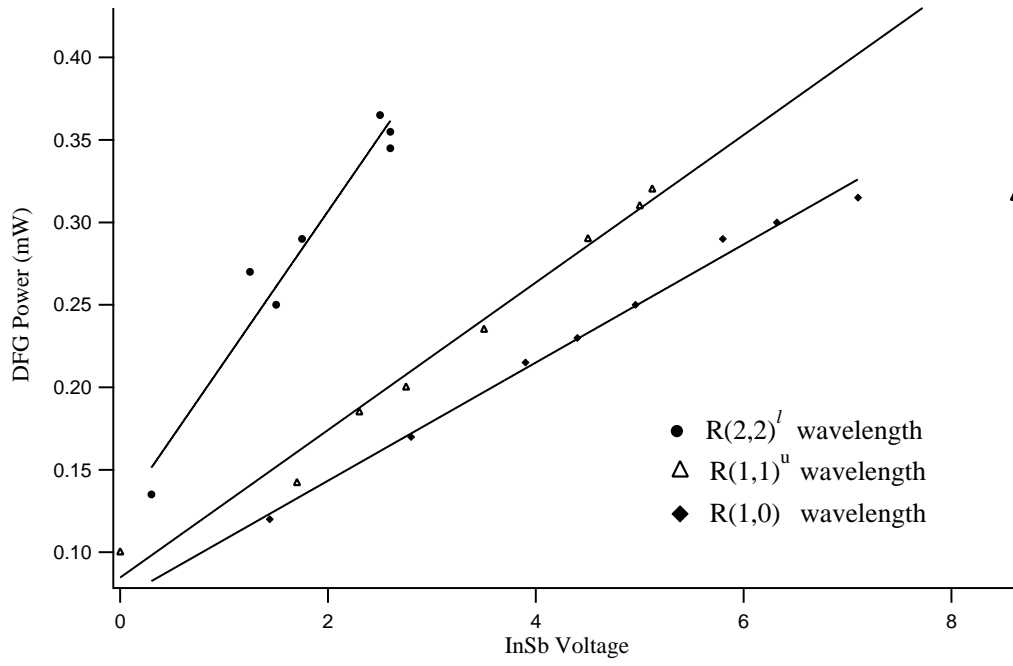


Figure 4.14: The InSb voltage response to power changes at the  $R(1,0)$ ,  $R(1,1)^u$ , and  $R(2,2)^l$  wavelengths.

## Number density

The  $\text{H}_2$  number densities were calculated assuming near ideal gas conditions and are listed in Table 4.5. The values for  $\text{H}_3^+$  were predicted from theory and were experimentally observed. Using the approximations for a positive column found in [6, p. 30] and [108, Figs. 61 and 126], along with a cathode diameter of 1.9 cm, a current of 1.25 A, and a pressure of 1.85 Torr, a number density of  $[\text{H}_3^+] \sim 1.6 \times 10^{11} \text{ cm}^{-3}$  was predicted. Using the procedures outlined in §4.1.3, we measured the equivalent widths of the lines generated from the  $T_{kin}$  scans, then used a 1680 cm pathlength to calculate number densities (the total path length through absorbing media for this White multipass configuration). The spectroscopic results are within an order of magnitude of the number densities predicted by theory, and are listed along with those for  $[\text{H}_2]$  in Table 4.5.

	300 K	180 K	130K
$[\text{H}_2]$	$\sim 6 \times 10^{16} \text{ cm}^{-3}$	$\sim 1 \times 10^{17} \text{ cm}^{-3}$	$\sim 6 \times 10^{17} \text{ cm}^{-3}$
$[\text{H}_3^+]$	$\sim 8 \times 10^{11} \text{ cm}^{-3}$	-	$\sim 1 \times 10^{12} \text{ cm}^{-3}$

Table 4.5: Hollow cathode number densities. The  $\text{H}_2$  values are calculated, while the  $\text{H}_3^+$  values were measured spectroscopically.

## 4.3 Future sources

New sources are currently undergoing development and testing in order to provide additional data that will ultimately complement this work.

### 4.3.1 CW supersonic expansion source

With the concurrent effort in our group to develop the SCRIBES (Sensitive Cooled Resolved Ion BEam Spectroscopy) experiment, a continuous flow supersonic expansion source is being designed to reliably produce rotationally cold ions for an extended operating lifetime (K. Crabtree and C. Kauffman). The source consists of a stainless steel nozzle and electrode, and macor spacers as seen in Figure 4.15. The pinhole is  $250 \mu\text{m}$  in diameter and opens into a  $500 \mu\text{m}$  channel. The distance from the pinhole to the electrode is 2.5 mm. The electrode itself is tapered like the bell of a trumpet, expanding from  $500 \mu\text{m}$  to 2 mm. The source is designed to operate with 1-3 bar backing pressure and a -200 to -400 V discharge potential (15-45 mA current).

### 4.3.2 Pulsed piezo source

A new pulsed piezo source has been designed to produce cold ions for another dissociative recombination experiment at the CRYRING ion storage ring or at the Test Storage Ring (TSR) in Heidelberg, Germany. The previously described solenoid pulsed source was prone to temperature excursions due to detuning or poppet damage. In contrast, piezo sources have been shown to consistently produce short duration pulses ( $\sim 200 \mu\text{s}$ ), with short rise times ( $\leq 100 \mu\text{s}$ ), over extended periods of use [109]. A first-generation piezo source design was tested, which led to improvements for the latest design.

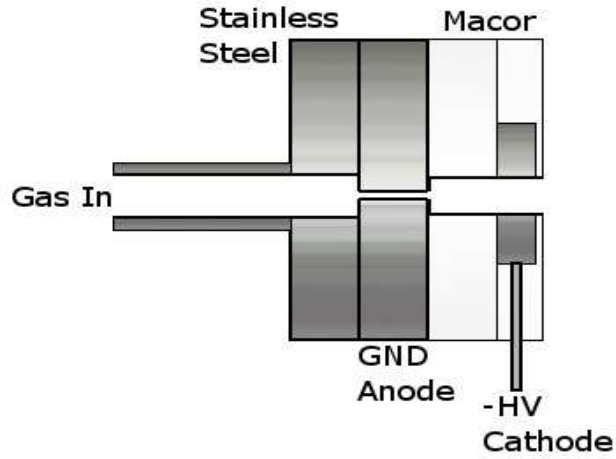


Figure 4.15: Continuous flow supersonic expansion ion source (courtesy of K. Crabtree).

Both the first and second-generation designs are based on a source used in the Continetti group at the University of California at San Diego. The latest design has been modified to mount to a custom-built flange on the outside of the vacuum chamber. Previously, the entire source had to be mounted inside the chamber, making mid-experiment adjustments difficult and time-consuming. Another improvement allows the piezo valve to be adjusted while the source is in operation by using permanently mounted tools connected through the back of the source by Ultra-Torr fittings (Figure 4.16). In the old design, the source must be shut down and opened to ambient air to perform such adjustments. Additionally, the older design is not electrically isolated, meaning that the discharge current is dumped into the housing of the source, and ultimately to the structure of the vacuum chamber. The new design incorporates changes to float the source so the ion current can be monitored.

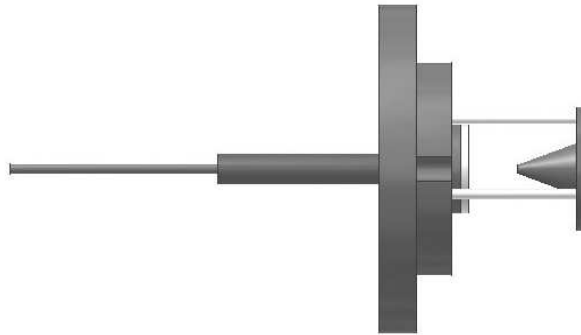


Figure 4.16: New piezo pulsed source (drawings by P. Buscay).

# Chapter 5

## Dissociative recombination

Dissociative recombination (DR) is the primary process by which  $\text{H}_3^+$  is destroyed in the diffuse interstellar medium. Theoretically determined rate coefficients for the DR of  $\text{H}_3^+$  have indicated that the *para* spin modification will be destroyed at a higher rate than the *ortho*, and preliminary experimental results indicate that this is so. We intended to measure the dissociative recombination rate of a single state of  $\text{H}_3^+$ , the ground state of *para*- $\text{H}_3^+$ . In so doing, we hoped to conclusively determine the differences between the rate coefficients of *ortho*- and *para*- $\text{H}_3^+$ . This chapter will provide a brief history of the search for the  $\text{H}_3^+$  dissociative recombination rate, followed by an introduction to the theoretical underpinnings of this important process. The details of the experiment will be described along with the results.

### 5.1 History and theory of $\text{H}_3^+$ dissociative recombination

#### History

The rate coefficient for the dissociative recombination of  $\text{H}_3^+$  with electrons has had a turbulent history, with values that have ranged over 4 orders of magnitude [110,111]. The first measurements were taken in 1949 by Biondi and Brown using a microwave afterglow technique [112]. In this technique, a microwave-generated plasma is suddenly extinguished, and the change in the resonant frequency of the cavity (dependent on the electron population) is monitored in order to measure the electron density. This technique was used repeatedly over the next twenty years until a merged beam experiment was performed by Peart and Dolder to measure recombination at relatively cold temperatures (4 K) [37,113]. This was the first of many experiments in which an inclined or merged beam of electrons was combined with a beam of ions, and the neutral products of recombination were counted. The mid 1980's saw the advent of flowing afterglow techniques in which ions are produced and subject to recombination, and electron density changes are measured in order to determine the rate of recombination. Ions are mass selected and identified in order to assign the decay to a particular ionic species [114]. It was a variant of the afterglow experiments that measured a much lower recombination rate, a rate that was used by many astrochemists to the detriment of the field [37, pg. 209-220]. Measurements were performed using laser spectroscopy and a hollow cathode in the late 1980s which raised the rate coefficient to close to currently accepted values [107,115]. In these experiments, a discharge was formed in a hollow cathode cell and the decay of the  $\text{H}_3^+$  absorption signal was monitored by observing some of the  $\nu_2 \leftarrow 0$  rovibrational transitions.

Finally, in 1993, one of the first storage ring experiments was undertaken by Larsson *et al.* [116]. With this experiment came the ability to precisely measure recombination in a rarefied environment

at low vibrational temperatures.

The development of the theory of  $\text{H}_3^+$  DR was equally storied, with many of the attempts to model the process falling short due to limited accounting of the many energetic degrees of freedom involved. Between 2001 and 2003, Kokoouline and Greene performed a full dimensional quantum calculation that included the significant effect of Jahn-Teller distortions on the DR cross section, along with additional vibrational and rotational degrees of freedom. This led to the first theoretical treatment that accurately predicted rate coefficients that were close to the storage ring measurements of the time, and within an order of magnitude of the now accepted rate coefficients [117,118]. This study also predicted that *ortho*- $\text{H}_3^+$  has a higher rate coefficient than *para*- $\text{H}_3^+$ .

At about the same time that the theoretical predictions were converging on experimental results, measurements of the currently accepted rate coefficients were being performed at the CRYRING ion storage ring in Stockholm, Sweden. Using a pulsed source that produced rotationally cold ions (30 K), McCall *et al.* measured the thermal rate coefficient for recombination with 23 K electrons to be  $2.6 \times 10^{-7} \text{ cm}^3 \text{ s}^{-1}$  [95]. This result was validated 3 years later by an experiment performed by Kreckel *et al.* at the Test Storage Ring (TSR) in Heidelberg, Germany [59]. The TSR experiment also included the first look at DR when using an enriched *para*- $\text{H}_3^+$  plasma, the result of which showed that the *para* spin modification had a higher DR rate coefficient. Shortly thereafter, a different theoretical treatment validated this result using more accurate wavefunctions and a greater number of rotational states [119]. Although a difference was observed in [59], it was not seen in a later experiment performed at the TSR [61]. A testament to the effort that has been expended on behalf of  $\text{H}_3^+$  dissociative recombination is found by inspecting the table of contents of the book *Dissociative Recombination of Molecular Ions with Electrons* [120, pg. xi-xv]. Over 20% of this volume is devoted to experiments, theoretical treatments, and observations of  $\text{H}_3^+$  DR!

## Theory

There are different pathways by which the dissociative recombination of  $\text{H}_3^+$  can take place. All lead to one of two product branches. The first branch gives three neutral atomic fragments



and the second gives only two fragments,



The branching ratios for these two product pathways were experimentally measured in [95] and [121]. In [95], where the ions were considered to be rotationally cold, these two pathways were observed to occur in roughly a 2:1 ratio, respectively.

The first dissociative recombination pathway, which was proposed by Bates, is called the direct path (Figure 5.1) [122]. Here, the captured electron possesses enough energy to excite one of the  $\text{H}_3^+$  electrons to a state described by an antibonding wavefunction which is an eigenfunction of a dissociating potential. The nuclei subsequently move apart and dissociation takes place [123]. The dissociation occurs on timescales fast enough that the neutral complex does not have time to autoionize (eject an electron) before it dissociates.



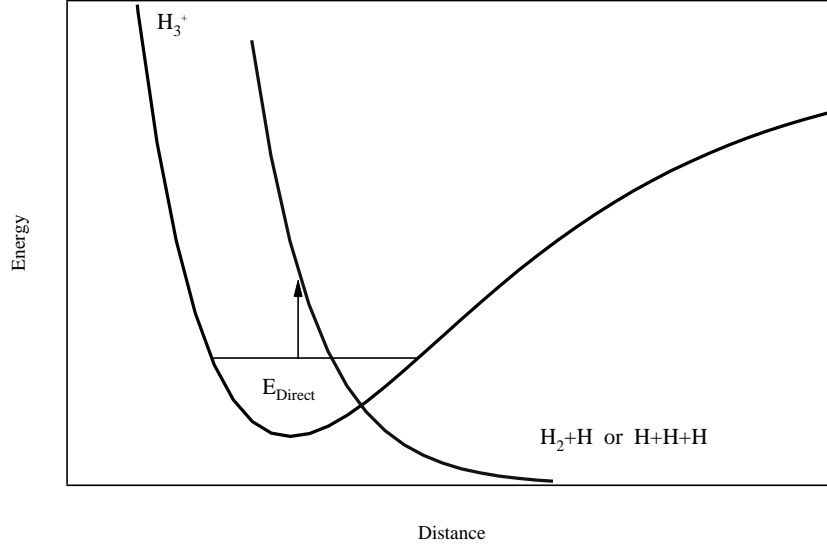


Figure 5.1: Direct dissociative recombination; the arrow represents the capture of an electron (energy  $E_{Direct}$ ) into an eigenstate of a dissociating potential.

This mechanism alone could not explain the recombination rates that were being observed in the 1950s and 1960s. To account for this, Bardsley described a second, indirect pathway in which the colliding electron is captured into a vibrationally excited Rydberg state (Figure 5.2) [124], which then mixes with a dissociating potential. The differences in the DR rate coefficients between *ortho*- and *para*- $H_3^+$  are presumed to arise from the differences in the available Rydberg states between the spin modifications.

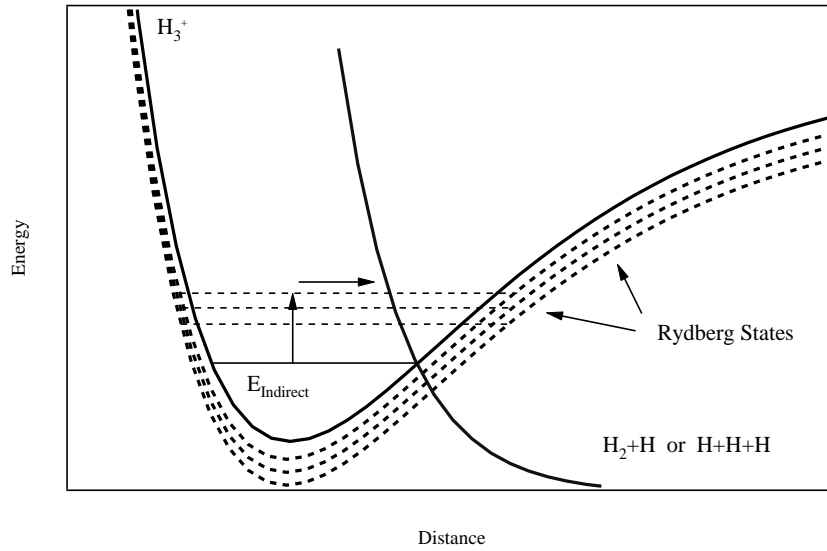


Figure 5.2: Indirect dissociative recombination; the arrow represents an electron that has been captured into a Rydberg state which subsequently mixes with a dissociating state.

DR can also occur via a tunneling mechanism (Figure 5.3). In this process the wavefunctions of

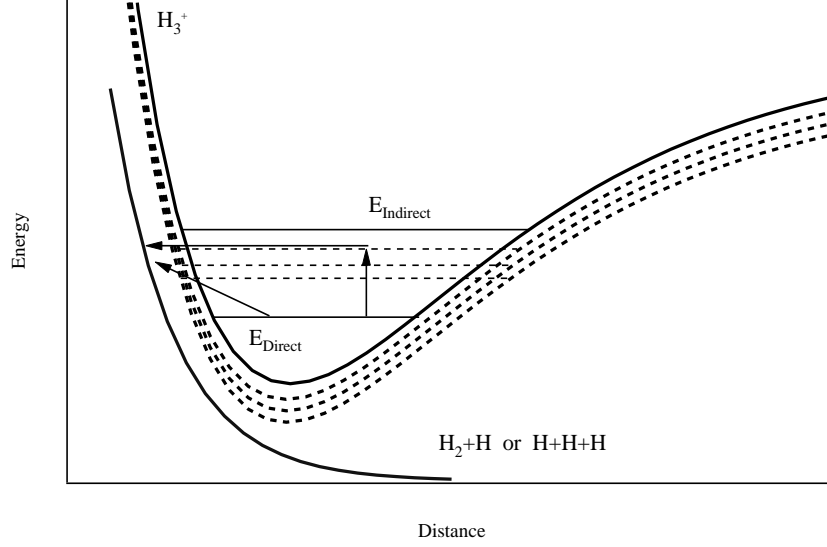


Figure 5.3: Tunneling dissociative recombination; the arrows represent electrons excited to states from which they tunnel to dissociating states.

the ion and the dissociative states mix, but only after the molecular potential has been penetrated. As with the indirect path, this can also take place via a Rydberg state which leads to a separation between direct and indirect tunneling [125, pg. 21].

## 5.2 Experiments

The objective of this experiment was to take precise measurements of the DR rate of *para*- $\text{H}_3^+$  in order to build on the preliminary results of [59]. In that experiment the *para* enrichment was not precisely known, nor were the differences in the rate coefficients of the two spin modifications quantified beyond rough comparisons. The experiment described here occurred in two parts. The first part was spectroscopic in nature, with the aim of optimizing the plasma's *para*- $\text{H}_3^+$  fraction. The second part consisted of the DR measurements at the CRYRING ion storage ring.

### 5.2.1 Spectroscopy

With the goal of producing  $\text{H}_3^+$  ions in a single quantum state (ground state *para*- $\text{H}_3^+$ ), the pulsed solenoid source was used to produce a rotationally cold expansion (§ 4.1), and experiments were performed to quantify the  $\text{H}_3^+$  *ortho:para* ratio in plasmas formed from various enrichments of *para*- $\text{H}_2$  feed gas as well as from different enrichments that had been diluted in an inert gas. This was motivated by the spin selection rules (see Chapter 6) which dictate that only *para*- $\text{H}_3^+$  will form if a *para*- $\text{H}_2$  feed gas is used to form the plasma. The temperature and enrichment of the expansion were measured spectroscopically using DFG system I (§ 3.1).

Spectroscopic experiments were initially performed before shipping the ion source to Sweden. During these pre-shipment experiments it was determined that the best *para*- $\text{H}_3^+$  enrichment could be achieved by diluting a highly enriched *para*- $\text{H}_2$  gas in a 1:99 ratio with argon. The reasons for

this will be discussed in Chapter 6. While in Stockholm, the source exhibited symptoms that it was producing rotationally hotter ions than had been observed in our laboratory, and so the decision was made to change the poppet and re-tune the solenoid ‘in the field.’ After this action, the data indicated that the ions were colder than with the initial poppet, and the experiment was completed (see §5.2.2). New enrichment and temperature experiments were performed once the source was returned to the University of Illinois, and it is these measurements that are reported here. As described in Chapter 4, the rotational temperature of the expansion was measured at  $80 \pm 20$  K.

Performing spectroscopic measurements after the DR experiment did have some advantages. Recall from Table 2.1 that stored *para*-H<sub>2</sub> has a back-conversion rate which can be used to calculate sample enrichment after known periods of time. The final DR experiment was performed 12 days after the sample had been produced (the sample gas was made at the University of Illinois and shipped to Sweden). As a result, the gas was at least 97% enriched at the time it was being used in Stockholm. Knowing this, it was possible to produce and measure almost the exact *para*-H<sub>3</sub><sup>+</sup> enrichments used in the DR experiments.

The enrichments were measured by scanning the peaks of both  $R(1,0)$  and  $R(1,1)^u$ . As described in § 4.1.3, the number density of ions can be measured by integrating the scanned peak to determine an equivalent width. By that same token, the peak heights of  $R(1,1)^u$  and  $R(1,0)$  can be used to compare values that are proportional to the number densities of these species, as long as the peaks are measured under similar expansion conditions.

In order to account for pulse to pulse differences in the ion density, the data were normalized by the plasma current as described in § 4.1.2. A sampling of these normalized measurements are presented in Figures 5.4 through 5.6. As can be seen in these figures, dilution greatly reduced the signal strength.

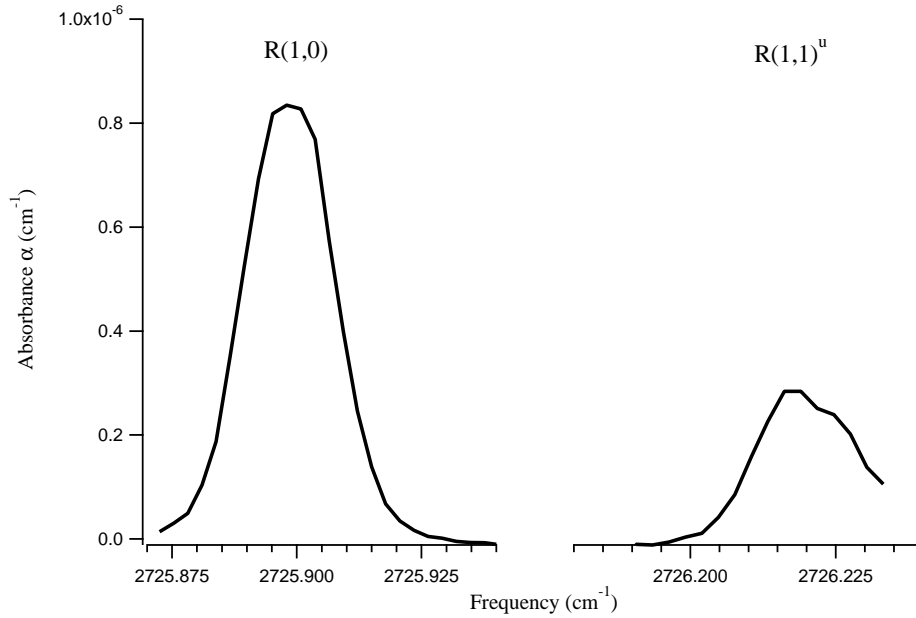


Figure 5.4: Current-normalized spectrum (normal H<sub>2</sub>).

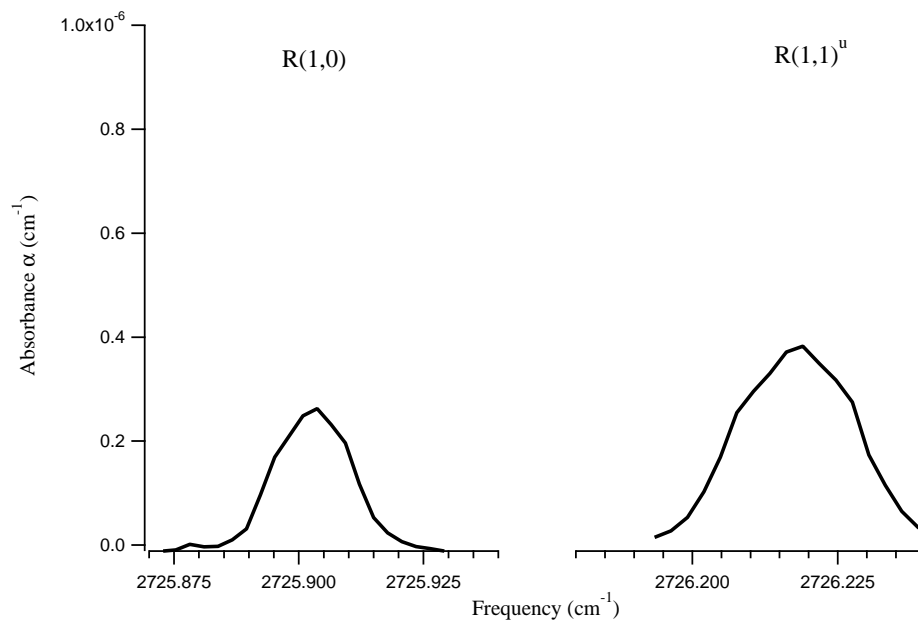


Figure 5.5: Current-normalized spectrum (97% *para*-H<sub>2</sub>).

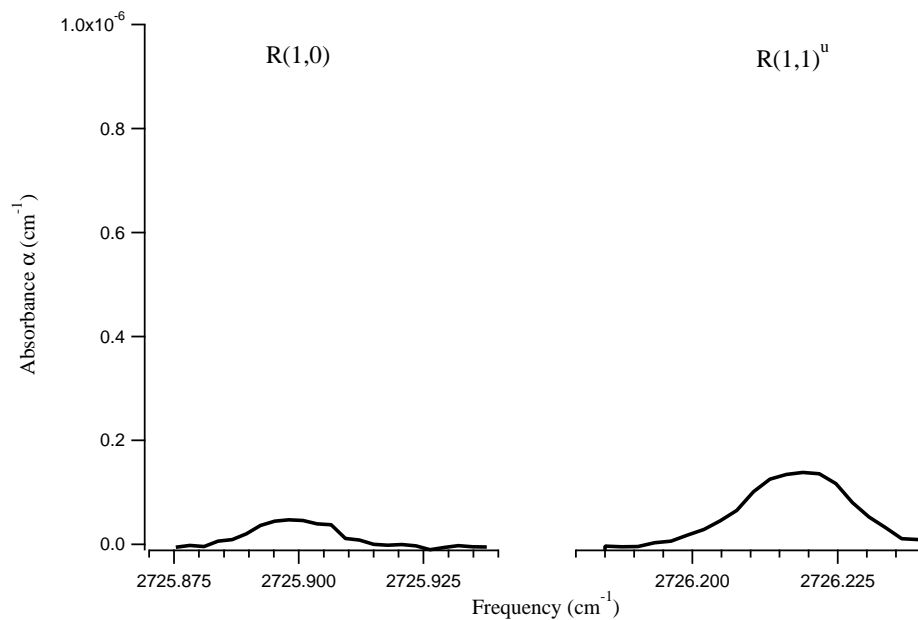


Figure 5.6: Current-normalized spectrum (diluted 97% *para*-H<sub>2</sub>).

A Gaussian curve was fit to these results, and the peak height ( $\alpha$ ) was obtained from the fit. The absorbance was converted to a value proportional to the number density by dividing the spectra by the respective transition dipole moments (see Table 1.5).

Finally, a Boltzmann ‘correction’ was applied to both observed ground state number densities ( $n$ ) in order to account for the unobserved ions populating the excited rotational states of a particular spin modification,

$$\sum_i^{all\ states} n_i = \frac{n_{observed}}{B_{(1,0)\ or\ (1,1)}}. \quad (5.3)$$

$B_{(1,0)\ or\ (1,1)}$  is the so-called Boltzmann correction. It is equal to  $n_{(1,0)\ or\ (1,1)}$ , the thermodynamically calculated population in the ground state at  $T_{rot}$ , divided by the partition function  $Z$  for that spin modification,

$$Z(T_{rot}) = \sum_i^{all\ states} g_{J(i)} g_{I(i)} e^{-E_i/k_B T_{rot}}, \quad (5.4)$$

The choice of the Boltzmann correction ( $B$ ) was based on the measured  $T_{rot}$  because the Boltzmann distribution was calculated over the rotational manifold. See Tables B.7 and B.8 for the values of  $B$  used in these calculations. The collected data can be found in Appendix A, and the results are summarized in Table 5.1.

% <i>para</i> -H <sub>2</sub> Feed	% <i>para</i> -H <sub>3</sub> <sup>+</sup>
25.0 (normal-H <sub>2</sub> )	49.1 ± 2.4
97.0 ± 0.8	74.7 ± 2.1
97.0 ± 0.8 (Ar dilution)	83.6 ± 1.9

Table 5.1: The *para*-H<sub>3</sub><sup>+</sup> enrichments used in the DR experiments.

The standard deviations were calculated from the population standard deviations (found in the tables of Appendix A), and from the standard deviations that arose from applying the Boltzmann corrections over a ±20 K temperature range. The latter values are not tabulated. The reason the highly enriched *para*-H<sub>2</sub> did not produce a more highly enriched *para*-H<sub>3</sub><sup>+</sup> plasma will be explained in Chapter 6.

				$n_i = g_{J(i)} g_{I(i)} e^{-\Delta E_i / k_B T}$															
J	G	I	$g_J$	$g_I$	Energy	T (K)=60	65	70	75	80	85	90	95	100					
1	1	0.50	3	2	64.12	6.0000	6.0000	6.0000	6.0000	6.0000	6.0000	6.0000	6.0000	6.0000					
2	2	0.50	5	2	169.3	0.8029	0.9748	1.1511	1.3296	1.5083	1.6858	1.8611	2.0333	2.2018					
2	1	0.50	5	2	237.36	0.1570	0.2161	0.2841	0.3603	0.4435	0.5327	0.6269	0.7253	0.8270					
3	2	0.50	7	2	428.02	0.0023	0.0044	0.0079	0.0130	0.0201	0.0296	0.0416	0.0566	0.0745					
3	1	0.50	7	2	494.78	0.0005	0.0010	0.0020	0.0036	0.0061	0.0096	0.0143	0.0206	0.0285					
4	4	0.50	9	2	502.03	0.0005	0.0011	0.0022	0.0040	0.0068	0.0109	0.0164	0.0237	0.0330					
5	5	0.50	11	2	729.02	0.0000	0.0000	0.0000	0.0001	0.0001	0.0003	0.0005	0.0009	0.0015					
$Z(T) = \sum g_{J(i)} g_{I(i)} e^{-\Delta E_i / k_B T} =$						6.96	7.2	7.45	7.71	7.98	8.27	8.56	8.86	9.17					
$B = n_{(1,1)} / Z(T) =$						0.8617	0.8336	0.8056	0.7781	0.7514	0.7256	0.7008	0.6771	0.6545					

Table 5.2: Boltzmann distributions for *para*-H<sub>3</sub><sup>+</sup> (80±20 K).

$$n_i = g_{J(i)} g_{I(i)} e^{-\Delta E_i / k_B T}$$

J	G	I	$g_J$	$g_I$	Energy	T (K)=60	65	70	75	80	85	90	95	100
1	0	1.50	3	4	86.96	12.0000	12.0000	12.0000	12.0000	12.0000	12.0000	12.0000	12.0000	12.0000
3	3	1.50	7	4	315.35	0.1171	0.1785	0.2561	0.3502	0.4605	0.5863	0.7268	0.8808	1.0471
3	0	1.50	7	4	516.87	0.0009	0.0021	0.0041	0.0073	0.0123	0.0193	0.0290	0.0416	0.0576
4	3	1.50	9	4	658.72	0.0000	0.0001	0.0003	0.0006	0.0012	0.0023	0.0039	0.0062	0.0096
6	6	1.50	13	4	995.88	0.0000	0.0000	0.0000	0.0000	0.0000	0.0000	0.0000	0.0001	0.0001
$Z(T) = \sum g_{J(i)} g_{I(i)} e^{-\Delta E_i / k_B T} =$						12.12	12.18	12.26	12.36	12.47	12.61	12.76	12.93	13.11
$B = n_{(1,0)} / Z(T) =$						0.9903	0.9852	0.9788	0.9710	0.9620	0.9518	0.9405	0.9282	0.9150

Table 5.3: Boltzmann distributions for *ortho*-H<sub>3</sub><sup>+</sup> (80±20 K).

### 5.2.2 Storage ring

The CRYRING ion storage ring is maintained and operated at the Manne Siegbahn Laboratory on the campus of the University of Stockholm. It was one of the first ion storage rings used for dissociative recombination experiments [126, pg. 7].

The ring is composed of 12 sections, and has a circumference of 51.63 meters (Figure 5.7) [125, pg. 29-42]. Ultra-high vacuum is maintained inside the ring by a series of getters, cryopumps and turbopumps. Ions are injected from a source into an accelerating ion optic stack (in this experiment the  $\text{H}_3^+$  ions were accelerated to 30 kV). They are further accelerated by a radio frequency quadrupole that increases their energy to 900 keV. An injection region deflects the beam that is already circulating within the ring, allowing the new ions to merge with the counterclockwise propagating flow. An additional radio frequency quadrupole serves to accelerate the beam to 13 MeV during the first 1 s of revolutions. It does so by first bunching the ions with an alternating RF signal, then synchronizing these bunches such that their next arrival coincides with an increasing electric field. Once this acceleration period is complete, the ion bunches are able to relax into a continuous stream of ions throughout the ring. It is this high ion energy that enables precise measurements with the cooled electron beam, an advantage of performing DR experiments in a storage ring.

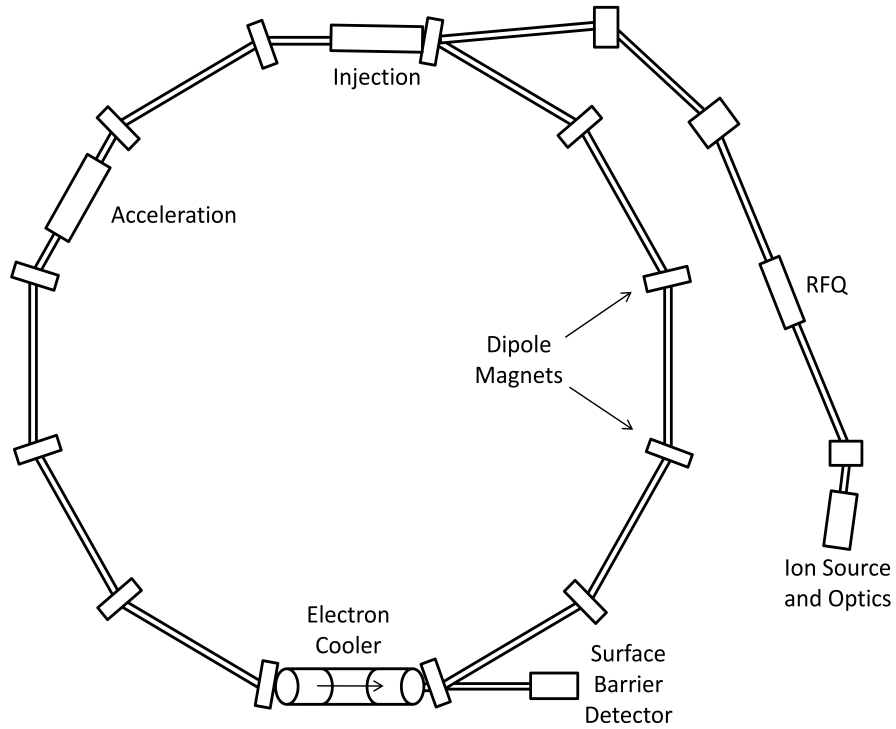


Figure 5.7: The CRYRING ion storage ring.

The ions continue to be stored in the ring under the influence of dipole bending magnets as well as quadrupole and sextupole focusing magnets. The period of time that the ions can be stored is another advantage of the ring. The storage time, on the order of seconds, allows the ions time to vibrationally relax. Experiments were performed at TSR in which the rotational and vibrational temperatures of



stored  $\text{H}_3^+$  ions were measured using Coulomb explosion techniques. The measurements were taken from a point in time immediately after injection all the way up to tens of seconds of storage. The results indicated that excited vibrational states of  $\text{H}_3^+$  relax within 2 s, in contrast to much slower rotational relaxation ( $\geq 10$  s) [127]. The latter emphasizes the importance of preparing ions in a rotationally cold state.

An electron cooler merges a steady stream of nearly monoenergetic electrons with the ion beam. The electrons in the cooler are produced by a cathode source with a 100 meV isotropic energy distribution, and are accelerated under the influence of supercooled solenoid magnets. The longitudinal energy spread is reduced to 0.1 meV and the transverse energy spread to 2 meV by adiabatic acceleration and expansion in a magnetic field of decreasing intensity. The electron beam is merged with the ion beam by a toroidal magnet, then bent out of the ion beam path by another.

The electron cooler serves two purposes. First, it cools the ion beam because of the Coulombic drag forces that exist between the positively charged ions and the nearly monoenergetic electrons. Second, the electrons in the beam initiate recombination events when the beam energy is ramped and the energy difference,  $E_d$ , is on resonance with a recombination pathway.  $E_d$  is known as the detuning energy, and it represents the energy of the electrons in the ion frame, not including the electron thermal spread. In this experiment, the electron cooler cathode voltage was ramped from 2965 to 1892 V over a 1 s interval. This produced  $E_d$  in the energy range of 0 to 30 eV.

Actual recombination events are counted when the product neutral particles, no longer subject to the forces of the ring's bending magnets, continue in a tangential direction from the cooler section. The particles are counted when they strike a surface barrier detector. The impact produces a current that is proportional to the energy of the striking particle. In addition to the surface barrier detector, a multi-channel plate (MCP) detector positioned upstream of the cooler measures the background recombination rate, which is used in calculating the actual recombination rate coefficient,

$$\alpha_{DR}(E_d) = \frac{R_b N_{DR} C_{ring}}{N_b n_e L_{cooler}}. \quad (5.5)$$

In this equation,  $R_b$  is the destruction rate per ion per unit time as measured at the MCP detector,  $N_{DR}$  represents the number of DR events counted by the surface barrier detector,  $C_{ring}$  is the circumference of the ring,  $N_b$  is the number of background counts measured by the MCP detector (a term closely related to  $R_b$ ),  $n_e$  is the electron density in, and  $L_{cooler}$  the length of, the cooling region. The destruction rate term is calculated using,

$$R_b = \frac{v_i q C_{ref}}{C_{ring} I_i}, \quad (5.6)$$

with  $v_i$  representing the ion velocity,  $q$  the charge of an electron,  $C_{ref}$  the count rate at the MCP detector ( $dN_B/dt$ ), and  $I_i$  the ion current [95].

Three separate storage ring experiments were performed. Each experiment collected approximately 20,000 counts of data taken over a period of 12 to 36 hours (depending on the ion current density). The first experiment was performed with the 83.6% enriched *para*- $\text{H}_3^+$  (from 97% enriched *para*- $\text{H}_2$  feed gas diluted to 1% in Ar), and was intended to obtain the best measurement of the *para*- $\text{H}_3^+$  recombination rate. The second experiment used the 49.1% *para*- $\text{H}_3^+$  gas (from normal- $\text{H}_2$ ) in the hopes of obtaining a baseline performance calibration and to compare the results of this set

of experiments with those of the measurements in 2002 [95]. Finally, an experiment was conducted with 74.7% *para*-H<sub>3</sub><sup>+</sup> (from the undiluted 97% enriched *para*-H<sub>2</sub>) in order to observe the difference made by smaller changes in the *para*-H<sub>3</sub><sup>+</sup> enrichment. The respective post-acceleration ion currents for these experiments were 8.16 nA, 54 nA, and 48 nA.

The raw data were corrected to account for the background contributions from ion beam interactions with residual gas in the ring. This subtraction did not affect the rate coefficients at small interaction energies because the DR signal in these regimes was orders of magnitude higher than that of the background counts. In addition, the data were corrected for the space-charge of the electrons and for the non-coaxial merging of the beams in the toroidal regions of the electron cooler [62].

### 5.3 Results

The results of the three experiments are presented in Figure 5.8. In this figure, the rate coefficients,  $\alpha_{DR}$ , have been multiplied by a factor of  $E_d^{1/2}$ . Multiplying the data from the different experiments by this factor does not change the relative differences between them, however, it does improve the presentation by removing the logarithmic scaling.

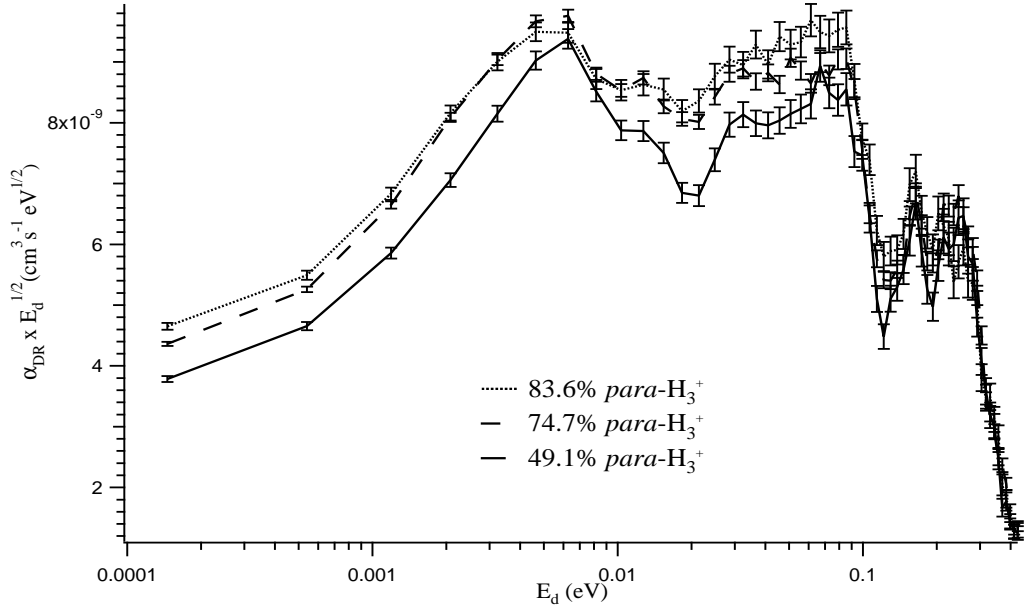


Figure 5.8: The dissociative recombination rate coefficient for three different *para*-H<sub>3</sub><sup>+</sup> enrichments.

The DR rate coefficient,  $\alpha_{DR}$ , clearly has a dependence on the H<sub>3</sub><sup>+</sup> spin modification. The differences continue up to  $\sim 200$  meV, with the exception of a region where they approach each other around 6-7 meV. There is a 16% systematic uncertainty, mostly due to inaccuracies in the electron energy measurement, that is not shown in these results. This uncertainty is not included because it affects all three results in the same way, and should not change the differences between them.

The experimentally determined 83.6% *para*-H<sub>3</sub><sup>+</sup> and 49.1% *para*-H<sub>3</sub><sup>+</sup> rate coefficients were used to extrapolate DR rate coefficients for hypothetical 100% *para*- and 100% *ortho*-H<sub>3</sub><sup>+</sup> plasmas by

simultaneously solving,

$$\begin{aligned}\alpha_{DR(83.6\%)} &= .836\alpha_{DR(100\% \text{ para})} + .164\alpha_{DR(100\% \text{ ortho})} \\ \alpha_{DR(49.1\%)} &= .491\alpha_{DR(100\% \text{ para})} + .509\alpha_{DR(100\% \text{ ortho})}.\end{aligned}$$

The results are presented in Figure 5.9, along with that of 49.1% *para*-H<sub>3</sub><sup>+</sup> (normal-H<sub>2</sub>) for comparison. The same extrapolated results can be found if the 74.7% spectrum is used in the calculation in place of the 83.6% rate coefficients.

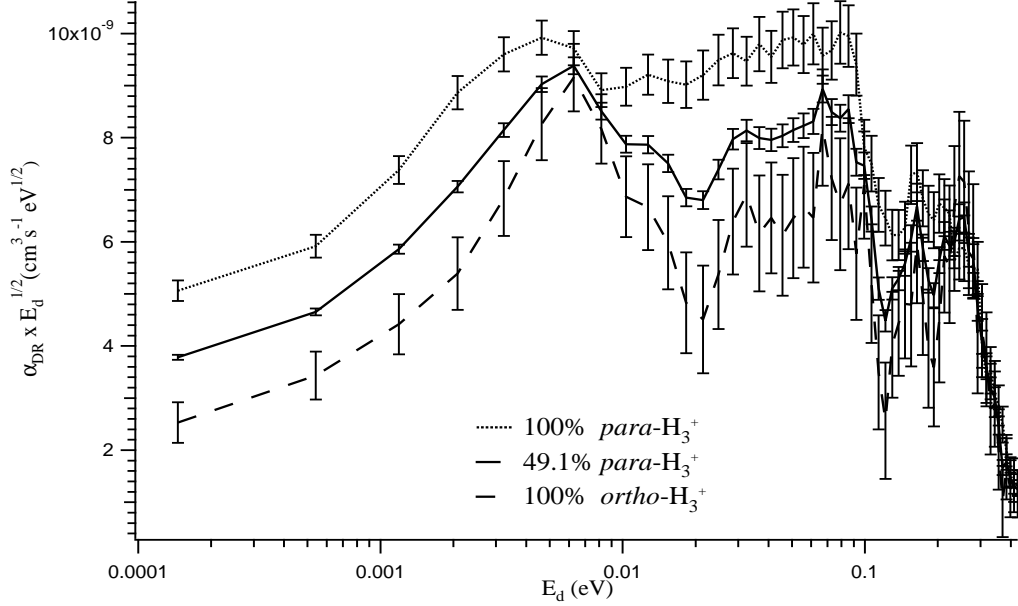


Figure 5.9: Extrapolated dissociative recombination rate coefficients for 100% *para* and 100% *ortho*-H<sub>3</sub><sup>+</sup>.

The rate coefficients that were measured were higher than those measured in the 2002 experiment for all detuning energies,  $E_d$ . It is possible that this disparity resulted from inaccurate ion current measurements in the present experiment. It is unlikely that there were errors in the ion current measurement for the 2002 experiment because a great deal of effort was expended at that time to precisely measure this quantity. We were unable to perform current measurements with as great a precision. Consequently, a correction factor of 0.65 was applied to these results in order to align the 10 eV resonance with that measured in 2002. This resonance has been used in the past to normalize data because it is not affected by the rotational temperature (see next paragraph) or the spin modification of the ions [59]. Similar to the systematic error arguments, the consistent application of this correction factor did not impact the observed differences between the three gas enrichments. A comparison of the corrected rate coefficients from this experiment, the 2002 experiment, and results from TSR can be found in Figure 5.10, and are in good agreement above  $10^{-2}$  eV [59, 95].

Below  $10^{-2}$  eV, the spectrum from this experiment is structurally smoother than the spectrum observed in 2002. This could be an indication that the ions produced in this experiment were rotationally hotter than the ions in 2002. The presence of rotationally hotter ions leads to a higher

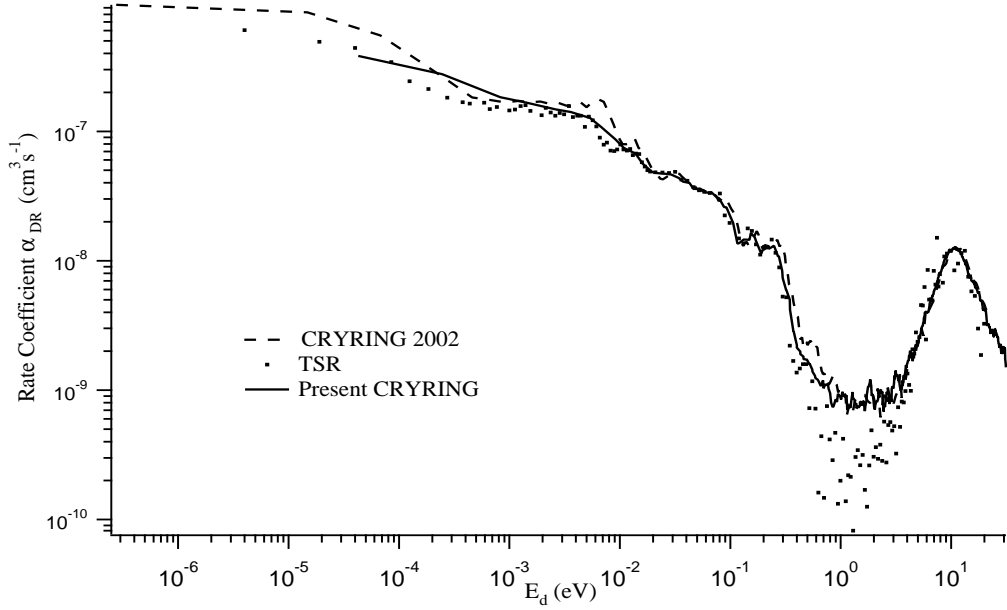


Figure 5.10: Comparison between previous  $\text{H}_3^+$  DR experiments and the present results (normal- $\text{H}_2$ ). Error bars are removed for ease the comparison.

number of Rydberg states. This results in an increase in the number of DR resonances available via the indirect mechanism (Figure 5.2), which when taken together have the effect of smoothing the structure that would be present if only a few rotational states were involved [119].

The rotational temperature of the ions in this experiment was measured at  $80 \pm 20$  K, while the temperature of the ions in 2002 was found to be  $\sim 30$  K. It would be surprising if this temperature difference could change the structure of the spectrum as much as was observed. An inspection of Tables B.7 and B.8 shows that the population of *ortho*- $\text{H}_3^+$  in the ground state (1,0) is relatively unperturbed at 80 K. On the other hand, the rotational states of *para*- $\text{H}_3^+$  show a decrease of  $\sim 24\%$  in the population of the ground state (1,1) between 30 and 80 K (at 30 K, 99% of the *para*- $\text{H}_3^+$  are in the ground state). It is important to remember that the comparison in Figure 5.10 is between 49.1% *para*- $\text{H}_3^+$  samples, so only  $\sim 12\%$  of the ions should be affected.

Another possible explanation was that the ions were heated by residual collisions with neutral particles in the ring. The most recent theoretical papers argue that the experimental results (from both CRYRING and TSR) must have been measured at rotational temperatures upwards of 1000 K, and that this may have been due to residual heating [119]. Experiments were performed at TSR specifically to measure this effect, and found that this type of heating could not change the rotational temperature by more than about 100-200 K [60]. In the end, all that can be said is that the smoothing observed in these rate coefficient spectra was likely due to a combination of rotationally warm ions from the expansion source and some rotational heating in the ring. However, the rotational heating was not to the level being suggested by current theoretical models.

Although the rotational distribution of ions may have been altered during this experiment, the total number of ions within the *ortho* and *para* population sets should not have been affected during the time in which the ions were stored. First, the *para*- $\text{H}_3^+$  enrichment cannot be modified by reactive

collisions in a way that will affect the DR measurements. Any reaction between  $\text{H}_3^+$  and  $\text{H}_2$  (the dominant neutral species in the ring) would produce products at far too low an energy to continue being stored. Second, it was determined that the differences between the *ortho* and *para* DR rate coefficients could not significantly alter the enrichment. The ions were stored for approximately 4 s after acceleration and before a measurement was taken. The resulting change in *para* enrichment due to DR was on the order of -2-3% over this period, which was approximately the same as the uncertainty in the enrichment value itself. A comparison between the diluted and undiluted *para*- $\text{H}_2$  experiments in Figure 5.8 shows that small changes like this have little effect on the rate coefficient.

Problems with the ion current measurement, rotational heating, and electron energy calibration prevented a precise measurement of the absolute rate coefficients of the specific spin modifications, as was our original intent. Nevertheless, we were able to quantify the differences between the rate coefficients. Improvements to the experiment including a new piezo source (§4.3.2) and some much needed maintenance at CRYRING should change this in the near future.

### 5.3.1 Astrophysical implications

The DR rate coefficient by itself is not particularly useful for interpreting astrophysical observations. To make the measurements relevant, they must be converted to a thermal rate coefficient,  $\alpha(T_e)$ , which represents the rate of DR with a Maxwellian distribution of electron energies at a given temperature  $T_e$ .

The first step in this process is to extract the electron energy-dependent DR cross-section,  $(\sigma(E_d))$  from the rate coefficient. For energies greater than a few meV, this can be accomplished using the equation,

$$\sigma(E_d) \sim \frac{\alpha_{DR}}{\sqrt{E_d}}. \quad (5.7)$$

For energies lower than a few meV, one must deconvolve the cross section using,

$$\alpha_{DR}(E_d) = \int_0^\infty f(E_\perp) \sigma(E_\perp + E_d) v_{rel}(E_\perp + E_d) dE_\perp, \quad (5.8)$$

where  $E_\perp$  is the transverse electron energy (2 meV at CRYRING),  $v_{rel}$  is the relative velocity, and  $f(E_\perp)$  is a Maxwell energy distribution,

$$f(E_\perp) = \frac{1}{kT_\perp} e^{-E_\perp/kT_\perp} \text{ for } E_\perp \geq 0, \quad (5.9)$$

in which  $T_\perp$  is the transverse electron temperature. This works because the rate coefficient is an energy weighted cross section integrated over the electron velocity spread. The details of this unfolding can be found in [128].

With the energy-dependent cross section, it is then possible to calculate the thermal rate coefficients. This is accomplished by convolving the cross section with a Maxwellian electron distribution at different temperatures. The equation used for this is,

$$\alpha(T_e) = \frac{8\pi m_e}{(2\pi m_e k_B T_e)^{3/2}} \int \sigma(E) E e^{-E/k_B T_e} dE. \quad (5.10)$$

The results for the 49.1% *para*- $\text{H}_3^+$  are presented in Figure 5.11, and the extrapolated thermal

rate coefficients are plotted in Figure 5.12. The thermal rate coefficient for rotationally cold 49.1% enriched  $para\text{-H}_3^+$  (normal- $\text{H}_2$ ) with a 300 K electron distribution was measured to be  $6.79 \pm 0.14 \times 10^{-8} \text{ cm}^3 \text{ s}^{-1}$ , which is in good agreement with the 2002 results where  $\alpha(T_e) = 6.8 \times 10^{-8} \text{ cm}^3 \text{ s}^{-1}$ . Although these values were in good agreement, the results from the present experiment diverged to higher values at lower electron temperatures. A range of thermal rate coefficients are presented in Table 5.4. The table presents values that are centered around the measured rotational temperature of the expansion. Temperatures outside of this range are not presented because it is assumed that electron and ion temperatures will be thermalized in an astrophysical plasma.

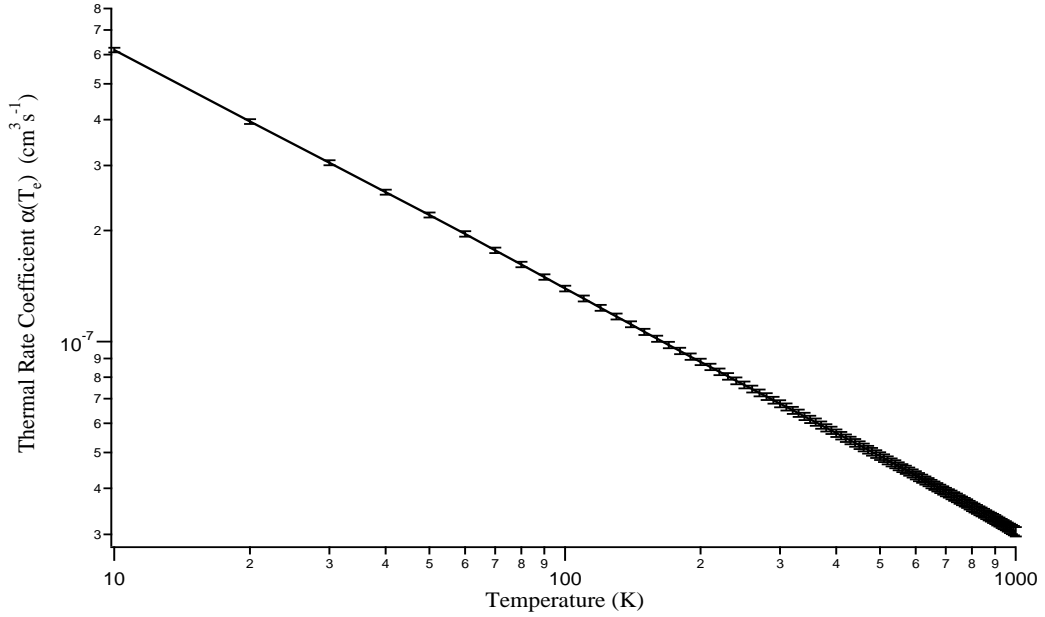


Figure 5.11: The thermal rate coefficient  $\alpha(T_e)$  for 49.1% enriched  $para\text{-H}_3^+$  (normal- $\text{H}_2$ ).

% $para\text{-H}_3^+$	$\alpha(T_e) (10^{-8} \text{ cm}^3 \text{ s}^{-1})$		
	$T_e=60 \text{ K}$	80 K	100 K
0	$15.5 \pm 1.7$	$13.0 \pm 1.5$	$11.3 \pm 1.3$
$49.1 \pm 2.4$	$19.6 \pm 0.3$	$16.2 \pm 0.3$	$13.9 \pm 0.3$
100	$23.9 \pm 0.9$	$19.6 \pm 0.7$	$16.8 \pm 0.6$

Table 5.4: Thermal rate coefficients for a range of  $T_e$ .

At diffuse cloud temperatures,  $para\text{-H}_3^+$  has a higher dissociative recombination rate with electrons than  $ortho\text{-H}_3^+$ . This fact is borne out by both the  $E_d$ -dependent rate coefficients and the thermal rate coefficients. As can be seen in Figure 5.12, the  $para$  thermal rate coefficient is almost two times larger than  $ortho$  at the lowest electron temperature distributions. Theory predicts that this ratio goes from a factor of 10 at cold temperatures all the way down to unity at warmer temper-

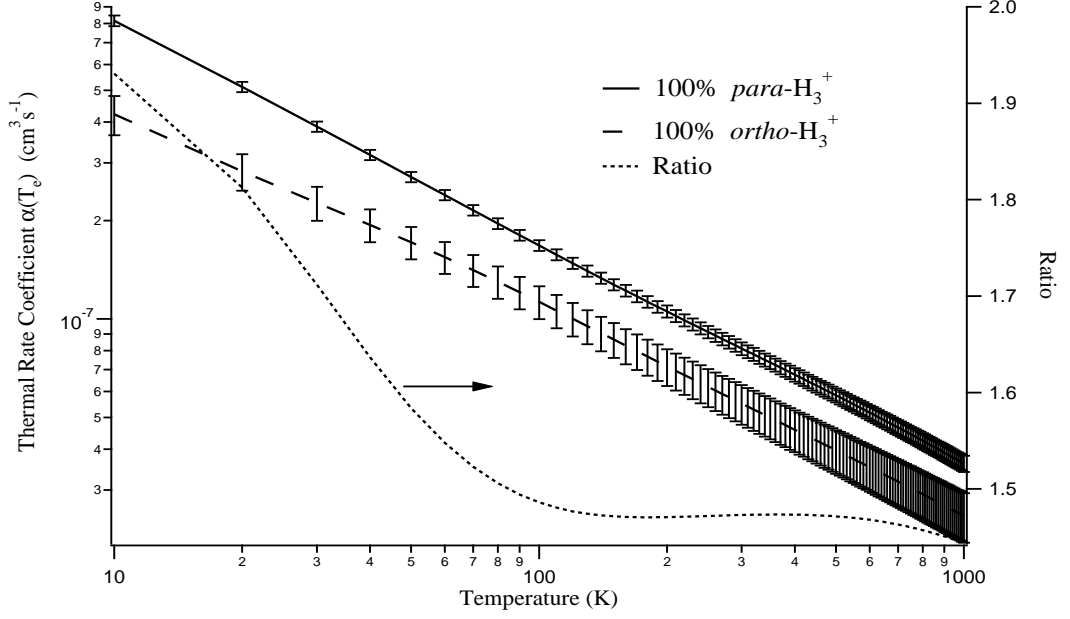


Figure 5.12: The extrapolated thermal rate coefficients  $\alpha(T_e)$  for *ortho*- and *para*- $\text{H}_3^+$ .

atures [119]. It is important to keep in mind that the thermal rate coefficient values calculated from this experiment are approximate values only because of the calibration problems described earlier. However, the calibration errors are assumed to have affected the different measurements equally, therefore the relative differences that were measured between the rate coefficients should remain valid.

Due to the fact that the difference in the thermal rate coefficients is relatively small, dissociative recombination cannot be the source of the fractionation between  $\text{H}_3^+$  spin modifications observed in the diffuse interstellar medium. An even more convincing argument for this is the fact that *para* dissociative recombination occurs at a faster rate than the *ortho*, but *para*- $\text{H}_3^+$  is enriched in diffuse clouds [35].

# Chapter 6

## $\text{H}_3^+ + \text{H}_2$ reaction dynamics

Given that  $\text{H}_2$  and  $\text{H}_3^+$  are the most abundant molecule and molecular ion in the universe, and that the reaction between the two occurs at a high Langevin rate, it follows that,



is the most common bimolecular reaction [129]. The seemingly fundamental nature of reaction (6.1), not to mention the simplicity of its constituents, conceals a complexity that will be explored in this chapter. Theoretical work has been performed to probe some of these details [130, 131]. In addition, experiments have been carried out at room temperature using hydrogen, and at colder temperatures using deuterium [63, 64, 132]. Still, the behavior of reaction (6.1) under the cold astrophysical conditions where it almost always occurs has been largely unexplored.

The experiments described here were possible because of the existence of the *ortho* and *para* spin modifications of  $\text{H}_2$  and  $\text{H}_3^+$ . These spin modifications were used as tracers, identifiable by their spectroscopic signatures, to observe how protons are transferred between the reactants. In the process, a great deal was learned about the steady state conditions of the *ortho* and *para* spin modifications, and how the *ortho:para* ratio of  $\text{H}_3^+$  can be used as a probe of interstellar environments.

The symmetry-based derivations for the statistical weights of the *ortho* and *para* modifications for  $\text{H}_2$  and  $\text{H}_3^+$  were presented in Chapter 1. The first part of this chapter will show how statistical calculations can be extended to predict the spin modifications of both species during formation and subsequent reactions. Current theories about reaction (6.1) will also be presented. Finally, the experiments used to explore this reaction at room and astrophysical temperatures will be discussed, along with results and astrophysical implications.

### 6.1 Theory

The theory behind the  $\text{H}_3^+ + \text{H}_2$  reaction is complex and must be treated in separate parts. The first part of this section will describe how to calculate the spin branching ratios of reaction (6.1) using statistics. Closely related to this, the statistically-based high temperature model for reaction (6.1) will be discussed, followed by the quantum mechanical model for cold temperatures.

#### 6.1.1 Statistical weights

The statistical weights of the  $\text{H}_2$  and  $\text{H}_3^+$  spin modifications, presented in Chapter 1, are calculated without consideration of the energy required for the molecule or ion to be in one state or another.



The weights are based purely on the degeneracies of the levels or, in terms of symmetry, the order of the various classes and the characters of the representations that describe the symmetry of the molecule. Neglecting energetic considerations, it is also possible to calculate the statistical outcomes of a reaction given the spin modifications of the reactants. Using group theory, Quack [130] sought to do just this in order to examine what happened in reaction (6.1) as the reactants progress to a completely ‘scrambled’ reaction intermediate, and finally to the product states.

Oka [131] developed a different but equivalent method to account for the distribution of spin modifications. His method is simpler because it only considers nuclear spin, and employs angular momentum algebra instead of group theory to calculate the weights of the product spin modifications. It is important to note that both methods are successful because nuclear spin is essentially conserved in these reactions (there are hyperfine interactions that prevent nuclear spin from being ‘rigorously’ conserved, but they are very weak [64]).

Angular momentum algebra [133, pg. 99-101] uses the following formula to calculate these weights,

$$\mathcal{D}_{I_1} \otimes \mathcal{D}_{I_2} = \mathcal{D}_{I_1+I_2} \oplus \mathcal{D}_{I_1+I_2-1} \oplus \cdots \oplus \mathcal{D}_{|I_1-I_2|}, \quad (6.2)$$

where the  $\mathcal{D}_I$  are symbols that represent the nuclear spin modifications. A simple case involves the calculation of the product weights for the formation reaction,



which was first presented as reaction (1.2) in §1.2. In this reaction,  $\text{H}_4^+$  represents the intermediate state. The first step is to calculate the spin species of the reaction intermediate from the reactants using equation (6.2). Here, the reactant ( $\text{H}_2$  and  $\text{H}_2^+$ ) spin modifications could be either *ortho* ( $\mathcal{D}_1$ ) or *para* ( $\mathcal{D}_0$ ),

$$(\mathcal{D}_1 \oplus \mathcal{D}_0) \otimes (\mathcal{D}_1 \oplus \mathcal{D}_0) \rightarrow \mathcal{D}_2 \oplus 3\mathcal{D}_1 \oplus 2\mathcal{D}_0 \quad (6.4)$$

Next, a similar calculation is carried out, but this time starting with the product states,  $\text{H}_3^+$  (where *ortho* is represented as  $\mathcal{D}_{3/2}$  and *para* is  $\mathcal{D}_{1/2}$ ), and  $\text{H}$  ( $\mathcal{D}_{1/2}$ ),

$$\mathcal{D}_{3/2} \otimes \mathcal{D}_{1/2} \rightarrow \mathcal{D}_2 \oplus \mathcal{D}_1 \quad (6.5)$$

$$\mathcal{D}_{1/2} \otimes \mathcal{D}_{1/2} \rightarrow \mathcal{D}_1 \oplus \mathcal{D}_0. \quad (6.6)$$

The right side of expressions (6.5) and (6.6) both represent the  $\text{H}_4^+$  intermediate. The total nuclear spin degeneracies ( $2I + 1$ ) of these must be balanced with the total spin degeneracy from the right side of (6.4) which also represents  $\text{H}_4^+$ . The easiest way to do this is by multiplying expression (6.6) by a factor of 2,

$$\mathcal{D}_{3/2} \otimes \mathcal{D}_{1/2} \rightarrow \mathcal{D}_2 \oplus \mathcal{D}_1 \quad (6.7)$$

$$2(\mathcal{D}_{1/2} \otimes \mathcal{D}_{1/2}) \rightarrow 2(\mathcal{D}_1 \oplus \mathcal{D}_0). \quad (6.8)$$

By invoking Frobenius’ reciprocity, these two expressions can be written in reverse with the individual

product states (representing  $H_4^+$ ) going to reactants,

$$\begin{aligned}\mathcal{D}_2 &\rightarrow \mathcal{D}_{3/2} \otimes \mathcal{D}_{1/2} \\ 3\mathcal{D}_1 &\rightarrow (\mathcal{D}_{3/2} \otimes \mathcal{D}_{1/2}) \oplus 2(\mathcal{D}_{1/2} \otimes \mathcal{D}_{1/2}) \\ 2\mathcal{D}_0 &\rightarrow 2(\mathcal{D}_{1/2} \otimes \mathcal{D}_{1/2}).\end{aligned}$$

The next step is to balance the degeneracies on either side of these equations, which Oka [131] refers to as ‘balancing the dimensions.’ In this step the nuclear spin degeneracy of each term is calculated, then that term is divided by (or the opposite side is multiplied by) that value in order to make the degeneracies equal on both sides of the expression. It is important not to neglect the coefficients (in this case 3 and 2) in this balancing, meaning that these terms must be treated along with the degeneracies in order to balance the expression. The results are,

$$\begin{aligned}\mathcal{D}_2 &\rightarrow 5(\mathcal{D}_{3/2} \otimes \mathcal{D}_{1/2}/8) \\ \mathcal{D}_1 &\rightarrow (\mathcal{D}_{3/2} \otimes \mathcal{D}_{1/2}/8) \oplus 2(\mathcal{D}_{1/2} \otimes \mathcal{D}_{1/2}/4) \\ \mathcal{D}_0 &\rightarrow (\mathcal{D}_{1/2} \otimes \mathcal{D}_{1/2}/4).\end{aligned}$$

With these products it is possible to determine the product spin weights for any combination of  $H_2$  and  $H_2^+$ . One merely needs to substitute these products for the nuclear spin modifications of the  $H_4^+$  intermediate. For example,

$$ortho\text{-}H_2 + para\text{-}H_2^+ = \mathcal{D}_1 \otimes \mathcal{D}_0 \rightarrow \mathcal{D}_1 \rightarrow (\mathcal{D}_{3/2} \otimes \mathcal{D}_{1/2}/8) \oplus 2(\mathcal{D}_{1/2} \otimes \mathcal{D}_{1/2}/4),$$

indicating that the product distribution from this reaction will be  $1/3$  *ortho*- $H_3^+$ +H and  $2/3$  *para*- $H_3^+$ +H. A relationship which is key for this work, and which partially explains the process of making a highly enriched *para*- $H_3^+$  plasma used for the dissociative recombination experiments, is the reaction between pure *para* species.

$$para\text{-}H_2 + para\text{-}H_2^+ = \mathcal{D}_0 \otimes \mathcal{D}_0 \rightarrow \mathcal{D}_0 = (\mathcal{D}_{1/2} \otimes \mathcal{D}_{1/2}/4),$$

This shows that a reaction between *para*- $H_2$  and *para*- $H_2^+$  will only produce *para*- $H_3^+$ . These fractions are then multiplied by the ‘weight’ of the reaction to obtain branching weights. The branching weights for these two examples, along with the branching weights for the other permutations of reaction (6.3) are listed in Table 6.1. The terms in the ‘weight’ column represents the total weight

$H_2 + H_2^+ \rightarrow H_3^+ + H$		Products	
Reactants	Weight	<i>o</i> - $H_3^+$ + H	<i>p</i> - $H_3^+$ + H
<i>o</i> - $H_2$ + <i>o</i> - $H_2^+$	9	6	3
<i>o</i> - $H_2$ + <i>p</i> - $H_2^+$	3	1	2
<i>p</i> - $H_2$ + <i>o</i> - $H_2^+$	3	1	2
<i>p</i> - $H_2$ + <i>p</i> - $H_2^+$	1	0	1

Table 6.1: The product spin weights for  $H_2 + H_2^+ \rightarrow H_3^+ + H_2$ .

of the particular reactant pathway, based on the reactant nuclear spin degeneracies. For example, the weight of the *ortho*-H<sub>2</sub>+*ortho*-H<sub>2</sub><sup>+</sup> pathway would be  $(2I_{ortho} + 1) \times (2I_{ortho} + 1) = 3 \times 3 = 9$ .

The values for H<sub>3</sub><sup>+</sup> + H<sub>2</sub> → H<sub>2</sub> + H<sub>3</sub><sup>+</sup> (6.1) can be found in almost the same way. The first step is to calculate the representations for the H<sub>5</sub><sup>+</sup> intermediate state,

$$(\mathcal{D}_{3/2} \oplus 2\mathcal{D}_{1/2}) \otimes (\mathcal{D}_1 \oplus \mathcal{D}_0) \rightarrow \mathcal{D}_{5/2} \oplus 4\mathcal{D}_{3/2} \oplus 5\mathcal{D}_{1/2}. \quad (6.9)$$

The  $(\mathcal{D}_{3/2} \oplus 2\mathcal{D}_{1/2})$  on the left side of (6.9) are the H<sub>3</sub><sup>+</sup> spin species representations, and  $(\mathcal{D}_1 \oplus \mathcal{D}_0)$  are the H<sub>2</sub>. The factor of 2 applied to the  $\mathcal{D}_{1/2}$  is necessary to account for the fact that there are twice as many *para*-H<sub>3</sub><sup>+</sup> states as there are *ortho*-H<sub>3</sub><sup>+</sup> (recall from §1.2, the quantum number  $G = 3n \pm 1$  for *para* and  $G = 3n$  for *ortho*). An interesting property of reaction (6.1) is that the reactant and product sides of the equation both contain H<sub>3</sub><sup>+</sup> and H<sub>2</sub>, so deriving the expressions from the reactants is equivalent to deriving the expressions from the products. To proceed, it is necessary to break out the separate products that make up (6.9),

$$\begin{aligned} \mathcal{D}_{3/2} \otimes \mathcal{D}_1 &\rightarrow \mathcal{D}_{5/2} \oplus \mathcal{D}_{3/2} \oplus \mathcal{D}_{1/2} \\ \mathcal{D}_{3/2} \otimes \mathcal{D}_0 &\rightarrow \mathcal{D}_{3/2} \\ 2\mathcal{D}_{1/2} \otimes \mathcal{D}_1 &\rightarrow 2\mathcal{D}_{3/2} \oplus 2\mathcal{D}_{1/2} \\ 2\mathcal{D}_{1/2} \otimes \mathcal{D}_0 &\rightarrow 2\mathcal{D}_{1/2}. \end{aligned}$$

Next, by balancing the degeneracies and coefficients (balancing the dimensions), the representations of the H<sub>5</sub><sup>+</sup> intermediate can be written as,

$$\begin{aligned} \mathcal{D}_{5/2} &\rightarrow 6(\mathcal{D}_{3/2} \otimes \mathcal{D}_1/12) \\ \mathcal{D}_{3/2} &\rightarrow (\mathcal{D}_{3/2} \otimes \mathcal{D}_1/12) \oplus (\mathcal{D}_{3/2} \otimes \mathcal{D}_0/4) \oplus 2(\mathcal{D}_{1/2} \otimes \mathcal{D}_1/6) \\ \mathcal{D}_{1/2} &\rightarrow 2/5(\mathcal{D}_{3/2} \otimes \mathcal{D}_1/12) \oplus 4/5(\mathcal{D}_{1/2} \otimes \mathcal{D}_1/6) \oplus 4/5(\mathcal{D}_{1/2} \otimes \mathcal{D}_0/2). \end{aligned}$$

Using these expressions it is possible to calculate the branching weights for the product spin species in the same manner as before. The results are presented in Table 6.2.

H <sub>3</sub> <sup>+</sup> + H <sub>2</sub> → H <sub>2</sub> + H <sub>3</sub> <sup>+</sup>		Products			
Reactants	Weight	<i>o</i> -H <sub>3</sub> <sup>+</sup> + <i>o</i> -H <sub>2</sub>	<i>o</i> -H <sub>3</sub> <sup>+</sup> + <i>p</i> -H <sub>2</sub>	<i>p</i> -H <sub>3</sub> <sup>+</sup> + <i>o</i> -H <sub>2</sub>	<i>p</i> -H <sub>3</sub> <sup>+</sup> + <i>p</i> -H <sub>2</sub>
<i>o</i> -H <sub>3</sub> <sup>+</sup> + <i>o</i> -H <sub>2</sub>	12	37/5	1	14/5	4/5
<i>o</i> -H <sub>3</sub> <sup>+</sup> + <i>p</i> -H <sub>2</sub>	4	1	1	2	0
2( <i>p</i> -H <sub>3</sub> <sup>+</sup> + <i>o</i> -H <sub>2</sub> )	12	14/5	2	28/5	8/5
2( <i>p</i> -H <sub>3</sub> <sup>+</sup> + <i>p</i> -H <sub>2</sub> )	4	4/5	0	8/5	8/5

Table 6.2: The product spin weights for H<sub>3</sub><sup>+</sup>+H<sub>2</sub> → H<sub>2</sub>+H<sub>3</sub><sup>+</sup>.

There is an added complication in the reaction H<sub>3</sub><sup>+</sup> + H<sub>2</sub> → H<sub>2</sub> + H<sub>3</sub><sup>+</sup> (6.1). This is because there are three different pathways by which (6.1) can proceed. Namely, these are the identity (6.10), the proton hop (6.11), and the proton exchange (6.12).

$$\text{H}_3^+ + \tilde{\text{H}}_2 \rightarrow \text{H}_3^+ + \tilde{\text{H}}_2, \quad (6.10)$$

$\text{H}_3^+ + \text{H}_2 \rightarrow \text{H}_3^+ + \text{H}_2$			Products			
Reactants	Weight		$o\text{-H}_3^+ + o\text{-H}_2$	$o\text{-H}_3^+ + p\text{-H}_2$	$p\text{-H}_3^+ + o\text{-H}_2$	$p\text{-H}_3^+ + p\text{-H}_2$
$o\text{-H}_3^+ + o\text{-H}_2$	12	ID	6/5	0	0	0
		Hop	12/5	0	6/5	0
		Exch	19/5	1	8/5	4/5
$o\text{-H}_3^+ + p\text{-H}_2$	4	ID	0	2/5	0	0
		Hop	0	0	6/5	0
		Exch	1	3/5	4/5	0
$2(p\text{-H}_3^+ + o\text{-H}_2)$	12	ID	0	0	6/5	0
		Hop	6/5	6/5	3/5	3/5
		Exch	8/5	4/5	19/5	1
$2(p\text{-H}_3^+ + p\text{-H}_2)$	4	ID	0	0	0	2/5
		Hop	0	0	3/5	3/5
		Exch	4/5	0	1	3/5

Table 6.3: The product spin weights for  $\text{H}_3^+ + \text{H}_2 \rightarrow \text{H}_2 + \text{H}_3^+$ , broken down by reaction pathway.



The  $\tilde{\text{H}}$  initially in the  $\tilde{\text{H}}_2$  are so designated in order to illustrate the differences between the three reactions. Because there are five protons involved in this reaction, there are  $5!/3!2! = 10$  possible outcomes; 1 identity, 3 hops, and 6 exchanges. It is possible to show the contribution from each of these reaction pathways to the spin modification distributions. The derivation of these path-specific branching weights is presented in Appendix C. A complete product weight listing, broken down by identity, hop, and exchange, is presented in Table 6.3.

The data are presented in a different way in Table 6.4. Here, the columns representing either *ortho* or *para*- $\text{H}_3^+$  are summed to show the total fraction of  $\text{H}_3^+$  that will go to one spin modification or the other, depending on whether the reaction is the identity, hop, or exchange.

There is no  $\text{H}_3^+$  spin conversion in the identity reaction (6.10). If *para*- $\text{H}_3^+$  combines with *para*- $\text{H}_2$  in the proton hop reaction (6.11) the product  $\text{H}_3^+$  also emerges without spin conversion. The outcome of the hop will vary with other reactant spin state modifications as can be seen in Table 6.4. The exchange reaction can result in the conversion of *para*- $\text{H}_3^+$  to *ortho*- $\text{H}_3^+$ , or vice versa, regardless of the reactant spin states. This, combined with the properties of the  $\text{H}_3^+$  formation pathway described earlier, make the exchange reaction the dominant mechanism by which *para*- $\text{H}_3^+$  is converted to *ortho*- $\text{H}_3^+$  in a plasma formed from pure *para*- $\text{H}_2$ .

It is for this reason that a 100% enriched *para*- $\text{H}_3^+$  plasma was never observed in the dissociative recombination experiments. This is also why the enriched *para*- $\text{H}_2$  gas was diluted in argon to generate a highly enriched *para*- $\text{H}_3^+$  plasma. A 1% dilution reduced the number of  $\text{H}_3^+$  collisions with  $\text{H}_2$ , thereby reducing the number of exchange reactions that could potentially convert *para*- $\text{H}_3^+$  to *ortho*- $\text{H}_3^+$ .

Clearly the *para*- $\text{H}_3^+$  enrichment of a plasma has a strong dependence on the relative rates of the hop and the exchange reactions. That being said, the ratio that relates the rate coefficients of the two reactions  $\alpha = k_{\text{Hop}}/k_{\text{Exchange}}$  is an important quantity to understand, especially at astrophysical

Reactant Spin Modification and Reaction Mechanism	Product Fractions		
	<i>ortho</i> -H <sub>3</sub> <sup>+</sup>	<i>para</i> -H <sub>3</sub> <sup>+</sup>	
<i>ortho</i> -H <sub>3</sub> <sup>+</sup> + <i>ortho</i> -H <sub>2</sub>			
Identity	→	1	0
Proton Hop	→	2/3	1/3
Hydrogen Exchange	→	2/3	1/3
<i>ortho</i> -H <sub>3</sub> <sup>+</sup> + <i>para</i> -H <sub>2</sub>			
Identity	→	1	0
Proton Hop	→	0	1
Hydrogen Exchange	→	2/3	1/3
<i>para</i> -H <sub>3</sub> <sup>+</sup> + <i>ortho</i> -H <sub>2</sub>			
Identity	→	0	1
Proton Hop	→	2/3	1/3
Hydrogen Exchange	→	1/3	2/3
<i>para</i> -H <sub>3</sub> <sup>+</sup> + <i>para</i> -H <sub>2</sub>			
Identity	→	0	1
Proton Hop	→	0	1
Hydrogen Exchange	→	1/3	2/3

Table 6.4: A concise summary of product spin fractions for  $\text{H}_3^+ + \text{H}_2 \rightarrow \text{H}_2 + \text{H}_3^+$ .

temperatures.

### 6.1.2 The high temperature model

It is important to emphasize that in this work the development of models for both high and low temperature conditions serves two purposes. First, the models provide a framework upon which to build our understanding of reaction (6.1). Second, in the development of both models it was possible to determine that changes in the observables (such as the ratio of *ortho*- to *para*-H<sub>3</sub><sup>+</sup>) can be isolated to processes occurring in reaction (6.1), versus external processes. This is an important condition if experimental measurements are going to provide useful information about this reaction.

The underlying assumption in the model and calculations for nuclear spin conversion that were described in §6.1.1 (referring to the collective model of Quack [130] and Oka [131] which predict the same results) is that the product nuclear spin states will be formed from combinations of reactant nuclear spin states according solely to the constraints imposed by the conservation of nuclear spin. This assumption is valid at high temperatures, where there is sufficient energy to access a large number of the excited states for each spin modification. With this approach, it is possible to derive relatively simple equations to describe the relationship between, and time-dependent evolution of, the fractions of *ortho* and *para* H<sub>3</sub><sup>+</sup> and H<sub>2</sub> in hydrogen plasmas.

To develop expressions that describe the behavior of this system at high temperature, we began with the rate equations found in [64] for the time dependence of the number densities of the ionic species. These equations are derived using all of the sources and sinks of the two spin species of H<sub>3</sub><sup>+</sup>. At times the source or the sink is the H<sub>3</sub><sup>+</sup> + H<sub>2</sub> reaction itself, in which case the branching fractions from Table 6.4 are used. Destruction mechanisms such as dissociation by electrons are also included. One can derive similar equations for H<sub>2</sub>, however, the rate of change for the neutral species is small

in comparison with the rate of change in  $H_3^+$  spin fractions because there is so much more  $H_2$  in comparison (see §4.1.3). The rate equations are,

$$\begin{aligned} \frac{d}{dt}[p-H_3^+] &= k_1 \left( \frac{2}{3}[o-H_2] + [p-H_2] \right) [p-H_2^+] + k_1 \left( \frac{1}{3}[o-H_2] + \frac{2}{3}[p-H_2] \right) [o-H_2^+] \\ &\quad + \left\{ k_H \left( -\frac{2}{3}[o-H_2] \right) + k_E \left( -\frac{1}{3}[o-H_2] - \frac{1}{3}[p-H_2] \right) \right. \\ &\quad \left. - (k_{r(para)}[e_r^-] + \gamma_{(para)}) \right\} [p-H_3^+] \\ &\quad + \left\{ k_H \left( \frac{1}{3}[o-H_2] + [p-H_2] \right) + k_E \left( \frac{1}{3}[o-H_2] + \frac{1}{3}[p-H_2] \right) \right\} [o-H_3^+], \end{aligned} \quad (6.13)$$

$$\begin{aligned} \frac{d}{dt}[o-H_3^+] &= k_1 \left( \frac{1}{3}[o-H_2] \right) [p-H_2^+] + k_1 \left( \frac{2}{3}[o-H_2] + \frac{1}{3}[p-H_2] \right) [o-H_2^+] \\ &\quad + \left\{ k_H \left( \frac{2}{3}[o-H_2] \right) + k_E \left( \frac{1}{3}[o-H_2] + \frac{1}{3}[p-H_2] \right) \right\} [p-H_3^+] \\ &\quad + \left\{ k_H \left( -\frac{1}{3}[o-H_2] - [p-H_2] \right) + k_E \left( -\frac{1}{3}[o-H_2] - \frac{1}{3}[p-H_2] \right) \right. \\ &\quad \left. - (k_{r(ortho)}[e_r^-] + \gamma_{(ortho)}) \right\} [o-H_3^+], \end{aligned} \quad (6.14)$$

where the rate coefficient and number density terms are,

Term	Definition
$k_1$	The rate coefficient for $H_3^+$ formation
$k_H$	The rate coefficient for the hop reaction
$k_E$	The rate coefficient for the exchange reaction
$k_r$	The state-specific rate coefficient for dissociative recombination
$[e_r^-]$	The number density of electrons in the energy range of dissociative recombination (assume $[e_r^-] \sim [H_3^+]$ )
$\gamma$	The state-specific rate coefficient for $H_3^+$ destruction after ambipolar diffusion to the walls of the containment vessel (if one is in contact with the plasma)

If equations (6.13) and (6.14) are summed, the result is,

$$\begin{aligned} \frac{d}{dt}[total-H_3^+] &= k_1[total-H_2][total-H_2^+] \\ &\quad - (k_{r(ortho)}[e_r^-] + \gamma_{(ortho)})[o-H_3^+] \\ &\quad - (k_{r(para)}[e_r^-] + \gamma_{(para)})[p-H_3^+]. \end{aligned} \quad (6.15)$$

Defining the  $para-H_3^+$  fraction as,

$$p_3 = \frac{[p-H_3^+]}{[p-H_3^+] + [o-H_3^+]}, \quad (6.16)$$

and using the quotient rule,

$$\frac{d}{dt} \left( \frac{A}{B} \right) = \frac{B \frac{dA}{dt} - A \frac{dB}{dt}}{B^2}, \quad (6.17)$$

where  $A = [p\text{-H}_3^+]$  and  $B = [p\text{-H}_3^+] + [o\text{-H}_3^+] = [\text{total-H}_3^+]$ , a relationship for the time-dependent behavior of the  $\text{para-H}_3^+$  fraction can be written,

$$\frac{d}{dt}p_3 = \frac{[\text{total-H}_3^+] \frac{d}{dt}[p\text{-H}_3^+] - [p\text{-H}_3^+] \frac{d}{dt}[\text{total-H}_3^+]}{[\text{total-H}_3^+]^2}. \quad (6.18)$$

If equations (6.13) and (6.15) are substituted into (6.18), and the term,

$$p_2 = \frac{[\text{para-H}_2]}{[\text{para-H}_2] + [\text{ortho-H}_2]}, \quad (6.19)$$

is used, the simplified result becomes,

$$\begin{aligned} \frac{d}{dt}p_3 = & k_1[\text{total-H}_2] \left\{ \frac{2}{3} \frac{[p\text{-H}_2^+]}{[\text{total-H}_3^+]} + \frac{1}{3} \frac{[o\text{-H}_2^+]}{[\text{total-H}_3^+]} + \left( \frac{1}{3}p_2 - p_3 \right) \frac{[\text{total-H}_2^+]}{[\text{total-H}_3^+]} \right\} \\ & + \left\{ (k_{r(\text{ortho})} - k_{r(\text{para})})[e_r^-] + (\gamma_{\text{ortho}} - \gamma_{\text{para}}) \right\} p_3 \\ & - \left\{ (k_{r(\text{ortho})} - k_{r(\text{para})})[e_r^-] + (\gamma_{\text{ortho}} - \gamma_{\text{para}}) \right\} p_3^2 \\ & + k_H[\text{total-H}_2] \left( \frac{2}{3}p_2 - p_3 + \frac{1}{3} \right) + k_E[\text{total-H}_2] \left( \frac{1}{3} - \frac{2}{3}p_3 \right). \end{aligned} \quad (6.20)$$

The steps required to go from equation (6.18) to equation (6.20) are presented in Appendix C. Equation (6.20) can be further simplified by the elimination of terms that have negligible contributions. For instance, the dissociative recombination (DR) terms can be removed. As discussed in Chapter 5, there is a difference between the DR thermal rate coefficients of  $\text{para-}$  and  $\text{ortho-H}_3^+$ , meaning  $k_{r(\text{ortho})} - k_{r(\text{para})}$  does not cancel, and these rate constants are 2 orders of magnitude greater than either the hop or exchange rate constants. However, the  $[e_r^-]$  are  $\sim 5$  orders of magnitude smaller than the  $[\text{total-H}_2]$  number densities that are contained in the last two terms on the right hand side of equation (6.20). Put together, this factor of 1000 difference between the DR terms and those containing  $[\text{H}_2]$  justifies neglecting the smaller dissociative recombination terms. Regarding  $\gamma$ , there is no evidence indicating that the rate of destruction by ambipolar diffusion would be different for  $\text{para-}$  and  $\text{ortho-H}_3^+$ , despite being labeled as such for completeness. In fact, the only experiment in this work for which this could be a factor uses the hollow cathode cell. Amano found that ambipolar diffusion is not a significant process for the destruction of  $\text{H}_3^+$  in hollow cathodes [115], so it is logical to neglect the  $\gamma$  terms as well. Taking what remains and rearranging to isolate the terms containing  $p_3$  gives,

$$\begin{aligned} \frac{d}{dt}p_3 = & \left\{ \frac{1}{3}k_1[\text{total-H}_2]p_2 \frac{[\text{total-H}_2^+]}{[\text{total-H}_3^+]} + \frac{2}{3}k_1[\text{total-H}_2] \frac{[p\text{-H}_2^+]}{[\text{total-H}_3^+]} + \frac{1}{3}k_1[\text{total-H}_2] \frac{[o\text{-H}_2^+]}{[\text{total-H}_3^+]} \right. \\ & \left. + \frac{2}{3}k_H[\text{total-H}_2]p_2 + \frac{1}{3}k_H[\text{total-H}_2] + \frac{1}{3}k_E[\text{total-H}_2] \right\} \\ & - \left\{ k_1[\text{total-H}_2] \frac{[\text{total-H}_2^+]}{[\text{total-H}_3^+]} + \frac{2}{3}k_E[\text{total-H}_2] + k_H[\text{total-H}_2] \right\} p_3. \end{aligned} \quad (6.21)$$

Additional terms can be eliminated from equation (6.21). The efficiency of the formation reaction (6.3) leads to the condition where  $[H_2^+] < [H_3^+]$  [115, 134], which means that any terms containing the ratio  $[H_2^+]/[total-H_3^+]$  can be neglected because  $k_1 \sim k_E \sim k_H$ . This is valid for hollow cathode experiments, as well as for expansions as determined by mass spectrometry at the CRYRING ion storage ring in which the number density of  $H_2^+$  was measured to be three orders of magnitude less than  $H_3^+$ . The elimination of the  $[H_2^+]/[total-H_3^+]$  terms results in,

$$\begin{aligned} \frac{d}{dt}p_3 = & \left\{ \frac{2}{3}k_H[total-H_2]p_2 + \frac{1}{3}k_H[total-H_2] + \frac{1}{3}k_E[total-H_2] \right\} \\ & - \left\{ \frac{2}{3}k_E[total-H_2] + k_H[total-H_2] \right\}p_3. \end{aligned} \quad (6.22)$$

If a steady state condition is assumed where  $dp_3/dt = 0$ , then (6.22) can be written as,

$$\begin{aligned} & \left\{ \frac{2}{3}k_H[total-H_2]p_2 + \frac{1}{3}k_H[total-H_2] + \frac{1}{3}k_E[total-H_2] \right\} = \\ & \left\{ \frac{2}{3}k_E[total-H_2] + k_H[total-H_2] \right\}p_3. \end{aligned} \quad (6.23)$$

After solving for  $p_3$ , and canceling the  $[total-H_2]$  this leaves,

$$p_3 = \frac{\left\{ \frac{2}{3}k_H p_2 + \frac{1}{3}k_H + \frac{1}{3}k_E \right\}}{\left\{ \frac{2}{3}k_E + k_H \right\}}. \quad (6.24)$$

Multiplying the top and bottom by  $3/k_E$  and substituting  $\alpha = k_H/k_E$ , equation (6.24) becomes,

$$p_3 = \frac{2\alpha p_2 + \alpha + 1}{2 + 3\alpha}. \quad (6.25)$$

In the high temperature limit, this surprisingly simple equation relates the variables that can be observed ( $p_2$  and  $p_3$ ), and the variable of interest ( $\alpha$ ). Of course, this depends on the validity of the  $dp_3/dt = 0$  steady state assumption.

To test if steady state is a valid assumption, the differential equation (6.22) can be solved for  $p_3$  as a function of time. The form of this differential equation is,

$$\frac{dx}{dt} = A - Bx. \quad (6.26)$$

where  $x(t) = p_3(t)$ . Changing variables to  $u = A - Bx$  and  $du = -Bdx \rightarrow dx = -du/B$ ,

$$\frac{-du}{Bu} = u \rightarrow \frac{du}{dt} = -Bu, \quad (6.27)$$

the solution to which is,

$$u(t) = u_0 e^{-Bt}, \quad (6.28)$$

where a reasonable constant of integration, defined at  $t = 0$ , is  $u_0 = (A - Bx_0)$ . Re-substituting A



and B,

$$A - Bx(t) = (A - Bx_o)e^{-Bt} \rightarrow x(t) = \frac{A}{B} - \left(\frac{A}{B} - x_o\right)e^{-Bt}, \quad (6.29)$$

and finally inserting the original terms for A and B from equation (6.22),

$$p_3(t) = p_{3,\infty} - (p_{3,\infty} - p_{3,o})e^{-\left(\frac{2}{3}k_E[total-H_2] + k_H[total-H_2]\right)t} \quad (6.30)$$

where  $p_{3,\infty}$  is the steady state value of  $p_3$  (6.24), and  $p_{3,o}$  is the initial value of  $p_3$ . This equation implies that  $p_3$  converges to  $p_{3,\infty}$  within a few collision times because the exponential argument essentially represents the collision rate with  $H_2$ . Thus, the steady state assumption is valid. In terms of timescales based on number densities in the hollow cathode and expansion experiments (see Chapter 4), this would be  $\sim 10$  ns in the former and less than 1 ns to  $\sim 1$   $\mu$ s in the latter, depending on the location in the expansion. In contrast, it would take months to achieve  $H_3^+$  steady state in diffuse clouds, and approximately 1 day in dense clouds.

Similar equations can be derived to describe the time-dependent behavior of the  $H_2$  spin modifications. Using fractions that can be calculated from Table 6.3,

$$\begin{aligned} \frac{d}{dt}[p-H_2] = & \left\{ \frac{1}{4}k_E[o-H_3^+] + \frac{1}{2}k_H[p-H_3^+] + \frac{1}{4}k_E[p-H_3^+] \right\} [o-H_2] \\ & - \left\{ k_H[o-H_3^+] + \frac{3}{4}k_E[o-H_3^+] + \frac{1}{2}k_H[p-H_3^+] \right. \\ & + \left. \frac{3}{4}k_E[p-H_3^+] + k_d[e_d^-] + k_1[H_2^+] + k_i[e_i^-] \right\} [p-H_2] \\ & + \frac{1}{3}k_{r(para)}[e_r^-][p-H_3^+] + \frac{1}{4}k_f[H]^2 - \frac{1}{2}k_c[H^+][p-H_2] + \frac{1}{6}k_c[H^+][o-H_2], \end{aligned} \quad (6.31)$$

$$\begin{aligned} \frac{d}{dt}[o-H_2] = & \left\{ k_H[o-H_3^+] + \frac{3}{4}k_E[o-H_3^+] + \frac{1}{2}k_H[p-H_3^+] \right. \\ & + \left. \frac{3}{4}k_E[p-H_3^+] \right\} [p-H_2] \\ & - \left\{ \frac{1}{4}k_E[o-H_3^+] + \frac{1}{2}k_H[p-H_3^+] + \frac{1}{4}k_E[p-H_3^+] \right. \\ & + \left. k_d[e_d^-] + k_1[H_2^+] + k_i[e_i^-] \right\} [o-H_2] \\ & + \frac{1}{3}k_{r(ortho)}[e_r^-][o-H_3^+] + \frac{3}{4}k_f[H]^2 + \frac{1}{2}k_c[H^+][p-H_2] - \frac{1}{6}k_c[H^+][o-H_2], \end{aligned} \quad (6.32)$$

where the new rate coefficient and number density terms are,

Term	Definition
$k_d$	The rate coefficient for $H_2$ dissociation with electrons
$[e_d^-]$	The number density of electrons with energy to dissociate $H_2$
$k_i$	The rate coefficient for the ionization of $H_2$
$[e_i^-]$	The number density of electrons with energy to ionize $H_2$
$k_c$	The rate coefficient for the reaction $H^+ + H_2$
$k_f$	The rate coefficient for the formation of $H_2$ from atomic H

The factor of 1/3 applied to the  $H_3^+$  dissociative recombination source term comes from the fact that only 1/3 of  $H_3^+$  dissociations result in a product  $H_2$  (see §5.1). Additionally, conservation of nuclear spin requires that *para*- $H_2$  can only be formed from *para*- $H_3^+$ , and a parallel argument exists for *ortho*- $H_2$ . The factors 1/4 and 3/4 that appear in front of the  $k_f$  terms represent the ratio in which *para*- and *ortho*- $H_2$  will form from the recombination of H atoms. Finally, the coefficients for the  $k_c$  terms arise from conservation of nuclear spin in the reaction  $H^+ + H_2$ . Summing equations (6.31) and (6.32) gives,

$$\begin{aligned} \frac{d}{dt}[total-H_2] = & \frac{1}{3}(k_{r(ortho)}[o-H_3^+] + k_{r(para)}[p-H_3^+])[e_r^-] + k_f[H]^2 - k_d[e_d^-][total-H_2] \\ & - k_1[H_2^+][total-H_2] - k_i[e_i^-][total-H_2]. \end{aligned} \quad (6.33)$$

Using the quotient rule (6.17) in a similar derivation as was done for  $dp_3/dt$ , the time dependence of  $p_2$  is found to be,

$$\begin{aligned} \frac{d}{dt}p_2 = & \left( \frac{1}{4}k_E[total-H_3^+] + \frac{1}{2}k_H[p-H_3^+] + \frac{1}{6}k_c[H^+] \right) (1 - p_2) \\ & - \left( \frac{3}{4}k_E[total-H_3^+] + k_H[o-H_3^+] + \frac{1}{2}k_H[p-H_3^+] - \frac{2}{3}k_c[H^+] \right) p_2 \\ & + \left( \frac{1}{3}k_{r(para)}[e_r^-][p-H_3^+] + \frac{1}{4}k_f[H]^2 \right) \frac{1}{[total-H_2]} \\ & - \left( \frac{1}{3}(k_{r(para)}[p-H_3^+] + k_{r(ortho)}[o-H_3^+])[e_r^-] + k_f[H]^2 \right) \frac{p_2}{[total-H_2]}. \end{aligned} \quad (6.34)$$

As with  $dp_3/dt$ , equation (6.34) can be simplified by the elimination of terms. The  $k_c$  terms describing the contribution or removal of *para*- $H_2$  by reaction with  $H^+$  can be neglected by making order of magnitude arguments. In the expansion experiment, the number density of  $H_3^+$  was observed to be  $30\times$  greater than that of  $H^+$ . The ratio of these ions was not measured in the hollow cathode cell, however, Saporoschenko [134] and Albritton *et al.* [135] found an order of magnitude difference between the more abundant  $H_3^+$  ion and  $H^+$  in a plasma source similar to the hollow cathode. This, combined with the fact that  $k_c$  is an order of magnitude smaller than either  $k_E$  or  $k_H$  [8,64], indicates that the  $k_c$  terms can be neglected. These assumptions, and therefore this model, cannot be used for diffuse cloud conditions where the abundance of  $H^+$  is four orders of magnitude greater than that of  $H_3^+$  [43]. However, it is applicable under dense cloud conditions where the abundance of  $H^+$  is estimated to be an order of magnitude less than  $H_3^+$  [136].

The two  $H_2$  formation terms ( $k_f[H]^2$ ) can also be eliminated using order of magnitude comparisons. The number density of atomic H is slightly greater than that of  $H_3^+$  because H is primarily formed along with  $H_3^+$  in reaction (6.3), while contributions from other pathways such as the dissociation of  $H_2$  by electrons will increase this value by an order of magnitude at most [64]. Based on  $[H]$  calculated from  $H_3^+$  number densities measured in the expansion and the hollow cathode cell (see Tables 4.2 and 4.5),  $[H]^2/[total-H_2]$  will typically be 2-4 orders of magnitude smaller than  $[H_3^+]$ . In addition, the rate coefficient for the gas phase formation of  $H_2$ ,  $k_f$ , is smaller than  $3 \times 10^{-17} \text{ cm}^3 \text{ s}^{-1}$  at temperatures below 1000 K [137]. It is important to note that this value for  $k_f$  does not apply for the hollow cathode experiments, where there is a large surface upon which recombination can take place. This is a special case that will be addressed in §6.2.1. In dense clouds, atomic H is

more abundant than in the laboratory plasmas described here [138], however, the formation of  $H_2$  on grain surfaces has a small impact on  $p_2$  due to the relatively small value of  $k_f$  ( $\sim 1 \times 10^{-17} \text{ cm}^3 \text{ s}^{-1}$ ).

The dissociative recombination terms ( $k_r$ ) can also be neglected if one considers the fact that the ratio  $[e_r^-]/[total-H_2]$  is  $\sim 1 \times 10^{-5}$ . This is calculated using the number densities of  $H_2$  and  $H_3^+$  taken from Tables 4.2 and 4.5, along with the assumption that  $[e_r^-] \sim [H_3^+]$  because  $H_3^+$  is the dominant ion in the plasma. Even with a 2 order of magnitude difference between the rate coefficients ( $k_H \sim .01k_r$  and  $k_E \sim .01k_r$ ), the dissociative recombination terms are 1000 times smaller, and can be eliminated from the expression. This certainly applies in dense clouds where the dominant destruction mechanism for  $H_3^+$  is by reaction with CO [32]. The  $k_r$  and  $[e_r^-]$  terms are simply replaced by terms representing reactions with CO. Although the dense cloud ratio  $[CO]/[H_2] \sim 10^{-4}$  is larger than the laboratory plasma estimate for  $[e_r^-]/[H_2] \sim 10^{-5}$ , the rate coefficient for the reaction with CO is  $k_{CO} = 2 \times 10^{-9} \text{ cm}^3 \text{ s}^{-1}$ , which is smaller than  $k_r$ . After eliminating these terms, equation (6.34) can be simplified to,

$$\begin{aligned} \frac{d}{dt}p_2 = & \left( \frac{1}{4}k_E[total-H_3^+] + \frac{1}{2}k_H[p-H_3^+] \right) \\ & - \left( k_E[total-H_3^+] + k_H[total-H_3^+] \right) p_2. \end{aligned} \quad (6.35)$$

Euler's method was used to integrate equation (6.35), and the results are shown in Figure 6.1. The

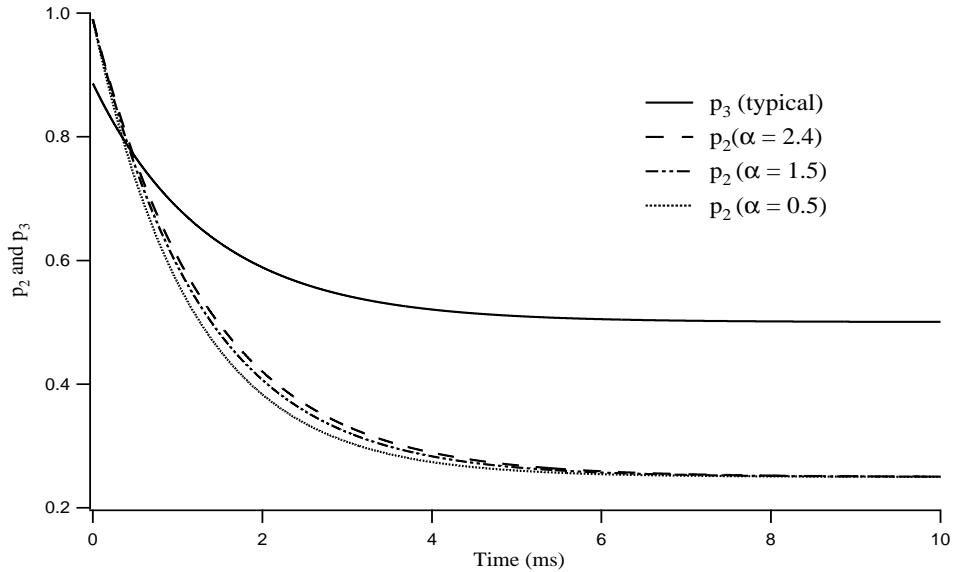


Figure 6.1: The time dependence of *para*- $H_2$  ( $p_2$ ) and *para*- $H_3^+$  ( $p_3$ ) enrichments, as predicted by the high temperature model.

model always predicts a normal- $H_2$  steady state, with a *para*- $H_3^+$  fraction ( $p_3$ ) that changes with the evolving *para*- $H_2$  enrichment. The figure also shows that a decrease in  $\alpha$  only shortens the time constant for the decay to a normal- $H_2$  steady state. These simulations were run using the number densities of the hollow cathode cell (described in §4.2)). When the model was run using the

conditions of the expansion source (§4.1), the *para*-H<sub>2</sub> enrichment ( $p_2$ ) took much longer to reach steady state.

The relationship between the *para*-H<sub>3</sub><sup>+</sup> fraction ( $p_3$ ) and the *para*-H<sub>2</sub> fraction ( $p_2$ ) is depicted in Figure 6.2 for different values of  $\alpha$ . The higher the  $\alpha$ , the higher the  $p_3$  for a given  $p_2$ . When  $p_2 = 0.25$  (representing normal 3:1 H<sub>2</sub>), the fraction  $p_3$  is always equal to 0.5 no matter what the value of  $\alpha$ .

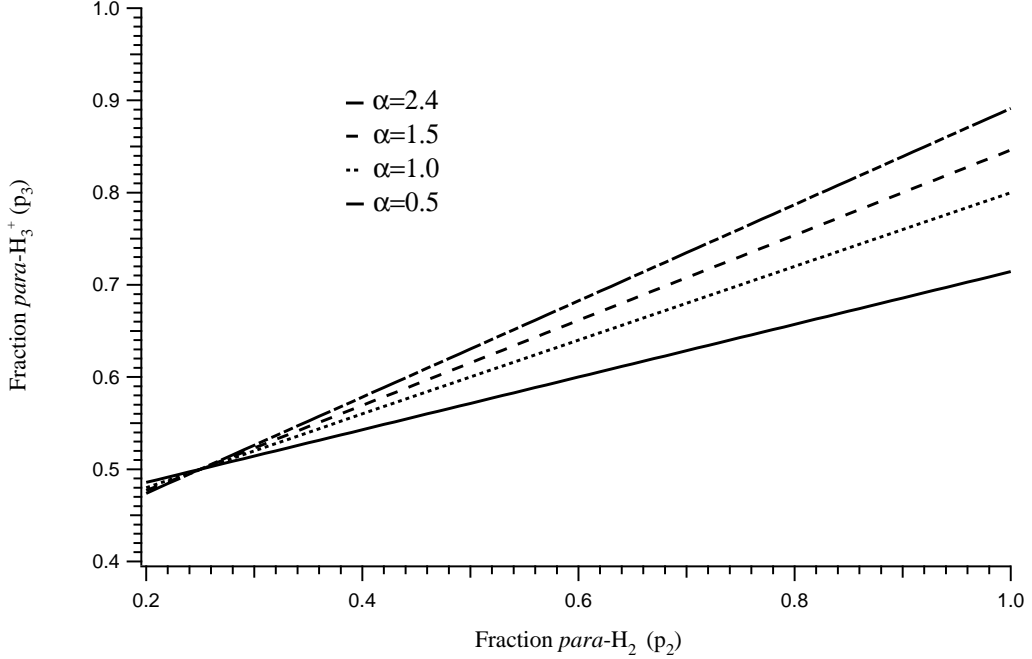


Figure 6.2: Relationship between  $p_2$  and  $p_3$  based on the high temperature model.

Uy *et al.* [63], and Cordonnier *et al.* [64], were the first to experimentally observe the spin selection rules in a hydrogen discharge at  $\sim 300$ -400 K. They did so by observing the fraction *para*-H<sub>3</sub><sup>+</sup> ( $p_3$ ) when an enriched *para*-H<sub>2</sub> was used as the precursor gas instead of normal H<sub>2</sub>. In both papers, the measurements indicated that the proton hop and hydrogen exchange reactions occurred with a ratio  $\alpha = k_{Hop}/k_{Exchange} = 2.4$ .

Even before the the studies done in [63] and [64], Gerlich performed similar experiments (at least in objective) using D<sub>3</sub><sup>+</sup> and H<sub>2</sub> in a merged beam apparatus, which was thought to achieve temperatures as low as 20 K [132]. His experiments were carried out using a spin-normal hydrogen/deuterium gas mixture versus pure *para*-H<sub>2</sub>, and demonstrated a temperature dependence of  $k_{Hop}/k_{Exchange}$ . This was determined from a change in the ratio of H<sub>2</sub>D<sup>+</sup> to HD<sub>2</sub><sup>+</sup>, corresponding to a change in the relative dominance between the hop (6.11) and exchange (6.12). Gerlich's results indicated a trend towards the limit of  $\alpha = k_{Hop}/k_{Exchange} = 0.5$  at the coldest temperatures, which is the statistical result. Nevertheless, the applicability of Gerlich's work to a purely hydrogenic plasma is limited as exemplified by differences in energetics. In contrast to the thermoneutral H<sub>3</sub><sup>+</sup>+H<sub>2</sub> reaction, the reaction involving deuterated species is endothermic.

### 6.1.3 Low temperature model

Some of the assumptions that make the statistical model valid at higher temperatures do not apply at the colder temperatures of the interstellar medium. In these regimes there is insufficient energy for certain spin-conserving, but energetically unfavorable reactions to occur. Reactions in which *para*-H<sub>2</sub> must be converted to *ortho*-H<sub>2</sub> are such an example, because the energy difference between the ground states of these species is 118.5 cm<sup>-1</sup> (170 K). A quick inspection of Table 6.3 shows there are many such reactions in which this type of H<sub>2</sub> conversion must occur in order to conserve nuclear spin.

As a result, the high temperature model appears ill-equipped to explain the H<sub>3</sub><sup>+</sup> + H<sub>2</sub> reaction in cold laboratory plasmas or in the interstellar medium. Park and Light [139] developed a model that accounts for the energetics of reaction (6.1), especially at cold temperatures. Their model calculates the energy available to the different reactant species (at a given temperature), and uses these to generate so-called cumulative reaction probabilities from which reaction rate coefficients can be derived. The model itself was provided to us by K. Park in the form of a Windows executable with input parameters of kinetic and rotational temperature and  $\alpha = k_H/k_E$ . The model's output is in the form of rate coefficients for the different permutations of the *ortho/para*-H<sub>3</sub><sup>+</sup> and *ortho/para*-H<sub>2</sub> reactant and product states. The rate coefficients describe the rates at which ground-state reactants go to all product states (to include excited). For example,  $k_{popo}$  represents the rate coefficient for the reaction  $p\text{-H}_3^+ + o\text{-H}_2 \rightarrow p\text{-H}_3^+ + o\text{-H}_2$ . Because the output of the model was in the form of multiple rate coefficients, it was necessary to derive new equations to represent the time dependent relationship between  $p_3$  and  $p_2$ . The detailed rate equations are,

$$\begin{aligned} \frac{d}{dt}[p\text{-H}_3^+] = & k_1\left(\frac{2}{3}[o\text{-H}_2] + [p\text{-H}_2]\right)[p\text{-H}_2^+] + k_1\left(\frac{1}{3}[o\text{-H}_2] + \frac{2}{3}[p\text{-H}_2]\right)[o\text{-H}_2^+] \\ & + \left\{ (k_{oopp} + k_{oopo})[o\text{-H}_2] + (k_{oppo} + k_{oppo})[p\text{-H}_2] \right\} [o\text{-H}_3^+] \\ & - \left\{ (k_{poop} + k_{pooo})[o\text{-H}_2] + (k_{ppop} + k_{ppoo})[p\text{-H}_2] \right\} [p\text{-H}_3^+] \\ & - k_{r(para)}[e_r^-][p\text{-H}_3^+], \end{aligned} \quad (6.36)$$

$$\begin{aligned} \frac{d}{dt}[o\text{-H}_3^+] = & k_1\left(\frac{1}{3}[o\text{-H}_2]\right)[p\text{-H}_2^+] + k_1\left(\frac{2}{3}[o\text{-H}_2] + \frac{1}{3}[p\text{-H}_2]\right)[o\text{-H}_2^+] \\ & + \left\{ (k_{poop} + k_{pooo})[o\text{-H}_2] + (k_{ppop} + k_{ppoo})[p\text{-H}_2] \right\} [p\text{-H}_3^+] \\ & - \left\{ (k_{oopp} + k_{oopo})[o\text{-H}_2] + (k_{oppo} + k_{oppo})[p\text{-H}_2] \right\} [o\text{-H}_3^+] \\ & - k_{r(ortho)}[e_r^-][o\text{-H}_3^+]. \end{aligned} \quad (6.37)$$

Equations (6.36) and (6.37) use the same H<sub>3</sub><sup>+</sup> formation terms as the high temperature model. The terms involving  $\gamma$  were not included because of the arguments presented in the previous section. Summing (6.36) and (6.37) together gives a result for  $[total\text{-H}_3^+]$  that is nearly identical to that

found at high temperature,

$$\begin{aligned} \frac{d}{dt}[total-H_3^+] &= k_1[total-H_2][total-H_2^+] \\ &\quad - k_{r(ortho)}[e_r^-][o-H_3^+] \\ &\quad - k_{r(para)}[e_r^-][p-H_3^+]. \end{aligned} \quad (6.38)$$

Substituting (6.36) and (6.38) into the quotient rule equation (6.17), and simplifying as before gives the result,

$$\begin{aligned} \frac{d}{dt}p_3 &= k_1 \left( \frac{2}{3}[o-H_2] + [p-H_2] \right) \frac{[p-H_2^+]}{[total-H_3^+]} + k_1 \left( \frac{1}{3}[o-H_2] + \frac{2}{3}[p-H_2] \right) \frac{[o-H_2^+]}{[total-H_3^+]} \\ &\quad + \left\{ (k_{oopp} + k_{oopo})[o-H_2] + (k_{oppp} + k_{oppo})[p-H_2] \right\} (1 - p_3) \\ &\quad - \left\{ (k_{poop} + k_{pooo})[o-H_2] + (k_{ppop} + k_{ppoo})[p-H_2] \right\} p_3 \\ &\quad - k_{r(para)}[e_r^-]p_3 - k_{r(ortho)}[e_r^-](1 - p_3)p_3 - k_{r(para)}[e_r^-]p_3^2 \\ &\quad - \frac{k_1[total-H_2][total-H_2^+]p_3}{[total-H_3^+]}. \end{aligned} \quad (6.39)$$

Although the form of  $dp_3/dt$  and the rate coefficients have changed between the high and low temperature models, the number densities and actual physical conditions of the plasmas have not. As a result, certain terms can be neglected just as they were for the previous model. For instance, because the number density of electrons,  $[e_r^-]$ , is at least 5 orders of magnitude smaller than  $[H_2]$ , the dissociative recombination terms can be neglected. This leaves the equation,

$$\begin{aligned} \frac{d}{dt}p_3 &= k_1 \left( \frac{2}{3}[o-H_2] + [p-H_2] \right) \frac{[p-H_2^+]}{[total-H_3^+]} + k_1 \left( \frac{1}{3}[o-H_2] + \frac{2}{3}[p-H_2] \right) \frac{[o-H_2^+]}{[total-H_3^+]} \\ &\quad + \left\{ (k_{oopp} + k_{oopo})[o-H_2] + (k_{oppp} + k_{oppo})[p-H_2] \right\} (1 - p_3) \\ &\quad - \left\{ (k_{poop} + k_{pooo})[o-H_2] + (k_{ppop} + k_{ppoo})[p-H_2] \right\} p_3 \\ &\quad - \frac{k_1[total-H_2][total-H_2^+]p_3}{[total-H_3^+]}. \end{aligned} \quad (6.40)$$

By again assuming a steady state condition for  $para-H_3^+$  ( $dp_3/dt = 0$ ) and solving for  $p_3$ , a relationship between the  $p_3$  and the  $para-H_2$  fraction ( $p_2$ ) can be found.

$$p_3 = \frac{(k_{oppo})[p-H_2] + (k_{oopp} + k_{oopo})[o-H_2] + k_1\zeta_p \left( \frac{2}{3}[o-H_2] + [p-H_2] \right) + k_1\zeta_o \left( \frac{1}{3}[o-H_2] + \frac{2}{3}[p-H_2] \right)}{k_1\zeta_{tot}[total-H_2] + (k_{oppo} + k_{ppoo})[p-H_2] + (k_{oopp} + k_{oopo} + k_{poop} + k_{pooo})[o-H_2]}, \quad (6.41)$$

where,

$$\begin{aligned}\zeta_p &= \frac{[p\text{-H}_2^+]}{[total\text{-H}_3^+]} \\ \zeta_o &= \frac{[o\text{-H}_2^+]}{[total\text{-H}_3^+]} \\ \zeta_{tot} &= \frac{[total\text{-H}_2^+]}{[total\text{-H}_3^+]}.\end{aligned}$$

The terms  $k_{opp}$  and  $k_{ppop}$  have been eliminated from equation (6.41) because these pathways do not conserve nuclear spin (Table 6.3). In order to use the relationship  $p_2 = [p\text{-H}_2]/[total\text{-H}_2]$ , the top and bottom of equation (6.41) are divided by  $[total\text{-H}_2]$ . The result is,

$$p_3 = \frac{(k_{oppo})p_2 + (k_{oop} + k_{oopo})(1 - p_2) + k_1\zeta_p(\frac{2}{3}(1 - p_2) + p_2) + k_1\zeta_o(\frac{1}{3}(1 - p_2) + \frac{2}{3}p_2)}{k_1\zeta_{tot} + (k_{oppo} + k_{ppoo})p_2 + (k_{oop} + k_{oopo} + k_{pop} + k_{pooo})(1 - p_2)}.\quad (6.42)$$

As was the case in the high temperature model, the  $\zeta$  terms containing the ratio  $[H_2^+]/[H_3^+]$  can be neglected because  $[H_2^+] \ll [H_3^+]$ . Although the average  $k_{xxxx}$  coefficient is an order of magnitude smaller than  $k_1$ , the contribution of the latter (with the factor of  $[H_2^+]/[H_3^+]$ ) is less than 1%. With the elimination of these terms, the final form of the equation is,

$$p_3 = \frac{(k_{oop} + k_{oopo}) + (k_{oppo} - k_{oop} - k_{oopo})p_2}{(k_{oppo} + k_{ppoo})p_2 + (k_{oop} + k_{oopo} + k_{pop} + k_{pooo})(1 - p_2)}.\quad (6.43)$$

Using equation (6.43) along with the rate coefficients calculated by the low temperature model, the

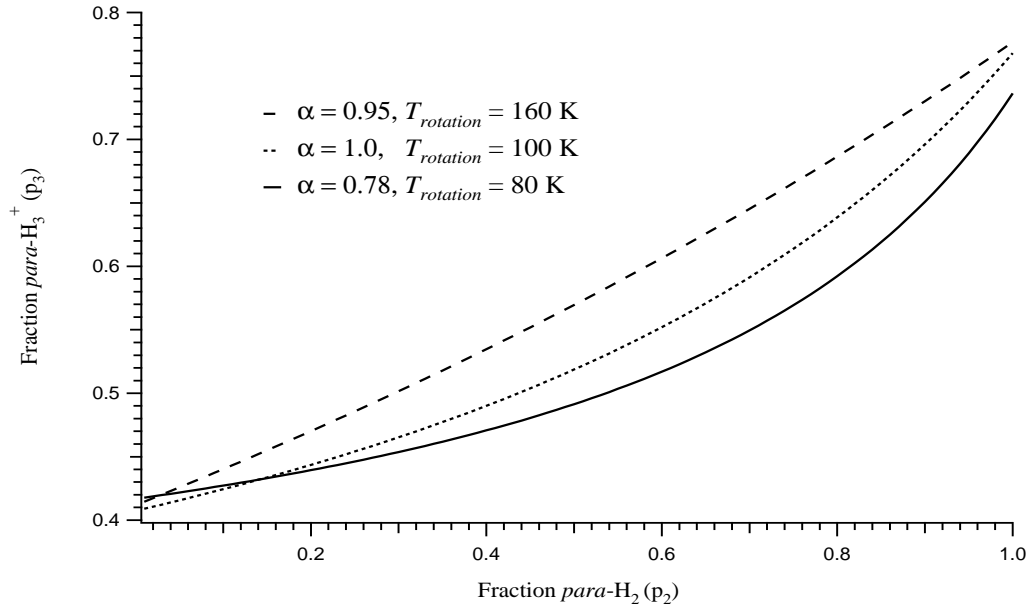


Figure 6.3: Relationship between  $p_2$  and  $p_3$  based on the low temperature model.

relationship between  $p_2$  and  $p_3$  is depicted for various temperatures and  $\alpha$  (see Figure 6.3). This figure shows that the  $para\text{-H}_3^+$  fraction ( $p_3$ ) at a given  $para\text{-H}_2$  fraction ( $p_2$ ) increases with  $\alpha$ . The shape of the curve has an even stronger dependence on temperature, with the relationship between  $p_3$  and  $p_2$  becoming more linear (similar to the high temperature model) at the model's limiting temperature of 160 K.

Similarly, the system of rate coefficients can be used to find a cold temperature  $dp_2/dt$ . The derivation begins with the detailed rate equations for the spin modifications of  $\text{H}_2$ ,

$$\begin{aligned} \frac{d}{dt}[p\text{-H}_2] = & \left\{ (k_{oopp} + k_{ooop})[o\text{-H}_2] \right\} [o\text{-H}_3^+] + \left\{ (k_{pooop} + k_{popp})[o\text{-H}_2] \right\} [p\text{-H}_3^+] \\ & - \left\{ (k_{oppo} + k_{opoo})[p\text{-H}_2] \right\} [o\text{-H}_3^+] - \left\{ (k_{ppoo} + k_{pppo})[p\text{-H}_2] \right\} [p\text{-H}_3^+] \\ & - k_d[e_d^-][p\text{-H}_2] - k_1[\text{H}_2^+][p\text{-H}_2] - k_i[e_i^-][p\text{-H}_2] + \frac{1}{3}k_r(para)[e_r^-][p\text{-H}_3^+] \\ & + \frac{1}{4}k_f[\text{H}]^2 - \frac{1}{2}k_c[\text{H}^+][p\text{-H}_2] + \frac{1}{6}k_c[\text{H}^+][o\text{-H}_2], \end{aligned} \quad (6.44)$$

$$\begin{aligned} \frac{d}{dt}[o\text{-H}_2] = & \left\{ (k_{oppo} + k_{opoo})[p\text{-H}_2] \right\} [o\text{-H}_3^+] + \left\{ (k_{ppoo} + k_{pppo})[p\text{-H}_2] \right\} [p\text{-H}_3^+] \\ & - \left\{ (k_{oopp} + k_{ooop})[o\text{-H}_2] \right\} [o\text{-H}_3^+] - \left\{ (k_{pooop} + k_{popp})[o\text{-H}_2] \right\} [p\text{-H}_3^+] \\ & - k_d[e_d^-][o\text{-H}_2] - k_1[\text{H}_2^+][o\text{-H}_2] - k_i[e_i^-][o\text{-H}_2] + \frac{1}{3}k_r(ortho)[e_r^-][o\text{-H}_3^+] \\ & + \frac{1}{4}k_f[\text{H}]^2 + \frac{1}{2}k_c[\text{H}^+][p\text{-H}_2] - \frac{1}{6}k_c[\text{H}^+][o\text{-H}_2], \end{aligned} \quad (6.45)$$

where the first two lines on the right hand sides of equations (6.44) and (6.45) represent the changing  $\text{H}_2$  enrichment due to the reaction with  $\text{H}_3^+$ . The next five terms, respectively, represent losses to electron impact dissociation, formation of  $\text{H}_3^+$ , and ionization, and gains due to the dissociative recombination of  $\text{H}_3^+$ , and formation from atomic hydrogen. The last two terms account for the changing enrichment due to reactions with  $\text{H}^+$ . These equations, along with the quotient rule (6.17), can be used to solve for  $dp_2/dt$ . After simplification, the insignificant terms ( $k_r$ ,  $k_f$ , and  $k_c$ ) are eliminated as was done for equation (6.34) and the resulting differential equation for  $dp_2/dt$  is,

$$\begin{aligned} \frac{d}{dt}p_2 = & \left\{ (k_{oopp} + k_{ooop}) \right. \\ & - p_2(k_{oopp} + k_{ooop} + k_{oppo} + k_{opoo}) - p_3(k_{oopp} + k_{ooop} - k_{pooop} - k_{popp}) \\ & \left. + p_2p_3(k_{oopp} + k_{ooop} - k_{pooop} - k_{popp} + k_{oppo} + k_{opoo} - k_{ppoo} - k_{pppo}) \right\} [total\text{-H}_3^+]. \end{aligned} \quad (6.46)$$

Instead of solving the differential equation (6.46), the function was numerically integrated using Euler's method. The steady state approximation and equation (6.43) were used to update  $p_3$  as the value of  $p_2$  evolved. Continuing use of the steady state approximation for the value of  $p_3$  was reasonable because the solution for (6.40) after the elimination of negligible terms is,

$$p_3(t) = p_{3,\infty} - (p_{3,\infty} - p_{3,0})e^{-\left\{ (k_{oopp} + k_{ooop} + k_{pooop} + k_{popp})[o\text{-H}_2] + (k_{oppo} + k_{opoo})[p\text{-H}_2] \right\}t},$$



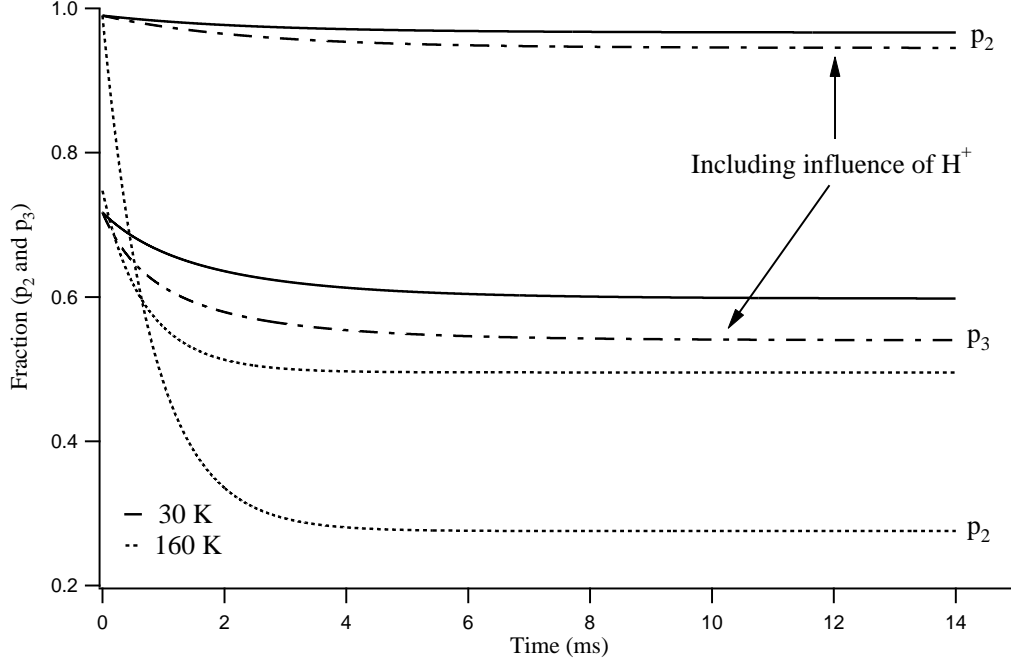


Figure 6.4: The time dependence of  $p_2$  and  $p_3$  at low temperature.

the derivation of which is similar to that of (6.30). Once again, the value of  $p_3$  will converge to a steady state in the timeframe for a collision with  $\text{H}_2$ , which is on the order of 10 ns to  $\mu\text{s}$ .

Three simulations, all with a starting  $p_2=0.99$  are presented in Figure 6.4. The simulations were run at different temperature conditions but with  $\alpha=0.78$  (changes in  $\alpha$  have a smaller effect on the result than do changes in temperature). The solid or dashed lines represent a data pair ( $p_2$  and  $p_3$ ) that propagate at the same temperature. The dotted-dashed lines are the results from a model run at 30 K, but using a form of  $dp_2/dt$  that included  $k_c[\text{H}^+]$  terms (discussed below). The slow change in  $p_3$  represents its response to the changing value of  $p_2$ . Clearly, according to the low temperature model, temperature drives both the  $\text{H}_2$  and  $\text{H}_3^+$  enrichments. The predicted curves seem to indicate that the fraction  $p_3$  follows the fraction  $p_2$ . The  $p_2$  steady state value calculated by the model for 30 K closely matches the predicted thermal enrichment of *para*- $\text{H}_2$  for that temperature, 97%. The steady state value of 27.7% at 160 K does not match the thermally predicted value of 24.4%.

The simulation using the form of  $dp_2/dt$  that included the  $k_c[\text{H}^+]$  terms was run in order to test the effect of an abundance of  $\text{H}^+$  on the values of  $p_2$  and  $p_3$ . Although the  $k_c$  terms were neglected because of order of magnitude arguments, the test was run because protons are likely to have the strongest influence on  $p_2$  outside of reaction (6.1) in the interstellar medium. Recall that protons outnumber  $\text{H}_3^+$  ions in diffuse clouds, but are less abundant in dense clouds. The  $[\text{H}^+]$  was assumed to be one order of magnitude less than the  $[\text{H}_3^+]$ , much as is predicted for dense clouds. The inclusion of these terms decreased the overall  $p_2$  by  $\sim 4\%$ , with a greater decrease for  $p_3$ . There was an imperceptible change from the plotted results when running a simulation like this for the 160 K condition. Despite the influence of  $\text{H}^+$ , the reaction with  $\text{H}_3^+$  has a stronger, temperature dependent influence on the fraction of *para*- $\text{H}_2$ .

The process of deriving the models showed that the interactions of  $\text{H}_3^+$  and  $\text{H}_2$  are the primary

factors that govern the observables  $p_2$  and  $p_3$ . That is, experimental measurements in hydrogen plasmas can be used to obtain information about reaction (6.1), including the value of  $\alpha = k_H/k_E$ . The experiments in this work were designed to explore the relationship between  $p_2$  and  $p_3$  at low temperature, thereby obtaining information that will help shed light on the temperature regions where the two models are applicable, gain insight into the behavior of  $\alpha$  with temperature, and provide an understanding of how the spin modifications are affected.

## 6.2 Experiments

Two sets of experiments were performed to understand reaction (6.1), one set that consisted of measurements over a wide temperature range in the hollow cathode cell described in §4.2 and the other set in a supersonic expansion produced by the source described in §4.1. Each will be discussed in turn below.

### 6.2.1 Hollow cathode cell experiments

In order to better understand the ratio  $\alpha = k_{Hop}/k_{Exchange}$  as well as reaction (6.1) at astrophysical temperatures, the number densities of *para*- and *ortho*-H<sub>3</sub><sup>+</sup> were spectroscopically measured for different *para*-H<sub>2</sub> feed gas enrichments. The hollow cathode cell was used to generate plasmas over a wide range of temperatures (as described in Chapter 4); 310, 180, and 130 K. The experiments and results at each of these temperature conditions will be described below.

A 200  $\mu$ s, 1 kV discharge pulse was sent to the anode of the hollow cathode cell once every 5 seconds, generating the conditions described in §4.2.3. Direct absorption spectroscopy was performed using a White multipass arrangement as described in §3.3.2. The  $R(1,0)$  and  $R(1,1)^u$  transitions of *ortho*- and *para*-H<sub>3</sub><sup>+</sup> were measured separately by tuning DFG system I to one of the transition wavelengths, and measuring the intensity signal on a liquid nitrogen-cooled DC InSb detector both before and during the pulses. The resulting data from this arrangement were,

$$-\ln \frac{I_t}{I_o} = \alpha L, \quad (6.47)$$

where  $I_t$  is the transmitted intensity and  $I_o$  is the initial intensity. In all cases, the data analysis compared the ratios of different transitions (e.g.  $R(1,1)^u$  with  $R(1,0)$ ), therefore the length terms ( $L$ ) cancelled because the measurements were always taken over the same path length. It is important to emphasize that there are two separate  $\alpha$  being discussed in this chapter. One, just mentioned, describes the absorbance of mid-IR electromagnetic radiation, and the other is the ratio of the rate constants for the hop and exchange reactions. The difference between the two should be contextually clear throughout the chapter.

Measuring the  $R(1,0)$  and  $R(1,1)^u$  absorption peaks was accomplished by one of two methods. In the first method, the DFG was tuned to a starting frequency that was within .005 cm<sup>-1</sup> of the transition's center frequency. The operator would then initiate the locally-designed LabView code (B. Siller and B. Tom), which would acquire data for a total of 10 discharge pulses. After 10 measurements were collected, the data from the pulses were averaged by the acquisition routine and saved as a text file which was then imported into the IGOR application for further analysis.

Using IGOR, the absorption data were normalized by the initial intensity ( $I_o$ ) in equation (6.47), and plotted. The laser frequency was then incremented by 30 MHz ( $.001 \text{ cm}^{-1}$ ), and data from another 10 pulses would be collected and averaged. The center frequency was identified by the operator as the point where absorption was greatest after a series of points had been collected. This process would continue until  $\sim 3$  measurements had been taken at the center frequency. After the pulse data had been acquired for both the  $R(1,0)$  and  $R(1,1)^u$  transitions, the data were processed by another IGOR function in order to find the point in the pulse that was to be used for data analysis (see Figure 6.5). First, the function would select a maximum closest to the onset of an  $R(1,1)^u$  pulse and compare this with a point at the same time location in the  $R(1,0)$  pulse. The function would repeat the measurement between the  $R(1,1)^u$  and  $R(1,0)$  pulses, this time using the maximum of the  $R(1,0)$  peak as the comparison point.

The next step in the analysis was to correct the measured absorptions with their respective transition dipoles (see Table 1.5). This step was accomplished in order to approximate the number density of the *ortho* and *para* spin species,

$$\frac{\alpha}{|\mu|^2} \propto n. \quad (6.48)$$

These absorption data were used in the equation,

$$p_3 = \frac{[para-H_3^+]}{[total-H_3^+]} = \frac{\sum_i^{all\ para} n_i}{\sum_i^{all\ para} n_i + \sum_i^{all\ ortho} n_i}, \quad (6.49)$$

where the  $\sum_i^{all\ states} n_i$  come from applying the Boltzmann correction for a given temperature as in §5.2.1. The Boltzmann correction terms used in this chapter are tabulated in Appendix B. Although the temperature was measured over the entire discharge pulse as described in §4.2.3, it was only the temperature at the beginning of the pulse (near the point at which the pulse datum was taken) that was used to determine which Boltzmann correction term to use.

Finally, these results were averaged. With 2-3 measurements taken at the center frequency of the  $R(1,0)$  and  $R(1,1)^u$  transitions, there were 4-9 separate calculations of  $p_3$ . These  $p_3$  were then averaged to calculate an overall  $p_3$  for a measurement at a given *para*-H<sub>2</sub> enrichment ( $p_2$ ).

The second method used to collect data employed an automated scan, however, this method was only used in the 130 K experiments. In this method, the rate at which the laser was stepped was synchronized with the rate at which the digital delay generator triggered the discharge pulses in the hollow cathode cell. The rate of the scan was typically  $\sim 6 \text{ MHz s}^{-1}$ . During the course of the scan, the data acquisition software was programmed to select the pulse maximum much as the IGOR function did in the manual scanning method. The software then normalized and saved these results in a text file for later use. After the data were acquired for both  $R(1,0)$  and  $R(1,1)^u$ , the absorption maxima at the center frequencies of the scanned peaks were compared in the manner described above to find  $p_3$ .

As an added precaution with both methods, measurements were taken at the maximum near the beginning of the pulse because this is where the *para*-H<sub>2</sub> enrichment was most accurately known. The *para*-H<sub>2</sub> enrichment changes by dissociation of H<sub>2</sub> by electron impact, followed by atomic recombination on the cathode walls (as mentioned in §6.1.2). The dissociation takes place by way of

the highly efficient reaction,



in which dissociation occurs due to highly energetic electrons emitted from the cathode (40 eV) and secondary electrons ejected from  $\text{H}_2$  ionization events. The atomic H are then free to migrate to the cathode surface where they can recombine to form  $\text{H}_2$ . This results in the thermalization of the  $\text{H}_2$  population to a normal enrichment (3:1) because of the roughly 4.5 eV of energy that is released when H atoms recombine to form  $\text{H}_2$ . Any experiment in the hollow cathode cell involving *para*-enriched feed gas will exhibit a changing *para*- $\text{H}_2$  enrichment due to recombination on the walls. There were no measurements taken in this experiment to quantify the rate of *para*- $\text{H}_2$  conversion in the hollow cathode cell. As such, a model from [64] was used. This model describes an exponential decay,

$$[\textit{para} - \text{H}_2] = \left(1 - \frac{3}{4}(1 - e^{-t/\tau})\right) [\textit{para} - \text{H}_2]_0. \quad (6.51)$$

The time constant ( $\tau$ ) was calculated from observations made in [64], and is equal to 3.5 ms. In order to determine a ‘correction factor’ (equal to the term in front of the  $[\textit{para} - \text{H}_2]$  on the right hand side of equation (6.51)), it was necessary to determine the nominal time from plasma turn-on to measurement in this experiment. This time was measured for each of the collected samples, and is depicted in Figure 6.5. The average time ( $t$ ) was 48  $\mu\text{s}$ , which when used in equation (6.51) yields

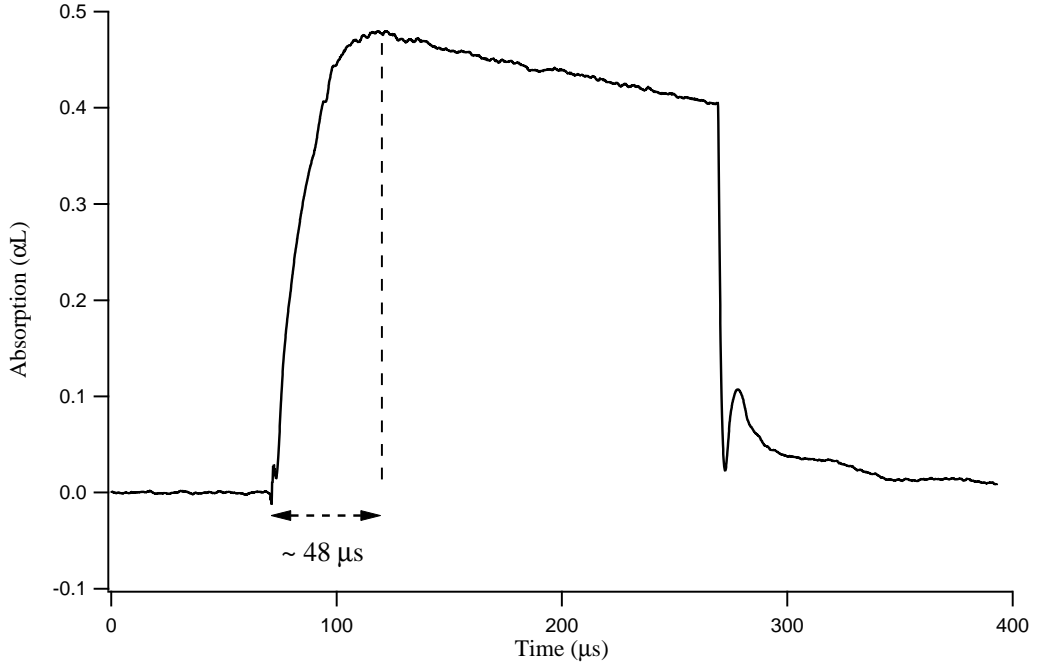


Figure 6.5: A typical discharge pulse; the nominal time from discharge turn-on to the measurement point is depicted.

a value of 0.9898. Each starting *para*- $\text{H}_2$  fraction was multiplied by this correction factor in order to account for the back conversion of *para*- $\text{H}_2$  due to recombination on the walls of the hollow cathode.

The rise time of the signal seen in Figure 6.5 can be attributed to two factors; the time it took for the plasma to fill the cathode, and the response time of the detector. The primary contributor was the detector response time, which was  $\sim 35 \mu\text{s}$ .

The water-cooled 310 K experiments were the first to be performed in this hollow cathode cell, with the intent of duplicating the results from [63, 64] that measured  $\alpha = k_H/k_E = 2.4$ . Averaged scan spectra, acquired using the manual method, are presented in Figure 6.6. Experimental evidence for the predicted nuclear spin selection rules is given by an increasing  $\textit{para}\text{-H}_3^+$  absorption and a decreasing  $\textit{ortho}\text{-H}_3^+$  absorption with higher enrichments of  $\textit{para}\text{-H}_2$ .

The results of the 310 K experiments are presented in Table 6.5, along with the values calculated for  $\alpha$  using equation (6.25). An  $\alpha$  was not calculated for the normal- $\text{H}_2$  (24.9%) plasma because

% $\textit{para}\text{-H}_2$	% $\textit{para}\text{-H}_3^+$	$\alpha$
$99.0 \pm 0.5$	$88.2 \pm 0.3$	$2.30 \pm 0.08$
$98.9 \pm 0.5$	$88.2 \pm 0.2$	$2.30 \pm 0.05$
$80.9 \pm 2.5$	$78.2 \pm 0.2$	$2.07 \pm 0.04$
$75.7 \pm 0.7$	$76.5 \pm 0.2$	$2.42 \pm 0.10$
$65.9 \pm 2.5$	$68.9 \pm 0.3$	$1.50 \pm 0.05$
$44.1 \pm 0.7$	$58.1 \pm 0.4$	$1.16 \pm 0.11$
25.1	$49.9 \pm 0.4$	-
$\alpha$ (average <sub>(<math>p_2=99\%,98.9\%,75.7\%</math>)</sub> )		$2.34 \pm 0.09$
$\alpha$ (high temp., best fit)		$2.15 \pm 0.15$

Table 6.5: The  $\textit{para}\text{-H}_3^+$  enrichment and  $\alpha$  calculated for different  $\textit{para}\text{-H}_2$  enrichments in the  $310 \pm 20$  K hollow cathode discharge. The average  $\alpha$  and the best fit  $\alpha$  for the high temperature model are also presented. The uncertainties are  $1 \sigma$ .

with this  $\textit{para}\text{-H}_2$  enrichment, any value of  $\alpha$  will form a plasma in which the  $\textit{para}\text{-}$  and  $\textit{ortho}\text{-H}_3^+$  populations are produced in a 1:1 ratio. As in Chapter 5, the  $p_3$  errors were calculated by combining the standard deviation of individual measurements with the standard deviation that arose from applying the Boltzmann correction over a range of  $\pm 20$  K. The  $\alpha$  errors were statistical, originating from the population of  $p_3$  values, or from the linear fit in the case of  $\alpha$  (high temp., best fit).

An analysis of variance test (ANOVA) was performed to determine if the  $\alpha$  listed in Table 6.5 came from the same population of data, which would mean that they could be averaged to find a single mean value for  $\alpha$ . The details for performing an ANOVA test are described in [141, pg. 558-565, Table 8]. In short, given a known number of populations that are each made up of a known number of samples, one can calculate if the populations are statistically consistent with having come from a single large population with a single mean. For the 310 K experiments, there were 6 separate populations of data representing 6 different  $\textit{para}\text{-H}_2$  enrichments, and there were 48 samples across all of these populations. The null hypothesis was that all populations had the same mean value for  $\alpha$  ( $H_o : \mu_{99.0\%} = \mu_{98.9\%} = \mu_{80.9\%} = \mu_{75.7\%} = \mu_{65.9\%} = \mu_{44.1\%}$ , where the  $\mu$  are the mean values of the  $\alpha$  populations) with the probability of a false positive being 0.01. The test failed, meaning that these populations did not comprise some larger population. Upon further analysis, the test indicated that  $\mu_{99.0\%} = \mu_{98.9\%} = \mu_{75.7\%} \neq \mu_{80.9\%} \neq \mu_{65.9\%} \neq \mu_{44.1\%}$ .

The  $\alpha$  calculated from the 80.9% enriched  $\textit{para}\text{-H}_2$  sample appeared to be an outlier because it

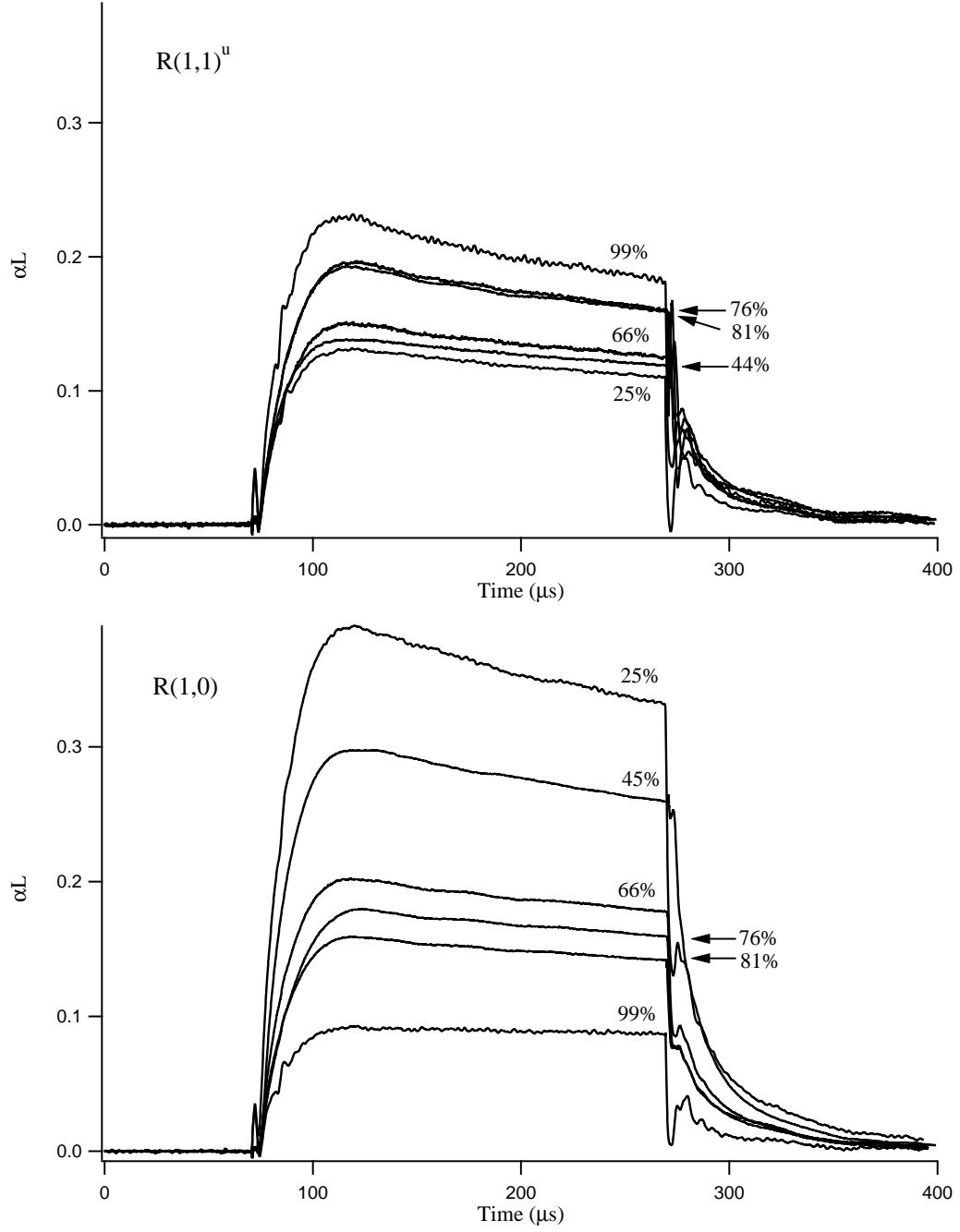


Figure 6.6:  $R(1,1)^u$  and  $R(1,0)$  absorption data taken in the hollow cathode at  $310 \pm 20$  K. The % labels indicate the  $para$ -H<sub>2</sub> enrichment of the feed gas.

was bounded by measurements that the ANOVA test indicated are part of the same population. Although there were no abnormal conditions noted at the time of the experiment, the apparent inversion with the 75.7%  $R(1,1)^u$  data, as can be seen in Figure 6.6, indicates the data may have

been inaccurate. However, another possible explanation was that the 75.7% enriched sample was the outlier. This sample was prepared as an  $\sim 80\%$  enriched sample, but thermal conductance indicated it was at 75.7% enrichment. If there was a mis-calibration between the thermal conductance and NMR methods at the time, and the *para*-H<sub>2</sub> enrichment was in reality closer to 80%, then the  $\alpha$  for this datum would actually be  $\sim 1.7$ .

In Figure 6.7 the measured fractions are plotted along with a line of best fit. The fit indicates that  $\alpha = 2.15 \pm .15$  based on all of the points taken at 310 K. This is influenced by the 66% and 44% enriched points which show a departure from linearity that might indicate behavior more in line with low temperature model predictions. It is interesting to note that the average  $\alpha$  as calculated from the higher enrichments is in good agreement with the  $\alpha$  measured with only highly enriched *para*-H<sub>2</sub> in [64], yet when the lower enriched points are taken into consideration, the measured  $\alpha$  is lower. The intermediate enrichment points may be indicating a departure from high temperature behavior, even at 310 K. There is insufficient data to be certain.

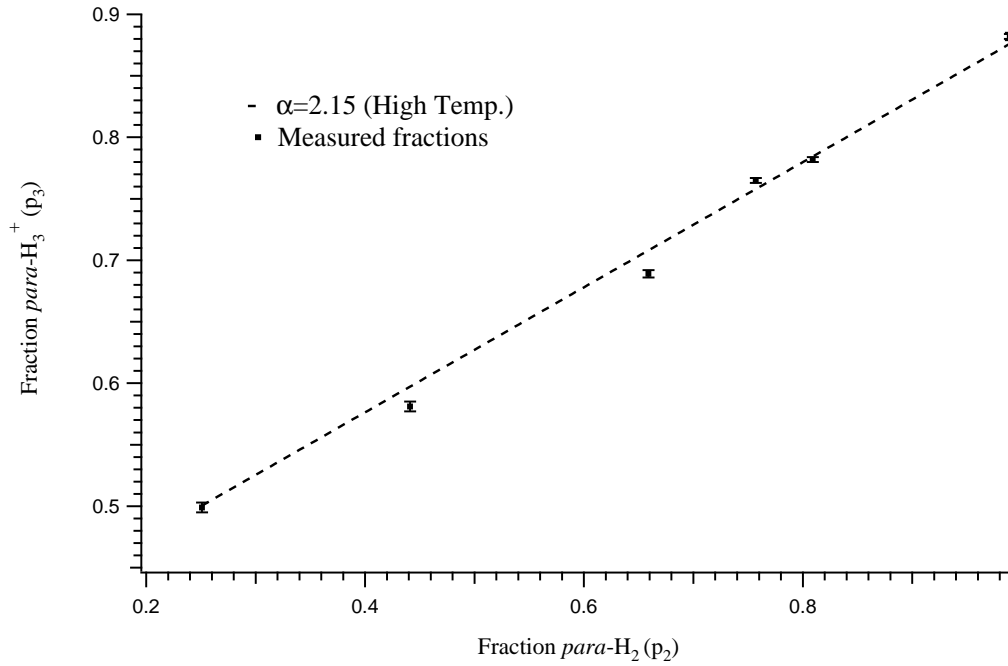


Figure 6.7: Measured *para*-H<sub>3</sub><sup>+</sup> enrichments at  $310 \pm 20$  K plotted along with a high temperature model for  $\alpha=2.15$ .

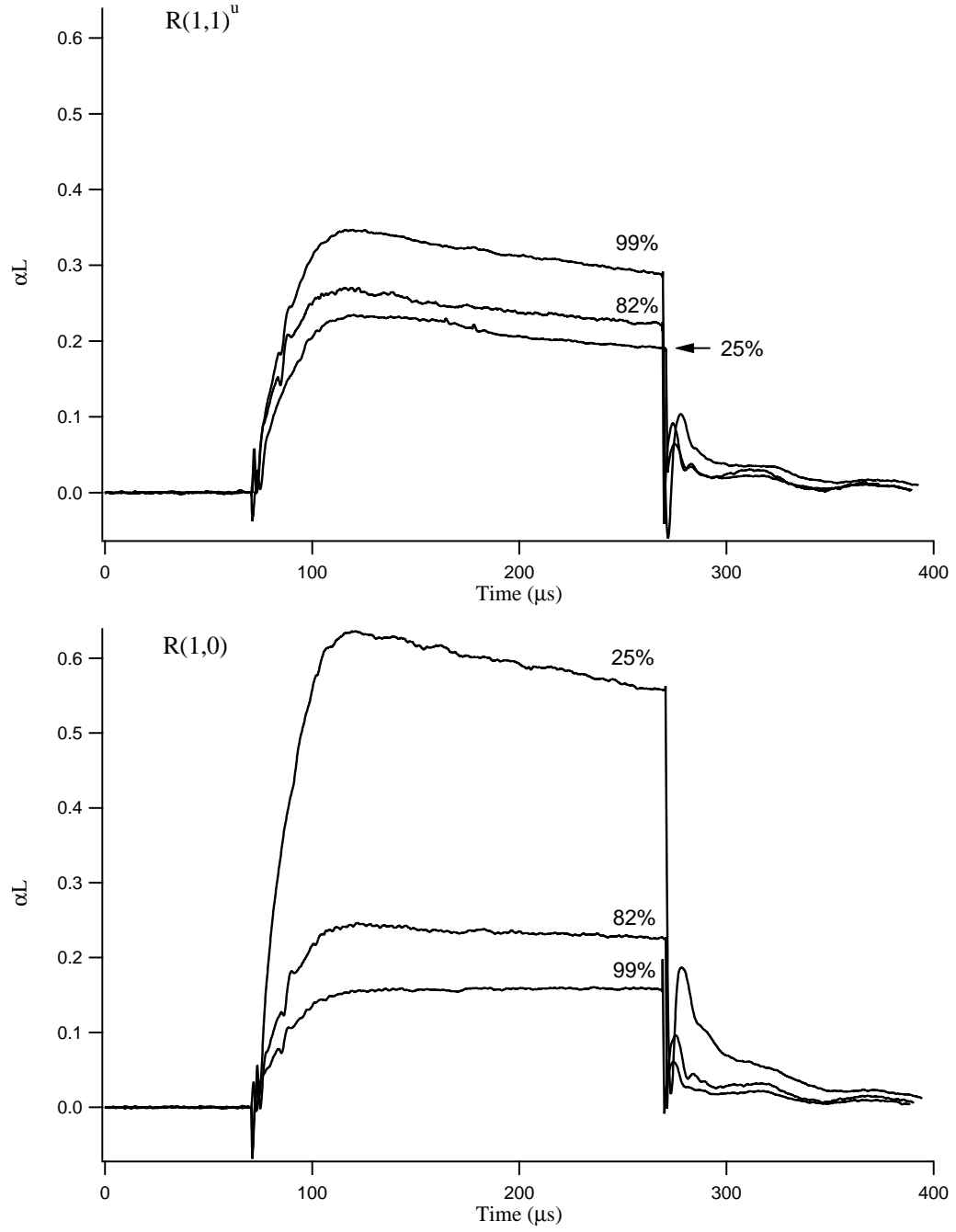


Figure 6.8:  $R(1,1)^u$  and  $R(1,0)$  absorption data taken in the hollow cathode at  $180 \pm 10$  K. The % labels indicate the  $\text{para-H}_2$  enrichment of the feed gas.



The data from the liquid nitrogen-cooled experiments were collected in the same fashion as those from the 310 K experiments. The o-ring seals began to leak at cryogenic temperatures, which limited the number of samples that were acquired. In addition, it wasn't until after the experiment was completed that data analysis indicated that measurements were taken in two separate temperature regimes. The two temperatures resulted from different cryogen flow rates, with the warmer temperatures occurring immediately after the liquid N<sub>2</sub> dewar had been re-filled. Most likely there hadn't been sufficient time for an adequate backing pressure to build. The first data to be discussed are those measured when the plasma temperature was  $180 \pm 10$  K.

The 180 K data included 99%, 82%, and 25% *para*-H<sub>2</sub> enriched test points. Averaged pulses are shown in Figure 6.8. It is interesting to observe that the overall absorption is increased with respect to the 310 K pulses (Figure 6.6) due to the decrease in Doppler broadening as well as the higher proportion of ions in the ground states. The results for  $p_3$  as well as  $\alpha$  are presented in Table 6.6, with the error calculations being the same as described for the 310 K results.

% <i>para</i> -H <sub>2</sub>	% <i>para</i> -H <sub>3</sub> <sup>+</sup>	$\alpha$
99.0 $\pm$ 0.5	86.0 $\pm$ 0.2	1.81 $\pm$ 0.03
81.5 $\pm$ 0.7	74.9 $\pm$ 0.3	1.30 $\pm$ 0.03
25.1	50.7 $\pm$ 0.4	-
$\alpha$ (high temp., best fit)		1.59 $\pm$ 0.19
$\alpha$ (low temp., best fit)		2.0

Table 6.6: The *para*-H<sub>3</sub><sup>+</sup> enrichment and  $\alpha$  calculated for different *para*-H<sub>2</sub> enrichments in the  $180 \pm 10$  K hollow cathode discharge. Best fit  $\alpha$ 's for high and low temperature models are also presented. The uncertainties are 1  $\sigma$ .

An ANOVA test was run for the  $\alpha$  values in this data set, and the result indicated that the  $\alpha$  are not from the same population. This was not surprising because the  $\alpha$  were calculated using equation (6.25) which is a high temperature model result. Figure 6.9 shows the measured data along side predicted results from both the low and high temperature models. The data appear to depart from the linear high temperature model, especially at the 82% enrichment point, and are best fit by the low temperature model run using 160 K and  $\alpha=2.0$  input parameters. Because the low temperature model is not optimized to run at 180 K, there is uncertainty in this value. Additionally, the experimental data and the low temperature model do not correlate for the normal-H<sub>2</sub> test point. Table 6.6 lists values for  $\alpha$  derived from a best fit for both the high and the low temperature models.

The data acquired at  $130 \pm 10$  K included test points at 99%, 90%, 75%, 64%, and normal *para*-H<sub>2</sub> enrichments. One 99% test point, as well as the 75% and normal test points were acquired using the scan acquisition technique described above. Figure 6.10 shows the pulses collected using the manual technique. Again, the intensity of the absorptions increased because of the colder temperatures, and can most easily be seen by comparing the 99% absorption between Figures 6.10 and 6.8.

Figure 6.11 shows the results from the scan technique. A comparison of the  $R(1,1)^u$  peaks in Figures 6.10 and 6.11 shows that there is an intensity difference between these points, with the scanned peak having a greater absorption intensity. This is most likely due to a temperature

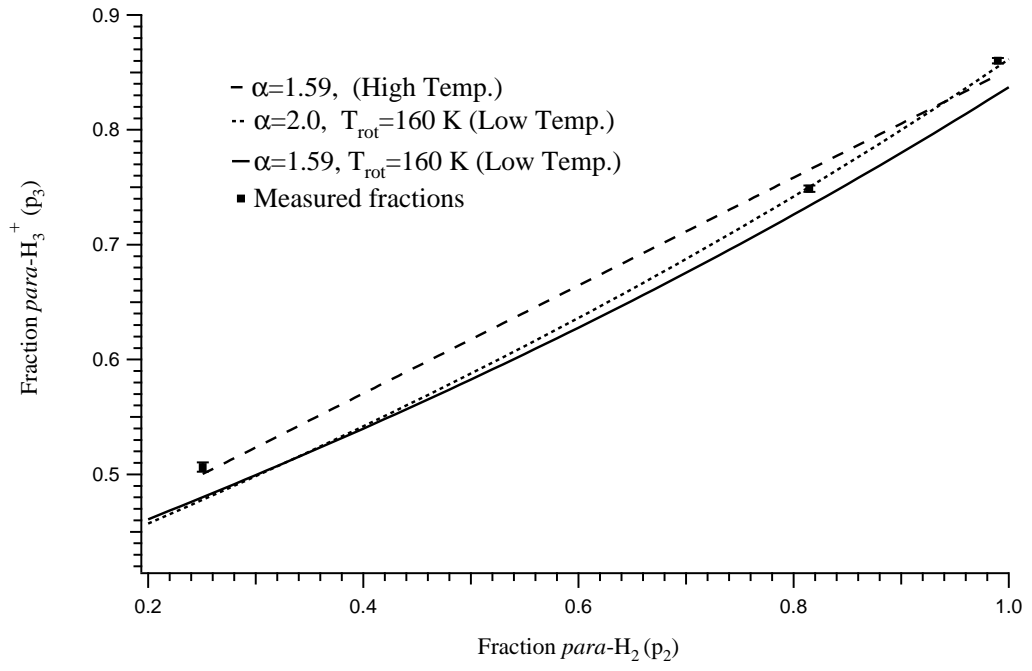


Figure 6.9: Measured  $\text{para-H}_3^+$  enrichments at  $180 \pm 10$  K plotted along with high and low temperature model results.

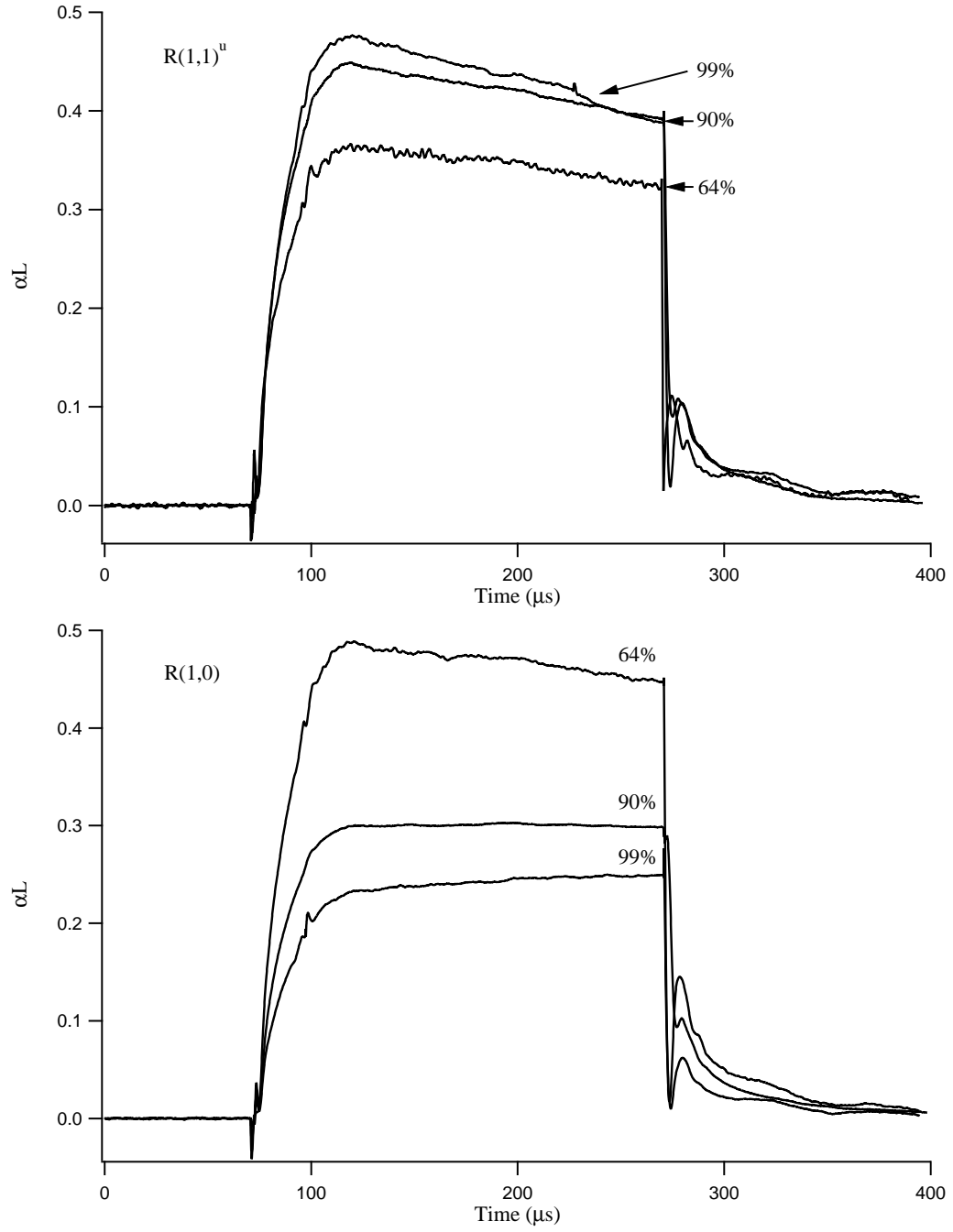


Figure 6.10:  $R(1,1)^u$  and  $R(1,0)$  absorption data taken in the hollow cathode at  $130 \pm 10$  K. The % labels indicate the  $para$ -H<sub>2</sub> enrichment of the feed gas.

difference between the two experiments (the peaks should have the same intensity if the temperatures are equivalent). The temperatures measured in the two experiments indicated that the data collected to make Figure 6.10 was from a plasma that was approximately 8 K warmer than the plasma from which the data in Figure 6.11 was collected. The effect of such a small temperature change should be negligible, however, the temperature measured in the former was a rotational temperature. As was seen in Chapter 4, the results of rotational temperature measurements in the hollow cathode have been questionable.

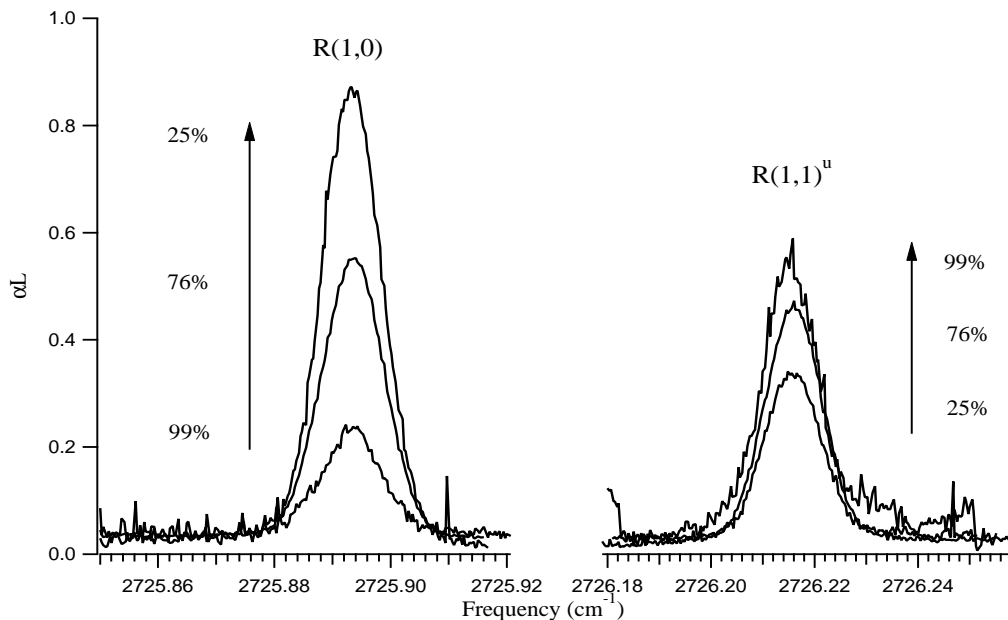


Figure 6.11:  $R(1,1)^u$  and  $R(1,0)$  absorption scan data taken in the hollow cathode at  $130 \pm 10$  K. The % indicate the *para*-H<sub>2</sub> enrichment of the feed gas.

As with the measurements taken at 310 K and 180 K, an ANOVA test was performed to determine if any of the  $\alpha$  could be averaged. The 99.0% and 98.9% data sets were the only data that passed the test, which in this case only served as a measure of the repeatability of the results. The data are plotted in Figure 6.12. The relationship between  $p_2$  and  $p_3$  is nonlinear, but the disparity between experiment and the low temperature model is even greater at this temperature than at 180 K. In order to match experiment and theory, the model was run using a temperature of 160 K and  $\alpha=1.70$ . There is a high level of confidence that the plasma temperature was  $130 \pm 10$  K, as this temperature was confirmed by both kinetic and excitation temperature measurements with normal-H<sub>2</sub>. The high temperature model should be less accurate under these conditions due to the thermodynamics, yet at the same time the low temperature model does not match the experimental results. The best fit  $\alpha$  from the high temperature model as well as the best fit from the low temperature model are listed in Table 6.7.

## 6.2.2 Expansion experiments

With the objective of measuring  $\alpha$  at even colder temperatures, experiments were carried out using the pulsed supersonic expansion source described in Chapter 4. In these experiments, the  $R(1,0)$

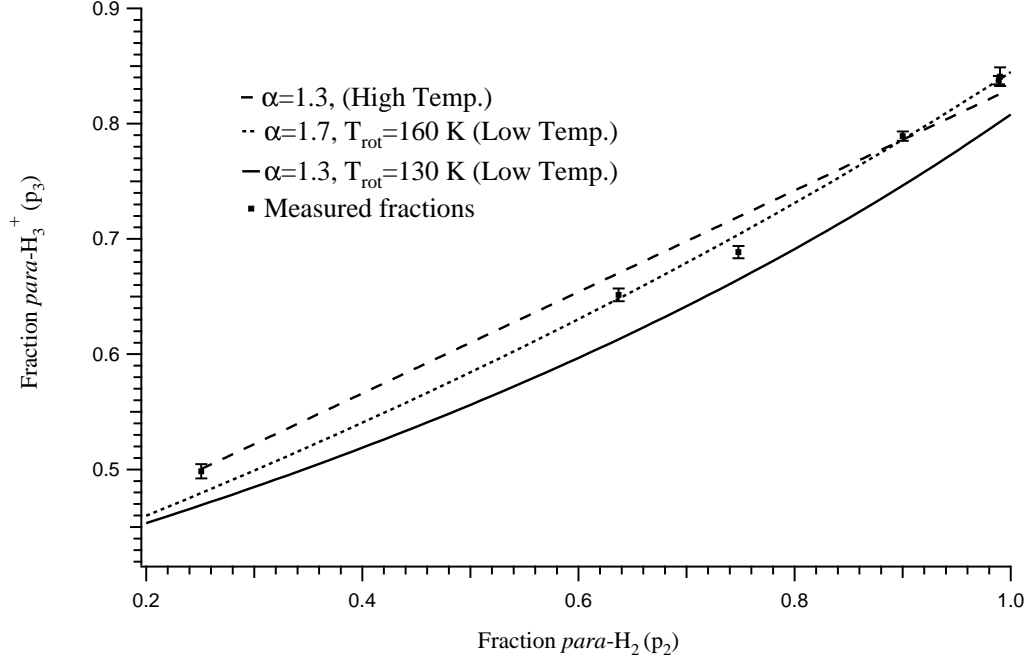


Figure 6.12: Measured  $\text{para-H}_3^+$  enrichments at  $130 \pm 10$  K plotted along with high and low temperature model results.

% $\text{para-H}_2$	% $\text{para-H}_3^+$	$\alpha$
$99.0 \pm 0.5$	$84.6 \pm 0.3$	$1.56 \pm 0.01$
$98.9 \pm 0.5$	$83.8 \pm 0.4$	$1.45 \pm 0.02$
$90.0 \pm 2.5$	$78.9 \pm 0.4$	$1.34 \pm 0.01$
$74.8 \pm 2.5$	$68.9 \pm 0.5$	$0.88 \pm 0.05$
$63.7 \pm 2.5$	$65.2 \pm 0.6$	$0.95 \pm 0.02$
25.1	$49.8 \pm 0.6$	-
$\alpha$ (high temp., best fit)		$1.30 \pm 0.12$
$\alpha$ (low temp., best fit)		1.70

Table 6.7: The  $\text{para-H}_3^+$  enrichment and  $\alpha$  calculated for different  $\text{para-H}_2$  enrichments in the  $130 \pm 10$  K hollow cathode discharge. Best fit  $\alpha$ 's for high and low temperature models are also presented. The uncertainties are  $1 \sigma$ .

and  $R(1,1)^u$  transitions were measured by cavity ringdown with DFG system I using different  $\text{para-H}_2$  enrichments. The data were collected in the manner described in §4.1.2, with a varying number of samples taken at each point (the data are listed in Appendix A). The peak heights were analyzed and compared in order to determine the  $\text{para-H}_3^+$  fraction. The samples that were tested included 99.99%, 97%, 90%, 75%, and 25% enriched  $\text{para-H}_2$ . A comparison of the averaged  $R(1,0)$  and  $R(1,1)^u$  spectra are presented in Figure 6.13. These spectra are normalized to the  $R(1,1)^u$  absorption peak. As predicted by both the hot and cold temperature models, and as observed in the hollow cathode experiments, the fraction of  $\text{para-H}_3^+$  increases with the enrichment of the  $\text{para-H}_2$ . These data were analyzed using the methods described in §5.2.1, and the results are presented in

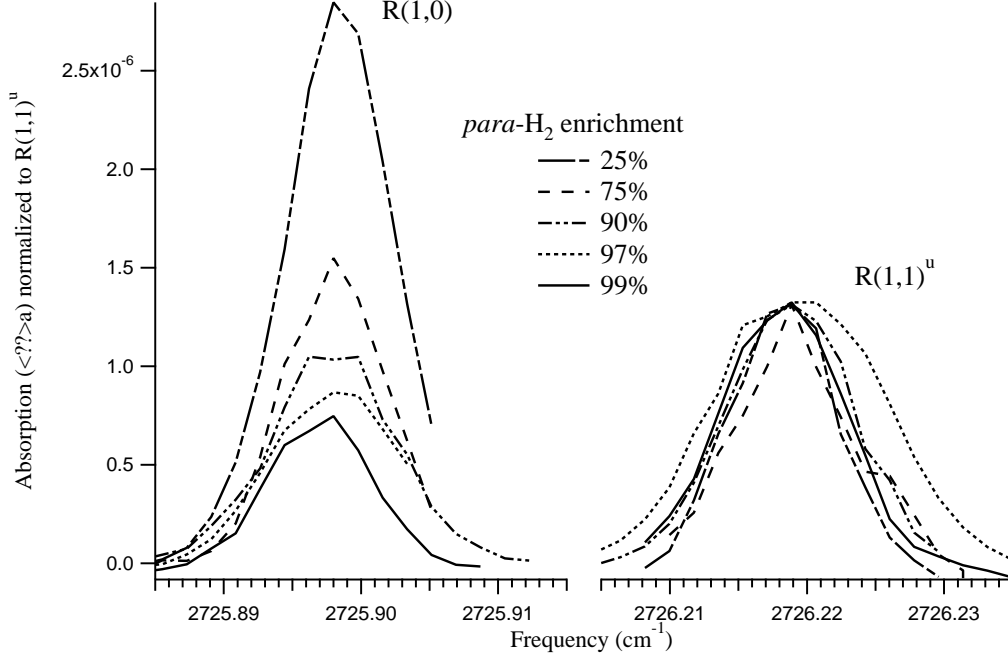


Figure 6.13: A comparison of  $R(1,0)$  and  $R(1,1)^u$  absorption peaks for various  $para\text{-H}_2$  enrichments.

Table 6.8, along with the  $\alpha = k_{Hop}/k_{Exchange}$  calculations.

% $para\text{-H}_2$	% $para\text{-H}_3^+$	$\alpha$
$99.9 \pm 0.8$	$78.5 \pm 2.2$	$0.89 \pm 0.19$
$97.0 \pm 0.8$	$74.7 \pm 2.1$	$0.71 \pm 0.15$
$90.0 \pm 0.8$	$72.7 \pm 2.6$	$0.73 \pm 0.21$
$75.0 \pm 0.8$	$70.6 \pm 14.1$	-
$25.0 \pm 0.8$	$49.1 \pm 2.4$	-
$\alpha$ (high temp., best fit)		$0.78 \pm 0.27$
$\alpha$ (low temp., best fit)		1.0

Table 6.8: The  $para\text{-H}_3^+$  enrichment and  $\alpha$  calculated for different  $para\text{-H}_2$  enrichments in the  $80 \pm 20$  K supersonic expansion. Best fit  $\alpha$ 's for high and low temperature models are also presented.

As with the hollow cathode experiments, the values for  $\alpha$  were inferred using equation (6.25) of the high temperature model, because the form of the output from the low temperature model does not lend itself to the derivation of such an equation. An  $\alpha$  was calculated for each feed gas enrichment, except in the case of measurements taken with the 75% enriched and the normal- $\text{H}_2$  feed gas. A value for  $\alpha$  was not calculated for the 75%  $para\text{-H}_2$  data because of the large uncertainty associated with this measurement, nor for the normal feed gas because normal  $\text{H}_2$  will always form a 1:1 ratio of *ortho* to  $para\text{-H}_3^+$  for any value of  $\alpha$ . The mean values of  $\alpha$  for each measurement along with the standard deviations were subject to an ANOVA test in which the null hypothesis was  $\mu_{99.9} = \mu_{97.0} = \mu_{90.0}$ . The null hypothesis was true with a 99% confidence level. It is likely that this

result was due to the large standard deviations associated with the expansion data set. The errors were larger in this experiment than in the hollow cathode experiment because of the pulse to pulse variability in the measurements.

With this statistical test indicating that the inferred values of  $\alpha$  were distributed about the same mean, an average  $\alpha$  was calculated from the 99.9%, 97%, and 90% *para*-enriched measurements. Thus, for  $80 \pm 20$  K,  $\alpha = k_{Hop}/k_{Exchange} \sim 0.78 \pm 0.27$ , a result which indicates that the exchange reaction is dominant in this low temperature regime. The results are plotted in Figure 6.14. A temperature of 130 K and  $\alpha=1.0$  were the input parameters to the low temperature model that provided the best fit to the experimental data.

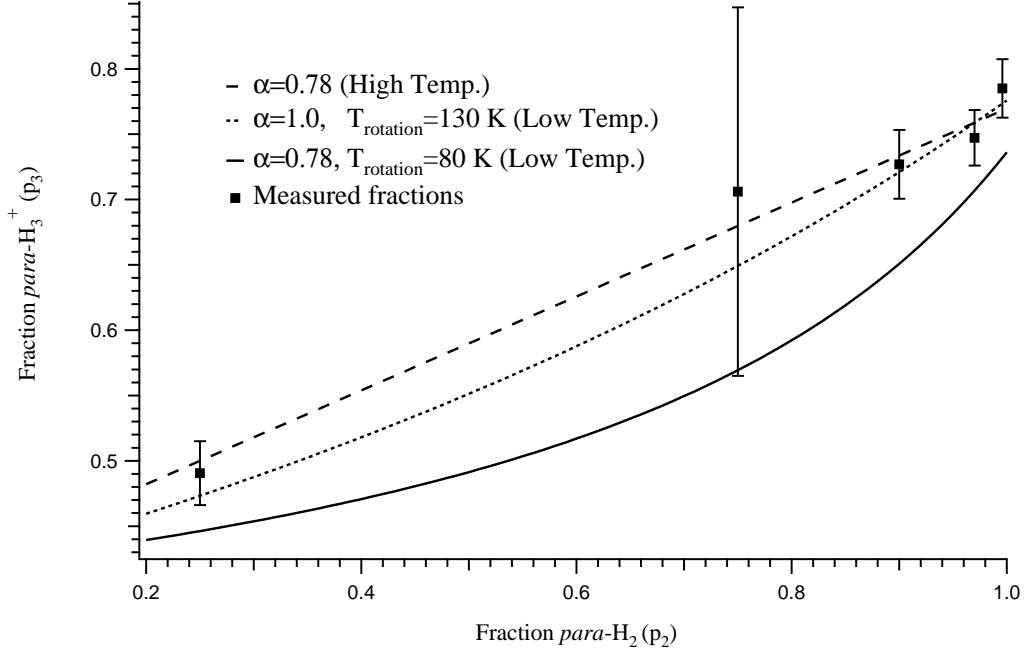


Figure 6.14: Measured  $para\text{-H}_3^+$  enrichments at  $80 \pm 20$  K plotted along with high and low temperature models.

### Dilution experiments

In addition to the measurements taken with pure samples of enriched *para*-H<sub>2</sub>, other experiments were performed with the expansion source in which the different enrichments were diluted in inert gas. The dilution measurements were performed in the hopes of increasing the *para*-H<sub>3</sub><sup>+</sup> enrichment for the dissociative recombination experiments. The gas was diluted by mixing a known pressure of H<sub>2</sub> with the inert gas to a target total pressure. For example, a 1% dilution of hydrogen was produced by diluting 20 mbar of hydrogen to a 2 bar total pressure of mixed gas. The results of the dilution experiments are listed in Table 6.9. As described in §6.1, the primary reason that a 100% enriched *para*-H<sub>3</sub><sup>+</sup> plasma was never observed is the result of the exchange reaction (6.12), and the hop reaction (6.11) once a sufficient quantity of *ortho*-H<sub>2</sub> has formed. By diluting the H<sub>2</sub> in an inert gas such as argon or neon, there is a reduction in the quantity [H<sub>2</sub>], which in turn reduces the occurrence of H<sub>3</sub><sup>+</sup>+H<sub>2</sub> collisions, effectively reducing the rate at which this conversion occurs. As can

Starting <i>para</i> -H <sub>2</sub> (%)	Percent H <sub>2</sub> in Ar	<i>para</i> -H <sub>3</sub> <sup>+</sup> (%)
25.0±0.8	100	49.1 ± 2.4
75.0±0.8	100	70.6 ± 14.1
	15	61.3 ± 3.2
	10	59.0 ± 2.6
	1	69.4 ± 2.7
90.0±0.8	100	72.7 ± 2.6
	10	68.6 ± 4.1
97.0±0.8	100	74.7 ± 2.1
	10	68.9 ± 2.2
	1	83.6 ± 1.9
99.9±0.8	100	78.5 ± 2.2
	15	78.0 ± 1.8
	5	70.9 ± 2.2
	0.8	83.3 ± 1.8

Table 6.9: The *para*-H<sub>3</sub><sup>+</sup> fraction over a range of *para*-H<sub>2</sub> enrichments and dilutions.

be seen from the table, the highest enrichment of *para*-H<sub>3</sub><sup>+</sup> was achieved with a 1% dilution of highly *para*-enriched H<sub>2</sub> gas. These data are displayed in Figure 6.15. The drop in the *para* enrichment at intermediate dilutions was a consistent result, but the reason for this depletion of *para*-H<sub>3</sub><sup>+</sup> is not understood at present.

A few samples were run with enriched *para*-H<sub>2</sub> diluted in neon instead of argon. When using a 10% dilution, the spectrum appeared much as it did when argon was the diluent, with comparable *para*-H<sub>3</sub><sup>+</sup> fractions. When diluted to 1%, however, the  $R(1,1)^u$  absorption was almost completely quenched. The reason for this loss of signal is not known, however, the possibility exists that hydrogen ions of greater mass were being formed. Macdonald and co-workers found that if a very dilute sample of hydrogen in neon ( $\sim 0.001\%$ ) was discharged and cooled to 128 K, the H<sub>5</sub><sup>+</sup> population became larger than that of the H<sub>3</sub><sup>+</sup> [114].

### 6.2.3 Future work

This work will benefit from added measurements in the hollow cathode cell and in an expansion. Additional data are needed at intermediate *para*-H<sub>2</sub> enrichments at both room and astrophysical temperatures in order to better characterize the relationship between  $p_2$  and  $p_3$ .

For the hollow cathode measurements, special attention must be given to the more mundane aspects of the experiment. For instance, the liquid N<sub>2</sub> dewar should be filled at least a day in advance in order to allow sufficient backing pressure to build. This will ensure a constant flow of cryogen that will result in a more consistent plasma temperature. In addition, the scanning method was found to be more efficient (and less operator-intensive) for data acquisition. The scanning method enables the simultaneous collection of peak height, number density (by peak integration), and kinetic temperature.

Additional expansion measurements should be performed using a cw expansion source versus a



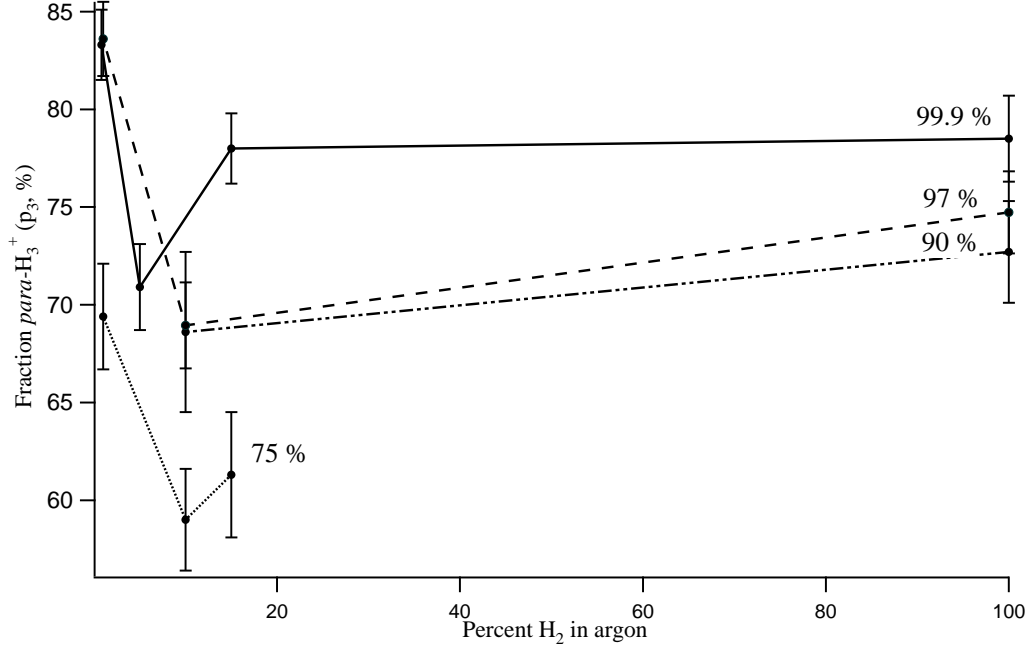


Figure 6.15: The fraction of  $para\text{-H}_3^+$  ( $p_3$ ) as a function of dilution in argon.

pulsed source. Use of a cw source will decrease errors in comparison to those of the pulsed source because there will be no pulse to pulse number density fluctuations, and arcing occurrences should be reduced. A cw expansion may also provide a decreased plasma temperature, enabling the exploration of conditions that more closely approximate those of dense clouds. Another method that can be used to explore reaction (6.1) at colder temperatures would involve the use of an ion trap as a source of cooled ions.

Finally, measurements that probe the effects of reaction (6.1) on the  $para\text{-H}_2$  enrichment ( $p_2$ ) are needed. DFG system II was designed to generate IR light in the range of  $\sim 2.1\text{-}5\ \mu\text{m}$ , which places the S(0) and S(1) quadrupole transitions of  $\text{H}_2$  ( $4497.84\ \text{cm}^{-1}$  and  $4712.91\ \text{cm}^{-1}$  [20]) within reach. The plasma source, however, will have to be carefully selected in order to obtain the extended path length needed to observe the weak quadrupole-allowed absorption features ( $|\mu|_{S(0)}^2 = 2.99 \times 10^{-11}\ \text{D}^2$  and  $|\mu|_{S(1)}^2 = 1.29 \times 10^{-11}\ \text{D}^2$  [142]), but at the same time reduce the number of reactions external to  $\text{H}_3^+ + \text{H}_2$  that can lead to changes in  $p_2$ . For example, the hollow cathode cell provides sufficient path length, however, the formation of  $\text{H}_2$  on the walls with the ratio  $ortho:para=3:1$  will prevent an accurate measurement of the relationship between  $p_2$  and  $p_3$ .

### 6.3 Analysis and astrophysical implications

These experiments improved our understanding of the underlying physics of the  $\text{H}_3^+ + \text{H}_2$  reaction, and provided information that will improve the interpretation of  $\text{H}_3^+$  and  $\text{H}_2$  observational data.

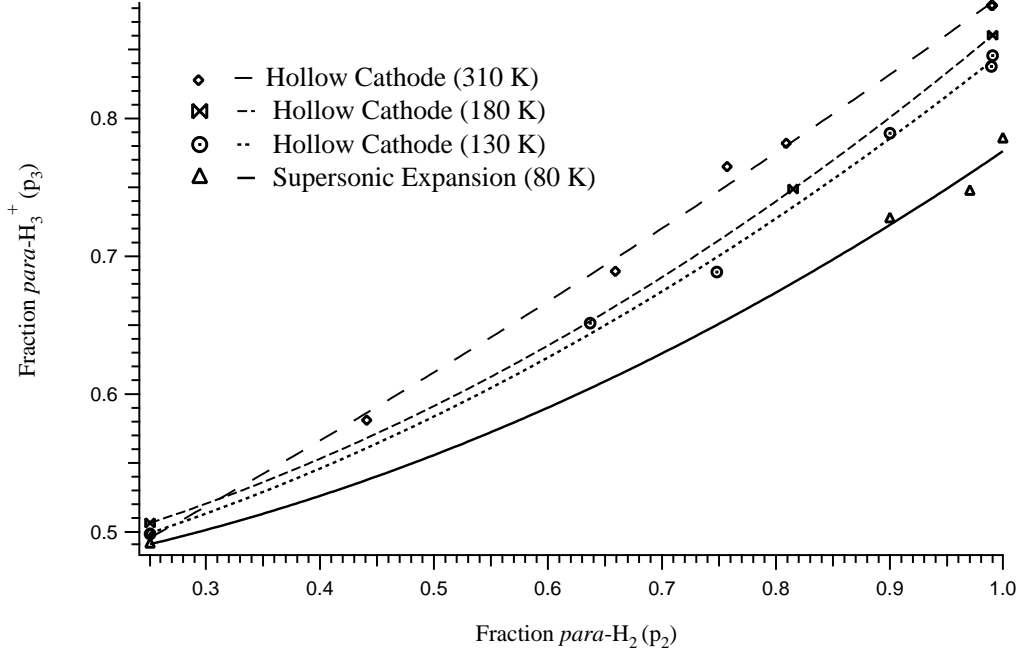


Figure 6.16: Data from the hollow cathode and expansion experiments, fit with 3rd order polynomials.

### 6.3.1 Comparison of experimental results and models

Both the high and low temperature models explain aspects of reaction (6.1), however, this work has shown that neither is sufficient for describing the reaction over all temperatures. At high temperatures (in this experiment  $>300$  K), the statistical approach appears to predict the relationship between the  $para\text{-H}_2$  and  $para\text{-H}_3^+$  enrichments, and can be used to infer a value for the ratio of the rate constants,  $k_{Hop}$  and  $k_{Exchange}$ . The data from the 310 K hollow cathode experiment supports the validity of this approach, because the entire set can be fit with a line calculated with this statistical model. The data set does include some outlying points, and further experiments at intermediate  $para\text{-H}_2$  enrichments would be useful in order to determine whether these results are due to experimental error, or if they actually represent a physical behavior of the system that is more accurately described by the quantum mechanical low temperature model. Figure 6.16 shows the different temperature data sets, each fit with a 3rd order polynomial. The fit for the 310 K data is very close to linear.

In contrast, the data taken at colder temperatures using the hollow cathode cell and the supersonic expansion sources indicate a departure from linearity. This departure is predicted by the low temperature model, and is likely the consequence of the increased role of quantum mechanical effects at cold temperatures [139]. In particular, this reflects the influence of the energetically unfavorable conversion of  $para\text{-H}_2$  to  $ortho\text{-H}_2$  on the  $ortho:para$  product distributions of reaction (6.1). Comparing experimental results and the low temperature model indicates that there are limitations with how the model implements temperature. Figures 6.9, 6.12, and 6.14 show that in colder plasmas, the model has to be run at higher temperatures if it is to replicate experimental results. This doesn't apply for the 180 K experiment because the model cannot predict the behavior of reaction (6.1) at

temperatures above 160 K. In the case of the 130 K data, the model must be run at 160 K in order to match experiment. For the 80 K data, the model must be run at 130 K. Limitations such as these call into question the accuracy of the values for  $\alpha$  predicted by the model. Nevertheless an equal, if not greater degree of uncertainty exists when using the high temperature statistical approach at cold temperatures. For these reasons, the  $\alpha$  in this work were calculated using both models.

Both the high and low temperature models show that the ratio  $\alpha = k_{Hop}/k_{Exchange}$  has a temperature dependence, with lower  $\alpha$  at lower temperatures. Using a phenomenological description, the hop reaction involves a single transfer of a proton from the former  $H_3^+$  component in the  $H_5^+$  intermediate to the  $H_2$  component. In contrast, the exchange reaction requires that an additional proton transfer occur from the  $H_2$  back to the  $H_3^+$ . Another way of looking at the exchange reaction is as a combination of two consecutive hops. Statistically speaking, the ratio between the hop and exchange reactions (the number of ways in which each can occur), is 3:6. This would translate to the number of times the hop and exchange pathways would be observed if the reaction were governed by statistics alone. Given the observed behavior of  $\alpha$ , the statistics appear to dominate at low temperature. Perhaps the lower temperature leads to a longer-lived  $H_5^+$  reaction intermediate in which more complete scrambling of the protons can occur.

A difference between the low temperature model and experimental results is apparent in the normal- $H_2$  data. In all cases, the model underpredicts the fraction of *para*- $H_3^+$  that was experimentally observed (see Figures 6.9, 6.12, and 6.14). The value of  $p_3$  in normal- $H_2$  plasmas also appears to be invariant over at least a 80-310 K temperature range. This behavior is predicted by the high temperature model (see Figure 6.2), and has important consequences for temperature measurement in hydrogenic plasmas, which will be discussed next.

### 6.3.2 Temperature

The concept of ‘excitation’ temperature was introduced in Chapter 4. In order to calculate an excitation temperature, the populations of the ground states of *ortho*- and *para*- $H_3^+$  are compared, the underlying assumption being that these two states are found in a ratio that results from thermalization between the spin modifications. As has been discussed, there is no such radiative or non-reactive collisional pathway for thermalization. In the interstellar medium, the excitation temperature is observed to be tens of degrees colder than temperatures measured by other means. Additional, more convincing evidence for this effect was found when calculating excitation temperatures for the different plasmas (differing by the enrichments of *para*- $H_2$ ) in this work. The excitation temperatures,  $T_{ex}$ , are calculated for each of the plasma conditions, and are presented in Tables 6.10 through 6.13.

The  $T_{ex}$  that are calculated for enriched *para*- $H_2$  plasmas consistently underestimate the temperature, however, the  $T_{ex}$  in normal- $H_2$  plasmas match the actual temperature (assuming the other methods used to calculate temperature for these plasmas were accurate). This can be understood by considering the previous assumptions that have gone into the calculation. Originally it was assumed that the calculation of excitation temperature was a comparison between the ground states alone, differing only by their energies and nuclear spin degeneracies. The familiar expression was,

$$\frac{n_{(1,0)}}{n_{(1,1)}} = \frac{g_{(1,0)} \text{ spin}}{g_{(1,1)} \text{ spin}} e^{-\Delta E_{(1,0)-(1,1)}/k_B T_{ex}}, \quad (6.52)$$

% <i>para</i> -H <sub>2</sub>	% <i>para</i> -H <sub>3</sub> <sup>+</sup>	T <sub>ex</sub> (K)
99.0 ± 0.5	88.2 ± 0.3	~15
98.9 ± 0.5	88.2 ± 0.2	~16
80.9 ± 2.5	78.2 ± 0.2	~24
75.7 ± 0.7	76.5 ± 0.2	~25
65.9 ± 2.5	68.9 ± 0.3	~37
44.1 ± 0.7	58.1 ± 0.4	~76
25.1	49.9 ± 0.4	~343

Table 6.10: The excitation temperature ( $T_{ex}$ ) calculated for different *para*-H<sub>2</sub> enrichments at 310 K.

% <i>para</i> -H <sub>2</sub>	% <i>para</i> -H <sub>3</sub> <sup>+</sup>	T <sub>ex</sub> (K)
99.0 ± 0.5	86.03 ± 0.23	~17
81.5 ± 0.7	74.87 ± 0.27	~26
25.1	50.65 ± 0.41	~179

Table 6.11: The excitation temperature ( $T_{ex}$ ) calculated for different *para*-H<sub>2</sub> enrichments at 180 K.

% <i>para</i> -H <sub>2</sub>	% <i>para</i> -H <sub>3</sub> <sup>+</sup>	T <sub>ex</sub> (K)
99.0 ± 0.5	84.56 ± 0.34	~17
98.9 ± 0.5	83.77 ± 0.36	~17
90.0 ± 2.5	78.92 ± 0.41	~21
74.8 ± 2.5	68.86 ± 0.53	~31
63.7 ± 2.5	65.15 ± 0.55	~37
25.1	49.84 ± 0.61	~130

Table 6.12: The excitation temperature ( $T_{ex}$ ) calculated for different *para*-H<sub>2</sub> enrichments at 130 K.

% <i>para</i> -H <sub>2</sub>	% <i>para</i> -H <sub>3</sub> <sup>+</sup>	T <sub>ex</sub> (K)
99.9 ± 0.8	78.5 ± 2.2	~19
97.0 ± 0.8	74.7 ± 2.1	~22
90.0 ± 0.8	72.7 ± 2.6	~23
75.0 ± 0.8	70.6 ± 14.1	~30
25.1 ± 0.8	49.1 ± 2.4	~80

Table 6.13: The excitation temperature ( $T_{ex}$ ) calculated for different *para*-H<sub>2</sub> enrichments at 80 K.

which contains a prefactor of 2 because  $g_{(1,0) \text{ spin}}/g_{(1,1) \text{ spin}} = 4/2 = 2$ . The physical reasons why this equation sometimes successfully predicted temperature were not well understood. As has been shown in this work, equation (6.52) is in fact only accurate for normal-H<sub>2</sub> plasmas.

A more physically accurate expression can be derived using equations that describe the fraction of the *para* and *ortho* spin modifications in the ground rotational states,

$$\frac{n_{(1,0)}}{n_{all \text{ ortho}}} = \frac{g_I g_J e^{-(E_{(1,0)} - E_0)/kT_{rot}}}{\sum_i g_I g_{J(i)} e^{-(E_i - E_0)/kT_{rot}}} = \frac{g_J e^{-(E_{(1,0)} - E_0)/kT_{rot}}}{\sum_i g_{J(i)} e^{-(E_i - E_0)/kT_{rot}}}, \quad (6.53)$$

$$\frac{n_{(1,1)}}{n_{all \text{ para}}} = \frac{g_I g_J e^{-(E_{(1,1)} - E_0)/kT_{rot}}}{\sum_i g_I g_{J(i)} e^{-(E_i - E_0)/kT_{rot}}} = \frac{g_J e^{-(E_{(1,1)} - E_0)/kT_{rot}}}{\sum_i g_{J(i)} e^{-(E_i - E_0)/kT_{rot}}}. \quad (6.54)$$

Notice that the spin degeneracy terms ( $g_I$ ) were eliminated by cancellation in equations (6.53) and (6.54). Adopting  $E_0 = E_{(1,1)}$  for both spin modifications, and dividing (6.53) by (6.54), it is possible to obtain a new expression for temperature,

$$\frac{n_{(1,0)}}{n_{(1,1)}} = \frac{n_{ortho}}{n_{para}} \left( e^{-(E_{(1,0)} - E_{(1,1)})/kT_{rot}} \right) \frac{\sum_i^{para} g_{J(i)} e^{-(E_i - E_{(1,1)})/kT_{rot}}}{\sum_i^{ortho} g_{J(i)} e^{-(E_i - E_{(1,1)})/kT_{rot}}}, \quad (6.55)$$

where  $n_{ortho}/n_{para} = (1 - p_3)/p_3$ . This term is the ratio of the total  $ortho\text{-H}_3^+$  and  $para\text{-H}_3^+$  number densities, and does not exist in the original equation for excitation temperature (6.52). The last term on the right hand side of equation (6.55) is the quotient of the partition functions for  $ortho$ - and  $para\text{-H}_3^+$ , each having been reduced by a factor of the nuclear spin degeneracies.

Temperature (K) =	20	40	55	75	100	150	250	350	450	550
$\frac{\sum_i^{para} g_{J(i)} e^{-(E_i - E_{(1,1)})/kT}}{\sum_i^{ortho} g_{J(i)} e^{-(E_i - E_{(1,1)})/kT}} =$	5.17	2.37	2.03	1.93	1.93	1.94	1.98	2.00	2.00	2.00

Table 6.14: The temperature dependence of the ratio  $g_{I(ortho)}Z_{para}/g_{I(para)}Z_{ortho}$ .

As can be seen in Table 6.14, this quotient of the modified partition functions is  $\sim 2$  when the temperature is above 55 K. When  $p_3=0.5$ , then  $n_{ortho}/n_{para} = (1 - p_3)/p_3 = 1$ , and equations (6.55) and (6.52) are equivalent. This is the case when normal- $\text{H}_2$  is used. When the  $para\text{-H}_3^+$  is enriched, then  $(1 - p_3)/p_3 \neq 1$ , and the two expressions are no longer equivalent. Equation (6.55) shows that an accurate expression for temperature isn't a comparison between the populations of the two spin modification ground states, as is done for the excitation temperature measurements. Rather, it is a comparison of the ground state proportions within each spin modification's rotational manifold that is physically relevant. The original equation (6.52) failed because it did not include the effect of changing  $para\text{-H}_3^+$  enrichments ( $p_3$ ), and it was comparing two populations that were not thermally connected.

The experiments in this work have demonstrated that  $p_3$  is greater than 0.5 whenever the  $para\text{-H}_2$  ( $p_2$ ) is enriched above the fraction found in normal- $\text{H}_2$ . This has been observed over a wide range of temperatures, including temperatures that are cold enough to represent astrophysical environments. This explains why temperatures in the diffuse interstellar medium, calculated using the (1,0) and (1,1) ground states of  $\text{H}_3^+$ , are typically colder than those measured by other means. As described in the introductory chapter, the  $para\text{-H}_2$  is enriched with respect to normal- $\text{H}_2$  in both diffuse and dense clouds, therefore, the  $\text{H}_3^+$  excitation temperature cannot be used as a proxy for rotational or kinetic temperature in these regions of space without considering the  $p_3$  enrichment.

Setting equations (6.55) and (6.52) equal to each other, using  $\Delta E_{(1,0)-(1,1)}/k_B = 32.86$  K, and solving for  $T_{ex}$  gives,

$$T_{ex} = \left[ \frac{1}{T_{rot}} - \frac{1}{32.86\text{K}} \ln \left( \frac{1 - p_3}{p_3} \right) \right]^{-1}, \quad (6.56)$$

if the temperature is above 55 K. Figure 6.17 shows that the relationship between the two measures of temperature is not a particularly useful one unless  $p_3 = 0.5$ . The higher the  $para\text{-H}_3^+$  enrichment the

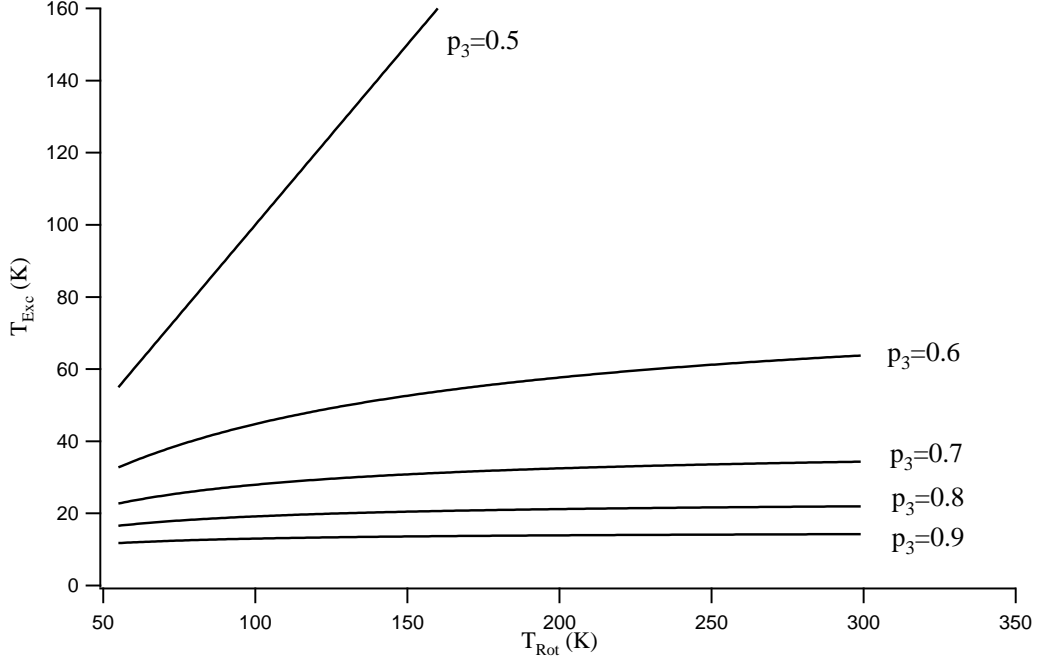


Figure 6.17:  $T_{ex}$  as a function of  $T_{Rot}$  for different  $para\text{-H}_3^+$  enrichments ( $p_3$ )

less sensitive the  $T_{ex}$  is as a measure of  $T_{rot}$ . The temperature independent, statistically-predicted property that normal- $\text{H}_2$  will generate a plasma in which  $p_3=0.5$  is beneficial for temperature measurement in laboratory plasmas, but the conditions under which a normal  $para\text{-H}_2$  enrichment will persist are unlikely to be found in the interstellar medium.

### 6.3.3 Astrophysical implications for the $\text{H}_3^+$ *ortho/para* ratio

The laboratory results show that the  $para\text{-H}_3^+$  enrichment has a strong and reproducible dependence on the  $para\text{-H}_2$  enrichment. The high and low temperature models indicate that this relationship does not lead to a thermalization between the  $\text{H}_3^+$  spin modifications, but rather to a steady state condition where the distribution of  $\text{H}_3^+$  spin modifications is driven by the enrichment of  $para\text{-H}_2$ . This conclusion has direct applicability to both diffuse and dense interstellar clouds, because  $\text{H}_2$  is highly abundant in both regimes.

Before any valid comparison can be made between the laboratory and astrophysical plasmas, however, it is important to confirm that the former accurately reflects the conditions of the latter. This was carried out in conjunction with the derivations in §6.1.2 and §6.1.3 for  $\text{H}_2$ , but will be accomplished here for  $\text{H}_3^+$ . The pressures found in diffuse and dense clouds are significantly lower than those of the laboratory plasmas described in this work, but the temperatures were close, at least for the diffuse cloud case. Despite the pressure differences, the constituent makeup should be similar. According to equations (6.13) and (6.14), the only reactants outside of  $\text{H}_2$  and  $\text{H}_3^+$  that play a significant role in  $dp_3/dt$  are  $\text{H}_2^+$  and electrons. The abundance of  $\text{H}_2^+$  has been measured mass spectrometrically in the expansion source in this experiment to be 3 orders of magnitude less than  $\text{H}_3^+$ . This is largely due to the high number density of neutral  $\text{H}_2$ , which quickly reacts with

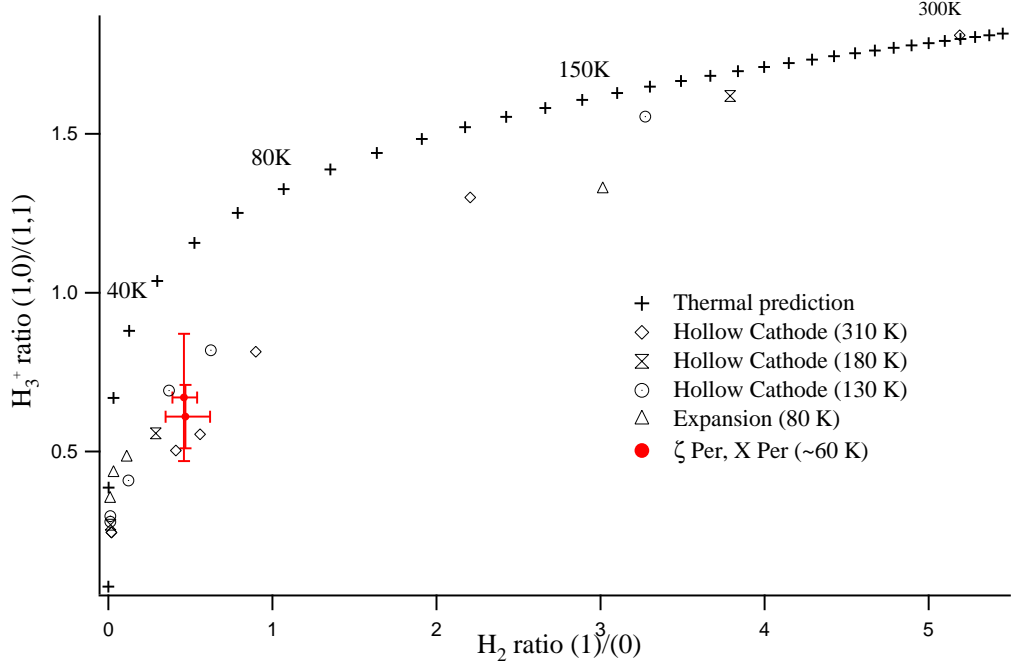


Figure 6.18: A comparison of laboratory and astronomically observed ratios of *ortho* and *para* ground states of  $\text{H}_3^+$  and  $\text{H}_2$ .

the  $\text{H}_2^+$  to form  $\text{H}_3^+$ . The same is true in the interstellar medium given the abundance of neutral  $\text{H}_2$ . The number density of electrons is estimated to be  $\sim 1 \times 10^{-2} \text{ cm}^{-3}$  in diffuse clouds, which means that a typical  $\text{H}_3^+$  will undergo hundreds of collisions with  $\text{H}_2$  before it is destroyed by a dissociative recombination collision with an electron [36]. The primary destructive pathway for  $\text{H}_3^+$  in dense clouds is by reaction with CO, and the lifetime of the ion is even longer as a result of the rate coefficient  $k_{\text{CO}}$ , which is 2 orders of magnitude smaller than the dissociative recombination rate  $k_r$  [36]. Therefore the comparison of laboratory measurements and the interstellar medium for  $\text{H}_3^+$  is valid, with  $\text{H}_2$  being the molecule with which  $\text{H}_3^+$  interacts most frequently. Although it has been assumed by others that the  $\text{H}_3^+ + \text{H}_2$  reaction drives the spin modification steady state of  $\text{H}_3^+$ , it has not been verified in the laboratory under astrophysical temperature conditions.

Figure 6.18 plots the ground state ratio of *ortho* to *para*  $\text{H}_3^+$  and  $\text{H}_2$ , measured in the hollow cathode and expansion experiments ( $J = 1$  for *ortho*- $\text{H}_2$ , and  $J = 0$  for *para*- $\text{H}_2$ ). The data are presented without the Boltzmann corrections so that the laboratory results can be compared directly with astronomical observations without any assumptions regarding temperature. This figure also plots the hypothetical thermal ratios that would exist for both species if the spin modifications were actually thermalized (+). It is clear that the  $\text{H}_3^+$  spin modifications are not distributed thermodynamically, and the separation between the data points obtained at different temperatures would make it difficult to use such a plot to infer temperature in interstellar clouds. Nevertheless, it is evident that the relationship between  $\text{H}_2$  and  $\text{H}_3^+$  ground state enrichments obtained from the X Persei and  $\zeta$  Persei observations correlate well with the data obtained in these experiments. This is direct evidence that the  $\text{H}_3^+ + \text{H}_2$  reaction is driving the distribution of  $\text{H}_3^+$  spin modifications in these diffuse interstellar clouds.

### 6.3.4 Astrophysical implications for the $\text{H}_2$ *ortho*/*para* ratio

The distribution of  $\text{H}_2$  spin modifications will reflect the thermal conditions in which the  $\text{H}_2$  was formed, or it will reflect the conditions under which subsequent thermalizing reactions take place. In diffuse clouds, the  $\text{H}_2$  is thermalized by reactions with  $\text{H}^+$ , which is more abundant than  $\text{H}_3^+$  by four orders of magnitude [43]. The product distributions of the  $\text{H}_2 + \text{H}^+$  reaction will be dictated by thermal conditions. On the other hand in dense clouds, the thermalization of  $\text{H}_2$  must occur by way of reactions with  $\text{H}_3^+$  which is more abundant than  $\text{H}^+$  [136], and which possesses an order of magnitude faster rate constant (for  $\text{H}^+ + \text{H}_2$ ,  $k \sim 2 \times 10^{-10}$ , [8]).

The high and low temperature  $dp_2/dt$  were developed solely to predict the outcome of the  $\text{H}_3^+ + \text{H}_2$  reaction in the context of astrophysical environments because the means to measure the *para*- $\text{H}_2$  enrichment in the laboratory were not available for this work. As was shown in §6.1.2 and §6.1.3, the reaction of  $\text{H}_2$  with  $\text{H}_3^+$  can drive the *para* enrichment of  $\text{H}_2$ , and has a dependence on temperature, however, the high and low temperature models predict different outcomes. For the high temperature model there is no temperature dependence outside of  $\alpha$ , which governs the rate at which steady state is reached, and the steady state is always a normal- $\text{H}_2$  enrichment. In contrast, the low temperature model predicts that the steady state enrichment will be close to a thermal distribution, where thermalization is achieved by reactions with  $\text{H}_3^+$ . The experimental data show trends that indicate the relevance of the low temperature model, especially the nonlinear relationship between  $p_3$  and  $p_2$  at cold temperatures. The time-dependent results of this model for  $\text{H}_2$  thus present the tantalizing prospect that the  $\text{H}_3^+ + \text{H}_2$  reaction is the thermalization pathway for *para*- $\text{H}_2$  in dense interstellar clouds.

With the insight gained through this work comes the potential for increased applicability of the hydrogen spin modifications as astrophysical probes. The data that describes the relationship between  $p_2$  and  $p_3$  will enable theorists to improve models for the  $\text{H}_3^+ + \text{H}_2$  reaction at cold, astrophysical temperatures. This in turn will lead to an improved ability to understand the temperature dependence of the hop and exchange reaction rates, which will ultimately enable the prediction of the  $\text{H}_3^+$  and  $\text{H}_2$  spin modification distributions at different temperatures. As can be seen in Figure 6.18, the correlation between experimental results and astronomical observation already indicates that the results of this work can be used to predict the *para*- $\text{H}_2$  enrichment from observed  $\text{H}_3^+$  ground states. These results are important for the astrochemist because the deuterium chemistry in the interstellar medium has a strong dependence on the level of *ortho*- $\text{H}_2$  enrichment. The reaction that drives the deuteration of  $\text{H}_3^+$  will proceed more rapidly with lower fractions of *ortho*- $\text{H}_2$  [45]. As discussed in the introduction,  $\text{H}_3^+$  is the precursor molecule to many of the heavier constituents of the interstellar medium, therefore, knowing the rate at which it is deuterated will impact our understanding of the deuterium chemistry for a much wider range of molecular species.



# Chapter 7

## References

- [1] E. Anders and N. Grevesse, *Geochim. et Cosmochim. Acta*, **53**, 197 (1989).
- [2] T. Oka, *PNAS* **103**, 12235 (2006).
- [3] A. J. Dempster, *Phil. Mag.* **31**, 438 (1916).
- [4] W. D. Watson, *Astrophys. J.* **183**, L17 (1973).
- [5] E. Herbst and W. Klemperer, *Astrophys. J.* **185**, 505 (1973).
- [6] B. J. McCall, *Spectroscopy of  $H_3^+$  in Laboratory and Astrophysical Plasmas*, Ph.D. Thesis, University of Chicago, (2001).
- [7] J. C. Raich and R. H. Good, *Astrophys. J.* **139**, 1004 (1964).
- [8] D. Gerlich, *J. Chem. Phys.* **92**, 2377 (1990).
- [9] E. Wigner, *Z. f. Phys. Chem.* **23**, 28 (1933).
- [10] W. Heisenberg, *Z. f. Physik* **41**, 239 (1927).
- [11] F. Hund, *Z. f. Physik* **42**, 93 (1927).
- [12] K. F. Bonhoeffer and P. Hartek, *Naturwiss.* **17**, 182 (1929).
- [13] K. F. Bonhoeffer and P. Hartek, *Z. Phys. Chem.* **B4**, 113 (1929).
- [14] P. F. Bernath, *Spectra of Atoms and Molecules, 2nd Ed.*, Oxford Univ. Press, New York (2005).
- [15] D. M. Bishop, *Group Theory and Chemistry*, Dover Publications, Inc., New York (1973).
- [16] P. R. Bunker and P. Jensen, *Molecular Symmetry and Spectroscopy, 2nd Ed.*, NRC Research Press, Ottawa (1998).
- [17] J. M. Shull, J. Tumlinson, E. B. Jenkins, H. W. Moos, B. L. Rachford, B. D. Savage, K. R. Sembach, T. P. Snow, G. Sonneborn, D. G. York, W. P. Blair, J. C. Green, S. D. Friedman, and D. J. Sahnou, *Astrophys. J.* **538**, L73 (2000).
- [18] S. I. B. Cartledge, G. C. Clayton, K. D. Gordon, B. L. Rachford, B. T. Draine, P. G. Martin, J. S. Mathis, K. A. Misselt, U. J. Sofia, D. C. B. Whittet, and M. J. Wolff, *Astrophys. J.* **630**, 355 (2005).
- [19] Y. Sheffer, M. Rogers, S. R. Federman, N. P. Abel, R. Gredel, D. L. Lambert, and G. Shaw, *arXiv:0807.0940v1* (2008).
- [20] J. H. Lacy, R. Knacke, T. R. Geballe, and T. Tokunaga, *Astrophys. J.* **428**, L69 (1994).
- [21] J. J. Thomson, *Phil. Mag.* **21**, 225 (1911).
- [22] T. R. Hogness and E. G. Lunn, *Phys. Rev.* **26**, 44 (1925).

- [23] T. Oka, Phys. Rev. Lett. **45**, 531 (1980).
- [24] C. M. Lindsay and B. J. McCall, J. Mol. Spec. **210**, 60 (2001).
- [25] A. R. W. McKellar and J. K. G. Watson, J. Mol. Spec. **191**, 215 (1998).
- [26] M. Goto, B. J. McCall, T. R. Geballe, T. Usuda, N. Kobayashi, H. Terada, and T. Oka, PASJ **54**, 951 (2002).
- [27] D. W. Martin, E. W. McDaniel, and M. L. Meeks, Astrophys. J. **134**, 1012 (1961).
- [28] T. R. Geballe and T. Oka, Nature **384**, 334 (1996).
- [29] B. J. McCall, T. R. Geballe, K. H. Hinkle, and T. Oka, Science **279**, 1910 (1998).
- [30] J. H. Black, E. F. van Dishoeck, S. P. Willner, and R. C. Woods, Astrophys. J. **358**, 459 (1990).
- [31] T. R. Geballe, B. J. McCall, K. H. Hinkle, and T. Oka, Astrophys. J. **510**, 251 (1999).
- [32] B. J. McCall, K. H. Hinkle, T. R. Geballe, and T. Oka, Faraday Disc. **109**, 267 (1998).
- [33] B. J. McCall, T. R. Geballe, K. H. Hinkle, and T. Oka, Astrophys. J. **522**, 338 (1999).
- [34] B. J. McCall, A. J. Huneycutt, R. J. Saykally, T. R. Geballe, N. Djuric, G. H. Dunn, J. Semaniak, O. Novotny, A. Al-Khalili, A. Ehlerding, F. Hellberg, S. Kalhori, A. Neau, R. Thomas, F. Österdahl, and M. Larsson, Nature **422**, 500 (2003).
- [35] N. Indriolo, T. R. Geballe, T. Oka, and B. J. McCall, Astrophys. J. **671**, 1736 (2007).
- [36] T. Oka and E. Epp, Astrophys. J. **613**, 349 (2004).
- [37] T. Oka, in *Dissociative Recombination of Molecular Ions with Electrons*, edited by S. L. Guberman, Kluwer Academic/Plenum Publishers, New York (2003).
- [38] C. A. Kulesa, *Molecular Hydrogen and its Ions in Dark Interstellar Clouds and Star Forming Regions*, Ph.D. Thesis, University of Arizona (2002).
- [39] P. Sonnentrucker, D. E. Welty, J. A. Thorburn, and D. G. York, Astrophys. J. **168**, 58 (2007).
- [40] D. Wilgenbus, S. Cabrit, G. Pineau des Forêts, and D. Flower, in *Molecular Hydrogen in Space*, edited by F. Combes and G. Pineau des Forêts, Cambridge University Press, New York (2000).
- [41] S. Ramsay Howat, A. Chysostomou, P. Brand, M. Burton, and P. Puxley, in *Molecular Hydrogen in Space*, edited by F. Combes and G. Pineau des Forêts, Cambridge University Press, New York (2000).
- [42] L. Pagani, C. Vastel, E. Hugo, V. Kokoouline, C. H. Greene, A. Bacmann, E. Bayet, C. Ceccarelli, R. Peng, and S. Schlemmer, Astr. and Astrophys. **494**, 623 (2009).
- [43] G. Shaw, G. L. Ferland, R. Srianand, N. P. Abel, P. A. M. van Hoof, and P. C. Stancil, Astrophys. J. **675**, 405 (2008).
- [44] T. R. Geballe and T. Oka, Astrophys. J. **342**, 855 (1989).
- [45] D. Gerlich, E. Herbst, E. Roueff, Plan. Space Sci. **50**, 1275 (2002).
- [46] I. F. Silvera, Rev. Mod. Phys. **52**, 393 (1980).
- [47] K. G. Petzinger and D. J. Scalapino, Phys. Rev. B **8**, 266 (1973).
- [48] E. Ilisca, Phys. Rev. Lett. **24**, 797 (1970).
- [49] B. F. Minaev and H. Ågren, J. Phys. Chem. **99**, 8936 (1995).

- [50] Y. Y. Milenko, R. M. Sibileva, and M. A. Strzhemechny, *J. Low Temp. Phys.* **107**, 77 (1997).
- [51] H.-H. Limbach, G. Buntowsky, J. Matthes, S. Gründemann, T. Pery, B. Walaszek, and B. Chaudret, *Chem. Phys. Chem.* **7**, 551 (2006).
- [52] G. Buntkowsky, B. Walaszek, A. Adamczyk, Y. Xu, H.-H. Limbach, and B. Chaudret, *Phys. Chem. Chem. Phys.*, **8**, 1929 (2006).
- [53] S. B. Duckett and C. J. Sleigh, *J. Prog. in NMR* **34**, 71 (1998).
- [54] T. Momose and T. Shida, *Bull. Chem. Soc. Jpn.* **71**, 1 (1998).
- [55] L. Andrews and X. Wang, *Rev. Sci. Inst.* **75**, 3039 (2004).
- [56] M. E. Fajardo and S. Tam, *J. Chem. Phys.* **108**, 4237 (1998).
- [57] Y-P. Lee, Y-J. Wu, and J. T. Hougen, *J. Chem. Phys.* **129**, 104502 (2008).
- [58] A. C. Clark, X. Lin, and M. H. W. Chan, *Phys. Rev. Lett.* **97**, 245301 (2006).
- [59] H. Kreckel, M. Motsch, J. Mikosch, J. Glosík, R. Plašil, S. Altevogt, V. Andrianarijaona, H. Buhr, J. Hoffmann, L. Lammich, M. Lestinsky, I. Nevo, S. Novotny, D. A. Orlov, H. B. Pedersen, F. Sprenger, A. S. Terekhov, J. Toker, R. Wester, D. Gerlich, D. Schwalm, A. Wolf, and D. Zajfman, *Phys. Rev. Lett.* **95**, 263201 (2005).
- [60] H. Kreckel, A. Petrigani, M. Berg, D. Bing, S. Reinhardt, S. Altevogt, H. Buhr, M. Froese, J. Hoffmann, B. Jordon-Thaden, C. Krantz, M. Lestinsky, M. Mendes, O. Novotny, S. Novotny, H. B. Pedersen, D. A. Orlov, J. Mikosch, R. Wester, R. Plašil, J. Glosík, D. Schwalm, D. Zajfman, and A. Wolf, *J. Phys.: Conf. Ser.* **88**, 012064 (2007).
- [61] A. Petrigani, H. Kreckel, M. H. Berg, S. Altevogt, D. Bing, H. Buhr, M. Froese, J. Hoffmann, B. Jordon-Thaden, C. Krantz, M. B. Mendes, O. Novotný, S. Novotny, D. A. Orlov, S. Reinhardt, and A. Wolf, *arXiv: 0810.0405* (2008).
- [62] B. A. Tom, V. Zhaunerchyk, M. B. Wiczer, A. A. Mills, K. N. Crabtree, M. Kaminska, W. D. Geppert, M. Hamberg, M. af Ugglas, E. Vigren, W. J. van der Zande, M. Larsson, R. D. Thomas, and B. J. McCall, *J. Chem. Phys.* **130**, 031101 (2009).
- [63] D. Uy, M. Cordonnier, and T. Oka, *Phys. Rev. Lett.* **78**, 3844 (1997).
- [64] M. Cordonnier, D. Uy, R. M. Dickson, K. E. Kerr, Y. Zhang, and T. Oka, *J. Chem. Phys.* **113**, 3181 (2000).
- [65] S. B. Duckett, C. L. Newell, and R. Eisenberg, *J. Am. Chem. Soc.* **116**, 10548 (1994).
- [66] S. Tam and M. Fajardo, *Rev. Sci. Inst.* **70**, 1926 (1999).
- [67] S. O. Kasap, *Principles of Electronic Materials and Devices, 2nd Ed.*, McGraw Hill, (2002).
- [68] A. Farkas, *Orthohydrogen, Parahydrogen, and Heavy Hydrogen*, Cambridge Univ. Press, London (1935).
- [69] A. T. Stewart and G. L. Squires, *J. Scientific Inst.* **32**, 26 (1955).
- [70] M. J. Assael, M. Dix, A. Lucas, and W. A. Wakeham, *J. Chem. Soc.: Faraday Trans. 1* **77**, 439 (1981).
- [71] C. Szántay, Jr., *Trends in Analytical. Chem.* **11**, 332 (1992).
- [72] W. Koechner, *Solid-State Laser Engineering, 5th Ed.*, Springer-Verlag, New York (1999).
- [73] A. W. Tucker, M. Birnbaum, C. L. Fincher, and J. W. Erler, *J. Appl. Phys.* **48**, 4907 (1977).

- [74] R. A. Fields, M. Birnbaum, and C. L. Fincher, Appl. Phys. Lett. **51**, 1885 (1987).
- [75] J. R. O'Connor, Appl. Phys. Lett. **9**, 407 (1966).
- [76] P. F. Moulton, J. Opt. Soc. Am. B **3**, 125 (1986).
- [77] *Matisse User's Guide Ver. 1.8*, Sirah Laser und Plasmatechnik, GmbH (2009).
- [78] *AO Device Set Up Instructions Ver. 1*, Brimrose Corp. of America, (2008).
- [79] A. S. Pine, J. Opt. Soc. Am. **64**, 1683 (1974).
- [80] G. D'Amico, G. Pesce, G. Rusciano, and A. Sasso, Opt. Las. Eng. **37**, 481 (2002).
- [81] C. Fischer and M. W. Sigrist, in *Solid-State Mid-Infrared Laser Sources*, edited by I. T. Sorokina and K. L. Vodopyanov, Springer-Verlag, Berlin (2003).
- [82] K. P. Petrov, S. Waltman, E. J. Dlugokencky, M. Arbore, M. M. Fejer, F. K. Tittel, and L. W. Hollberg, App. Phys. B. **64**, 567 (1997).
- [83] L. Deng, L. Han, W. Liang, Z. Cao, C. Xu, W. Zhang, Z. Gong, and X. Gao, Opt. Las. in Eng. **45**, 1055 (2007).
- [84] W.-P. Deng, B. Gao, C.-F. Cheng, G.-S. Cheng, S.-M. Hu, and Q.-S. Zhu, Rev. Sci. Inst. **79**, 123101 (2008).
- [85] D. H. Jundt, Opt. Lett. **22**, 1553 (1997).
- [86] F. P. Schäfer, in *Topics in Applied Physics: Dye Lasers, V.1*, edited by F. P. Schäfer, Springer-Verlag, Berlin (1977).
- [87] *Coherent 899-21 Dye Ring Laser User's Manual, Section II*, Coherent Laser Group.
- [88] S. M. Kostritskii, O. G. Sevostyanov, M. Aillerie, and P. Bourson, J. App. Phys. **104**, 114104 (2008).
- [89] O. F. Schirmer, O. Thiemann, and M. Wöhlecke, J. Phys. Chem. Solids **52**, 185 (1991).
- [90] A. O'Keefe and D. A. G. Deacon, Rev. Sci. Inst. **59**, 2544 (1988).
- [91] K. W. Busch and M. A. Busch, *Cavity-Ringdown Spectroscopy*, Oxford University Press (1999).
- [92] D. Romanini, A. A. Kachanov, N. Sadeghi, and F. Stoeckel, Chem. Phys. Lett. **264**, 316 (1997).
- [93] S. L. Widicus Weaver, M. B. Wiczer, B. Negru, J. P. DiGangi, B. A. Tom, and B. J. McCall, J. Mol. Spec. **249**, 14 (2008).
- [94] J. U. White, J. Opt. Soc. Am. **32**, 285 (1942).
- [95] B. J. McCall, A. J. Huneycutt, R. J. Saykally, N. Djuric, G. H. Dunn, J. Semaniak, O. Novotny, A. Al-Khalili, A. Ehlerding, F. Hellberg, S. Kalhori, A. Neau, R. D. Thomas, A. Paal, F. Österdahl, and M. Larsson, Phys. Rev. A **70**, 052716 (2004).
- [96] P. Birza, T. Motylewski, D. Khoroshev, A. Chirokolava, H. Linnartz, and J.P. Maier, Chem. Phys. **283**, 119 (2002).
- [97] C. E. Klotz, J. Chem. Phys. **72**, 192 (1980).
- [98] R. Campargue, J. Phys. Chem. **88**, 4466 (1984).
- [99] G. Scoles, D. Bassi, U. Buck, and D. C. Laine, Eds. *Atomic and Molecular Beam Methods: Vol 1*, Oxford University Press, (1988).

- [100] F. C. van den Heuvel and A. Dymanus, Chem. Phys. Lett. **92**, 219 (1982).
- [101] S. C. Foster, A. R. W. McKellar, and T. J. Sears, J. Chem. Phys. **81**, 578 (1984).
- [102] T. Amano, J. Opt. Soc. Am. B **2**, 790 (1985).
- [103] B. A. McGuire, *Design and Implementation of a Liquid Nitrogen-Cooled Hollow Cathode Discharge Source for the Study of the Reaction  $H_3^+ + H_2 \rightarrow H_2 + H_3^+$  at Astronomically Relevant Temperatures*, Senior Thesis, University of Illinois at Urbana-Champaign, (2009).
- [104] J. Verberne, I. Ozier, L. Zandee, and J. Reuss, Mol. Phys. **35**, 1649 (1978).
- [105] P. Vankan, D. C. Schram, and R. Engeln, J. Chem. Phys. **121**, 9876 (2004).
- [106] K. Koura, Phys. Fluids **24**, 583 (1981).
- [107] T. Amano, J. Chem. Phys. **92**, 6492 (1990).
- [108] A. von Engel, *Ionized Gases*, reprint edition, AIP Press, Woodbury, New York (1994).
- [109] D. Proch and T. Trickl, Rev. Sci. Instr. **60**, 713 (1989).
- [110] M. Larsson, Phil. Trans. R. Soc. A **358**, 2433 (2000).
- [111] M. Larsson, B. J. McCall, and A. E. Orel, Chem. Phys. Lett. **462**, 145 (2008).
- [112] M. A. Biondi and S. C. Brown, Phys. Rev. **76**, 1697 (1949).
- [113] B. Peart and K. T. Dolder, J. Phys. B. **7**, 1948 (1974).
- [114] J. A. MacDonald, M. A. Biondi, and R. Johnsen, Planet Space Sci. **32**, 651 (1984).
- [115] T. Amano, Ap. J. **329**, L121 (1988).
- [116] M. Larsson, H. Danared, J. R. Mowat, P. Sigra, G. Sundström, L. Broström, A. Filevich, A. Källberg, S. Mannervik, K. G. Rensfelt, and S. Datz, Phys. Rev. Lett. **70**, 430 (1993).
- [117] V. Kokoouline, C. H. Greene, and B. D. Esry, Nature **412**, 891 (2001).
- [118] V. Kokoouline and C. H. Greene, Phys. Rev. A. **68**, 012703 (2003).
- [119] S. F. dos Santos, V. Kokoouline, and C. H. Greene, J. Chem. Phys. **127**, 124309 (2007).
- [120] S. L. Guberman, editor, *Dissociative Recombination of Molecular Ions with Electrons*, Kluwer Academic/Plenum Publishers, New York (2003).
- [121] S. Datz, G. Sundström, Ch. Biedermann, L. Broström, H. Danared, S. Mannervik, J. R. Mowat, and M. Larsson, Phys. Rev. Lett. **74**, 896 (1995).
- [122] D. R. Bates, Phys. Rev. **78**, 492 (1950).
- [123] J. B. A. Mitchell, Phys. Lett. **186**, 215 (1990).
- [124] J. N. Bardsley, J. Phys. B. **1**, 365 (1968).
- [125] A. Neau, *Dissociative Processes of Relevance in Low Temperature Plasmas*, Ph.D. Thesis, University of Stockholm (2002).
- [126] V. Zhaunerchyk, *Dynamics in the Dissociative Recombination of Small Polyatomic Molecular Ions*, Ph.D. Thesis, University of Stockholm (2008).
- [127] H. Kreckel, S. Krohn, L. Lammich, M. Lange, J. Levin, M. Scheffel, D. Schwalm, J. Tennyson, Z. Vager, R. Wester, A. Wolf, and D. Zajfman, Phys. Rev. A. **66**, 052509 (2002).

- [128] J. R. Mowat, H. Danared, G. Sundström, M. Carlson, L. H. Andersen, L. Vejby-Christensen, M. af Ugglas, and M. Larsson, *Phys. Rev. Lett.* **74**, 50 (1995).
- [129] A. Dalgarno, in *Molecular Hydrogen in Space*, edited by F. Combes and G. Pineau des Forêts, Cambridge University Press, New York (2000).
- [130] M. Quack, *Mol. Phys.* **34**, 477 (1977).
- [131] T. Oka, *J. Mol. Spec.* **228**, 635 (2004).
- [132] D. Gerlich, *J. Chem. Soc. Faraday Trans.* **89**, 2199 (1993).
- [133] L. D. Landau and E. M. Lifshitz, *Quantum Mechanics, Vol. 3, 3rd Ed.*, Butterworth Heine-  
mann (2003).
- [134] M. Saporoschenko, *Phys. Rev.* **139**, A349 (1965).
- [135] D. L. Albritton, T. M. Miller, D. W. Martin, and E. W. McDaniel, *Phys. Rev.* **171**, 94 (1968).
- [136] H.- H. Lee, R. P. A. Bettens, and E. Herbst, *Astron. and Astrophys. Supp.* **119**, 111 (1996).
- [137] S. C. O. Glover, *Astrophys. J.* **584**, 331 (2003).
- [138] P. F. Goldsmith, D. Li, and M. Krčo, *Astrophys. J.* **654**, 273 (2007).
- [139] K. Park and J. C. Light, *J. Chem. Phys.* **126**, 044305 (2007).
- [140] I. Takagi, H. Hashimoto, H. Fujita, and K. Higashi, *Fus. and Eng. Des.* **41**, 73 (1998).
- [141] R. L. Ott and W. Mendenhall, *Understanding Statistics*, Duxbury Press, Belmont (1994).
- [142] J. Turner, K. Kirby-Docken, and A. Dalgarno, *Astrophys. J.* **35**, 281 (1977).

# Appendix A

## Spectroscopic data

The first 6 tables in this appendix contain data from the expansion experiments. The upper section of each table presents the data from the *ortho* and *para* measurements, progressing from raw, to Gaussian fit, to current-corrected, to current-corrected Gaussian fit peak heights. The lower section of each table shows the respective *para*-H<sub>3</sub><sup>+</sup> fractions ( $p_3$ ), as well as the  $p_3$  calculated from Boltzmann-corrected data.

Hollow cathode cell  $p_3$  and (1,0)/(1,1) data are presented in the remaining tables of the appendix. The method by which the data were obtained is described in Chapter 6. Multiple  $p_3$  were calculated for each condition by comparing all  $R(1, 0)$  and  $R(1, 1)^u$  measurements for that condition.

Sample	$R(1,1)^u$ Absorbance ( $\text{cm}^{-1}$ )			$R(1,0)$ Absorbance ( $\text{cm}^{-1}$ )		
	Raw	Gaussian	Normalized	Raw	Gaussian	Normalized
1	5.35E-07	5.84E-07	9.60E-07	1.42E-06	1.42E-06	2.36E-06
2	5.35E-07	5.84E-07	9.60E-07	1.49E-06	1.50E-06	2.43E-06
3	8.99E-07	9.10E-07	1.63E-06	1.92E-06	1.97E-06	3.50E-06
4	8.51E-07	9.34E-07	1.47E-06	1.92E-06	1.97E-06	3.50E-06
5	8.51E-07	9.34E-07	1.47E-06	1.94E-06	1.90E-06	3.36E-06

Fraction  $para\text{-H}_3^+$  (%);  $\mu^2$ -corrected.

Sample	Un-Normalized		Un-Normalized Gaussian	Normalized	Normalized Gaussian	Boltzmann Corrected
1	38.18	40.27		39.60	41.71	47.81
2	37.05	38.96		39.60	41.00	47.08
3	43.42	43.09		43.36	43.89	50.03
4	42.08	43.73		40.84	43.74	49.88
5	41.83	44.62		40.78	44.75	50.90

Average	40.51	42.13	40.84	43.01	49.14
Standard Deviation	2.74	2.41	1.54	1.59	1.62

Table A.1: Expansion data for normal- $\text{H}_2$  ( $80 \pm 20$  K). This is representative data, there were many more normal- $\text{H}_2$  measurements.



Sample	$R(1,1)^u$ Absorbance ( $\text{cm}^{-1}$ )			$R(1,0)$ Absorbance ( $\text{cm}^{-1}$ )		
	Raw	Gaussian	Normalized	Raw	Gaussian	Normalized
1	9.29E-07	9.45E-07	1.34E-06	1.39E-06	5.77E-07	6.40E-07
2	1.07E-06	1.09E-06	1.30E-06	1.35E-06	6.17E-07	6.41E-07
3	9.22E-07	-	1.35E-06	-	5.83E-07	8.11E-07
Fraction $para\text{-H}_3^+$ (%); $\mu^2$ -corrected.						
Sample	Un-Normalized			Normalized		
	Un-Normalized	Un-Normalized	Normalized	Un-Normalized	Normalized	Corrected
1	72.52	70.76	76.33	75.24	79.55	
2	73.98	73.60	72.36	72.80	77.41	
3	72.16	-	73.18	-	-	
Average	72.89	72.18	73.96	74.02	78.48	
Standard Deviation	0.96	2.00	2.10	1.73	1.52	

Table A.2: Expansion data for 99% enriched  $para\text{-H}_2$  ( $80 \pm 20$  K). Data for sample 3 could not be fit with a Gaussian curve.

Sample	$R(1,1)^u$ Absorbance ( $\text{cm}^{-1}$ )			$R(1,0)$ Absorbance ( $\text{cm}^{-1}$ )		
	Raw	Gaussian	Normalized	Raw	Gaussian	Normalized
1	1.88E-06	2.06E-06	3.62E-07	1.56E-06	1.68E-06	3.15E-07
2	2.06E-06	2.27E-06	4.09E-07	1.56E-06	1.68E-06	3.15E-07
3	2.23E-06	2.35E-06	3.83E-07	1.58E-06	1.68E-06	2.60E-07

Fraction  $para\text{-H}_3^+$  (%);  $\mu^2$ -corrected.

Sample	Un-Normalized	Un-Normalized	Normalized	Normalized	Boltzmann
1	66.39	66.78	65.32	68.48	73.56
2	68.40	68.90	68.03	70.53	75.39
3	69.82	69.63	70.72	70.37	75.25

Average	68.20	68.44	68.02	69.79	74.73
Standard Deviation	1.72	1.48	2.70	1.14	1.02

Table A.3: Expansion data for 97% enriched  $para\text{-H}_2$  ( $80 \pm 20$  K).

Sample	$R(1,1)^u$ Absorbance ( $\text{cm}^{-1}$ )			$R(1,0)$ Absorbance ( $\text{cm}^{-1}$ )		
	Raw	Gaussian	Normalized	Normalized	Raw	Normalized
1	9.06E-07	9.32E-07	1.14E-07	1.20E-07	3.89E-07	3.55E-07
2	9.06E-07	9.32E-07	1.14E-07	1.20E-07	4.05E-07	3.89E-07
3	9.06E-07	9.32E-07	1.14E-07	1.20E-07	4.76E-07	4.46E-07
4	1.14E-06	9.88E-07	1.40E-07	1.30E-07	3.78E-07	4.28E-07
5	1.03E-06	9.72E-07	1.27E-07	1.21E-07	3.78E-07	4.28E-07
6	1.02E-06	1.16E-06	1.22E-07	1.51E-07	4.34E-07	4.59E-07
7	1.12E-06	1.18E-06	1.38E-07	1.45E-07	4.34E-07	4.59E-07

Fraction  $para\text{-H}_3^+$  (%);  $\mu^2$ -corrected.

Sample	Fraction $para\text{-H}_3^+$ (%); $\mu^2$ -corrected.			Boltzmann Corrected		
	Un-Normalized	Un-Normalized	Normalized	Normalized	Normalized	Normalized
1	79.24	81.14	80.18	81.72	85.13	85.13
2	78.57	79.71	77.55	79.90	83.57	83.57
3	75.73	77.40	76.25	77.66	81.65	81.65
4	83.18	79.10	82.94	79.54	83.27	83.27
5	81.71	78.83	81.52	78.35	82.25	82.25
6	79.39	80.56	78.99	81.39	84.85	84.85
7	80.88	80.82	80.96	80.77	84.32	84.32

Average	79.81	79.65	79.77	79.9	83.6
Standard Deviation	2.41	1.32	2.33	1.52	1.30

Table A.4: Expansion data for a 1% dilution of 97% enriched  $para\text{-H}_2$  in Ar ( $80 \pm 20$  K).

Sample	Raw	$R(1,1)^u$ Absorbance ( $\text{cm}^{-1}$ )			$R(1,0)$ Absorbance ( $\text{cm}^{-1}$ )		
		Gaussian	Normalized	Normalized Gaussian	Raw	Gaussian	Normalized Gaussian
1	3.65E-07	3.76E-07	1.20E-06	1.22E-06	4.11E-07	3.61E-07	9.83E-07
2	3.90E-07	3.57E-07	1.02E-06	1.04E-06	3.53E-07	3.38E-07	8.62E-07
3	4.22E-07	3.91E-07	1.21E-06	1.24E-06	3.53E-07	3.38E-07	8.62E-07

Fraction  $para\text{-H}_3^+$  (%);  $\mu^2$ -corrected.

Sample	Fraction $para\text{-H}_3^+$ (%); $\mu^2$ -corrected.				Boltzmann Corrected
	Un-Normalized	Un-Normalized Gaussian	Normalized Gaussian	Normalized Gaussian	
1	59.28	63.06	66.68	67.11	72.32
2	64.43	63.39	65.98	65.83	71.15
3	66.21	65.47	69.71	69.67	74.62

Average	63.31	63.98	67.46	67.54	72.70
Standard Deviation	3.60	1.31	1.98	1.95	1.77

Table A.5: Expansion data for a 90% enriched  $para\text{-H}_2$  ( $80 \pm 20$  K).

Sample	$R(1,1)^u$ Absorbance ( $\text{cm}^{-1}$ )			$R(1,0)$ Absorbance ( $\text{cm}^{-1}$ )		
	Raw	Gaussian	Normalized	Normalized	Raw	Gaussian
1	5.55E-07	5.80E-07	1.71E-06	1.46E-06	1.31E-06	-
2	5.55E-07	5.80E-07	1.71E-06	1.46E-06	1.20E-06	1.21E-06
3	3.64E-07	3.99E-07	4.15E-06	3.91E-06	1.31E-06	-
4	3.64E-07	3.99E-07	4.15E-06	3.91E-06	1.20E-06	1.21E-06

Fraction  $para\text{-H}_3^+$  (%);  $\mu^2$ -corrected.

Sample	Un-Normalized			Normalized		
	Un-Normalized	Un-Normalized	Gaussian	Normalized	Normalized	Boltzmann Corrected
1	40.99	-	-	59.98	-	-
2	43.12	44.00	-	58.12	54.60	60.63
2 3	31.29	-	-	78.44	-	-
4	33.21	35.09	-	77.10	76.31	80.48

Average	37.15	39.55	68.41	65.45	70.55
Standard Deviation	5.78	6.30	10.85	15.35	14.04

Table A.6: Expansion data for a 75% enriched  $para\text{-H}_2$  ( $80 \pm 20$  K).  $R(1,0)$  data for points 1 and 3 could not be fit with a Gaussian curve.

$p_3$				
	T=290 K	310 K	330 K	(1,0)/(1,1)
1	0.8800	0.8808	0.8814	0.2435
2	0.8777	0.8785	0.8792	0.2489
3	0.8864	0.8871	0.8878	0.2289
4	0.8837	0.8844	0.8851	0.2351
5	0.8807	0.8815	0.8821	0.2419
6	0.8803	0.8810	0.8817	0.2429

Table A.7: Hollow cathode cell data for  $p_2=.990\pm.005$ ,  $(1)/(0)=.018\pm.005$ ,  $(310\pm 20\text{ K})$ .

$p_3$				
	T=290 K	310 K	330 K	(1,0)/(1,1)
1	0.8797	0.8805	0.8812	0.2442
2	0.8814	0.8822	0.8829	0.2402
3	0.8832	0.8840	0.8847	0.2361
4	0.8792	0.8800	0.8807	0.2454
5	0.8804	0.8813	0.8819	0.2426
6	0.8834	0.8842	0.8848	0.2356
7	0.8785	0.8793	0.8800	0.2470
8	0.8800	0.8808	0.8815	0.2435
9	0.8835	0.8843	0.8849	0.2355

Table A.8: Hollow cathode cell data for  $p_2=.989\pm.005$ ,  $(1)/(0)=.020\pm.005$ ,  $(310\pm 20\text{ K})$ .

$p_3$				
	T=290 K	310 K	330 K	(1,0)/(1,1)
1	0.7803	0.7816	0.7827	0.5028
2	0.7802	0.7815	0.7826	0.5030
3	0.7821	0.7833	0.7844	0.4976
4	0.7793	0.7806	0.7817	0.5057
5	0.7807	0.7819	0.7830	0.5017
6	0.7814	0.7827	0.7838	0.4995
7	0.7787	0.7800	0.7811	0.5075
8	0.7790	0.7802	0.7814	0.5067
9	0.7814	0.7827	0.7838	0.4995

Table A.9: Hollow cathode cell data for  $p_2=.809\pm.007$ ,  $(1)/(0)=.411\pm.007$ ,  $(310\pm 20\text{ K})$ .

$p_3$				
	T=290 K	310 K	330 K	(1,0)/(1,1)
1	0.7649	0.7662	0.7674	0.5490
2	0.7651	0.7664	0.7675	0.5484
3	0.7663	0.7677	0.7688	0.5445
4	0.7606	0.7619	0.7631	0.5622
5	0.7609	0.7622	0.7634	0.5613
6	0.7626	0.7640	0.7651	0.5558

Table A.10: Hollow cathode cell data for  $p_2=.757\pm.007$ ,  $(1)/(0)=.559\pm.007$ ,  $(310\pm 20\text{ K})$ .

$p_3$				
	T=290 K	310 K	330 K	(1,0)/(1,1)
1	0.6882	0.6898	0.6912	0.8090
2	0.6889	0.6905	0.6918	0.8068
3	0.6896	0.6912	0.6926	0.8038
4	0.6857	0.6872	0.6886	0.8188
5	0.6847	0.6863	0.6877	0.8223
6	0.6881	0.6897	0.6910	0.8096
7	0.6847	0.6863	0.6877	0.8223
8	0.6853	0.6869	0.6883	0.8202
9	0.6878	0.6894	0.6907	0.8107

Table A.11: Hollow cathode cell data for  $p_2=.659\pm.025$ ,  $(1)/(0)=.898\pm.025$ ,  $(310\pm 20\text{ K})$ .

$p_3$				
	T=290 K	310 K	330 K	(1,0)/(1,1)
1	0.5746	0.5764	0.5780	1.3219
2	0.5769	0.5787	0.5802	1.3099
3	0.5776	0.5794	0.5810	1.3060
4	0.5795	0.5813	0.5829	1.2957
5	0.5822	0.5840	0.5856	1.2813
6	0.5829	0.5847	0.5863	1.2779
7	0.5767	0.5784	0.5800	1.3110
8	0.5793	0.5811	0.5826	1.2971
9	0.5796	0.5814	0.5830	1.2953

Table A.12: Hollow cathode cell data for  $p_2=.441\pm.007$ ,  $(1)/(0)=2.205\pm.007$ ,  $(310\pm 20\text{ K})$ .

$p_3$				
	T=290 K	310 K	330 K	(1,0)/(1,1)
1	0.4924	0.4943	0.4959	1.8408
2	0.4918	0.4936	0.4953	1.8454
3	0.4999	0.5018	0.5034	1.7864
4	0.4999	0.5017	0.5033	1.7867
5	0.4980	0.4998	0.5014	1.8003
6	0.4983	0.5002	0.5018	1.7978

Table A.13: Hollow cathode cell data for  $p_2=.251$ ,  $(1)/(0)=5.189$  ( $310\pm 20$  K).

$p_3$				
	T=290 K	310 K	330 K	(1,0)/(1,1)
1	0.5001	0.5020	0.5036	1.7848
2	0.4992	0.5011	0.5027	1.7913
3	0.4903	0.4921	0.4937	1.8569
4	0.4925	0.4944	0.4960	1.8399
5	0.4973	0.4992	0.5007	1.8055
6	0.4976	0.4994	0.5011	1.8030

Table A.14: Hollow cathode cell data for  $p_2=.251$ ,  $(1)/(0)=5.189$  ( $310\pm 20$  K).



$p_3$				
	T=170 K	180 K	190 K	(1,0)/(1,1)
1	0.8615	0.8629	0.8641	0.2639
2	0.8601	0.8615	0.8628	0.2670
3	0.8606	0.8620	0.8633	0.2659
4	0.8586	0.8600	0.8613	0.2703
5	0.8601	0.8616	0.8628	0.2669
6	0.8580	0.8594	0.8607	0.2716
7	0.8565	0.8579	0.8592	0.2750
8	0.8567	0.8582	0.8594	0.2745
9	0.8574	0.8588	0.8601	0.2730

Table A.15: Hollow cathode cell data for  $p_2=.990\pm.005$ ,  $(1)/(0)=.013\pm.005$ ,  $(180\pm10$  K).

$p_3$				
	T=170 K	180 K	190 K	(1,0)/(1,1)
1	0.7486	0.7508	0.7528	0.5513
2	0.7463	0.7485	0.7505	0.5582
3	0.7491	0.7514	0.7533	0.5496
4	0.7456	0.7478	0.7498	0.5600
5	0.7452	0.7475	0.7494	0.5613
6	0.7474	0.7496	0.7516	0.5548
7	0.7440	0.7462	0.7482	0.5648
8	0.7464	0.7487	0.7505	0.5576
9	0.7454	0.7477	0.7497	0.5605

Table A.16: Hollow cathode cell data for  $p_2=.815\pm.007$ ,  $(1)/(0)=.289\pm.007$ ,  $(180\pm10$  K).

$p_3$				
	T=170 K	180 K	190 K	(1,0)/(1,1)
1	0.5002	0.5032	0.5058	1.6399
2	0.4992	0.5022	0.5049	1.6462
3	0.5052	0.5082	0.5108	1.6081
4	0.5049	0.5079	0.5105	1.6096
5	0.5061	0.5090	0.5117	1.6030
6	0.5057	0.5087	0.5113	1.6055

Table A.17: Hollow cathode cell data for  $p_2=.251$ ,  $(1)/(0)=3.791$ ,  $(180\pm10$  K).

$p_3$				
	T=120 K	130 K	140 K	(1,0)/(1,1)
1	0.8330	0.8365	0.8395	0.2991
2	0.8332	0.8368	0.8397	0.2986
3	0.8377	0.8412	0.8440	0.2891
4	0.8343	0.8378	0.8407	0.2964
5	0.8355	0.8390	0.8419	0.2937
6	0.8325	0.8360	0.8389	0.3003
7	0.8354	0.8389	0.8417	0.2940
8	0.8330	0.8365	0.8394	0.2992
9	0.8333	0.8368	0.8397	0.2986

Table A.18: Hollow cathode cell data for  $p_2=.989\pm.005$ ,  $(1)/(0)=.012\pm.005$ ,  $(130\pm 10\text{ K})$ .

$p_3$				
	T=120 K	130 K	140 K	(1,0)/(1,1)
1	0.7845	0.7888	0.7923	0.4099
2	0.7847	0.7892	0.7926	0.4093
3	0.7856	0.7899	0.7934	0.4072

Table A.19: Hollow cathode cell data for  $p_2=.900\pm.025$ ,  $(1)/(0)=.122\pm.025$ ,  $(130\pm 10\text{ K})$ .

$p_3$				
	T=120 K	130 K	140 K	(1,0)/(1,1)
1	0.6453	0.6511	0.6560	0.8201
2	0.6448	0.6506	0.6555	0.8221
3	0.6470	0.6528	0.6577	0.8141

Table A.20: Hollow cathode cell data for  $p_2=.637\pm.025$ ,  $(1)/(0)=.625\pm.025$ ,  $(130\pm 10\text{ K})$ .

# Appendix B

## Boltzmann distributions

The following tables include the partition functions and populations for *ortho*- and *para*-H<sub>3</sub><sup>+</sup> states. These tables include the Boltzmann corrections ( $B$ ) that were used throughout this work.

$$n_i = g_{J(i)} g_{I(i)} e^{-E_i/k_B T}$$

J	G	I	$g_J$	$g_I$	Energy	T (K)=290	295	300	305	310	315	320	325	330
1	1	0.50	3	2	64.12	6.0000	6.0000	6.0000	6.0000	6.0000	6.0000	6.0000	6.0000	6.0000
2	2	0.50	5	2	169.3	5.9344	5.9871	6.0385	6.0886	6.1375	6.1853	6.2319	6.2774	6.3218
2	1	0.50	5	2	237.36	4.2337	4.2958	4.3567	4.4165	4.4751	4.5326	4.5889	4.6443	4.6986
3	2	0.50	7	2	428.02	2.3015	2.3730	2.4443	2.5152	2.5858	2.6561	2.7260	2.7955	2.8646
3	1	0.50	7	2	494.78	1.6526	1.7135	1.7746	1.8357	1.8969	1.9580	2.0191	2.0802	2.1411
4	4	0.50	9	2	502.03	2.0496	2.1265	2.2036	2.2808	2.3580	2.4354	2.5127	2.5900	2.6672
5	5	0.50	11	2	729.02	0.8123	0.8590	0.9067	0.9554	1.0050	1.0554	1.1067	1.1588	1.2116
4	2	0.50	9	2	768.48	0.5464	0.5798	0.6140	0.6489	0.6846	0.7211	0.7583	0.7961	0.8347
4	1	0.50	9	2	833.58	0.3956	0.4220	0.4493	0.4773	0.5061	0.5356	0.5658	0.5968	0.6284
5	4	0.50	11	2	928.97	0.3012	0.3239	0.3475	0.3720	0.3973	0.4234	0.4504	0.4782	0.5067
5	2	0.50	11	2	1187.12	0.0837	0.0920	0.1008	0.1101	0.1199	0.1302	0.1411	0.1525	0.1644
6	5	0.50	13	2	1238.46	0.0767	0.0846	0.0931	0.1021	0.1116	0.1217	0.1324	0.1436	0.1553
5	1	0.50	11	2	1250.31	0.0612	0.0676	0.0744	0.0817	0.0894	0.0976	0.1062	0.1153	0.1248
7	7	0.50	15	2	1302.14	0.0645	0.0716	0.0791	0.0872	0.0958	0.1050	0.1147	0.1250	0.1358
6	4	0.50	13	2	1430.71	0.0295	0.0331	0.0370	0.0412	0.0457	0.0506	0.0558	0.0613	0.0672
8	8	0.50	17	2	1647.27	0.0132	0.0151	0.0171	0.0194	0.0219	0.0246	0.0275	0.0307	0.0342
6	2	0.50	13	2	1679.81	0.0086	0.0098	0.0112	0.0127	0.0144	0.0162	0.0182	0.0203	0.0227
6	1	0.50	13	2	1740.91	0.0063	0.0073	0.0084	0.0095	0.0108	0.0123	0.0138	0.0155	0.0174
7	5	0.50	15	2	1818.16	0.0050	0.0058	0.0067	0.0076	0.0087	0.0099	0.0113	0.0127	0.0143
8	7	0.50	17	2	1972.8	0.0026	0.0031	0.0036	0.0042	0.0048	0.0056	0.0064	0.0073	0.0083
7	4	0.50	15	2	2002.46	0.0020	0.0024	0.0028	0.0032	0.0037	0.0043	0.0049	0.0056	0.0064

$$Z(T) = \sum g_{J(i)} g_{I(i)} e^{-E_i/k_B T} =$$

$$B = n_{(1,1)}/Z(T) =$$

$$0.2441$$

$$0.2393$$

$$0.2347$$

$$0.2302$$

$$0.2258$$

$$0.2216$$

$$0.2175$$

$$0.2135$$

$$0.2096$$

Table B.1: Boltzmann distributions for *para*-H<sub>3</sub><sup>+</sup> (310±20 K).

$$n_i = g_{J(i)} g_{I(i)} e^{-E_i/k_B T}$$

J	G	I	$g_J$	$g_I$	Energy	T (K)=290	295	300	305	310	315	320	325	330
1	0	1.50	3	4	86.96	12.0000	12.0000	12.0000	12.0000	12.0000	12.0000	12.0000	12.0000	12.0000
3	3	1.50	7	4	315.35	9.0164	9.1912	9.3634	9.5331	9.7002	9.8648	10.0269	10.1866	10.3439
3	0	1.50	7	4	516.87	3.3174	3.4395	3.5618	3.6843	3.8068	3.9293	4.0517	4.1740	4.2962
4	3	1.50	9	4	658.72	2.1100	2.2140	2.3193	2.4259	2.5338	2.6428	2.7529	2.8640	2.9759
6	6	1.50	13	4	995.88	0.5721	0.6176	0.6649	0.7142	0.7653	0.8183	0.8732	0.9298	0.9883
5	3	1.50	11	4	1080.49	0.3181	0.3459	0.3750	0.4054	0.4373	0.4705	0.5050	0.5410	0.5783
5	0	1.50	11	4	1271.25	0.1235	0.1364	0.1502	0.1649	0.1804	0.1968	0.2142	0.2325	0.2517
6	3	1.50	13	4	1577.33	0.0320	0.0362	0.0409	0.0460	0.0515	0.0575	0.0639	0.0709	0.0783
7	6	1.50	15	4	1586.59	0.0352	0.0400	0.0451	0.0508	0.0569	0.0636	0.0707	0.0785	0.0868
9	9	1.50	19	4	2030.62	0.0049	0.0058	0.0068	0.0079	0.0092	0.0106	0.0122	0.0139	0.0159
7	3	1.50	15	4	2142.09	0.0022	0.0027	0.0031	0.0037	0.0043	0.0050	0.0058	0.0067	0.0077

$$Z(T) = \sum g_{J(i)} g_{I(i)} e^{-E_i/k_B T} =$$

$$B = n_{(1,0)}/Z(T) =$$

Table B.2: Boltzmann distributions for *ortho*-H<sub>3</sub><sup>+</sup> (310±20 K).

$$Z(T) =$$

$$B =$$

$n_i = g_{J(i)}g_{I(i)}e^{-E_i/k_B T}$										
J	G	I	$g_J$	$g_I$	Energy	T (K)=170	175	180	185	190
1	1	0.50	3	2	64.12	6.0000	6.0000	6.0000	6.0000	6.0000
2	2	0.50	5	2	169.3	4.1058	4.2116	4.3140	4.4131	4.5092
2	1	0.50	5	2	237.36	2.3079	2.4067	2.5038	2.5993	2.6931
3	2	0.50	7	2	428.02	0.6435	0.7026	0.7635	0.8260	0.8899
3	1	0.50	7	2	494.78	0.3657	0.4058	0.4478	0.4915	0.5367
4	4	0.50	9	2	502.03	0.4422	0.4916	0.5433	0.5972	0.6532
5	5	0.50	11	2	729.02	0.0791	0.0929	0.1082	0.1249	0.1431
4	2	0.50	9	2	768.48	0.0464	0.0550	0.0646	0.0752	0.0868
4	1	0.50	9	2	833.58	0.0267	0.0322	0.0384	0.0453	0.0530
5	4	0.50	11	2	928.97	0.0146	0.0180	0.0219	0.0264	0.0315
5	2	0.50	11	2	1187.12	0.0016	0.0022	0.0028	0.0035	0.0045
6	5	0.50	13	2	1238.46	0.0013	0.0017	0.0022	0.0028	0.0036
5	1	0.50	11	2	1250.31	0.0010	0.0013	0.0017	0.0022	0.0028
7	7	0.50	15	2	1302.14	0.0008	0.0011	0.0015	0.0020	0.0025
6	4	0.50	13	2	1430.71	0.0002	0.0003	0.0005	0.0006	0.0008
8	8	0.50	17	2	1647.27	0.0001	0.0001	0.0001	0.0002	0.0002
$Z(T) = \Sigma g_{J(i)}g_{I(i)}e^{-E_i/k_B T} =$						14.04	14.42	14.81	15.21	15.61
$B = n_{(1,1)}/Z(T) =$						0.4274	0.4160	0.4050	0.3945	0.3843

Table B.3: Boltzmann distributions for *para*-H<sub>3</sub><sup>+</sup> (180±10 K).

$n_i = g_{J(i)}g_{I(i)}e^{-E_i/k_B T}$										
J	G	I	$g_J$	$g_I$	Energy	T (K)=170	175	180	185	190
1	0	1.50	3	4	86.96	12.0000	12.0000	12.0000	12.0000	12.0000
3	3	1.50	7	4	315.35	4.0518	4.2819	4.5112	4.7393	4.9661
3	0	1.50	7	4	516.87	0.7360	0.8167	0.9009	0.9886	1.0795
4	3	1.50	9	4	658.72	0.2849	0.3271	0.3727	0.4217	0.4741
6	6	1.50	13	4	995.88	0.0237	0.0295	0.0364	0.0442	0.0533
5	3	1.50	11	4	1080.49	0.0098	0.0125	0.0156	0.0194	0.0238
5	0	1.50	11	4	1271.25	0.0020	0.0026	0.0034	0.0044	0.0056
6	3	1.50	13	4	1577.33	0.0002	0.0002	0.0003	0.0005	0.0007
7	6	1.50	15	4	1586.59	0.0002	0.0003	0.0004	0.0005	0.0007
9	9	1.50	19	4	2030.62	0.0000	0.0000	0.0000	0.0000	0.0000

$$Z(T) = \sum g_{J(i)}g_{I(i)}e^{-E_i/k_B T} =$$

$$B = n_{(1,0)}/Z(T) =$$

Table B.4: Boltzmann distributions for *ortho*-H<sub>3</sub><sup>+</sup> (180±10 K).

$$n_i = g_{J(i)} g_{I(i)} e^{-E_i/k_B T}$$

J	G	I	$g_J$	$g_I$	Energy	T (K)=120	125	130	135	140
1	1	0.50	3	2	64.12	6.0000	6.0000	6.0000	6.0000	6.0000
2	2	0.50	5	2	169.3	2.8335	2.9801	3.1221	3.2597	3.3928
2	1	0.50	5	2	237.36	1.2529	1.3614	1.4699	1.5781	1.6857
3	2	0.50	7	2	428.02	0.1783	0.2123	0.2494	0.2896	0.3326
3	1	0.50	7	2	494.78	0.0801	0.0985	0.1191	0.1421	0.1675
4	4	0.50	9	2	502.03	0.0944	0.1164	0.1414	0.1692	0.1998
5	5	0.50	11	2	729.02	0.0076	0.0104	0.0140	0.0184	0.0237
4	2	0.50	9	2	768.48	0.0039	0.0054	0.0074	0.0099	0.0129
4	1	0.50	9	2	833.58	0.0018	0.0026	0.0036	0.0049	0.0066
5	4	0.50	11	2	928.97	0.0007	0.0010	0.0015	0.0022	0.0030
5	2	0.50	11	2	1187.12	0.0000	0.0001	0.0001	0.0001	0.0002
6	5	0.50	13	2	1238.46	0.0000	0.0000	0.0001	0.0001	0.0001

$$Z(T) = \sum g_{J(i)} g_{I(i)} e^{-E_i/k_B T} =$$

$$10.45$$

$$10.79$$

$$11.13$$

$$11.47$$

$$11.83$$

$$B = n_{(1,1)}/Z(T) =$$

$$0.5740$$

$$0.5562$$

$$0.5391$$

$$0.5229$$

$$0.5074$$

Table B.5: Boltzmann distributions for *para*-H<sub>3</sub><sup>+</sup> (130±10 K).



$$n_i = g_{J(i)} g_{I(i)} e^{-E_i/k_B T}$$

J	G	I	$g_J$	$g_I$	Energy	T (K)=120	125	130	135	140
1	0	1.50	3	4	86.96	12.0000	12.0000	12.0000	12.0000	12.0000
3	3	1.50	7	4	315.35	1.8107	2.0203	2.2353	2.4547	2.6776
3	0	1.50	7	4	516.87	0.1616	0.1986	0.2402	0.2865	0.3375
4	3	1.50	9	4	658.72	0.0379	0.0499	0.0643	0.0812	0.1010
6	6	1.50	13	4	995.88	0.0010	0.0015	0.0022	0.0032	0.0046
5	3	1.50	11	4	1080.49	0.0003	0.0005	0.0007	0.0011	0.0016
5	0	1.50	11	4	1271.25	0.0000	0.0001	0.0001	0.0001	0.0002
6	3	1.50	13	4	1577.33	0.0000	0.0000	0.0000	0.0000	0.0000

$$Z(T) = \sum g_{J(i)} g_{I(i)} e^{-E_i/k_B T} =$$

$$B = n_{(1,0)}/Z(T) =$$

Table B.6: Boltzmann distributions for *ortho*-H<sub>3</sub><sup>+</sup> (130±10 K).

				$n_i = g_{J(i)} g_{I(i)} e^{-\Delta E_i / k_B T}$															
J	G	I	$g_J$	$g_I$	Energy	T (K)=60	65	70	75	80	85	90	95	100					
1	1	0.50	3	2	64.12	6.0000	6.0000	6.0000	6.0000	6.0000	6.0000	6.0000	6.0000	6.0000					
2	2	0.50	5	2	169.3	0.8029	0.9748	1.1511	1.3296	1.5083	1.6858	1.8611	2.0333	2.2018					
2	1	0.50	5	2	237.36	0.1570	0.2161	0.2841	0.3603	0.4435	0.5327	0.6269	0.7253	0.8270					
3	2	0.50	7	2	428.02	0.0023	0.0044	0.0079	0.0130	0.0201	0.0296	0.0416	0.0566	0.0745					
3	1	0.50	7	2	494.78	0.0005	0.0010	0.0020	0.0036	0.0061	0.0096	0.0143	0.0206	0.0285					
4	4	0.50	9	2	502.03	0.0005	0.0011	0.0022	0.0040	0.0068	0.0109	0.0164	0.0237	0.0330					
5	5	0.50	11	2	729.02	0.0000	0.0000	0.0000	0.0001	0.0001	0.0003	0.0005	0.0009	0.0015					
$Z(T) = \sum g_{J(i)} g_{I(i)} e^{-\Delta E_i / k_B T} =$						6.96	7.2	7.45	7.71	7.98	8.27	8.56	8.86	9.17					
$B = n_{(1,1)} / Z(T) =$						0.8617	0.8336	0.8056	0.7781	0.7514	0.7256	0.7008	0.6771	0.6545					

Table B.7: Boltzmann distributions for *para*-H<sub>3</sub><sup>+</sup> (80±20 K).

$$n_i = g_{J(i)} g_{I(i)} e^{-\Delta E_i / k_B T}$$

J	G	I	$g_J$	$g_I$	Energy	T (K)=60	65	70	75	80	85	90	95	100
1	0	1.50	3	4	86.96	12.0000	12.0000	12.0000	12.0000	12.0000	12.0000	12.0000	12.0000	12.0000
3	3	1.50	7	4	315.35	0.1171	0.1785	0.2561	0.3502	0.4605	0.5863	0.7268	0.8808	1.0471
3	0	1.50	7	4	516.87	0.0009	0.0021	0.0041	0.0073	0.0123	0.0193	0.0290	0.0416	0.0576
4	3	1.50	9	4	658.72	0.0000	0.0001	0.0003	0.0006	0.0012	0.0023	0.0039	0.0062	0.0096
6	6	1.50	13	4	995.88	0.0000	0.0000	0.0000	0.0000	0.0000	0.0000	0.0000	0.0001	0.0001

$$Z(T) = \sum g_{J(i)} g_{I(i)} e^{-\Delta E_i / k_B T} =$$

$$B = n_{(1,0)} / Z(T) = \quad 0.9903 \quad 0.9852 \quad 0.9788 \quad 0.9710 \quad 0.9620 \quad 0.9518 \quad 0.9405 \quad 0.9282 \quad 0.9150$$

Table B.8: Boltzmann distributions for *ortho*-H<sub>3</sub><sup>+</sup> (80±20 K).

# Appendix C

## Select derivations

This appendix describes how to calculate specific spin modification branching weights from the identity, hop, and exchange pathways for reaction (6.1). This derivation is presented in more detail than in [131]. The appendix also presents the steps taken to derive equation (6.20) from equation (6.18).

## C.1 Deriving the branching weights for the identity, hop and exchange reactions

In order to obtain the spin modification branching weights from the identity (6.10), hop (6.11), and exchange (6.12) pathways of,



one can use the same angular momentum algebra techniques described in [131] and Chapter 6. The calculation of the hop contribution is trivial, and simply requires the multiplication of the weighting coefficients from Table 6.3 (e.g. 12, 4, 12, and 4) by the proportion of reactions that proceed via the identity (1/10). The result is,

$$\begin{pmatrix} 6/5 & 0 & 0 & 0 \\ 0 & 2/5 & 0 & 0 \\ 0 & 0 & 6/5 & 0 \\ 0 & 0 & 0 & 2/5 \end{pmatrix} \quad (\text{C.2})$$

The ordering of the elements in this matrix matches the ordering of the reactants and products in Table 6.3.

Finding the branching weights for the hop reaction is slightly more complex. First, one can represent the outcome of the hop reaction as proceeding by two distinct steps, the breakup of an  $\text{H}_3^+$  into  $\text{H}^+$  and  $\text{H}_2$ , and the formation of an  $\text{H}_3^+$  from  $\text{H}^+$  and  $\text{H}_2$ . Using angular momentum algebra, the equation,



can be expressed as,

$$\mathcal{D}_1 \otimes \mathcal{D}_{1/2} \rightarrow \mathcal{D}_{3/2} \oplus \mathcal{D}_{1/2}, \quad (\text{C.4})$$

or,

$$\mathcal{D}_0 \otimes \mathcal{D}_{1/2} \rightarrow \mathcal{D}_{1/2}. \quad (\text{C.5})$$

These expressions are used to calculate the product branching weights that are attributable to the reactant  $\text{H}_2$  spin species. Using Frobenius reciprocity with equations (C.4) and (C.5),  $2\mathcal{D}_{1/2}$  for *para*- $\text{H}_3^+$ , and balancing the dimensions, one can write the expressions for,



as,

$$\mathcal{D}_{3/2} \rightarrow 4(\mathcal{D}_1 \otimes \mathcal{D}_{1/2}), \quad (\text{C.7})$$

and,

$$\mathcal{D}_{1/2} \rightarrow (\mathcal{D}_1 \otimes \mathcal{D}_{1/2}/6) \oplus (\mathcal{D}_0 \otimes \mathcal{D}_{1/2}/2). \quad (\text{C.8})$$

These two expressions are used to identify the product spin species given a particular  $\text{H}_3^+$  spin modification. Equations (C.4) and (C.5) as well as (C.7) and (C.8) provide all that is needed to derive the products from each reactant spin modification combination in the hop reaction. For example, if *ortho*- $\text{H}_3^+$  ( $I=3/2$ ) is combined with *ortho*- $\text{H}_2$  ( $I=1$ ), equation (C.4) shows that the  $\text{H}_3^+$  will be found in the ratio *ortho:para*=2:1 (based on the spin degeneracies of the products in equation

(C.4)), and equation (C.7) shows that all  $H_2$  will be in the *ortho* state. To further illustrate, consider the reaction between *para*- $H_3^+$  and *ortho*- $H_2$ . In this case, equation (C.4) shows that *ortho*- and *para*- $H_3^+$  will form in a 2:1 ratio (again, based on spin degeneracies), and equation (C.8) shows that *ortho*- and *para*- $H_2$  will form in a ratio of 1:1. Performing similar operations with the other two reactant permutations, it is possible to build a matrix in which the rows will sum to the total weight for each reactant combination.

$$\begin{pmatrix} 8 & 0 & 4 & 0 \\ 0 & 0 & 4 & 0 \\ 4 & 4 & 2 & 2 \\ 0 & 0 & 2 & 2 \end{pmatrix} \quad (C.9)$$

Finally, multiplying this matrix by 3/10 (the fraction of reactions that result in a hop), the result is,

$$\begin{pmatrix} 12/5 & 0 & 6/5 & 0 \\ 0 & 0 & 6/5 & 0 \\ 6/5 & 6/5 & 3/5 & 3/5 \\ 0 & 0 & 3/5 & 3/5 \end{pmatrix} \quad (C.10)$$

A matrix of branching weights for the exchange reaction can be obtained by subtracting the matrices (C.2) and (C.10) from the total values in Table 6.2, thereby obtaining the results depicted in Table 6.3.

## C.2 The detailed derivation of equation (6.20) from equation (6.18)

Substituting equations (6.13) and (6.15) into equation (6.18),

$$\frac{d}{dt}p_3 = \frac{[total-H_3^+]\frac{d}{dt}[p-H_3^+] - [p-H_3^+]\frac{d}{dt}[total-H_3^+]}{[total-H_3^+]^2},$$

results in,

$$\begin{aligned} \frac{d}{dt}p_3 = & \left[ [total-H_3^+] \left\{ k_1 \left( \frac{2}{3}[o-H_2] + [p-H_2] \right) [p-H_2^+] + k_1 \left( \frac{1}{3}[o-H_2] + \frac{2}{3}[p-H_2] \right) [o-H_2^+] \right. \right. \\ & + \left\{ k_H \left( -\frac{2}{3}[o-H_2] \right) + k_E \left( -\frac{1}{3}[o-H_2] - \frac{1}{3}[p-H_2] \right) - (k_{r(para)}[e_r^-] + \gamma_{(para)}) \right\} [p-H_3^+] \\ & + \left\{ k_H \left( \frac{1}{3}[o-H_2] + [p-H_2] \right) + k_E \left( \frac{1}{3}[o-H_2] + \frac{1}{3}[p-H_2] \right) \right\} [o-H_3^+] \Big\} \\ & - [p-H_3^+] \left\{ k_1 [total-H_2][total-H_2^+] - (k_{r(ortho)}[e_r^-] + \gamma_{(ortho)}) [o-H_3^+] \right. \\ & \left. \left. - (k_{r(para)}[e_r^-] + \gamma_{(para)}) [p-H_3^+] \right\} \right] [total-H_3^+]^{-2} \end{aligned} \quad (C.11)$$

Using  $p_3$  to simplify, this can be written as,

$$\begin{aligned}
\frac{d}{dt}p_3 = & \frac{1}{[total-H_3^+]} \left\{ k_1 \left( \frac{2}{3}[o-H_2] + [p-H_2] \right) [p-H_2^+] + k_1 \left( \frac{1}{3}[o-H_2] + \frac{2}{3}[p-H_2] \right) [o-H_2^+] \right\} \\
& + \left\{ k_H \left( -\frac{2}{3}[o-H_2] \right) + k_E \left( -\frac{1}{3}[o-H_2] - \frac{1}{3}[p-H_2] \right) - (k_{r(para)}[e_r^-] + \gamma_{(para)}) \right\} p_3 \\
& + \left\{ k_H \left( \frac{1}{3}[o-H_2] + [p-H_2] \right) + k_E \left( \frac{1}{3}[o-H_2] + \frac{1}{3}[p-H_2] \right) \right\} (1 - p_3) \\
& - p_3 \left\{ k_1 [total-H_2] \frac{[total-H_2^+]}{[total-H_3^+]} - (k_{r(ortho)}[e_r^-] + \gamma_{(ortho)}) (1 - p_3) \right. \\
& \left. - (k_{r(para)}[e_r^-] + \gamma_{(para)}) p_3 \right\}. \tag{C.12}
\end{aligned}$$

Multiplying the terms containing number densities of molecular hydrogen by  $[H_2]/[H_2]$  provides a means to insert the term  $p_2$ , giving,

$$\begin{aligned}
\frac{d}{dt}p_3 = & \frac{[total-H_2]}{[total-H_3^+]} \left\{ k_1 \left( \frac{2}{3}(1 - p_2) + p_2 \right) [p-H_2^+] + k_1 \left( \frac{1}{3}(1 - p_2) + \frac{2}{3}p_2 \right) [o-H_2^+] \right\} \\
& + \left\{ [total-H_2] \left( k_H \left( -\frac{2}{3}(1 - p_2) \right) + k_E \left( -\frac{1}{3}(1 - p_2) - \frac{1}{3}p_2 \right) \right) - (k_{r(para)}[e_r^-] + \gamma_{(para)}) \right\} p_3 \\
& + \left\{ k_H \left( \frac{1}{3}(1 - p_2) + p_2 \right) + k_E \left( \frac{1}{3}(1 - p_2) + \frac{1}{3}p_2 \right) \right\} (1 - p_3) [total-H_2] \\
& - p_3 \left\{ k_1 [total-H_2] \frac{[total-H_2^+]}{[total-H_3^+]} - (k_{r(ortho)}[e_r^-] + \gamma_{(ortho)}) (1 - p_3) \right. \\
& \left. - (k_{r(para)}[e_r^-] + \gamma_{(para)}) p_3 \right\}. \tag{C.13}
\end{aligned}$$

Grouping the terms with common rate coefficients gives,

$$\begin{aligned}
\frac{d}{dt}p_3 = & k_1 \frac{[total-H_2]}{[total-H_3^+]} \left\{ \left( \frac{2}{3} + \frac{1}{3}p_2 \right) [p-H_2^+] + \left( \frac{1}{3} + \frac{1}{3}p_2 \right) [o-H_2^+] - [total-H_2^+] p_3 \right\} \\
& + \left\{ (k_{r(ortho)} - k_{r(para)}) [e_r^-] + (\gamma_{ortho} - \gamma_{para}) \right\} p_3 \\
& - \left\{ (k_{r(ortho)} - k_{r(para)}) [e_r^-] + (\gamma_{ortho} - \gamma_{para}) \right\} p_3^2 \\
& + k_H [total-H_2] \left( \frac{2}{3}p_2 - p_3 + \frac{1}{3} \right) + k_E [total-H_2] \left( \frac{1}{3} - \frac{2}{3}p_3 \right). \tag{C.14}
\end{aligned}$$

With slight rearrangement this becomes,

$$\begin{aligned}
\frac{d}{dt}p_3 = & k_1[total-H_2] \left\{ \left( \frac{2}{3} + \frac{1}{3}p_2 \right) \frac{[p-H_2^+]}{[total-H_3^+]} + \left( \frac{1}{3} + \frac{1}{3}p_2 \right) \frac{[o-H_2^+]}{[total-H_3^+]} - \frac{[total-H_2^+]}{[total-H_3^+]} p_3 \right\} \\
& + \left\{ (k_{r(ortho)} - k_{r(para)})[e_r^-] + (\gamma_{ortho} - \gamma_{para}) \right\} p_3 \\
& - \left\{ (k_{r(ortho)} - k_{r(para)})[e_r^-] + (\gamma_{ortho} - \gamma_{para}) \right\} p_3^2 \\
& + k_H[total-H_2] \left( \frac{2}{3}p_2 - p_3 + \frac{1}{3} \right) + k_E[total-H_2] \left( \frac{1}{3} - \frac{2}{3}p_3 \right),
\end{aligned} \tag{C.15}$$

which can be simplified to,

$$\begin{aligned}
\frac{d}{dt}p_3 = & k_1[total-H_2] \left\{ \frac{2}{3} \frac{[p-H_2^+]}{[total-H_3^+]} + \frac{1}{3} \frac{[o-H_2^+]}{[total-H_3^+]} + \left( \frac{1}{3}p_2 - p_3 \right) \frac{[total-H_2^+]}{[total-H_3^+]} \right\} \\
& + \left\{ (k_{r(ortho)} - k_{r(para)})[e_r^-] + (\gamma_{ortho} - \gamma_{para}) \right\} p_3 \\
& - \left\{ (k_{r(ortho)} - k_{r(para)})[e_r^-] + (\gamma_{ortho} - \gamma_{para}) \right\} p_3^2 \\
& + k_H[total-H_2] \left( \frac{2}{3}p_2 - p_3 + \frac{1}{3} \right) + k_E[total-H_2] \left( \frac{1}{3} - \frac{2}{3}p_3 \right),
\end{aligned} \tag{C.16}$$

which is equation (6.20).



# Appendix D

## Schematics

This appendix includes the electrical diagrams for some of the components used in this work. The figure annotations describe the purpose of the component, as well as the origin of its design.



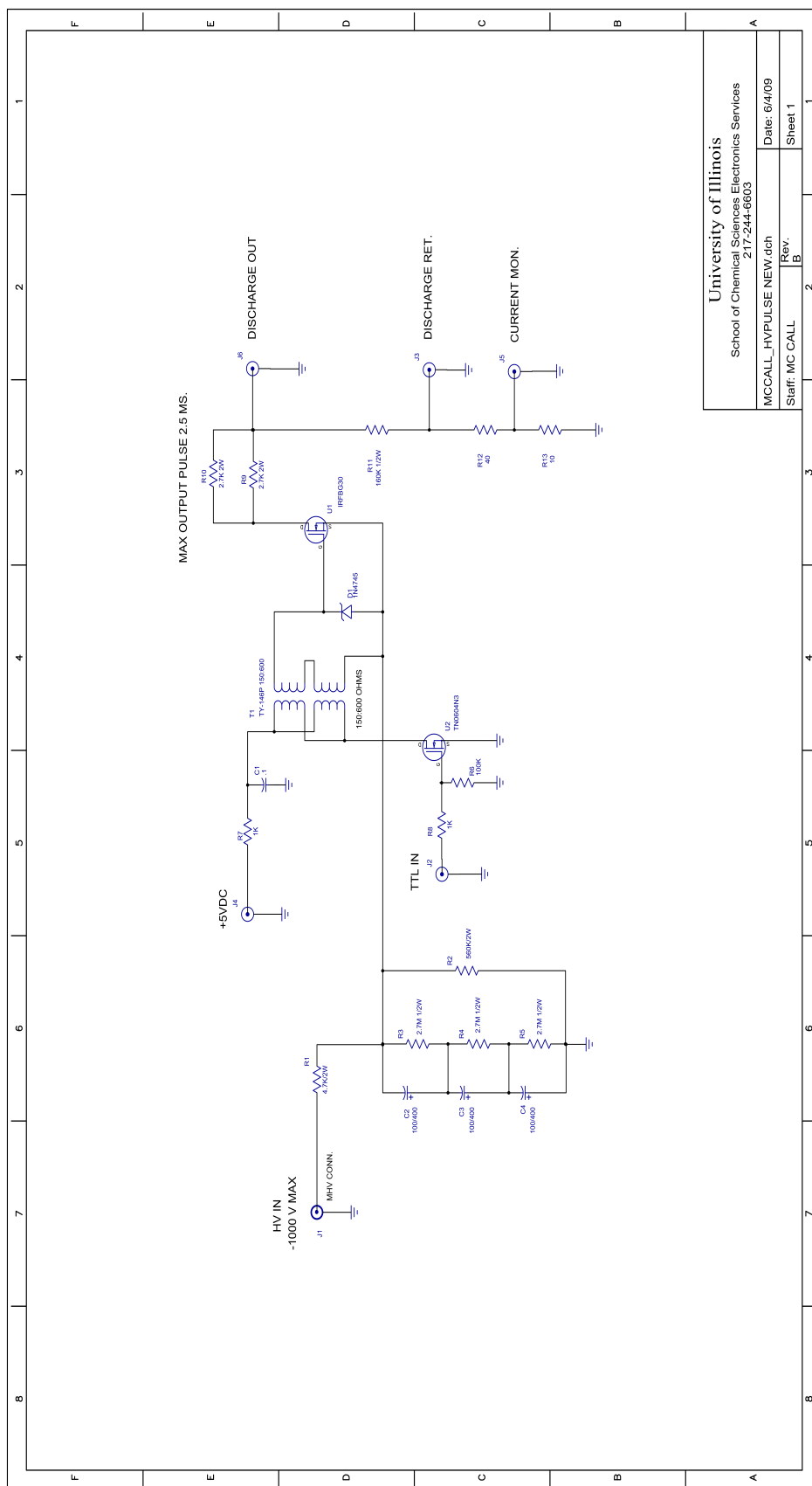


Figure D.2: The pulse driver used to activate the source valve in the pulsed experiments. This device was modeled after a driver designed and built at UC Berkeley. Upon receiving a TTL trigger pulse, the device sends a high voltage (HV) pulse for the length of the input TTL, up to 2.5 ms. Coaxial connections include the HV out and return, the TTL and HV inputs, and an output which allows the operator to monitor the current drawn across the HV terminals. The maximum input and output voltage is -1000 V. (Drawn by J. Wentz)

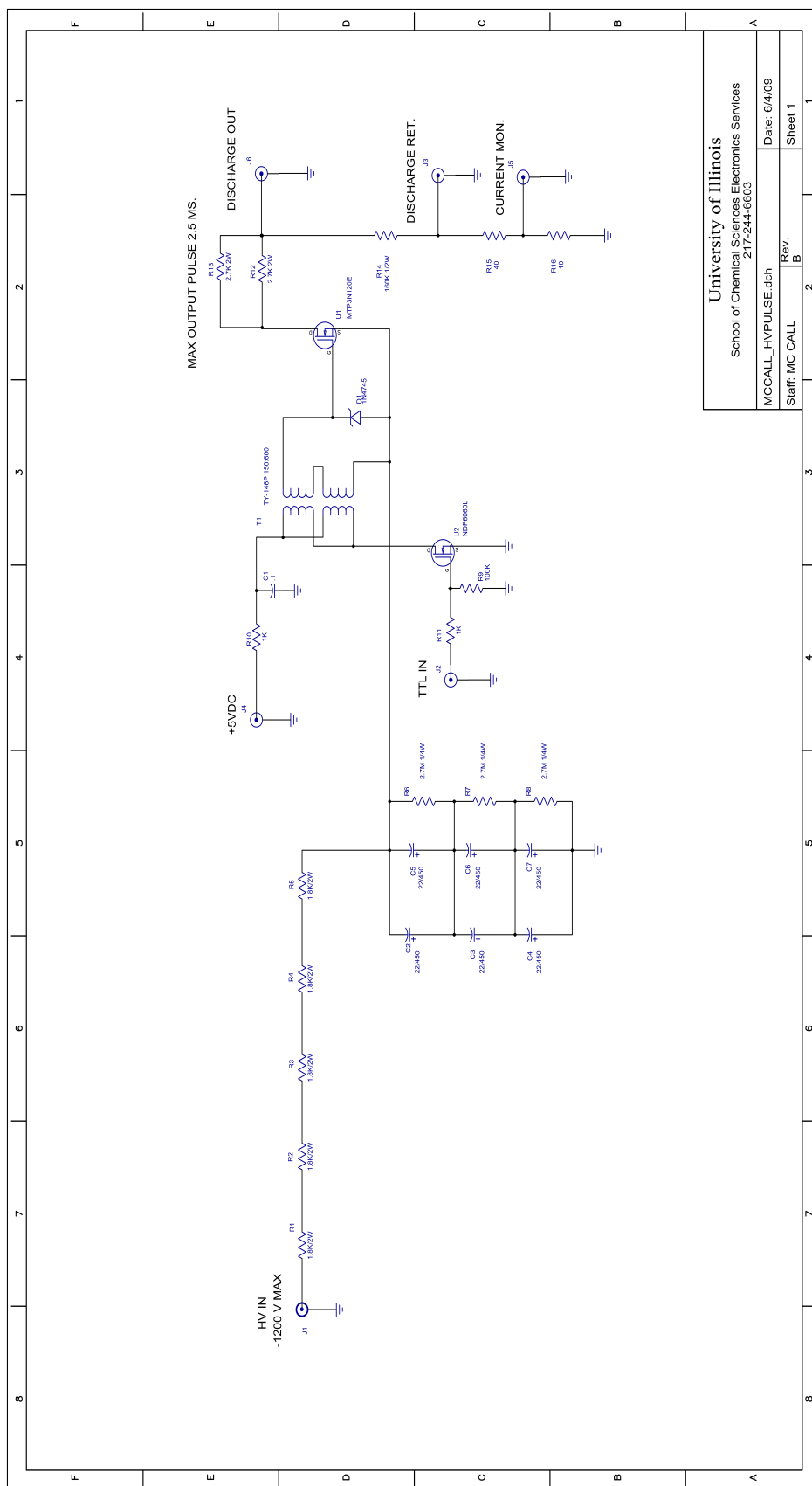


Figure D.3: The high voltage pulse driver that was used to modulate the discharge voltage for the pulsed experiments. This driver was designed and built at UC Berkeley. Upon receiving a TTL trigger pulse, the device sends an HV pulse for the length of the input TTL, up to 2.5 ms. Coaxial connections include the HV out and return, an input for a 5V power supply and the HV, the TTL input, and an output which allows the operator to monitor the current drawn across the HV terminals. The maximum input and output voltage is -1200 V. (Drawn by J. Wentz)

## Appendix E

# Solid hydrogen experiment

This appendix describes the solid hydrogen experiment. The purpose of the experiment was to measure the index of refraction of solid hydrogen with the ultimate goal of constructing a Raman laser. The first section describes the experiment and how to make a solid hydrogen crystal. The second section presents the data analysis procedures.

## E.1 Experimental details

The experiment was designed to measure the index of refraction of solid hydrogen at 3 to 4 different wavelengths. Specifically, at 632 nm (produced by a HeNe laser), and at 514, 496, and 476 nm (produced by an Ar ion laser). The crystal is formed in a small stainless steel cell that is coupled to the cold head of a liquid He cryostat (Infrared Laboratories). The cell is designed with two circular openings through which the laser beam is able to pass. The openings are covered by sapphire windows, one of which is intentionally tilted with respect to the incident beam. This angle induces a deflection of the beam that is dependent on the index of refraction of the solid hydrogen. The key experimental details include:

- 1) Manufacturing and installing the indium gaskets that seal the sapphire windows to the cell.
- 2) Temperature controller settings.
- 3) Making the solid hydrogen crystal.
- 4) Taking the measurements.

Each will be discussed, in turn, below.

### E.1.1 Indium gaskets

The indium used to form the gaskets comes in small tube-like strands 1-2 mm in diameter. The surfaces that are to be sealed together with the gaskets should be cleaned of dirt and old material. This can be done using a razor blade and extremely fine sandpaper (400, followed by Emery 352, Behr-Manning, Norton Abrasives or equivalent), but care should be taken to prevent scratching the surfaces (the sapphire windows usually do not need to be cleaned in this manner). The final preparatory step is a wash with methanol followed by air drying.

A small strand of indium is cut to a length that will produce a circumference that is slightly larger than desired. Using gloves, a clean surface, a razor, and small wooden sticks to manipulate the indium, make an angled cut at either end of the indium. The freshly cut sections should immediately be joined and pressed together using the wooden sticks. The indium ends will cold solder together within a minute. After the gasket is formed, it should be immersed in 1 M HCl, then dipped in methanol. The gasket should be placed on the solid hydrogen cell surface, followed by the sapphire window. The window is then tightened onto the cell using screws, which will compress the indium gasket between the surfaces. The installation and compression of the indium gasket should occur within one minute of the HCl/methanol cleaning to minimize the amount of oxidized film that forms on the surface of the gasket.

### E.1.2 Temperature controller

The same temperature controller (Lakeshore) used for the *para*-H<sub>2</sub> converter is also used to control the liquid He cryostat in which the solid hydrogen crystal is formed. For this reason, careful experimental timing is required with regards to production of parahydrogen for the crystal (necessary to prevent crystal boil-off upon the exothermic *ortho* to *para* conversion), and the formation of the crystal itself.

There are a total of two temperature sensing channels in the temperature controller. In addition, there are two temperature sensors in the cryostat (silicon diode and germanium). It is important

to connect the temperature sensors to the correct channel on the temperature controller, because the appropriate temperature response curves are only installed in certain channels. Channel A should be connected to the germanium sensor that measures the temperature of the cell itself, and channel B should be connected to the silicon sensor that measures the temperature of the cold head. The former will only show correct temperatures at or below 100 K. In addition to connecting the components properly, the channels must be set so that the correct temperature curves are used. This is done by adjusting the small toggle settings at the back of the controller (underneath the respective connectors). Only the last three toggles need to be adjusted as the first toggles do not matter. The correct settings are ‘110’ for Ge, and ‘101’ for Si. The silicon diode sensor on the closed-cycle He cryostat requires a setting of ‘111.’

The gain, rate, and reset should be set to 200, 40, and 300, respectively. The resistive heater response should be set to ‘-1’ or ‘max’ as anything less will not provide the necessary temperature control authority.

### E.1.3 Making the crystal

After ensuring the cryostat and cell are sufficiently leak-proof ( $\sim 1 \times 10^{-10}$  L atm s<sup>-1</sup>), the cell, lines, and vacuum sleeve should be evacuated. It is important to continue pumping the vacuum sleeve using a sealed-oil molecular turbopump throughout the experiment (the pressure measured by this pump also being a good indicator for leaks). The cryostat is first cooled by filling both the inner and outer dewars with liquid N<sub>2</sub>. After a period of hours, the operator can expect the cryostat to cool to 78-80 K. When the operator is ready to proceed with crystal production, the liquid N<sub>2</sub> should be purged from the inner (He) dewar. This is accomplished by sealing the opening of the dewar with a stopper that has a gaseous N<sub>2</sub> input line and a outflow tube long enough for one end to be immersed in the liquid N<sub>2</sub> in the bottom of the dewar. Care should be taken to ensure all of the liquid has been blown out before introducing the liquid He, otherwise a large ice block will form in the dewar.

The next step is to introduce the liquid He into the purged inner dewar. This will begin cooling the cell to the 15-20 K temperature target for the phase change of H<sub>2</sub> from gas to liquid. Once established in this temperature range, begin introducing the H<sub>2</sub> which will fill the cell as a liquid. After the cell is filled, slowly raise the temperature of the cell to 30-40 K in order to boil the liquid. Reserve this gas in a small teflon-lined cylinder (attached via 1/4-inch high pressure stainless steel tubing). This step is important because it is necessary to form the crystal under high pressure.

Re-fill the cell with a new batch of *para*-H<sub>2</sub> liquid. Once the cell is full, apply 10-30 atm of backing pressure to the liquid in the cell using the reserved gas from the small sample vessel. Begin lowering the temperature in the cryostat. The operator should observe crystal formation beginning between 12-15 K. The temperature can be adjusted using either the resistive heater (adjusted via the temperature controller) or the mechanical heat switch that connects the cold head table inside the cryostat to the dewar. Once the temperature is adjusted using the latter, the heat switch can be decoupled from the outer sleeve by sliding the knob outwards from the cryostat.

### E.1.4 Taking index measurements

A key assumption in this experiment is that all optical surfaces encountered by the laser beam are normal to the direction of beam propagation, except for the intentionally tilted window. The beam height is measured using a photodiode detector (Thorlabs Det 210) mounted on translation stages (Thorlabs PT-1). The beam is made level with the surface of the optics bench (within 5-10 thousands of an inch over the length of the table) to ensure that the measured deflection is primarily due to the tilted window/solid-H<sub>2</sub> interface.

The height of the beam is measured in two locations downstream of the cryostat. In addition, similar measurements are taken for a material of known index, such as liquid H<sub>2</sub>. It was discovered that the latter measurement is best taken after the crystal measurements. Convection currents do not seem to form in a liquid that forms from the melted solid in contrast to the liquid that is condensed from the gas.

## E.2 Data analysis

As mentioned earlier, the key assumption in the index data analysis is a beam that is normal to all optical surfaces but one. Snell's law and trigonometric relationships can be used to solve a system as depicted in Figure E.1 for the change in direction of a beam propagating from the solid hydrogen into the tilted sapphire window.

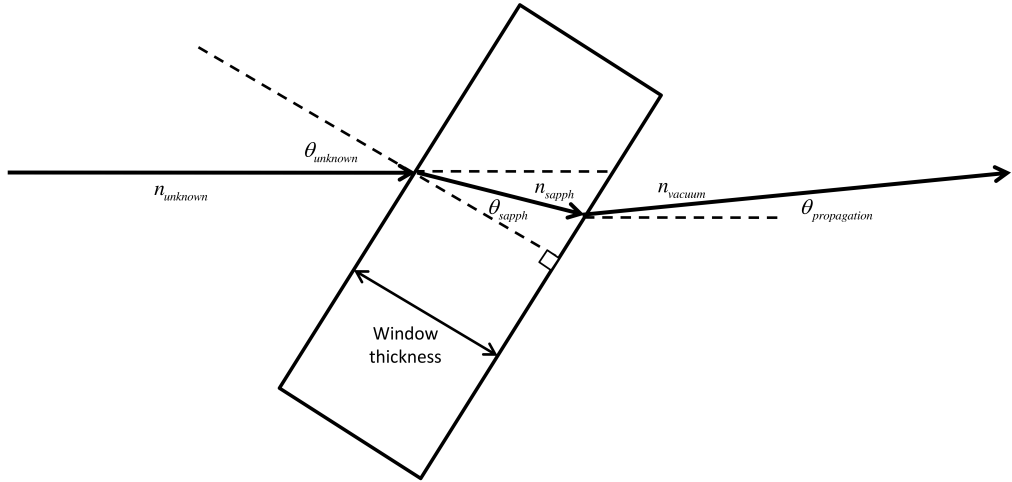


Figure E.1: The direction of travel for a beam propagating through the intentionally tilted window of the solid hydrogen cell.

In fact, it is possible to derive a complex trigonometric relationship that describes the vertical deflection of a beam as it passes through all the windows of a cryostat, however, taking measurements at different distances downstream of the cryostat collapses the relationship to a much simpler form



that is dependent on only a few variables. The equation,

$$D = A \cdot \tan \left\{ \arcsin \left( \frac{n_v}{n_a} \sin \left( \arcsin \left( \frac{n_u}{n_v} \sin (\theta_u) - \theta_u \right) \right) \right) \right\}, \quad (\text{E.1})$$

describes the vertical deflection of the beam ( $D$ ) in terms of the horizontal distance between measurement locations ( $A$ ), the index of refraction of air, vacuum, and the unknown sample ( $n_a$ ,  $n_v$ ,  $n_u$ ), and the vertical angle between the incident beam and the intentionally tilted window ( $\theta_u$ ). This equation is first solved for  $\theta_u$  using a substance of known index (e.g. liquid H<sub>2</sub>). Once the angle is known, the equation can be solved for  $n_u$  using data taken with an unknown sample. It is important that neither the path of the beam nor the position of the cryostat change between these measurements.

Due to the nature of equation (E.1) it is necessary to solve for  $\theta_u$  and  $n_u$  numerically. A program was written in Fortran 95 that allows the operator to input the measured  $D$  and  $A$ , along with various environmental conditions used for the precise calculation of  $n_a$ . The code is shown below so that it can be used for future experiments, or the pertinent constants can be picked out if designing new programs for analysing the data.

---

```

MODULE constants2

IMPLICIT NONE

INTEGER, PARAMETER :: dp = SELECTED_REAL_KIND(13)
REAL(dp), PARAMETER :: pi = 3.141592653589793238462643383279502884197_dp
LOGICAL :: airBit=.False.

END MODULE constants2

```

---

```

MODULE solidhydrogenmod

USE constants2, ONLY: pi,dp,airbit
IMPLICIT NONE

CONTAINS

SUBROUTINE anglefinder(j,z,a,nv,knownindex,tolerance,thetaUnknown)
!Purpose: This subroutine will calculate the angle of the cell window
!using either a measured change in height with vacuum in the cell, or
!a sample of known index.

USE constants2, ONLY: pi,dp
IMPLICIT NONE

!Declare intents
INTEGER(dp), INTENT(IN):: j
REAL(dp), INTENT(IN):: z
REAL(dp), INTENT(IN):: a
REAL(dp), INTENT(IN):: knownindex
REAL(dp), INTENT(IN):: tolerance

```

```

REAL(dp), INTENT(IN):: nv
REAL(dp), INTENT(OUT):: thetaUnknown

!Declare local variables
REAL(dp):: s=.125_dp      !sapphire window thickness
REAL(dp):: sapphIndex=1.75755_dp !index of sapphire windows at 640 nm
REAL(dp):: zTemp=0._dp    !the calculated vertical distance
REAL(dp):: delta=10._dp   !the difference between zTemp and z
REAL(dp):: thetaTemp=0._dp !the dummy value of theta used analysis
REAL(dp):: step=.000001_dp !value of theta step
REAL(dp):: na              !the index of refraction of air

IF (j==2 .AND. airbit == .False.) THEN
    CALL airIndexFinder(na)
END IF

!Reset variables
thetaTemp=0._dp
delta=10._dp

!Calculate thetaUnknown
DO WHILE (delta > tolerance .AND. thetaTemp <=pi/2._dp)

SELECT CASE (j)

    CASE(1) !when z is known and vacuum is used

        ! Calculate zTemp
        zTemp=(s)*Sin(thetaTemp-ASin((knownindex/sapphIndex)*Sin(thetaTemp)))&
            &/Cos(ASin((knownindex/sapphIndex)*Sin(thetaTemp)))

    CASE(2)

        ! Calculate zTemp
        zTemp=a*Tan(ASin((nv/na)*Sin(ASin((knownindex/nv)*Sin(thetaTemp))-thetaTemp)))

END SELECT

!Write(*,*) ztemp,thetaTemp*180._dp/pi,delta !for diagnosis

!Test for convergence
delta=Abs(zTemp-z)

!Increment thetaTemp
thetaTemp=thetaTemp+step

END DO

thetaUnknown=thetaTemp*180._dp/pi !convert from radians to degrees

END SUBROUTINE

```

---

```

SUBROUTINE indexfinder(thetaUnknown,a,z,nv,tolerance,unknownIndex)

!Purpose: This subroutine will calculate the unknown index of the media

```

```

USE constants2, ONLY: pi,dp
IMPLICIT NONE

!Declare intents
REAL(dp), INTENT(IN):: thetaUnknown
REAL(dp), INTENT(IN):: a
REAL(dp), INTENT(IN):: z
REAL(dp), INTENT(IN):: nv
REAL(dp), INTENT(IN):: tolerance
REAL(dp), INTENT(OUT):: unknownIndex

!Declare local variables
REAL(dp):: zTemp=0._dp      !the calculated vertical distance
REAL(dp):: delta=10._dp     !the difference between zTemp and z
REAL(dp):: tempIndex=0._dp  !the dummy value of index used for analysis
REAL(dp):: step=.000001_dp  !value of index step
REAL(dp):: na               !the index of refraction of air
REAL(dp):: tempTheta        !working value of window angle (in radians)
INTEGER:: l                 !index

!Calculate index of lab air
Call airIndexFinder(na)

!Reset variables
unknownIndex=0._dp
Delta=10._dp
tempTheta=thetaUnknown*pi/180._dp

!Calculate the index of the media (solid hydrogen)
l=1

DO WHILE (delta > tolerance .AND. unknownIndex <= 2._dp)

    zTemp=a*Tan(ASin((nv/na)*Sin(ASin((tempindex/nv)*Sin(tempTheta))-tempTheta)))

    !Test for convergence
    delta=Abs(zTemp-z)

    !Increment thetaTemp
    tempIndex=tempIndex+step

!write(*,*) delta ,ztemp ,tempindex
l=l+1
END DO

!Set index value
unknownIndex=tempIndex

END SUBROUTINE

```

---

```

SUBROUTINE airIndexFinder(na)

!Purpose: This subroutine calculates the index of refraction of lab air

```

```

USE constants2, ONLY: pi,dp
IMPLICIT NONE

!Declare intents
REAL(dp), INTENT(OUT):: na

!Declare local variables
REAL(dp):: airIndex=.00027656    !the index of refraction at 630 nm (n-1)
REAL(dp):: correction            !the value by which to multiply n-1 to correct
REAL(dp):: t                    !temperature
REAL(dp):: p                    !pressure
REAL(dp):: pressure=101325._dp   !the ambient pressure
REAL(dp):: temperature=15._dp   !the ambient temperature
CHARACTER(len=5):: defaultAnswer !the answer y or n

!Preparatory work: calculate the index of refraction of air at 630 nm
WRITE(*,*) ' '
WRITE(*,*) 'Please give me some information with which to calculate '
WRITE(*,*) 'the index of refraction of air in the lab.'
WRITE(*,*) ' '
WRITE(*,*) 'Do you want to use default values of 15 deg C and 101325 Pascals? (y/n)'
READ(*,*) defaultAnswer

IF (defaultAnswer=='n') THEN
    WRITE(*,*) 'What was the temperature in the lab (in degrees C)?'
    READ(*,*) t
    WRITE(*,*) 'What was the pressure in the lab (in Pascals)?'
    READ(*,*) p
ELSE
    t=temperature
    p=pressure
END IF

!Calculate correction factor
correction=p*(1._dp + p*(61.3_dp - t)*.0000000001)&
&/(96095.4_dp*(1._dp + 0.003661_dp*t))

!Apply correction factor
na=1._dp + correction*airIndex

!Write results
WRITE(*,*) ' '
WRITE(*,*) 'The index of refraction of the lab air was:',na

!Set airbit
!airbit=.True.

END SUBROUTINE

END MODULE



---


PROGRAM solidhydrogenprog
!
!Purpose:

```

```

!To find the angle of interest in the infrared laboratories cryostat or to find
!the index of refraction of an unknown.
!
USE constants2 , ONLY:dp
USE solidhydrogenmod

IMPLICIT NONE

!Parameter declaration
REAL(dp):: d                !the value of offset in the z axis
REAL(dp):: thetaUnknown     !the value of the unknown angle
REAL(dp):: knownIndex       !the index of refraction of the known media
REAL(dp):: unknownIndex     !the index of refraction that is unknown
REAL(dp):: a                !the distance of y-axis translation for the detector
REAL(dp):: nv=1.0_dp        !the index of refraction of vacuum
REAL(dp):: nu               !the unknown index of refraction
REAL(dp):: z               !the vertical displacement of the beam
REAL(dp):: tolerance=.00001 !the tolerance value to be used in convergence
INTEGER:: i,j              !the answers to initial operator questions
CHARACTER(len=5):: answer='y' !the answer to continue or not to continue

!Ask the operator what he or she wants to do

DO WHILE (answer=='y' .AND. i/=3)
WRITE(*,*) 'Do you want to calculate an unknown angle (1),an index (2), or Exit (3)?'
READ(*,*) i

SELECT CASE (i)
CASE (1)
WRITE(*,*) 'Are you calculating using a delta z and vacuum in the cell (1),'
WRITE(*,*) 'or using a known standard (2)?'
READ(*,*) j
SELECT CASE (j)
CASE (1)
WRITE(*,*) 'What is the observed change in beamheight (z, in inches)?'
!the above value is absolute inches, the '-' sign is incorporated
!in the calc.
READ(*,*) z
knownIndex=nv
CASE (2)
WRITE(*,*) 'What is the index of refraction of the known sample (n)?'
READ(*,*) knownIndex
WRITE(*,*) 'What horizontal distance did you move the detector (inches)?'
READ(*,*) a
WRITE(*,*) 'What was the observed change in beamheight (z, in inches)?'
READ(*,*) z
END SELECT

CALL anglefinder(j,z,a,nv,knownindex,tolerance ,thetaUnknown)

!Write results
WRITE(*,*) ' '
WRITE(*,*) 'The angle of the window on the cell is:', thetaUnknown

```

```

CASE (2)
    WRITE(*,*) 'What horizontal distance did you move the detector (in inches)?'
    READ(*,*) a
    WRITE(*,*) 'What was the observed change in beamheight (z, in inches)?'
    READ(*,*) z
    WRITE(*,*) 'What is the value of the window angle (in degrees)?'
    READ(*,*) thetaUnknown

    CALL indexfinder(thetaUnknown,a,z,nv,tolerance , unknownIndex)

    !Write results
    WRITE(*,*) 'The calculated index of refraction is:', unknownIndex

    END SELECT

IF (i/=3) THEN
    WRITE(*,*) ' '
    WRITE(*,*) 'Would you like to perform another operation? (y/n)'
    READ(*,*) answer
END IF

END DO

WRITE(*,*) ' '
WRITE(*,*) 'Goodbye valiant refraction explorer!'

END PROGRAM

```

# Author's biography

Brian Tom was born in Los Angeles, California. After graduation from the University of California at San Diego, he was commissioned in the United States Air Force. He has spent most of his career flying as a navigator, and recently returned to the physical sciences in preparation for a teaching assignment at the Air Force Academy.